



International Journal of
Molecular Sciences

Atherosclerosis and Vascular Imaging 2016

Edited by
Michael Henein

Printed Edition of the Special Issue Published in *IJMS*

Atherosclerosis and Vascular Imaging 2016

Special Issue Editor
Michael Henein

MDPI • Basel • Beijing • Wuhan • Barcelona • Belgrade



Special Issue Editor
Michael Henein
Umea University
Sweden

Editorial Office
MDPI AG
St. Alban-Anlage 66
Basel, Switzerland

This edition is a reprint of the Special Issue published online in the open access journal *International Journal of Molecular Sciences* (ISSN 1422-0067 from 2016–2017 (available at: http://www.mdpi.com/journal/ijms/special_issues/vascular_imaging2016).

For citation purposes, cite each article independently as indicated on the article page online and as indicated below:

Author 1; Author 2. Article title. *Journal Name Year, Article number, page range.*

First Edition 2017

ISBN 978-3-03842-432-1 (Pbk)
ISBN 978-3-03842-433-8 (PDF)

Articles in this volume are Open Access and distributed under the Creative Commons Attribution license (CC BY), which allows users to download, copy and build upon published articles even for commercial purposes, as long as the author and publisher are properly credited, which ensures maximum dissemination and a wider impact of our publications. The book taken as a whole is © 2017 MDPI, Basel, Switzerland, distributed under the terms and conditions of the Creative Commons license CC BY-NC-ND (<http://creativecommons.org/licenses/by-nc-nd/4.0/>).

Table of Contents

About the Special Issue Editor.....	v
Preface to "Atherosclerosis and Vascular Imaging 2016"	vii
Olga Kruszelnicka, Jolanta Świerszcz, Jacek Bednarek, Bernadeta Chyrchel, Andrzej Surdacki and Jadwiga Nessler	
Asymmetric Dimethylarginine <i>versus</i> Proton Pump Inhibitors Usage in Patients with Stable Coronary Artery Disease: A Cross-Sectional Study	
Reprinted from: <i>Int. J. Mol. Sci.</i> 2016 , <i>17</i> (4), 454; doi:10.3390/ijms17040454	1
Shoichi Ehara, Kenji Matsumoto and Kenei Shimada	
The Clinical Value of High-Intensity Signals on the Coronary Atherosclerotic Plaques: Noncontrast T1-Weighted Magnetic Resonance Imaging	
Reprinted from: <i>Int. J. Mol. Sci.</i> 2016 , <i>17</i> (7), 1187; doi:10.3390/ijms17071187	9
Jian Guo, Yang Li, Yi-Hong Ren, Zhijun Sun, Jie Dong, Han Yan, Yujun Xu, Dao Wen Wang, Gu-Yan Zheng, Jie Du and Xiao-Li Tian	
Mutant <i>LRP6</i> Impairs Endothelial Cell Functions Associated with Familial Normolipidemic Coronary Artery Disease	
Reprinted from: <i>Int. J. Mol. Sci.</i> 2016 , <i>17</i> (7), 1173; doi:10.3390/ijms17071173	19
Kentaro Fujimoto, Yoshiyasu Matsumoto, Kohki Oikawa, Jun-ichi Nomura, Yasuyoshi Shimada, Shunrou Fujiwara, Kazunori Terasaki, Masakazu Kobayashi, Kenji Yoshida and Kuniaki Ogasawara	
Cerebral Hyperperfusion after Revascularization Inhibits Development of Cerebral Ischemic Lesions Due to Artery-to-Artery Emboli during Carotid Exposure in Endarterectomy for Patients with Preoperative Cerebral Hemodynamic Insufficiency: Revisiting the "Impaired Clearance of Emboli" Concept	
Reprinted from: <i>Int. J. Mol. Sci.</i> 2016 , <i>17</i> (8), 1261; doi:10.3390/ijms17081261	32
Rachel Nicoll, Ying Zhao, Pranvera Ibrahim, Gunilla Olivecrona and Michael Henein	
Diabetes and Hypertension Consistently Predict the Presence and Extent of Coronary Artery Calcification in Symptomatic Patients: A Systematic Review and Meta-Analysis	
Reprinted from: <i>Int. J. Mol. Sci.</i> 2016 , <i>17</i> (9), 1481; doi:10.3390/ijms17091481	46
Sara Gargiulo, Matteo Gramanzini and Marcello Mancini	
Molecular Imaging of Vulnerable Atherosclerotic Plaques in Animal Models	
Reprinted from: <i>Int. J. Mol. Sci.</i> 2016 , <i>17</i> (9), 1511; doi:10.3390/ijms17091511	61
Yasushi Ogasawara, Yuiko Sato, Shinsuke Narumi, Makoto Sasaki, Shunrou Fujiwara, Masakazu Kobayashi, Kenji Yoshida, Yasuo Terayama and Kuniaki Ogasawara	
Preoperative 3D FSE T1-Weighted MR Plaque Imaging for Severely Stenotic Cervical ICA: Accuracy of Predicting Emboli during Carotid Endarterectomy	
Reprinted from: <i>Int. J. Mol. Sci.</i> 2016 , <i>17</i> (11), 1791; doi:10.3390/ijms17111791	105
Noriko Uesugi, Yoshihito Shimazu, Kazunori Kikuchi and Michio Nagata	
Age-Related Renal Microvascular Changes: Evaluation by Three-Dimensional Digital Imaging of the Human Renal Microcirculation Using Virtual Microscopy	
Reprinted from: <i>Int. J. Mol. Sci.</i> 2016 , <i>17</i> (11), 1831; doi:10.3390/ijms17111831	120

- Slaven Pikija, Jozef Magdic, Vladimir Trkulja, Peter Unterkreuter,
Johannes Sebastian Mutzenbach, Helmut F. Novak, Friedrich Weymayr, Larissa Hauer and
Johann Sellner**
Intracranial Thrombus Morphology and Composition Undergoes Time-Dependent Changes in
Acute Ischemic Stroke: A CT Densitometry Study
Reprinted from: *Int. J. Mol. Sci.* **2016**, *17*(11), 1959; doi:10.3390/ijms17111959132
- Pier-Luc Tardif, Marie-Jeanne Bertrand, Maxime Abran, Alexandre Castonguay, Joël Lefebvre,
Barbara E. Stähli, Nolwenn Merlet, Teodora Mihalache-Avram, Pascale Geoffroy,
Mélanie Mecteau, David Busseuil, Feng Ni, Abedelnasser Abulrob, Éric Rhéaume,
Philippe L'Allier, Jean-Claude Tardif and Frédéric Lesage**
Validating Intravascular Imaging with Serial Optical Coherence Tomography and Confocal
Fluorescence Microscopy
Reprinted from: *Int. J. Mol. Sci.* **2016**, *17*(12), 2110; doi:10.3390/ijms17122110144
- Bàrbbara Laviña**
Brain Vascular Imaging Techniques
Reprinted from: *Int. J. Mol. Sci.* **2017**, *18*(1), 70; doi:10.3390/ijms18010070156

About the Special Issue Editor

Michael Henein holds the Chair of Cardiology at Umea University, Sweden, and is a visiting Professor at the St. George University, London, and Brunel University, Middlesex. After 15 years of clinical and academic work at the Royal Brompton Hospital and Imperial College London, he started an international career establishing academic activities in Sweden, Italy, UK, Kosovo, and Egypt. He currently focuses on international cardiology research programs in the field of coronary artery atherosclerosis and calcification, incorporating imaging techniques, biochemistry, metabolomics and genetics. In addition, Professor Henein has a special interest in other areas of cardiology including heart failure and valve disease. He has published over 300 papers in peer reviewed journals, written four books and 15 chapters. He has supervised 15 PhD theses and has lectured in many international conferences. Professor Henein founded two new journals in the field of cardiology, the International Journal of Cardiology–Heart and Vasculature and the International Cardiovascular Forum, and has served as Associate Editor for the International Journal of Cardiology for 8 years. He has also served for two years as the Guest Editor for IJMS.

Preface to “Atherosclerosis and Vascular Imaging 2016”

Cardiovascular disease is the main cause of death in the West, and vascular disease is the most common cardiovascular clinical problem. The disease results in serious morbidity and mortality, and carries economic cost implications. While conventional risk factors are well established, and their biomarkers regularly monitored, patients may continue to suffer subclinical active disease, even in the absence of risk factors, until they present with sudden cardiac death or stroke. Early disease detection using direct imaging has shown to be more accurate in identifying vulnerable patients and unstable plaques than conventional risk factors. This IJMS Special Issue deals with the current opinion concerning the state-of-the-art imaging technologies available for clinical applications, and their unique value over the sole use of conventional risk factor analysis, in identifying vulnerable patients, recommending aggressive treatments, prognosticating, and in assessing related nutritional and environmental issues. This Special Issue is the continuation of our 2015 Special Issue “Atherosclerosis and Vascular Imaging” (http://www.mdpi.com/journal/ijms/special_issues/vascular_imaging).

Michael Henein
Special Issue Editor



Article

Asymmetric Dimethylarginine *versus* Proton Pump Inhibitors Usage in Patients with Stable Coronary Artery Disease: A Cross-Sectional Study

Olga Kruszelnicka ^{1,*}, Jolanta Świerszcz ², Jacek Bednarek ³, Bernadeta Chyrchel ²,
Andrzej Surdacki ^{2,†} and Jadwiga Nessler ^{1,†}

¹ Department of Coronary Artery Disease and Heart Failure, Jagiellonian University Medical College and John Paul II Hospital, 80 Prądnicka, 31-202 Cracow, Poland; jnessler@interia.pl

² Second Department of Cardiology, Jagiellonian University Medical College and University Hospital, 17 Kopernika, 31-501 Cracow, Poland; grasshoppers@interia.eu (J.Ś.); chyrchelb@gmail.com (B.C.); surdacki.andreas@gmx.net (A.S.)

³ Department of Electrocardiology, John Paul II Hospital, 80 Prądnicka, 31-202 Cracow, Poland; bednareks@op.pl

* Correspondence: olga.kruszelnicka@onet.pl; Tel.: +48-501-510-400

† Joint senior authors on this work.

Academic Editor: Michael Henein

Received: 30 January 2016; Accepted: 22 March 2016; Published: 15 April 2016

Abstract: A recent experimental study suggested that proton pump inhibitors (PPI), widely used to prevent gastroduodenal complications of dual antiplatelet therapy, may increase the accumulation of the endogenous nitric oxide synthesis antagonist asymmetric dimethylarginine (ADMA), an adverse outcome predictor. Our aim was to assess the effect of PPI usage on circulating ADMA in coronary artery disease (CAD). Plasma ADMA levels were compared according to PPI use for ≥ 1 month prior to admission in 128 previously described non-diabetic men with stable CAD who were free of heart failure or other coexistent diseases. Patients on PPI tended to be older and with insignificantly lower estimated glomerular filtration rate (GFR). PPI use was not associated with any effect on plasma ADMA (0.51 ± 0.11 (SD) vs. 0.50 ± 0.10 $\mu\text{mol/L}$ for those with PPI ($n = 53$) and without PPI ($n = 75$), respectively; $p = 0.7$). Additionally, plasma ADMA did not differ between PPI users and non-users stratified by a history of current smoking, CAD severity or extent. The adjustment for patients' age and GFR did not substantially change the results. Thus, PPI usage does not appear to affect circulating ADMA in non-diabetic men with stable CAD. Whether novel mechanisms of adverse PPI effects on the vasculature can be translated into clinical conditions, requires further studies.

Keywords: asymmetric dimethylarginine; coronary artery disease; proton pump inhibitors

1. Introduction

Proton pump inhibitors (PPI)—widely used to prevent gastroduodenal complications of dual antiplatelet therapy—have recently been demonstrated to raise intracellular levels of asymmetric dimethylarginine (ADMA), an endogenous inhibitor of nitric oxide (NO) synthesis, which was accompanied by a lower NO formation, depressed endothelium-mediated vasorelaxation *in vitro* and increased circulating ADMA by about 20% in mice. These effects were ascribed to a PPI-dependent direct inhibition of the activity of the major ADMA-degrading enzyme type 1 dimethylarginine dimethylaminohydrolase (DDAH-1) [1].

Because ADMA is a recognized adverse outcome predictor in coronary artery disease (CAD) patients [2–4], the PPI-ADMA interaction might contribute to an excessive cardiovascular risk in patients on PPI irrespective of the use of antiplatelet agents including clopidogrel, or a prior

history of myocardial infarction [5–11]. Importantly, an elevated risk of myocardial infarction was associated with the usage of PPI but not H₂-receptor antagonists also in the general population subjects, mainly without aspirin or clopidogrel, which may suggest an underlying mechanism not directly involving either platelet aggregation or changed drug absorption due to a rise in gastric pH [11,12]. Admittedly, potential negative clinical impacts of PPI on the risk of adverse cardiovascular events are still controversial [13] with conflicting results between randomized trials and observational studies [10,14]. Nevertheless, the proposed mechanistic concept [1] was not confirmed in a recent placebo-controlled, open-label, cross-over study where PPI administration for four weeks was not associated with significant effects on plasma ADMA or flow-dependent vasodilation in adults [15].

Therefore, our aim was to estimate the effect of PPI usage on circulating ADMA in stable CAD.

2. Results

Clinical and angiographic characteristics according to PPI use are shown in Table 1. Patients taking a PPI prior to admission (mainly omeprazole 20 mg o.i.d. or pantoprazole 20 mg o.i.d.) tended to be older and with lower estimated glomerular filtration rate (GFR).

Table 1. Characteristics of CAD patients according to PPI use prior to admission on a background of concomitant low-dose aspirin, ACEI and statin.

Characteristic	Patients on PPI (<i>n</i> = 53)	Patients without PPI (<i>n</i> = 75)	<i>p</i> -Value
Age (years)	59 ± 11	56 ± 10	0.12
Body-mass index (kg/m ²)	27.7 ± 3.6	27.4 ± 3.5	0.6
History of current smoking, <i>n</i> (%)	16 (30%)	20 (27%)	0.8
Multivessel CAD, <i>n</i> (%)	41 (77%)	54 (72%)	0.6
CAD extent score	31 (21–44)	28 (19–40)	0.5
Left ventricular ejection fraction (%)	70 ± 7	68 ± 6	0.2
Hypertension, <i>n</i> (%)	43 (80%)	56 (75%)	0.4
Mean blood pressure (mm Hg)	96 ± 11	95 ± 10	0.7
Estimated GFR (mL/min per 1.73 m ²)	69 ± 9	72 ± 11	0.09
LDL cholesterol (mmol/L)	2.8 ± 0.7	2.8 ± 0.6	0.8
HDL cholesterol (mmol/L)	0.9 ± 0.3	1.0 ± 0.3	0.2
Triglycerides (mmol/L)	1.4 ± 0.6	1.5 ± 0.7	0.3
Glucose (mmol/L)	5.8 ± 0.9	5.7 ± 0.8	0.5
High-sensitivity C-reactive protein (mg/L)	1.9 (1.1–4.0)	1.8 (1.0–3.8)	0.8

Data are shown as mean ± SD, median (interquartile range) or *n* (%); *p*-values by 2-tailed Student's *t*-test or Mann-Whitney *U* test, and chi-squared test for proportions. CAD: coronary artery disease; ADMA: asymmetric dimethylarginine; ACEI: angiotensin-converting enzyme inhibitors; GFR: glomerular filtration rate calculated according to the Modification of Diet in Renal Disease study formula; HDL: high-density lipoproteins; LDL: low-density lipoproteins; PPI: proton pump inhibitors.

The use of PPI was not associated with any effect on plasma ADMA (Table 2). In addition, there were no interactions between PPI use and the categorized potential confounders, *i.e.*, current smoking, angiographic CAD severity or extent in terms of plasma ADMA (*p* > 0.3), so that ADMA levels did not differ between PPI users and PPI non-users stratified by a history of current smoking, the presence of multivessel CAD or an over-median Sullivan score of angiographic CAD extent (Table 2). Adjustment for patients' age and GFR by means of ANCOVA did not substantially change the results.

Table 2. Plasma ADMA levels according to PPI use prior to admission.

	ADMA before Admission ($\mu\text{mol/L}$)		<i>p</i> -Value
	PPI Users (<i>n</i> = 53)	PPI Non-Users (<i>n</i> = 75)	
All CAD subjects, <i>n</i> = 128	0.51 ± 0.11	0.50 ± 0.10	0.7
History of current smoking			
Yes, <i>n</i> = 36	0.51 ± 0.11	0.50 ± 0.10	0.4
No, <i>n</i> = 92	0.51 ± 0.10	0.51 ± 0.11	0.8
Severity of angiographic CAD			
One-vessel disease, <i>n</i> = 33	0.48 ± 0.10	0.49 ± 0.10	0.7
Multivessel disease, <i>n</i> = 95	0.52 ± 0.11	0.51 ± 0.11	0.9
Extent of angiographic CAD			
Sullivan extent score ≤ 29, <i>n</i> = 65	0.48 ± 0.09	0.49 ± 0.10	0.6
Sullivan extent score > 29, <i>n</i> = 63	0.54 ± 0.11	0.52 ± 0.10	0.3

Data are shown as mean ± SD; *p*-values by 2-tailed Student's *t*-test. Abbreviations as in Table 1.

3. Discussion

Our salient finding was a similar plasma level of ADMA in PPI users and non-users. This observation appears inconsistent with the previously reported ability of PPI to augment ADMA accumulation *in vitro* and in an animal model through a direct inhibition of DDAH-1 [1], an enzyme influencing circulating ADMA [16–19]. On the other hand, in subjects with a history of vascular disease, Ghebremariam *et al.* [15] observed a more pronounced trend towards higher ADMA while on PPI compared to placebo in an interventional cross-over study, nevertheless the differences did not reach the statistical significance, which is in agreement with our cross-sectional retrospective analysis. To the best of our knowledge, our study is the second clinical report on ADMA levels in relation to PPI use.

3.1. Mechanistic Considerations

There are several potential explanations of these apparent discrepancies. First, all the patients were receiving angiotensin-converting enzyme inhibitors (ACEI), aspirin and statins, all of which had been previously shown to lower ADMA levels [20–22], thereby obscuring the putative influence of PPI on ADMA. On the other hand, ADMA concentrations in our patients were only slightly lower than ADMA levels measured by the same enzyme-linked immunosorbent assay (ELISA) in control groups of largely untreated subjects of similar age from European populations and without evidence of atherosclerotic vascular disease [23–25], which argues against the proposed explanation and strengthens our findings.

Second, even if the PPI-DDAH-1 interaction took place *in vivo*, its effects on plasma ADMA could be attenuated or nullified by an effective counter-regulatory mechanism. This hypothetical mechanism might involve any of the recognized determinants of circulating ADMA levels including DDAH-mediated ADMA degradation, urinary ADMA excretion, the activity of type I protein-arginine *N*-methyltransferases (PRMTs-I), proteolysis rate of proteins with dimethylated arginine residues, and interorgan ADMA transport [26]. Of note, Becker *et al.* [27] described depressed nicotinamide adenine dinucleotide phosphate (NADPH)-dependent superoxide release and augmented expression of the antioxidant defense enzyme type 1 heme oxygenase (HO-1) in human endothelial cells exposed for 8–24 h to lansoprazole at final concentrations as low as 30 $\mu\text{mol/L}$, *i.e.*, similar to PPI levels (20 $\mu\text{mol/L}$) that increased intracellular ADMA concentrations by about 30% via DDAH-1 inhibition as shown by Ghebremariam *et al.* [1]. The PPI-dependent HO-1 induction occurred at the level of transcription [27], in contrast to PPI direct effects on DDAH-1 activity [1], which can probably further potentiate the former effect in subjects on chronic PPI therapy. Accordingly, because oxidative stress stimulates PRMTs-I expression [28] and inhibits DDAH activity [29,30], the PPI-mediated decrease in endothelial superoxide formation [27] could possibly indirectly downregulate ADMA formation and

enhance ADMA degradation, thus counteracting the ADMA-increasing effect of the direct DDAH-1 inhibition by PPI [1].

Third, findings from animal experiments cannot be simply extrapolated to clinical conditions because the presence of atherosclerotic cardiovascular disease and risk factors may interfere with ADMA-regulating pathways. Nevertheless, in our hands, there were no significant interactions between PPI use and angiographic CAD extent or severity in terms of plasma ADMA and the results did not substantially change upon exclusion of current smokers from the analysis.

3.2. Study Limitations

First, a retrospective study design constrains conclusions drawn from our data. Second, our findings would be strengthened if we also assessed characteristics previously linked to adverse cardiovascular effects of PPI, *i.e.*, magnesium or homocysteine (due to a putative PPI-induced vitamin B₁₂ deficiency), and platelet response to aspirin (attributable to reduced aspirin absorption at a higher intragastric pH). Nevertheless, chronic PPI therapy is unlikely to induce clinically relevant changes in serum magnesium [31], vitamin B₁₂ or homocysteine [32]. With regard to aspirin antiplatelet effect, contradictory results were reported in patients on a low-dose aspirin treated with concomitant PPI [33,34] and no involvement of ADMA in this interaction [33] has been demonstrated so far. Third, coexistent diseases could affect our results, although we applied a wide range of exclusion criteria to limit the heterogeneity of the study population. Finally, PPI pharmacokinetics is profoundly modulated by genetic loss-of-function polymorphisms of cytochrome P450 (CYP) 2C19 isoform. Compared to so-called extensive metabolizers with both wild-type CYP2C19 alleles, poor metabolizers (those with both mutated CYP2C19 alleles) exhibit elevated circulating PPI levels, *e.g.*, after oral omeprazole its peak plasma level was about 5-fold higher and the area under the concentration-time curve approximately 9-fold higher [35]. Admittedly, we did not perform either genetic or epigenetic testing. However, our aim was to compare ADMA in relation to PPI use in real-world clinical practice irrespective of genotype status. Additionally, the frequency of CYP2C19 poor metabolizers in Caucasian populations averages only about 2%–3% [36,37].

4. Materials and Methods

4.1. Patients

We performed an additional analysis of the dataset including ADMA levels and clinical and angiographic characteristics of stable CAD men who had previously been described [38]. The study subjects were free of heart failure or diabetes and exhibited the presence of ≥ 1 significant epicardial coronary stenosis on elective coronary angiography in our tertiary-care center [38]. All the patients were receiving a low-dose aspirin, ACEI and statin for at least 3 months prior to the hospitalization. As described previously [38], a wide set of exclusion criteria had been applied, including significant valvular heart disease, infections within previous 2 months, relevant coexistent diseases (*e.g.*, severe renal insufficiency) and chronic non-cardiovascular medication with non-selective non-steroidal anti-inflammatory drugs or coxibs. Out of 151 CAD patients 23 were excluded from the current analysis due to missing data with regard to PPI use for ≥ 1 month before the index hospitalization.

In line with the Declaration of Helsinki, the study protocol was approved by the Bioethics Committee of the Jagiellonian University (Approval numbers: KBET/63/B/2006 dated 27 April 2006 and KBET/364/B/2012 dated 20 December 2012) and informed consent was obtained from the patients, as mentioned previously [38].

4.2. Procedure

A sample of peripheral venous blood was collected into ethylenediaminetetraacetic acid tubes in the fasting state in the morning prior to coronary angiography and plasma was kept frozen at -70°C for subsequent biochemical analyses.

ADMA levels were measured by a commercially available ELISA (DLD Diagnostika GmbH, Hamburg, Germany)—as reported in detail [38]—and compared between 2 subgroups of the study subjects divided on the basis of a history of PPI use for ≥ 1 month before blood sampling on admission for ADMA assay. In addition, we compared ADMA levels in PPI users and non-users according to a history of current smoking, angiographic CAD severity (multivessel *vs.* one-vessel CAD) [39] and CAD extent quantified by means of the Sullivan score representing a percentage of the vessels with vascular wall irregularities on coronary angiography [40].

4.3. Statistical Analysis

Data have been presented as means \pm SD (standard deviation) or medians (interquartile range) for continuous characteristics with normal and non-normal distribution, respectively. The concordance with a Gaussian distribution was checked by the Lilliefors' test. The patients were compared according to PPI use by 2-tailed Student's *t*-test or Mann-Whitney *U* test, and chi-squared test for continuous and categorical characteristics, respectively. According to a *post hoc* power calculation for the study group as a whole, the study design allowed to detect a difference in plasma ADMA between PPI users ($n = 53$) and non-users ($n = 75$) of $0.05 \mu\text{mol/L}$ (0.5 SD) with a power of 80% at a type I error rate of 0.05.

In order to test whether an effect of PPI use on circulating ADMA levels was modified by selected categorized covariates, a two-way analysis of variance (ANOVA) was performed to assess these potential interactions with plasma ADMA as a dependent variable and 2 independent factors: PPI use on the one hand and—on the other hand—a history of self-reported current smoking or angiographic CAD severity (multivessel *vs.* one-vessel CAD) or dichotomized CAD extent (an over-median (>29) *vs.* below-median (≤ 29) Sullivan score) as a coexistent factor; then an interaction between these factors was estimated. In addition, analysis of covariance (ANCOVA) was used to adjust for continuous clinical characteristics, for which the *p*-value in a univariate comparison between patients with and without PPI did not exceed 0.15. A *p*-value below 0.05 was inferred significant.

5. Conclusions

Thus, our preliminary cross-sectional findings suggest that PPI use does not appear to considerably affect circulating ADMA in non-diabetic men with stable CAD. Whether novel mechanisms of adverse PPI effects on the vasculature can be translated into clinical conditions, requires validation in large well-designed studies.

Acknowledgments: This work was supported in part by a research grant (No. K/ZDS/003761) from the Jagiellonian University Medical College, Cracow, Poland. The publication of this paper was supported by the Faculty of Medicine, Jagiellonian University Medical College, Leading National Research Center (KNOW) 2012–2017.

Author Contributions: Olga Kruszelnicka conceived and designed the study, analyzed and interpreted data, and wrote the manuscript. Jolanta Świerszcz, Jacek Bednarek and Bernadeta Chyrchel contributed to data collection and analysis. Jadwiga Nessler and Andrzej Surdacki contributed to study design and discussion, and supervised the study. All authors read, critically revised and approved the final manuscript.

Conflicts of Interest: The authors declare no conflict of interest.

Abbreviations

ACEI	angiotensin-converting enzyme inhibitors
ADMA	asymmetric dimethylarginine
ANCOVA	analysis of covariance
ANOVA	analysis of variance
CAD	coronary artery disease
CYP	cytochrome P450
DDAH-1	type 1 dimethylarginine dimethylaminohydrolase
ELISA	enzyme-linked immunosorbent assay

GFR	glomerular filtration rate
HDL	high-density lipoproteins
HO-1	type 1 heme oxygenase
LDL	low-density lipoproteins
NADPH	nicotinamide adenine dinucleotide phosphate
NO	nitric oxide
PPI	proton pump inhibitors
PRMTs-I	type I protein-arginine N-methyltransferases
SD	standard deviation

References

1. Ghebremariam, Y.T.; LePendu, P.; Lee, J.C.; Erlanson, D.A.; Slaviero, A.; Shah, N.H.; Leiper, J.; Cooke, J.P. Unexpected effect of proton pump inhibitors: Elevation of the cardiovascular risk factor asymmetric dimethylarginine. *Circulation* **2013**, *128*, 845–853. [CrossRef] [PubMed]
2. Schnabel, R.; Blankenberg, S.; Lubos, E.; Lackner, K.J.; Rupprecht, H.J.; Espinola-Klein, C.; Jachmann, N.; Post, F.; Peetz, D.; Bickel, C.; et al. Asymmetric dimethylarginine and the risk of cardiovascular events and death in patients with coronary artery disease: Results from the AtheroGene study. *Circ. Res.* **2005**, *97*, e53–e59. [CrossRef] [PubMed]
3. Meinitzer, A.; Seelhorst, U.; Wellnitz, B.; Halwachs-Baumann, G.; Boehm, B.O.; Winkelmann, B.R.; März, W. Asymmetrical dimethylarginine independently predicts total and cardiovascular mortality in individuals with angiographic coronary artery disease (the Ludwigshafen Risk and Cardiovascular Health study). *Clin. Chem.* **2007**, *53*, 273–283. [CrossRef] [PubMed]
4. Wang, Z.; Tang, W.H.; Cho, L.; Brennan, D.M.; Hazen, S.L. Targeted metabolomic evaluation of arginine methylation and cardiovascular risks: Potential mechanisms beyond nitric oxide synthase inhibition. *Arterioscler. Thromb. Vasc. Biol.* **2009**, *29*, 1383–1391. [CrossRef] [PubMed]
5. Ho, P.M.; Maddox, T.M.; Wang, L.; Fihn, S.D.; Jesse, R.L.; Peterson, E.D.; Rumsfeld, J.S. Risk of adverse outcomes associated with concomitant use of clopidogrel and proton pump inhibitors following acute coronary syndrome. *JAMA* **2009**, *301*, 937–944. [CrossRef] [PubMed]
6. Juurlink, D.N.; Gomes, T.; Ko, D.T.; Szmitko, P.E.; Austin, P.C.; Tu, J.V.; Henry, D.A.; Kopp, A.; Mamdani, M.M. A population-based study of the drug interaction between proton pump inhibitors and clopidogrel. *CMAJ* **2009**, *180*, 713–718. [CrossRef] [PubMed]
7. Charlot, M.; Ahlehoff, O.; Norgaard, M.L.; Jørgensen, C.H.; Sørensen, R.; Abildstrøm, S.Z.; Hansen, P.R.; Madsen, J.K.; Køber, L.; Torp-Pedersen, C.; et al. Proton-pump inhibitors are associated with increased cardiovascular risk independent of clopidogrel use: A nationwide cohort study. *Ann. Intern. Med.* **2010**, *153*, 378–386. [CrossRef] [PubMed]
8. Charlot, M.; Grove, E.L.; Hansen, P.R.; Olesen, J.B.; Ahlehoff, O.; Selmer, C.; Lindhardsen, J.; Madsen, J.K.; Køber, L.; Torp-Pedersen, C.; et al. Proton pump inhibitor use and risk of adverse cardiovascular events in aspirin treated patients with first time myocardial infarction: Nationwide propensity score matched study. *BMJ* **2011**, *342*, d2690. [CrossRef] [PubMed]
9. Goodman, S.G.; Clare, R.; Pieper, K.S.; Nicolau, J.C.; Storey, R.F.; Cantor, W.J.; Mahaffey, K.W.; Angiolillo, D.J.; Husted, S.; Cannon, C.P.; et al. Association of proton pump inhibitor use on cardiovascular outcomes with clopidogrel and ticagrelor: Insights from the platelet inhibition and patient outcomes trial. *Circulation* **2012**, *125*, 978–986. [CrossRef] [PubMed]
10. Kwok, C.S.; Jeevanantham, V.; Dawn, B.; Loke, Y.K. No consistent evidence of differential cardiovascular risk amongst proton-pump inhibitors when used with clopidogrel: Meta-analysis. *Int. J. Cardiol.* **2013**, *167*, 965–974. [CrossRef] [PubMed]
11. Shih, C.J.; Chen, Y.T.; Ou, S.M.; Li, S.Y.; Chen, T.J.; Wang, S.J. Proton pump inhibitor use represents an independent risk factor for myocardial infarction. *Int. J. Cardiol.* **2014**, *177*, 292–297. [CrossRef] [PubMed]
12. Shah, N.H.; LePendu, P.; Bauer-Mehren, A.; Ghebremariam, Y.T.; Iyer, S.V.; Marcus, J.; Nead, K.T.; Cooke, J.P.; Leeper, N.J. Proton pump inhibitor usage and the risk of myocardial infarction in the general population. *PLoS ONE* **2015**, *10*, e0124653. [CrossRef] [PubMed]

13. Agewall, S.; Cattaneo, M.; Collet, J.P.; Andreotti, F.; Lip, G.Y.; Verheugt, F.W.; Huber, K.; Grove, E.L.; Morais, J.; Husted, S.; *et al.* Expert position paper on the use of proton pump inhibitors in patients with cardiovascular disease and antithrombotic therapy. *Eur. Heart J.* **2013**, *34*, 1708–1713. [CrossRef] [PubMed]
14. Melloni, C.; Washam, J.B.; Jones, W.S.; Halim, S.A.; Hasselblad, V.; Mayer, S.B.; Heidenfelder, B.L.; Dolor, R.J. Conflicting results between randomized trials and observational studies on the impact of proton pump inhibitors on cardiovascular events when coadministered with dual antiplatelet therapy: Systematic review. *Circ. Cardiovasc. Qual. Outcomes* **2015**, *8*, 47–55. [CrossRef] [PubMed]
15. Ghebremariam, Y.T.; Cooke, J.P.; Khan, F.; Thakker, R.N.; Chang, P.; Shah, N.H.; Nead, K.T.; Leeper, N.J. Proton pump inhibitors and vascular function: A prospective cross-over pilot study. *Vasc. Med.* **2015**, *20*, 309–316. [CrossRef] [PubMed]
16. Wang, D.; Gill, P.S.; Chabashvili, T.; Onozato, M.L.; Raggio, J.; Mendonca, M.; Dennehy, K.; Li, M.; Modlinger, P.; Leiper, J.; *et al.* Isoform-specific regulation by N^G,N^G -dimethylarginine dimethylaminohydrolase of rat serum asymmetric dimethylarginine and vascular endothelium-derived relaxing factor/NO. *Circ. Res.* **2007**, *101*, 627–635. [CrossRef] [PubMed]
17. Lind, L.; Ingesson, E.; Kumar, J.; Syvänen, A.C.; Axelsson, T.; Teerlink, T. Genetic variation in the dimethylarginine dimethylaminohydrolase 1 gene (DDAH1) is related to asymmetric dimethylarginine (ADMA) levels, but not to endothelium-dependent vasodilation. *Vasc. Med.* **2013**, *18*, 192–199. [CrossRef] [PubMed]
18. Seppälä, I.; Kleber, M.E.; Lyytikäinen, L.P.; Hernesniemi, J.A.; Mäkelä, K.M.; Oksala, N.; Laaksonen, R.; Pilz, S.; Tomaschitz, A.; Silbernagel, G.; *et al.* Genome-wide association study on dimethylarginines reveals novel AGXT2 variants associated with heart rate variability but not with overall mortality. *Eur. Heart J.* **2014**, *35*, 524–531. [CrossRef] [PubMed]
19. Lüneburg, N.; Lieb, W.; Zeller, T.; Chen, M.H.; Maas, R.; Carter, A.M.; Xanthakis, V.; Glazer, N.L.; Schwedhelm, E.; Seshadri, S.; *et al.* Genome-wide association study of L-arginine and dimethylarginines reveals novel metabolic pathway for symmetric dimethylarginine. *Circ. Cardiovasc. Genet.* **2014**, *7*, 864–872. [CrossRef] [PubMed]
20. Delles, C.; Schneider, M.P.; John, S.; Gekle, M.; Schmieder, R.E. Angiotensin converting enzyme inhibition and angiotensin ii AT₁-receptor blockade reduce the levels of asymmetrical N^G,N^G -dimethylarginine in human essential hypertension. *Am. J. Hypertens.* **2002**, *15*, 590–593. [CrossRef]
21. Hetzel, S.; DeMets, D.; Schneider, R.; Borzak, S.; Schneider, W.; Serebruany, V.; Schröder, H.; Hennekens, C.H. Aspirin increases nitric oxide formation in chronic stable coronary disease. *J. Cardiovasc. Pharmacol. Ther.* **2013**, *18*, 217–221. [CrossRef] [PubMed]
22. Serban, C.; Sahebkar, A.; Ursoniu, S.; Mikhailidis, D.P.; Rizzo, M.; Lip, G.Y.; Kees Hovingh, G.; Kastelein, J.J.; Kalinowski, L.; Rysz, J.; *et al.* A systematic review and meta-analysis of the effect of statins on plasma asymmetric dimethylarginine concentrations. *Sci. Rep.* **2015**, *5*, 9902. [CrossRef] [PubMed]
23. Krempl, T.K.; Maas, R.; Sydow, K.; Meinertz, T.; Böger, R.H.; Kähler, J. Elevation of asymmetric dimethylarginine in patients with unstable angina and recurrent cardiovascular events. *Eur. Heart J.* **2005**, *26*, 1846–1851. [CrossRef] [PubMed]
24. Schulze, F.; Lenzen, H.; Hanefeld, C.; Bartling, A.; Osterziel, K.J.; Goudeva, L.; Schmidt-Lucke, C.; Kusus, M.; Maas, R.; Schwedhelm, E.; *et al.* Asymmetric dimethylarginine is an independent risk factor for coronary heart disease: Results from the multicenter Coronary Artery Risk Determination investigating the Influence of ADMA Concentration (CARDIAC) study. *Am. Heart J.* **2006**, *152*. [CrossRef] [PubMed]
25. Napora, M.; Graczykowska, A.; Próchniewska, K.; Zdrojewski, Z.; Ćalka, A.; Górný, J.; Stompór, T. Relationship between serum asymmetric dimethylarginine and left ventricular structure and function in patients with end-stage renal disease treated with hemodialysis. *Pol. Arch. Med. Wewn.* **2012**, *122*, 226–234. [PubMed]
26. Teerlink, T.; Luo, Z.; Palm, F.; Wilcox, C.S. Cellular ADMA: Regulation and action. *Pharmacol. Res.* **2009**, *60*, 448–460. [CrossRef] [PubMed]
27. Becker, J.C.; Grosser, N.; Waltke, C.; Schulz, S.; Erdmann, K.; Domschke, W.; Schröder, H.; Pohle, T. Beyond gastric acid reduction: Proton pump inhibitors induce heme oxygenase-1 in gastric and endothelial cells. *Biochem. Biophys. Res. Commun.* **2006**, *345*, 1014–1021. [CrossRef] [PubMed]

28. Böger, R.H.; Sydow, K.; Borlak, J.; Thum, T.; Lenzen, H.; Schubert, B.; Tsikas, D.; Bode-Böger, S.M. LDL cholesterol upregulates synthesis of asymmetrical dimethylarginine in human endothelial cells: Involvement of S-adenosylmethionine-dependent methyltransferases. *Circ. Res.* **2000**, *87*, 99–105. [CrossRef] [PubMed]
29. Ito, A.; Tsao, P.S.; Adimoolam, S.; Kimoto, M.; Ogawa, T.; Cooke, J.P. Novel mechanism for endothelial dysfunction: Dysregulation of dimethylarginine dimethylaminohydrolase. *Circulation* **1999**, *99*, 3092–3095. [CrossRef] [PubMed]
30. Palm, F.; Onozato, M.L.; Luo, Z.; Wilcox, C.S. Dimethylarginine dimethylaminohydrolase (DDAH): Expression, regulation, and function in the cardiovascular and renal systems. *Am. J. Physiol. Heart Circ. Physiol.* **2007**, *293*, H3227–H3245. [CrossRef] [PubMed]
31. Kieboom, B.C.; Kieft-de Jong, J.C.; Eijgelsheim, M.; Franco, O.H.; Kuipers, E.J.; Hofman, A.; Zietse, R.; Stricker, B.H.; Hoorn, E.J. Proton pump inhibitors and hypomagnesemia in the general population: A population-based cohort study. *Am. J. Kidney Dis.* **2015**, *66*, 775–782. [CrossRef] [PubMed]
32. Attwood, S.E.; Ell, C.; Galmiche, J.P.; Fiocca, R.; Hatlebakk, J.G.; Hasselgren, B.; Långström, G.; Jahreskog, M.; Eklund, S.; Lind, T.; et al. Long-term safety of proton pump inhibitor therapy assessed under controlled, randomised clinical trial conditions: Data from the SOPRAN and LOTUS studies. *Aliment. Pharmacol. Ther.* **2015**, *41*, 1162–1174. [CrossRef] [PubMed]
33. Würtz, M.; Grove, E.L.; Kristensen, S.D.; Hvass, A.M. The antiplatelet effect of aspirin is reduced by proton pump inhibitors in patients with coronary artery disease. *Heart* **2010**, *96*, 368–371. [CrossRef] [PubMed]
34. Adamopoulos, A.B.; Sakizlis, G.N.; Nasothimiou, E.G.; Anastasopoulou, I.; Anastasakou, E.; Kotsi, P.; Karafoulidou, A.; Stergiou, G.S. Do proton pump inhibitors attenuate the effect of aspirin on platelet aggregation? A randomized crossover study. *J. Cardiovasc. Pharmacol.* **2009**, *54*, 163–168. [CrossRef] [PubMed]
35. Uno, T.; Niioka, T.; Hayakari, M.; Yasui-Furukori, N.; Sugawara, K.; Tateishi, T. Absolute bioavailability and metabolism of omeprazole in relation to CYP2C19 genotypes following single intravenous and oral administrations. *Eur. J. Clin. Pharmacol.* **2007**, *63*, 143–149. [CrossRef] [PubMed]
36. Barter, Z.E.; Tucker, G.T.; Rowland-Yeo, K. Differences in cytochrome p450-mediated pharmacokinetics between Chinese and Caucasian populations predicted by mechanistic physiologically based pharmacokinetic modelling. *Clin. Pharmacokinet.* **2013**, *52*, 1085–1100. [CrossRef] [PubMed]
37. Krajčiová, L.; Petrovič, R.; Déžiová, L.; Chandoga, J.; Turčáni, P. Frequency of selected single nucleotide polymorphisms influencing the warfarin pharmacogenetics in Slovak population. *Eur. J. Haematol.* **2014**, *93*, 320–328. [CrossRef] [PubMed]
38. Kruszelnicka, O.; Surdacki, A.; Golay, A. Differential associations of angiographic extent and severity of coronary artery disease with asymmetric dimethylarginine but not insulin resistance in non-diabetic men with stable angina: A cross-sectional study. *Cardiovasc. Diabetol.* **2013**, *12*, 145. [CrossRef] [PubMed]
39. Kruszelnicka-Kwiatkowska, O.; Surdacki, A.; Goldsztajn, P.; Matysek, J.; Piwowarska, W.; Golay, A. Relationship between hyperinsulinemia and angiographically defined coronary atherosclerosis in non-diabetic men. *Diabetes Metab.* **2002**, *28*, 305–309. [PubMed]
40. Sullivan, D.R.; Marwick, T.H.; Freedman, S.B. A new method of scoring coronary angiograms to reflect extent of coronary atherosclerosis and improve correlation with major risk factors. *Am. Heart J.* **1990**, *119*, 1262–1267. [CrossRef]



© 2016 by the authors. Licensee MDPI, Basel, Switzerland. This article is an open access article distributed under the terms and conditions of the Creative Commons Attribution (CC BY) license (<http://creativecommons.org/licenses/by/4.0/>).



Review

The Clinical Value of High-Intensity Signals on the Coronary Atherosclerotic Plaques: Noncontrast T1-Weighted Magnetic Resonance Imaging

Shoichi Ehara ^{*}, Kenji Matsumoto and Kenei Shimada

Department of Cardiovascular Medicine, Osaka City University Graduate School of Medicine, Osaka 545-8585, Japan; matsumoto1110@hotmail.co.jp (K.M.); shimadak@med.osaka-cu.ac.jp (K.S.)

* Correspondence: ehara@med.osaka-cu.ac.jp; Tel.: +81-6-6645-3801; Fax: +81-6-6646-6808

Academic Editor: Michael Henein

Received: 7 June 2016; Accepted: 14 July 2016; Published: 21 July 2016

Abstract: Over the past several decades, significant progress has been made in the pathohistological assessment of vulnerable plaques and in invasive intravascular imaging techniques. However, the assessment of plaque morphology by invasive modalities is of limited value for the detection of subclinical coronary atherosclerosis and the subsequent prediction or prevention of acute cardiovascular events. Recently, magnetic resonance (MR) imaging technology has reached a sufficient level of spatial resolution, which allowed the plaque visualization of large and static arteries such as the carotids and aorta. However, coronary wall imaging by MR is still challenging due to the small size of coronary arteries, cardiac and respiratory motion, and the low contrast-to-noise ratio between the coronary artery wall and the surrounding structures. Following the introduction of carotid plaque imaging with noncontrast T1-weighted imaging (T1WI), some investigators have reported that coronary artery high-intensity signals on T1WI are associated with vulnerable plaque morphology and an increased risk of future cardiac events. Although there are several limitations and issues that need to be resolved, this novel MR technique for coronary plaque imaging could influence treatment strategies for atherothrombotic disease and may be useful for understanding the pathophysiological mechanisms of atherothrombotic plaque formation.

Keywords: acute coronary syndrome; atherosclerosis; magnetic resonance imaging; plaque; thrombosis; intraplaque hemorrhage

1. Introduction

Acute myocardial infarction or sudden cardiac death frequently occurs as the first symptom of coronary diseases, without prodromal angina [1]. Therefore, the prediction or prevention of acute cardiovascular events has become a crucial clinical issue.

The degree of luminal narrowing is used as a marker for high risk plaques [2], but it is widely recognized that plaque composition is likely to be much more clinically significant than luminal narrowing because the arterial lumen is often preserved by positive arterial remodeling [3]. Therefore, the direct evaluation of the arterial wall is an important goal in cardiovascular imaging. From the 1990s onward, pathohistological studies have demonstrated that plaque rupture or erosion of the endothelial surface with subsequent thrombus formation is the most important mechanisms in acute coronary syndromes (ACSs) [4–6]. A large lipid-pool, thin-cap fibroatheroma (TCFA), macrophage accumulation, and intraplaque hemorrhage have been identified as the key features of rupture-prone plaques [7]. Over the past several decades, significant progress has been made in the assessment of vulnerable plaques using invasive intravascular imaging, such as intravascular ultrasound (IVUS) [8–10], coronary angiography [11,12], or optimal coherence tomography (OCT) [13–15]. Those vulnerable

features in the coronary artery have been confirmed not only in patients who died from the disease but also in patients who survived an ACS. However, the assessment of plaque morphology by invasive modalities is of limited value for the detection of subclinical coronary atherosclerosis and the subsequent prediction or prevention of acute cardiovascular events.

Hence, there is widespread interest in alternative non-invasive modalities, such as magnetic resonance (MR) imaging or computed tomography (CT), to directly visualize the arterial wall and characterize plaque composition. MR imaging is an attractive option because it is performed with magnetic fields and it is a safe and completely non-invasive technique with excellent soft tissue contrast capable of differentiating the plaque components on the basis of their biophysical and biochemical parameters.

In this review, we focus on the accumulated data on vulnerable plaque imaging using MR techniques, and we also introduce the results from our recent studies.

2. The Beginning of Coronary Artery Plaque Imaging Based on High-Intensity Signal on Noncontrast T1-Weighted Imaging

With any imaging technique, its most important qualities are the spatial resolution required to visualize the lesion components and good contrast between the various components of the lesions. Recently, MR imaging technology has reached a sufficient level of spatial resolution, which allowed the plaque visualization of large and static arteries such as the carotids and aorta [16–20]. The advent of carotid plaque characterization with noncontrast T1-weighted imaging (T1WI) in MR has facilitated plaque imaging based on the presence of a high-intensity signal (HIS) within the thrombus or intraplaque hemorrhage caused by methemoglobin T1 shortening [6–21].

However, coronary wall imaging by MR is still challenging due to the small size of coronary arteries, cardiac and respiratory motion, and the low contrast-to-noise ratio between the coronary artery wall and the surrounding structures. Despite these challenges, coronary wall imaging by MR has been successfully applied in patients using breathhold [22,23] or respiratory gating (i.e., free-breathing) techniques [24–28]. It has been demonstrated that MR can measure coronary vessel area, wall thickness, plaque burden, or arterial remodeling [23]. However, the use of MR to identify plaque components in coronary arteries has been limited.

Some investigators have reported that coronary artery HISs on T1WI are associated with a vulnerable plaque morphology [24–26,28] and an increased risk of future cardiac events [27]. These coronary plaque images have been obtained while the patients were breathing freely by using a three-dimensional T1WI, inversion-recovery, gradient-echo technique with fat-suppression. Kawasaki et al. proposed the calculation “the ratio between the signal intensities of coronary plaque and cardiac muscle (PMR)”, which was defined as the highest signal intensity of the coronary plaque divided by the signal intensity of the left ventricular muscle near the coronary plaque [24]. Areas with a PMR >1.0 were defined as HIS in this report. They reported that the typical coronary HIS on T1WI was associated with a high frequency of IVUS-derived low attenuation and positive remodeling, remarkably low CT density, and transient slow-flow phenomena during percutaneous coronary intervention (PCI) [24]. These features seemed to represent vulnerable plaques. Jansen et al. reported that the HIS on T1WI correctly corresponded to the intracoronary thrombus detected by invasive coronary angiography in patients with acute myocardial infarction within 72 h after the initial onset of symptoms [25]. In our study involving a small number of patients, we demonstrated a direct association between coronary HISs on T1WI and the presence of intracoronary thrombus as detected through OCT (Figure 1) [26].

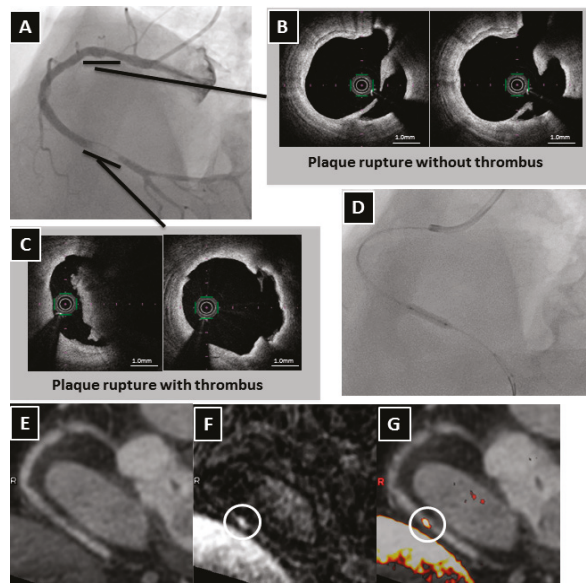


Figure 1. A representative case of a HIS lesion on T1WI associated with an intraluminal thrombus. (A) Coronary angiography revealing an intracoronary thrombus identified by the presence of intraluminal filling defects surrounded by contrast agents in the distal right coronary artery (RCA) and an ulceration in the proximal RCA; (B) The OCT examination showing a plaque rupture without a thrombus in the proximal RCA; (C) In contrast, the culprit lesion in the distal RCA with a plaque rupture with a large intracoronary thrombus; (D) Thrombus aspiration and plain old balloon angioplasty (POBA) performed on the culprit lesion; (E) Two days later after POBA, whole-heart coronary MR angiography revealing no significant stenosis in the distal RCA; (F) Coronary T1WI demonstrating intraluminal HIS on the culprit lesion (circle). However, there is no HIS at the ulceration of the proximal RCA; (G) Fused image showing intraluminal HIS in the area corresponding to the culprit lesion (circle). R in panels E–G indicates right side.

3. What Appears as High-intensity Signal on T1-Weighted Imaging in the Coronary Artery? What Is the Best PMR Cutoff Value?

There are two highly controversial topics related to HIS in the coronary artery. First, what appears as a HIS on T1WI in the coronary artery? At this stage, the precise characterization of HISs is not known, because no comparisons with histopathological data have been performed in the coronary artery studies; comparative studies have been done on the carotid artery. Therefore, indirect comparisons have been performed by using a surrogate marker mostly derived from other imaging modalities, such as IVUS or OCT. Recently, Teruo Noguchi et al. reported that coronary artery HISs on T1WI were associated with future cardiac events in patients with mildly atherosclerotic lesions that had not yet caused an acute coronary event or induced cardiac ischemia [27]. It seems unlikely that HISs localized within the vessel wall are associated with thrombus in the subclinical population. We investigated the relationship between localization of HISs on T1WI and plaque morphology detected on OCT in patients with either stable or unstable angina [28]. Areas with a PMR ≤ 1.0 were classified as non-HISs. HISs with a PMR > 1.0 were then classified into two types, according to the localization of HIS, using cross-sectional coronary T1WI. Areas that were localized within the coronary wall when the lumen was identified were defined as intrawall HISs, whereas areas that occupied the lumen when the lumen was not identified were defined as intraluminal HISs. The multivariate analysis revealed that intraluminal HISs were associated with thrombus and intimal vasculature assessed by OCT. In contrast,

macrophage accumulation and the absence of calcification were independent factors associated with intrawall HISs (Figure 2). The plaque morphology of the culprit lesions in ACS patients varies from thrombosis with or without plaque rupture to sudden luminal narrowing caused by intraplaque hemorrhage. When previous data are taken together with our findings, one can speculate that coronary intrawall HISs on T1WI may indicate intraplaque hemorrhage associated with inflammation. Some observations have indicated that hemorrhage components appear as signal-poor OCT regions that must be distinguished from lipid necrotic pools. Regrettably, the current imaging techniques, including OCT, do not allow a definitive discrimination between hemorrhage and lipid components, and that is a major issue that will require additional validation studies using histopathological materials from coronary, rather than carotid arteries. In addition, we found that in intrawall HIS lesions the presence of lipid-rich plaques was more frequent than in non-HIS lesions, although these differences were not statistically significant when analyzed by multivariate analysis [28]. Do lipid-rich plaques generate HIS? Although this MR technique uses a fat-suppressed sequence, perivascular fat, which is mainly composed of triglycerides, has a different appearance on MR than the lipids in atherosclerotic plaques. The plaque lipids consist primarily of unesterified cholesterol and cholesterol esters [29]. Therefore, it is not known whether the lipids within the atherosclerotic plaques were successfully suppressed. There is increasing evidence that multiple vulnerable plaques with lipid are present within the whole coronary tree in patients who experience an ACS, even though it may be a single localized culprit lesion that caused the acute cardiovascular event [30]. However, most lipid pools do not generate HISs except at the culprit lesion (Figure 3). The proportion, age, and volume of methemoglobin based on the presence of vulnerable complex plaques may determine the PMR values.

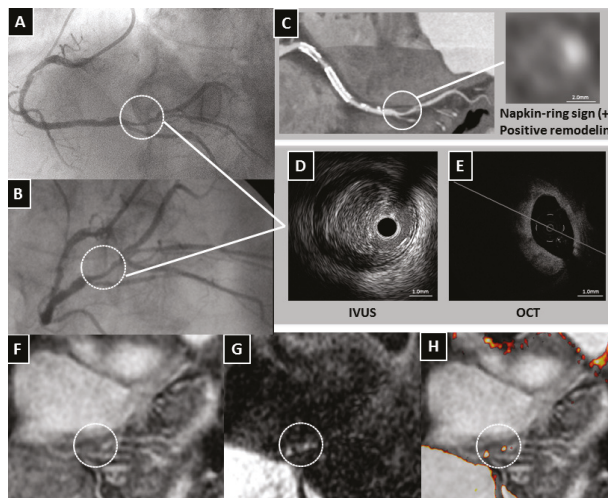


Figure 2. A representative case of an intrawall HIS lesion on T1WI compared with plaque morphology on CT, IVUS and OCT. (A,B) Coronary angiography revealing severe coronary stenosis (circle) in the distal right coronary artery (RCA); (C) Coronary CT angiography showing the napkin-ring sign and positive arterial remodeling; (D) The IVUS image showing a low attenuation plaque; (E) The OCT examination showing a signal-poor region with irregular high- or low-backscattering borders without thrombus; (F) Whole-heart coronary MR angiography showing significant stenosis in the distal RCA (circle); (G) Coronary T1WI demonstrating intrawall HIS (circle); (H) Fused image showing intrawall HIS (circle) in the area corresponding to the severe stenosis.

The second controversial topic is the fact that several MR studies used different PMR cutoff values to detect HIS, so there is no consensus on which cutoff is best for risk stratification.

Recently, two studies by Noguchi et al. demonstrated that the optimal PMR cutoff values for predicting future cardiac events and myocardial injury during elective PCI, defined as an increase in serum troponin T levels, were of 1.4 and 1.3, respectively [27,31]. At this stage, it is not known which PMR cutoff value is best or whether there is a need to determine the cutoff values. In our unpublished data, the PMR increased in proportion to the accumulation of the number vulnerable plaque features, such as intraluminal thrombus, lipid-rich plaque, plaque rupture, macrophage accumulation, and intimal vasculature. HISs with a higher PMR are likely to represent more vulnerable plaques. Future studies are needed to clarify the significance of PMR values on T1WI.

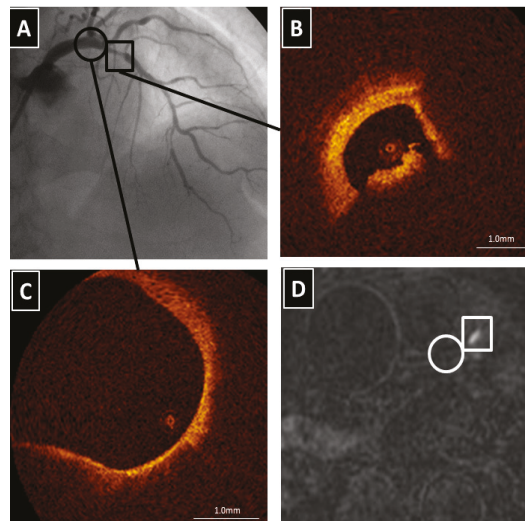


Figure 3. The culprit lesion in the proximal left anterior descending coronary artery (LAD). (A) Coronary angiography revealing severe coronary stenosis in the proximal LAD (square) and no significant stenosis in the left main coronary artery (LMCA) (circle); (B) The OCT examination showing intracoronary thrombus in the proximal LAD; (C) There is a lipid-rich plaque in the LMCA (circle); (D) Coronary T1WI demonstrating HIS in the area corresponding to the culprit lesion of the proximal LAD (square). However, no HIS in the LMCA with the lipid-rich plaque is found (circle).

4. The Clinical Implication of High-Intensity Signal in Coronary Atherosclerotic Plaques

What is the clinical implication of detecting HIS on noncontrast T1WI in MR in coronary atherosclerotic plaques? One of the goals of researchers is to investigate whether the presence of HIS on T1WI in subclinical coronary atherosclerosis is associated with the subsequent development of acute cardiovascular events. Noguchi et al. demonstrated that a PMR cutoff value of 1.4 was best for identifying vulnerable coronary plaques associated with future cardiac events, including nonfatal ST-segment elevation myocardial infarction, high-sensitivity cardiac troponin T-positive unstable angina pectoris or non-ST-segment elevation myocardial infarction, and ischemia-driven PCI due to progressive angina pectoris [27]. Moreover, their stratified analysis using PMR values of 1.0 and 1.4 revealed that the incidence of cardiac events was well differentiated: 25.8% for $\text{PMR} \geq 1.4$, 8.4% for $\text{PMR} 1.0\text{--}1.4$, and 1.1% for $\text{PMR} < 1.0$. Interestingly, of the segments with plaques with $\text{PMRs} \geq 1.4$, 17% were associated with coronary events, which developed in 51% of the segments in the first 12 months.

Moreover, some studies have demonstrated that the presence of HIS on noncontrast T1WI has the potential to predict a PCI-related myocardial injury, which is associated with worse short-term and long-term clinical outcomes [31–33]. Although the etiology of PCI-related myocardial injury

is a multifactorial phenomenon, the predominant mechanism involves the distal embolization of atherosomatous or thrombotic materials, and results from the mechanical fragmentation of the culprit plaque during PCI [34]. Asaumi et al. examined the relationship between HISs on T1WI and PCI-related myocardial injury, which is manifested by the elevation of cardiac troponin, in patients undergoing elective PCI [31]. They reported that the optimal PMR cutoff value for predicting PCI-related myocardial injury was 1.3, and the sensitivity and specificity were 67% and 86%, respectively. Hoshi et al. also reported that in patients with stable angina pectoris undergoing elective PCI, the PMR cutoff value of 1.44 predicted PCI-related myocardial injury, and the sensitivity and specificity were 78% and 82%, respectively [32]. In our study, which employed distal protection devices, we investigated predictors of the filter no-reflow (FNR) phenomenon during PCI by using multimodality, such as HIS on T1WI, plaque composition by using OCT, and serum biomarkers, in patients with either stable or unstable angina [33]. Our multivariate analysis revealed that only the presence of HISs with $\text{PMR} > 1.85$ remained an independent predictor of the FNR phenomenon, and the sensitivity and specificity were 65% and 93%, respectively. It is unclear why there are differences in PMR cutoff values for predicting cardiac events. In our study involving patients with unstable angina pectoris, FNR occurred at a high rate (40%) compared with the rate of PCI-related myocardial injury (26%) reported in a previous study [31]. HISs with a higher PMR are likely to represent more vulnerable plaques, and thus the occurrence of FNR might be more closely associated with vulnerable plaque morphology and plaque volume with a higher PMR than that of PCI-related myocardial injury assessed by troponin. The differences in study population or outcomes might be associated to the different PMR cutoff values.

A noninvasive imaging technique capable of identifying not only the presence of a thrombus or hemorrhage but also its stage of development would be invaluable. It has already been established that cerebral hemorrhage staging can be accurately assessed by MR using multicontrast images. Despite the existence of well-defined criteria for staging cerebral hemorrhages, few reports are available regarding the staging of an intraluminal thrombus or intraplaque hemorrhages. Recently, Tan et al. revealed that MR imaging was a precise and reproducible method for distinguishing an acute ipsilateral recurrent deep vein thrombosis from an at least six-month-old chronic residual thrombus in the leg veins, when recurrence was not suspected [35]. Moreover, Chu et al. have shown that multicontrast MR images can detect and classify a carotid intraplaque hemorrhage into three stages: fresh (<1 week), recent (1–6 weeks), and old (>6 weeks) [36]. If HIS on T1WI can be shown to be limited to a fixed term, its presence could be used to accurately identify recent plaque thrombosis or hemorrhage. This information may have several novel clinical implications in the field of PCI, including the prediction or prevention of no-flow phenomena or the aging of a chronic total occlusion. The precise assessment of recent plaque thrombosis or hemorrhage in the coronary occlusion site may influence procedural success rates for chronic total occlusions. Furthermore, although ACS patients with the high-risk should be considered for early invasive intervention, the differential diagnosis and treatment of the remaining patients is challenging in emergency triage. A noninvasive thrombus-detection technique would be useful for further risk stratification and for obtaining prognostic information in patients with coronary artery disease.

Finally, the extent of intraplaque hemorrhage corresponded positively to the size of necrotic core, and the development of hemorrhage resulted in plaque volume expansion and subsequent plaque rupture [37]. If coronary intrawall HISs on T1WI represent intraplaque hemorrhage, early identification of patients with hemorrhage may prove invaluable in optimizing management to minimize future cardiovascular events. Noguchi et al. reported that statin therapy reduced the PMR values, as well as low-density lipoprotein cholesterol and high-sensitivity C-reactive protein levels in patients with coronary artery disease [38]. If statin therapy not only modifies plaque morphology and makes it more stable, but also accelerates the degradation of methemoglobin, that could be invaluable for treatment strategies for atherosclerosis.

5. Limitations and Issues to Be Resolved in the Future

Several limitations should be mentioned in this study field. First, the major issue is that there was no evidence based on pathohistological findings. Therefore, the previous results should be interpreted with caution. Second, when an inversion-recovery gradient-echo sequence is used for the T1WI, issues with spatial resolution and partial volume effect could provide artifacts that look like HIS. This MR technique overcomes many of the difficulties associated with conventional techniques that generate a signal based on flowing blood. With T1WI, signal generation does not rely on flowing blood because it uses a non-slice-selective inversion recovery pulse for the black-blood method. Therefore, the image interpretation requires only the detection of a high signal, beyond the high-resolution display of vessel walls [21]. Although theoretically the T1WI technique is unaffected by blood flow, it is not known whether this supposition applies to actual clinical images. There is a possibility that the HIS might result from a gap in a null point. Future studies are needed to verify whether flow disturbance cause artifact like a HIS. Third, contrast agents such as gadopentetic acid (Gd-DTPA), attached to specific imaging probes targeted to biochemical and cellular markers of atherosclerotic plaque vulnerability, may be useful for plaque characterization [39]. Finally, previous coronary plaque imaging studies on MR used only a single-contrast sequence as T1WI [24–28,31–33,38]. The multi-contrast high-resolution protocol is ideal since they generate a wide range of contrast for the individual plaque characterization. However, the acquisition of multi-contrast images is time-consuming, especially in conjunction with the need for high spatial resolution.

6. Conclusions

To determine which plaque features pose a higher risk for future cardiovascular events, we need a noninvasive imaging tool that can identify high-risk plaque features. MR imaging has the potential to identify thrombus and distinguish intraplaque hemorrhage from other plaque components. Because this MR technique has a very short history and no comparisons with histopathological data or multicenter randomized trials have been carried out, many more studies will be needed before this method could be considered to be applied in the clinical arena. Although there are several limitations and issues that need to be resolved, this novel MR technique for coronary plaque imaging could influence treatment strategies for atherothrombotic disease and may be useful for understanding the pathophysiological mechanisms of atherothrombotic plaque formation.

Author Contributions: Shoichi Ehara was the primary author of the text, and conceived the report; Kenji Matsumoto performed patient recruitment, data collection, and analysis including statistics; Kenei Shimada supervised the interpretation of the clinical results.

Conflicts of Interest: The authors declare no conflict of interest.

Abbreviations

The following abbreviations are used in this manuscript:

ACS	acute coronary syndrome
TCFA	thin-cap fibroatheroma
IVUS	intravascular ultrasound
OCT	optical coherence tomography
MR	magnetic resonance
CT	computed tomography
T1WI	T1-weighted imaging
HIS	high-intensity signal
PMR	the ratio between the signal intensities of coronary plaque and cardiac muscle
PCI	percutaneous coronary intervention
FNR	filter no-reflow

References

1. Braunwald, E. Acute myocardial infarction—The value of being prepared. *N. Engl. J. Med.* **1996**, *334*, 51–52. [CrossRef] [PubMed]
2. Stone, G.W.; Maehara, A.; Lansky, A.J.; de Bruyne, B.; Cristea, E.; Mintz, G.S.; Mehran, R.; McPherson, J.; Farhat, N.; Marso, S.P.; et al. A prospective natural-history study of coronary atherosclerosis. *N. Engl. J. Med.* **2011**, *364*, 226–235. [CrossRef] [PubMed]
3. Glagov, S.; Weisenberg, E.; Zarins, C.K.; Stankunavicius, R.; Kolettis, G.J. Compensatory enlargement of human atherosclerotic coronary arteries. *N. Engl. J. Med.* **1987**, *316*, 1371–1375. [CrossRef] [PubMed]
4. Van der Wal, A.C.; Becker, A.E.; van der Loos, C.M.; Das, P.K. Site of intimal rupture or erosion of thrombosed coronary atherosclerotic plaques is characterized by an inflammatory process irrespective of the dominant plaque morphology. *Circulation* **1994**, *89*, 36–44. [CrossRef] [PubMed]
5. Arbustini, E.; dal Bello, B.; Morbini, P.; Burke, A.P.; Boccarelli, M.; Specchia, G.; Virmani, R. Plaque erosion is a major substrate for coronary thrombosis in acute myocardial infarction. *Heart* **1999**, *82*, 269–272. [CrossRef] [PubMed]
6. Virmani, R.; Kolodgie, F.D.; Burke, A.P.; Farb, A.; Schwartz, S.M. Lessons from sudden coronary death: A comprehensive morphological classification scheme for atherosclerotic lesions. *Arterioscler. Thromb. Vasc. Biol.* **2000**, *20*, 1262–1275. [CrossRef] [PubMed]
7. Finn, A.V.; Nakano, M.; Narula, J.; Kolodgie, F.D.; Virmani, R. Concept of vulnerable/unstable plaque. *Arterioscler. Thromb. Vasc. Biol.* **2010**, *30*, 1282–1292. [CrossRef] [PubMed]
8. Schoenhagen, P.; Ziada, K.M.; Kapadia, S.R.; Crowe, T.D.; Nissen, S.E.; Tuzcu, E.M. Extent and direction of arterial remodeling in stable versus unstable coronary syndromes: An intravascular ultrasound study. *Circulation* **2000**, *101*, 598–603. [CrossRef] [PubMed]
9. Ehara, S.; Kobayashi, Y.; Yoshiyama, M.; Shimada, K.; Shimada, Y.; Fukuda, D.; Nakamura, Y.; Yamashita, H.; Yamagishi, H.; Takeuchi, K.; et al. Spotty calcification typifies the culprit plaque in patients with acute myocardial infarction: An intravascular ultrasound study. *Circulation* **2004**, *110*, 3424–3429. [CrossRef] [PubMed]
10. Fujii, K.; Carlier, S.G.; Mintz, G.S.; Takebayashi, H.; Yasuda, T.; Costa, R.A.; Moussa, I.; Dangas, G.; Meran, R.; Lansky, A.J.; et al. Intravascular ultrasound study of patterns of calcium in ruptured coronary plaques. *Am. J. Cardiol.* **2005**, *96*, 352–357. [CrossRef] [PubMed]
11. Okamatsu, K.; Takano, M.; Sakai, S.; Ishibashi, F.; Uemura, R.; Takano, T.; Mizuno, K. Elevated troponin T levels and lesion characteristics in non-ST-elevation acute coronary syndromes. *Circulation* **2004**, *109*, 465–470. [CrossRef] [PubMed]
12. Ohtani, T.; Ueda, Y.; Mizote, I.; Oyabu, J.; Okada, K.; Hirayama, A.; Kodama, K. Number of yellow plaques detected in a coronary artery is associated with future risk of acute coronary syndrome: Detection of vulnerable patients by angioscopy. *J. Am. Coll. Cardiol.* **2006**, *47*, 2194–2200. [CrossRef] [PubMed]
13. Kubo, T.; Imanishi, T.; Takarada, S.; Kuroi, A.; Ueno, S.; Yamano, T.; Tanimoto, T.; Matsuo, Y.; Masho, T.; Kitabata, H.; et al. Assessment of culprit lesion morphology in acute myocardial infarction: Ability of optical coherence tomography compared with intravascular ultrasound and coronary angiography. *J. Am. Coll. Cardiol.* **2007**, *50*, 933–939. [CrossRef] [PubMed]
14. Mizukoshi, M.; Imanishi, T.; Tanaka, A.; Kubo, T.; Liu, Y.; Takarada, S.; Kitabata, H.; Tanimoto, T.; Komukai, K.; Ishibashi, K.; et al. Clinical classification and plaque morphology determined by optical coherence tomography in unstable angina pectoris. *Am. J. Cardiol.* **2010**, *106*, 323–328. [CrossRef] [PubMed]
15. Sinclair, H.; Bourantas, C.; Bagnall, A.; Mintz, G.S.; Kunadian, V. OCT for the identification of vulnerable plaque in acute coronary syndrome. *J. Am. Coll. Cardiol.* **2015**, *8*, 198–209. [CrossRef] [PubMed]
16. Hatsukami, T.S.; Ross, R.; Polissar, N.L.; Yuan, C. Visualization of fibrous cap thickness and rupture in human atherosclerotic carotid plaque in vivo with high-resolution magnetic resonance imaging. *Circulation* **2000**, *102*, 959–964. [CrossRef] [PubMed]
17. Yuan, C.; Mitsumori, L.M.; Beach, K.W.; Maravilla, K.R. Carotid atherosclerotic plaque: Noninvasive MR characterization and identification of vulnerable lesions. *Radiology* **2001**, *221*, 285–289. [CrossRef] [PubMed]
18. Cai, J.M.; Hatsukami, T.S.; Ferguson, M.S.; Small, R.; Polissar, N.L.; Yuan, C. Classification of human carotid atherosclerotic lesions with in vivo multicontrast magnetic resonance imaging. *Circulation* **2002**, *106*, 1368–1373. [CrossRef] [PubMed]

19. Moody, A.R.; Murphy, R.E.; Morgan, P.S.; Martel, A.L.; Delay, G.S.; Allder, S.; MacSweeney, S.T.; Tennant, W.G.; Gladman, J.; Lowe, J.; et al. Characterization of complicated carotid plaque with magnetic resonance direct thrombus imaging in patients with cerebral ischemia. *Circulation* **2003**, *107*, 3047–3052. [CrossRef] [PubMed]
20. Murphy, R.E.; Moody, A.R.; Morgan, P.S.; Martel, A.L.; Delay, G.S.; Allder, S.; MacSweeney, S.T.; Tennant, W.G.; Gladman, J.; Lowe, J.; et al. Prevalence of complicated carotid atheroma as detected by magnetic resonance direct thrombus imaging in patients with suspected carotid artery stenosis and previous acute cerebral ischemia. *Circulation* **2003**, *107*, 3053–3058. [CrossRef] [PubMed]
21. Kelly, J.; Hunt, B.J.; Moody, A. Magnetic resonance direct thrombus imaging: A novel technique for imaging venous thromboemboli. *Thromb. Haemost.* **2003**, *89*, 773–782. [PubMed]
22. Fayad, Z.A.; Fuster, V.; Fallon, J.T.; Jayasundera, T.; Worthley, S.G.; Helft, G.; Aguinaldo, J.G.; Badimon, J.J.; Sharma, S.K. Noninvasive *in vivo* human coronary artery lumen and wall imaging using black-blood magnetic resonance imaging. *Circulation* **2000**, *102*, 506–510. [CrossRef] [PubMed]
23. Terashima, M.; Nguyen, P.K.; Rubin, G.D.; Meyer, C.H.; Shimakawa, A.; Nishimura, D.G.; Ehara, S.; Iribarren, C.; Courtney, B.K.; Go, A.S.; et al. Right coronary wall CMR in the older asymptomatic advance cohort: positive remodeling and associations with type 2 diabetes and coronary calcium. *J. Cardiovasc. Magn. Reson.* **2010**, *12*, 1. [CrossRef] [PubMed]
24. Kawasaki, T.; Koga, S.; Koga, N.; Noguchi, T.; Tanaka, H.; Koga, H.; Serikawa, T.; Orita, Y.; Ikeda, S.; Mito, T.; et al. Characterization of hyperintense plaque with noncontrast T(1)-weighted cardiac magnetic resonance coronary plaque imaging: Comparison with multislice computed tomography and intravascular ultrasound. *J. Am. Coll. Cardiol.* **2009**, *2*, 720–728. [CrossRef] [PubMed]
25. Jansen, C.H.; Perera, D.; Makowski, M.R.; Wiethoff, A.J.; Phinikaridou, A.; Razavi, R.M.; Marber, M.S.; Greil, G.F.; Nagel, E.; Maintz, D.; et al. Detection of intracoronary thrombus by magnetic resonance imaging in patients with acute myocardial infarction. *Circulation* **2011**, *124*, 416–424. [CrossRef] [PubMed]
26. Ehara, S.; Hasegawa, T.; Nakata, S.; Matsumoto, K.; Nishimura, S.; Iguchi, T.; Kataoka, T.; Yoshikawa, J.; Yoshiyama, M. Hyperintense plaque identified by magnetic resonance imaging relates to intracoronary thrombus as detected by optical coherence tomography in patients with angina pectoris. *Eur. Heart J.* **2012**, *13*, 394–399. [CrossRef] [PubMed]
27. Noguchi, T.; Kawasaki, T.; Tanaka, A.; Yasuda, S.; Goto, Y.; Ishihara, M.; Nishimura, K.; Miyamoto, Y.; Node, K.; Koga, N. High-intensity signals in coronary plaques on non-contrast T1-weighted magnetic resonance imaging as a novel determinant of coronary events. *J. Am. Coll. Cardiol.* **2014**, *63*, 989–999. [CrossRef] [PubMed]
28. Matsumoto, K.; Ehara, S.; Hasegawa, T.; Sakaguchi, M.; Otsuka, K.; Yoshikawa, J.; Shimada, K. Localization of coronary high-intensity signals on T1-weighted MR imaging: Relation to plaque morphology and clinical severity of angina pectoris. *J. Am. Coll. Cardiol.* **2015**, *8*, 1143–1152. [CrossRef] [PubMed]
29. Quick, H.H.; Debatin, J.F.; Ladd, M.E. MR imaging of the vessel wall. *Eur. Radiol.* **2002**, *12*, 889–900. [CrossRef] [PubMed]
30. Kubo, T.; Imanishi, T.; Kashiwagi, M.; Ikejima, H.; Tsujioka, H.; Kuroi, A.; Ishibashi, K.; Komukai, K.; Tanimoto, T.; Ino, Y.; et al. Multiple coronary lesion instability in patients with acute myocardial infarction as determined by optical coherence tomography. *Am. J. Cardiol.* **2010**, *105*, 318–322. [CrossRef] [PubMed]
31. Asaumi, Y.; Noguchi, T.; Morita, Y.; Fujiwara, R.; Kanaya, T.; Matsuyama, T.A.; Kawasaki, T.; Fujino, M.; Yamane, T.; Nagai, T.; et al. High-intensity plaques on noncontrast T1-weighted imaging as a predictor of periprocedural myocardial injury. *J. Am. Coll. Cardiol.* **2015**, *8*, 741–743. [CrossRef] [PubMed]
32. Hoshi, T.; Sato, A.; Akiyama, D.; Hiraya, D.; Sakai, S.; Shindo, M.; Mori, K.; Minami, M.; Aonuma, K. Coronary high-intensity plaque on T1-weighted magnetic resonance imaging and its association with myocardial injury after percutaneous coronary intervention. *Eur. Heart J.* **2015**, *36*, 1913–1922. [CrossRef] [PubMed]
33. Matsumoto, K.; Ehara, S.; Hasegawa, T.; Otsuka, K.; Yoshikawa, J.; Shimada, K. Prediction of the filter no-reflow phenomenon in patients with angina pectoris by using multimodality: Magnetic resonance imaging, optical coherence tomography, and serum biomarkers. *J. Cardiol.* **2016**, *67*, 430–436. [CrossRef] [PubMed]
34. Kaul, S. The “no reflow” phenomenon following acute myocardial infarction: Mechanisms and treatment options. *J. Cardiol.* **2014**, *64*, 77–85. [CrossRef] [PubMed]

35. Tan, M.; Mol, G.C.; van Rooden, C.J.; Klok, F.A.; Westerbeek, R.E.; del Sol, A.I.; van de Ree, M.A.; de Roos, A.; Huisman, M.V. Magnetic resonance direct thrombus imaging differentiates acute recurrent ipsilateral deep vein thrombosis from residual thrombosis. *Blood* **2014**, *124*, 623–627. [CrossRef] [PubMed]
36. Chu, B.; Kampschulte, A.; Ferguson, M.S.; Kerwin, W.S.; Yarnykh, V.L.; O'Brien, K.D.; Polissar, N.L.; Hatsukami, T.S.; Yuan, C. Hemorrhage in the atherosclerotic carotid plaque: A high-resolution MRI study. *Stroke* **2004**, *35*, 1079–1084. [CrossRef] [PubMed]
37. Sun, J.; Underhill, H.R.; Hippe, D.S.; Xue, Y.; Yuan, C.; Hatsukami, T.S. Sustained acceleration in carotid atherosclerotic plaque progression with intraplaque hemorrhage: A long-term time course study. *J. Am. Coll. Cardiol.* **2012**, *5*, 798–804. [CrossRef] [PubMed]
38. Noguchi, T.; Tanaka, A.; Kawasaki, T.; Goto, Y.; Morita, Y.; Asaumi, Y.; Nakao, K.; Fujiwara, R.; Nishimura, K.; Miyamoto, Y.; et al. Effect of intensive statin therapy on coronary high-intensity plaques detected by noncontrast T1-weighted imaging. *J. Am. Coll. Cardiol.* **2015**, *66*, 245–256. [CrossRef] [PubMed]
39. Briley-Saebo, K.C.; Shaw, P.X.; Mulder, W.J.; Choi, S.H.; Vucic, E.; Aguinaldo, J.G.; Witztum, J.L.; Fuster, V.; Tsimikas, S.; Fayad, Z.A. Targeted molecular probes for imaging atherosclerotic lesions with magnetic resonance using antibodies that recognize oxidation-specific epitopes. *Circulation* **2008**, *117*, 3206–3215. [CrossRef] [PubMed]



© 2016 by the authors. Licensee MDPI, Basel, Switzerland. This article is an open access article distributed under the terms and conditions of the Creative Commons Attribution (CC BY) license (<http://creativecommons.org/licenses/by/4.0/>).

Article

Mutant *LRP6* Impairs Endothelial Cell Functions Associated with Familial Normolipidemic Coronary Artery Disease

Jian Guo ¹, Yang Li ¹, Yi-Hong Ren ², Zhijun Sun ², Jie Dong ¹, Han Yan ¹, Yujun Xu ³, Dao Wen Wang ³, Gu-Yan Zheng ¹, Jie Du ⁴ and Xiao-Li Tian ^{1,5,*}

- ¹ Department of Human Population Genetics, Institute of Molecular Medicine, Peking University, Beijing 100871, China; deidei@163.com (J.G.); ly1306386063@pku.edu.cn (Y.L.); djqiu@163.com (J.D.); yanhan@pku.edu.cn (H.Y.); zhengguyan@163.com (G.-Y.Z.)
- ² Department of Cardiovascular, PLA General Hospital, Beijing 100853, China; rainbowren301@163.com (Y.-H.R.); sunzj301@sohu.com (Z.S.)
- ³ The Institute of Hypertension and Department of Internal Medicine, Tongji Hospital, Tongji Medical College, Huazhong University of Science and Technology, Wuhan 430074, China; xuyujun3506@163.com (Y.X.); dwwang@tjh.tjmu.edu.cn (D.W.W.)
- ⁴ Beijing Anzhen Hospital, Capital Medical University, The Key Laboratory of Remodeling-Related Cardiovascular Diseases, Ministry of Education, Beijing Collaborative Innovation Center for Cardiovascular Disorders, Beijing Institute of Heart, Lung & Blood Vessel Disease, Beijing 100029, China; jiedubj@126.com
- ⁵ Department of Human Population Genetics, Human Aging Research Institute and School of Life Science, Nanchang University, Nanchang 330031, China
- * Correspondence: tianxiaoli@pku.edu.cn or tianxiaoli@ncu.edu.cn; Tel.: +86-10-6275-5397

Academic Editor: Michael Henein

Received: 21 June 2016; Accepted: 14 July 2016; Published: 22 July 2016

Abstract: Mutations in the genes low-density lipoprotein (LDL) receptor-related protein-6 (*LRP6*) and myocyte enhancer factor 2A (*MEF2A*) were reported in families with coronary artery disease (CAD). We intend to determine the mutational spectrum of these genes among hyperlipidemic and normolipidemic CAD families. Forty probands with early-onset CAD were recruited from 19 hyperlipidemic and 21 normolipidemic Chinese families. We sequenced all exons and intron-exon boundaries of *LRP6* and *MEF2A*, and found a novel heterozygous variant in *LRP6* from a proband with normolipidemic CAD. This variant led to a substitution of histidine to tyrosine (Y418H) in an evolutionarily conserved domain YWTD in exon 6 and was not found in 1025 unrelated healthy individuals. Co-segregated with CAD in the affected family, *LRP6_{Y418H}* significantly debilitated the Wnt3a-associated signaling pathway, suppressed endothelial cell proliferation and migration, and decreased anti-apoptotic ability. However, it exhibited no influences on low-density lipoprotein cholesterol uptake. Thus, mutation Y418H in *LRP6* likely contributes to normolipidemic familial CAD via impairing endothelial cell functions and weakening the Wnt3a signaling pathway.

Keywords: LDL receptor-related protein-6 (*LRP6*); normolipidemic; coronary artery disease; familial; endothelial cell dysfunction

1. Introduction

Coronary artery disease (CAD), the most common cause of death, is characterized by the stenosis or occlusions of coronary arteries that are mostly caused by the progressive deposition of lipids and fibrous matrix (atherosclerotic plaques) in the arterial wall [1]. The key steps of atherosclerosis include dysfunction of the endothelium, lipoprotein deposition, recruitment of monocytes and

lymphocytes, and proliferation of smooth muscle cells [2]. Endothelial cell survival, proliferation, and migration are critical to maintain the homeostasis and normal functions of endothelium [3].

The common form of CAD appears multi-factorial in etiology, involving an interaction between genetic and environmental factors [4,5]. Over the past decades, great efforts have been made to systematically search for genes or chromosomal loci associated with CAD at the genome level by family or population-based association studies, leading to the identification of numbers of susceptibility genes or loci [6–10]. In contrast, familial CAD is rare but highly penetrated, presenting a monogenic effect and Mendelian inheritance. Mutations in genes *MEF2A* and *LRP6* were previously identified as pathogenic or CAD-causing variants for familial CAD [11,12]. The detections of these loci or genes apparently increase our knowledge of understanding the molecular mechanism of CAD and may be helpful in improving the clinical treatment and drug discovery.

In addition to genetic influences, other risk factors for CAD are well established, such as elevated cholesterol, hypertension, obesity, and unhealthy lifestyles [13]. For example, hyperlipidemia, particularly the elevated level of low-density lipoprotein cholesterol (LDL-C), increases the risk for atherosclerosis which is fundamental to CAD [14–16]. In contrast, the high-density lipoprotein cholesterol (HDL-C) is inversely related with CAD [15–17]. Although hyperlipidemia is a significant risk factor for CAD, a considerable proportion of CAD patients are normolipidemic. It has been reported that only a third of CAD patients exhibit elevated cholesterol levels, especially LDL-C [18]. More than 40% and 60% of male CAD patients have normal ranges of serum LDL-C (<130 mg/dL, 3.4 mmol/L) and HDL-C levels (>35 mg/dL, 0.9 mmol/L) respectively [19]. Ultimately, how genetic determinants contribute differentially to hyperlipidemic and normolipidemic CAD remains largely unknown.

In this study, we recruited 40 Chinese Han families with early-onset hyperlipidemic or normolipidemic CAD, sequenced all exons and intron-exon boundaries of *LRP6* and *MEF2A*, two previously reported CAD genes, and characterized the functions of newly identified mutations.

2. Results

2.1. A Novel Mutation in *LRP6* Was Identified in a Family with Normolipidemic CAD

DNA was extracted from the peripheral blood lymphocytes of 40 probands, including 19 hyperlipidemic and 21 normolipidemic CAD patients from northern China (Table S1). After amplifying the genomic DNA with primers, as shown in Tables S2 and S3, all exons and intron-exon boundaries of *LRP6* and *MEF2A* were sequenced. As a result, a novel heterozygous variant in exon 6 of *LRP6* was identified in a proband, belonging to a patient who was 41 years old and diagnosed with myocardial infarction without hyperlipidemia. This proband (subject II7) was from a family with three generations, involving 20 patients and non-affected first-order relatives (Figure 1A). Two of his three major coronary arteries showed at least 80% stenosis (Figure 1B), leading to percutaneous coronary intervention. The variant was located in a domain named YWTD (Tyr-Trp-Thr-Asp), causing a substitution of histidine to tyrosine (Y418H) (Figure 1C). The multiple alignments using a basic local alignment search tool (BLAST) in the NCBI database showed that this region was highly conserved from *Denio rerio* to *Homo sapiens* (Figure 1D). Y418H was predicted to be a probable damaging change with a score of 0.994 in Polyphen-2 (available online: <http://genetics.bwh.harvard.edu/pph2/>, Table S4). We sequenced exon 6 of *LRP6* in another 1025 unrelated healthy individuals and found no variants.

In the Y418H family, another four members were previously diagnosed with CAD or suffered from sudden cardiac death before age 50 (men) or 55 (women), and two of them have been deceased. In addition to CAD, the proband (subject II7) and his sister (subject II5) were diagnosed with hypertension and diabetes. The third generation is too young and has no clinical symptoms, and is thus not subjected to clinical diagnosis. We genotyped 17 individuals from this family and found that the Y418H variant was co-segregated with CAD phenotypes (Figure 1A). It was speculated that this

mutation came from subject I2. Eleven family members were available for measurement of fasting glucose, total cholesterol (TC), triglycerides, LDL-C, and HDL-C (Table 1). For subject II3 (unaffected) and subject II5 (CAD), who had not taken lipid-lowering drugs during the past six months, blood lipid levels were similar. Additionally, despite the similar ages, the blood lipid levels of Y418H-carriers III7 and III8 were significantly different. These suggested that Y418H is not co-segregated with dyslipidemia and that this familial CAD is not linked to hyperlipidemia.

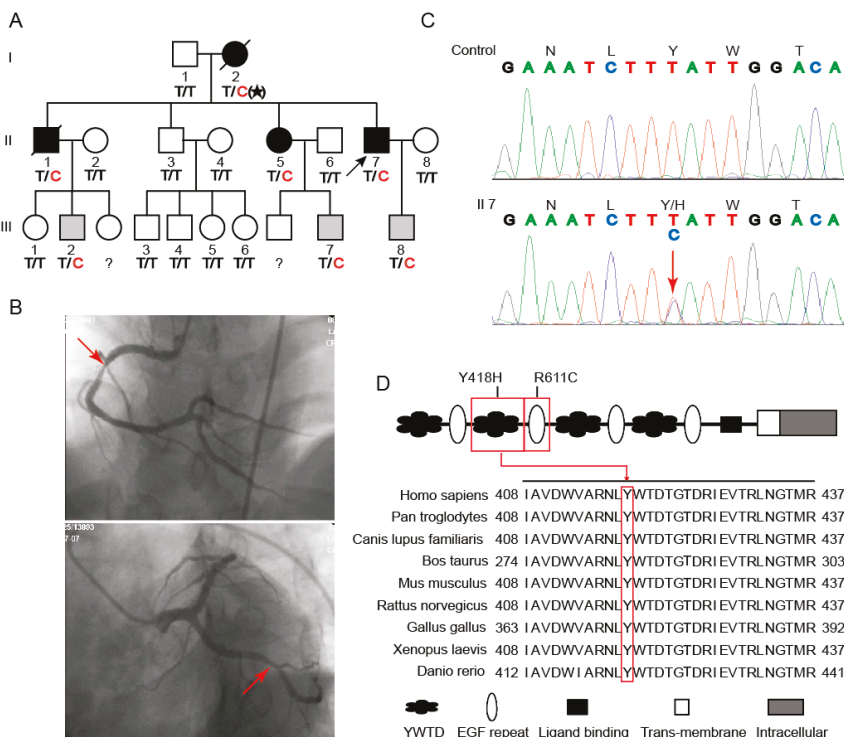


Figure 1. Novel mutation of *LRP6* identified in a CAD pedigree. (A) Pedigree of the family with the *LRP6* Y418H mutation. Numbered individuals correspond to those in Table 1. Circles represent females; Squares represent males; Proband is indicated by the arrow; Individuals with CAD are indicated by black symbols; Individuals without CAD are shown as unfilled symbols; Presymptomatic carriers are shown by symbols by gray symbols; Symbols with a slash through them indicate deceased subjects; Genotypes of the *LRP6* mutation were shown below the symbols who were willing to participate in the study; Filled stars indicates that the genotype of subject I2 was speculated; Individuals who were not available for studied are indicated with question mark; (B) Coronary angiogram of the proband. The red arrows indicates the stenosis; (C) DNA sequence analysis for a segment of *LRP6* exon 6 from a healthy control (**top**) and the proband (**below**). A red arrow points out a single base mutation in the proband, and it results in the substitution of histidine for tyrosine at codon 418; (D) Conservatism analysis by interspecies alignments. The mutation position is indicated with a red frame.

Although no other mutations in *LRP6* or *MEF2A* were found in the other 39 probands, we noticed several known single nucleotide polymorphisms (SNPs) included in the single nucleotide polymorphism database (dbSNP) during screening (data not shown). Nevertheless, we did not calculate their minor allele frequencies because of the limited number of samples.

Table 1. Clinical characteristic of members with CAD pedigree

ID	Age/Onset Age	Gender	BMI	SBP (mmHg)	DBP (mmHg)	Anti-HT Drug	Glucose mmol/L	Anti-D Drug	Triglyceride TC mmol/L	HDL-C 2.9~6.0 mmol/L	LDL-C 0.8~3.2 mmol/L	Anti-HL Drug	CAD Status
II	86	male	23.9	140	80	no	NA	no	NA	NA	NA	no	Unaffected CAD/Stroke
II ² *	65 ⁺ /NA	female	NA	NA	NA	NA	NA	NA	NA	NA	NA	NA	SCD
III *	49 ⁺ /49	male	NA	NA	NA	NA	NA	NA	NA	NA	NA	NA	Unaffected
II ³	58	male	25.0	140	80	no	6.06	no	1.80	5.46	1.31	3.53	no
II ⁵ *	47/46	female	27.9	170	100	yes	8.08	yes	1.35	6.93	2.10	3.76	no
II ⁷ *	44/41	male	25.4	135	80	yes	7.16	no	1.57	3.23	1.02	1.76	yes
III ¹	33	female	22.2	115	75	no	4.58	no	0.56	4.51	1.68	2.18	no
III ² *	31	male	24.9	130	80	no	4.69	no	2.24	6.24	1.18	3.66	no
III ³	34	male	23.7	150	100	no	4.53	no	1.24	4.87	1.12	3.31	no
III ⁴	28	male	24.2	140	80	no	3.83	no	1.26	4.93	1.65	2.32	no
III ⁵	35	female	23.4	120	80	no	4.54	no	0.68	4.59	1.62	2.27	no
III ⁶	30	female	20.3	105	70	no	3.42	no	0.94	3.97	1.38	2.12	no
III ⁷ *	22	male	21.2	110	70	no	4.76	no	1.18	3.60	1.23	1.77	no
III ⁸ *	20	male	30.1	130	85	no	4.58	no	1.29	6.12	1.48	3.81	no

ID corresponds to those in Figure 1; BMI: body mass index; SBP: systolic blood pressure; DBP: diastolic blood pressure; anti-HT: anti-hypertension; anti-D: anti-diabetes; anti-HL: anti-hyperlipidemia; TC: total cholesterol; HDL-C: high density lipoprotein cholesterol; LDL-C: low density lipoprotein cholesterol; *: Y418H carrier; ^t: deceased; SCD: sudden cardiac death; NA: not available.

2.2. *LRP6_{Y418H}* Weakened the Wnt Signaling Pathway

As a receptor, *LRP6* activates the canonical Wnt-mediated signal pathway. To determine whether the mutation Y418H impaired Wnt signaling transduction, a comparative study was carried out among wild-type (*LRP6_{WT}*), mutant *LRP6* with Y418H (*LRP6_{Y418H}*) and mutant *LRP6* with a previously reported mutation R611C (*LRP6_{R611C}*) [12]. We transfected human umbilical vein endothelial cells (HUVEC) with the same amount of plasmids encoding *LRP6_{WT}*, *LRP6_{R611C}* or *LRP6_{Y418H}*, which were supported by RT-PCR (Figure 2A). Western blot showed that when an equal amount of protein was loaded, the distribution of mutant LRP6 protein in the cellular membrane fraction was similar to wild type (Figure 2B–D). The luciferase reporter activity indicating the extent of Wnt signal activation was then measured. We found that the Wnt3a-induced signaling was decreased 20% and 30% for *LRP6_{R611C}* and *LRP6_{Y418H}* compared with *LRP6_{WT}*, respectively ($p < 0.05$) (Figure 2E). A more severe reduction was observed in the *LRP6_{Y418H}*-than in the *LRP6_{R611C}*-treated group ($p < 0.05$).

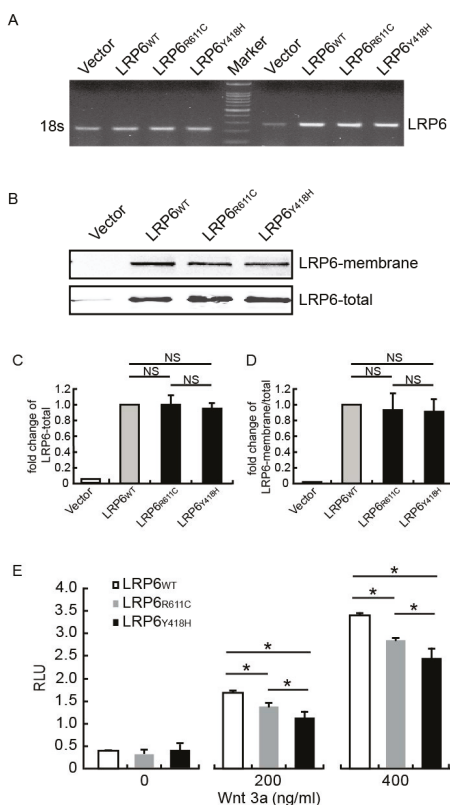


Figure 2. Effect of *LRP6_{Y418H}* and *LRP6_{R611C}* on Wnt signal transduction. (A) RT-PCR showed that there was no significant difference between the over-expression levels of *LRP6_{WT}*/*LRP6_{R611C}*/*LRP6_{Y418H}*; (B) Western blot showed no significant difference between total expression levels or membrane location of wild-type and mutant LRP6. Results were replicated three times and a representative figure was shown; (C,D) Statistical result of (B); (E) Luciferase assay was performed with different amount of Wnt3a. RLU: relative light units. Results were obtained with four independent transfections. Error bars, standard deviation. * indicate p -value for one-way ANOVA plus post-hoc test <0.05 . NS, not significant in one-way ANOVA plus post-hoc test.

2.3. *LRP6_{Y418H}* Impaired Endothelial Cell Functions

Endothelial cell dysfunction contributes to atherosclerosis. To investigate the possible mechanisms of atherosclerosis associated with *LRP6_{Y418H}*, we first screened the effect of this mutation on endothelial cell functions, including proliferation, migration, and anti-apoptosis, which were critical to maintaining the integrity of the endothelium. A significantly decreased proliferation and migration was observed in HUVEC over-expressing *LRP6_{R611C}* and *LRP6_{Y418H}* (all $p < 0.05$), and the effect of *LRP6_{Y418H}* was more profound than that of *LRP6_{R611C}* (Figure 3A,B as well as Supplementary Figure S1). The over-expression of *LRP6* (wild type and mutant) protected endothelial cells from the serum withdrawal-induced apoptosis, as shown by apoptotic DNA ladders (Figure 3C) and flow cytometric analyses (Figure 3D,E); the anti-apoptotic ability, however, was decreased in the cells infected by the mutant *LRP6* (*LRP6_{R611C}* and *LRP6_{Y418H}*). No significant difference was observed between the two mutations.

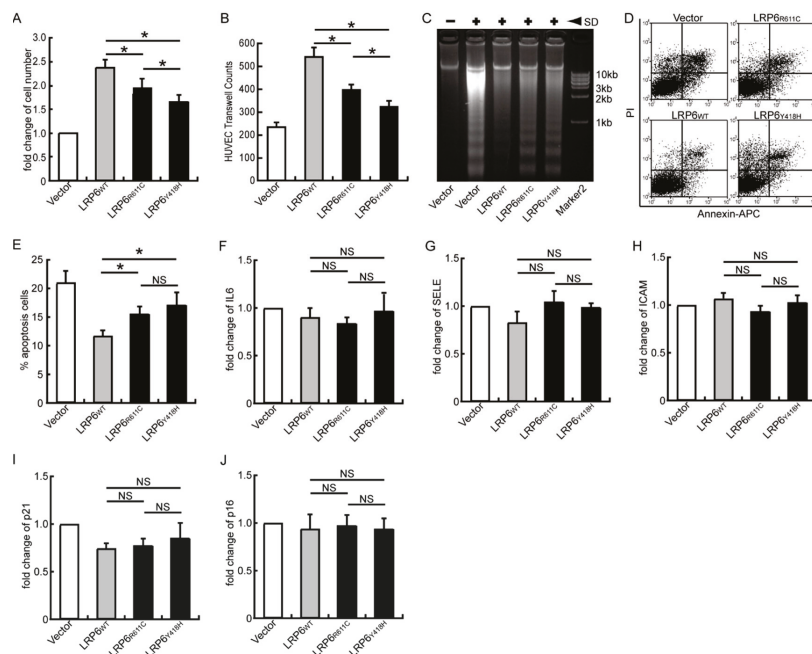


Figure 3. Effect of *LRP6_{Y418H}* and *LRP6_{R611C}* on endothelial cell functions; (A) Comparison of endothelial cells' proliferation. The same amount of cells was over-expressed with wild-type *LRP6* or mutant. After 48 h, cell number was counted for each group. Results were calculated using eight random fields from four independent biological replications; (B) Comparison of endothelial cell migration. Results were calculated using six views from three independent replications of Boyden chamber assay; (C) Electrophorogram for DNA ladder assay. SD, serum depletion; (D) Scatter diagram from flow cytometry assay. Data were presented in 2D diagrams plotting PI against Annexin-APC. Compensation for background fluorescence was performed by measuring target signals of single color controls and negative controls. Two quadrants in the right-side diagram represent apoptotic cells; (E) Statistical result for proportion of apoptotic cells in each group. Three biological repeats were taken into calculation; (F–J) Relative mRNA level of markers for endothelial cell activation (*IL6*, *SELE*, and *ICAM*) and senescence (*P21* and *P16*). Three biological repeats were taken into calculation. Error bars, standard deviation. * indicate p -value for one-way ANOVA plus post-hoc test <0.05 . NS, not significant.

We then assessed how the mutations influenced the inflammatory responses of endothelial cells and found no differences among the wild-type and two mutations in the mRNA expression of *IL6* (Figure 3F), *SELE* (Figure 3G), and *ICAM-1* (Figure 3H).

Finally, no differences were found in the mRNA expression of *P21* and *P16*, two markers for cell senescence, among all groups, suggesting senescence was not involved (Figure 3I,J).

2.4. The Influence of *LRP6_{Y418H}* on Cellular LDL-C Clearance

Compared with *LRP6_{WT}*, *LRP6_{R611C}* has been shown to decrease cellular LDL-C clearance. We examined whether *LRP6_{Y418H}* had a similar effect. After being incubated with LDL-C labeled by Dil (a red dye), cells transfected with *LRP6_{R611C}* presented a reduced LDL uptake compared to the *LRP6_{WT}* cells ($p < 0.05$) (Figure 4A,B), but no differences existed between *LRP6_{WT}* and *LRP6_{Y418H}*.

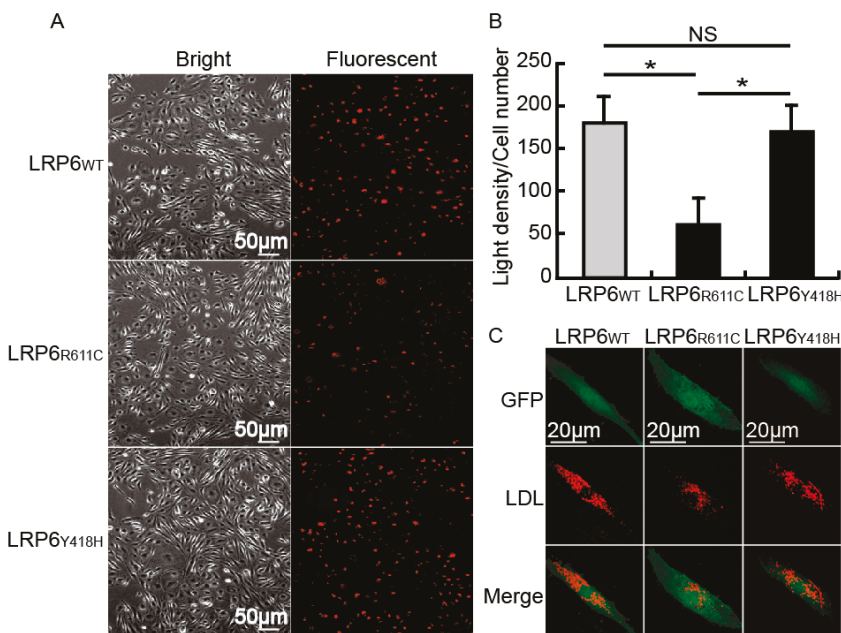


Figure 4. Effect of *LRP6_{Y418H}* and *LRP6_{R611C}* on LDL uptake in HUVEC. (A) An overview of the Dil-LDL uptake in HUVEC; Left, bright field; Right, Fluorescent field; (B) Quantitative results were calculated using six random views from three independent replications. Error bars, standard deviation. * indicate p -value for one-way ANOVA plus post-hoc test <0.05 . NS, not significant; (C) Enlarged views for single cells. Top, GFP translated by IRES following *LRP6*; Middle, Dil-LDL; Bottom, merged data.

3. Discussion

Here we report a novel heterozygous mutation of LRP6 in a Chinese normolipidemic CAD family, which leads to a substitution of histidine to tyrosine (Y418H) in an evolutionarily conserved domain, YWTD. *LRP6_{Y418H}* does not alter the lipid transportation; however, it weakens the Wnt signaling pathway and exhibits deleterious effects on the proliferation, migration, and survival of endothelial cells. Our study suggests that impaired endothelial functions caused by genetic mutation are critical in the pathogenesis of normolipidemic CAD.

Over the past decades, a large number of genetic studies have been performed to search for the genes or loci associated with CAD mostly with hyperlipidemia, but genetic knowledge on normolipidemic CAD remains limited [20]. Here, we identified a genetic variant (Y418H) of LRP6 in a

Chinese normolipidemic CAD family and provided several lines of evidence to show that this genetic variant was a possible defect for familial normolipidemic CAD. Genetically, Y418H occurred in an evolutionarily conserved YWTD domain, was co-segregated with CAD phenotypes in the family, and was not detected in 1025 healthy individuals in this study. In addition, we inspected this mutation in three other databases. Y418H was not found in the NHLBI GO Exome Sequencing Project (ESP) (6503 samples) and in the in-house control test (221 samples); however, there were two carriers in 1000GP (2504 samples), yielding an allele frequency of 0.0004 (Table S4). Due to the lack of diagnosis, we cannot rule out whether or not those carries are potential CAD patients occurring in Han Chinese South (CHS). It is very interesting to note that we have observed LRP6 mutations in sporadic Chinese CAD patients [21]. With the notion from the present study that *LRP6* can be a candidate gene for normolipidemic CAD, we checked the blood lipid levels and found that they were not elevated in their first clinic visits (Table S5). Differently, mutations in *LRP6* were screened out in American kindreds with early-onset hyperlipidemic CAD [22]. With the limited numbers of mutations found by far, it is difficult to make solid correlations between race, genotypes (positions of the mutations in *LRP6* gene) and phenotypes (normolipidemic or hyperlipidemic CAD). It appears clear that *LRP6* is a plausible candidate gene for both normolipidemic and hyperlipidemic CAD.

Functionally, Y418H is predicted to be a damaging allele with a Polyphen2 score of 0.994 that is higher than that of R611C. We demonstrated that LRP6Y418H weakened the ability in proliferation, migration, and survival of endothelial cells when exposed to stress. It is known that homeostasis or prompt renewal of endothelial cells is critical to maintain the integrity of the endothelium. Denuded by mechanical injuries, the endothelium can be amended by adjacent endothelial cells and endothelial progenitor cells as well [3,23–31]. This suggests that, in addition to endothelial progenitor cells, the survival, proliferation, and migration of endothelial cells localized in the zone adjacent to the injured region are important to maintain the homeostasis. The impaired or dysfunctional endothelium associated with LRP6Y418H should increase the susceptibility, together with other risk factors, such as hypertension and diabetes in the affected individuals, to develop atherosclerosis in coronary arteries. Finally, we showed that LRP6Y418H weakened the Wnt signaling pathway that had been reported to contribute to familial CAD [12]. The extracellular structure of the LRP6 protein is mainly composed of four beta propellers (BP) that contain six YWTD repeats which are separated by four EGF-like domains. It was reported that the four BPs have different functions, for example BP1 and BP2 are mainly responsible for the binding of Wnt and Wise [32,33]. Strikingly, most mutations in Supplementary Table S4 that were predicted to be seriously functionally damaged reside in the second propeller and EGF-like domain, suggesting the importance of the second YWTD-EGF structure and Wnt signal for CAD. This genetic and functional evidence supports that *LRP6* is a reasonable candidate gene for normolipidemic familial CAD.

Since R611C and Y418H were found in two CAD families, we compared clinical phenotypes and functions of the two mutant LRP6s. In clinical phenotypes, two families had some overlapping phenotypes: (1) some individuals in the families suffered from sudden cardiac death; and (2) the affected subjects (after age 40) had multiple CAD risk factors such as hypertension and diabetes. However, the blood lipid was dramatically different between the CAD patients in the two families: the Y418H family was normolipidemic while the R611C family was hyperlipidemic; high levels of LDL-C and triglycerides were co-segregated with CAD in the R611C family. Functionally distinct from Y418H, the R611C mutation was in the EGF-like domain and impaired the cellular LDL-C uptake. This was in agreement with a recent finding that the R611C mutation resulted in decreased LDL-C clearance [34] and reduced LRP6 activity in LRP6R611C mice that had elevated plasma LDL-C and TG levels and fatty liver [35]. Nonetheless, two mutations (Y418H and R611C) at the different positions of the *LRP6* gene can be linked to normolipidemic and hyperlipidemic CAD, two subtypes of familial CAD, suggestive of the importance of LRP6.

LRP6, a trans-membrane protein of the low-density lipoprotein receptor (LDLR) family, was identified based on its homology with the LDLR gene [36]. As a receptor of the canonical

Wnt signaling pathway, LRP6, together with LRP5 and Frizzled, activates β -catenin-TCF/LEF and regulates downstream signaling which is important in the development and maintenance of the cardiovascular system [37]. For example, activation of this pathway induces the proliferation, migration, and survival of endothelial cells [38–40]. We in this study demonstrated that LRP6Y418H attenuated the Wnt3a-activated signaling pathway, decreased proliferation and mobility, and weakened the anti-apoptotic response of endothelial cells. Similarly, it has been shown that mutations of LRP6 found in sporadic CAD patients attenuated proliferation and migration of HUVEC as well as the Wnt signal [21]. LRP6R611C also attenuated the Wnt3a-activated signaling pathway [12]. These suggest that mutant LRP6 impairs endothelial cell functions, possibly through the attenuation of the Wnt-signaling pathway. However, how other risk factors, such as hypertension and diabetes, interact with the genetic defect in atherosclerogenesis needs to be further investigated.

Several limitations exist in this study: (1) the third generation of the studied pedigree is still young, and we cannot claim whether or not the mutation carriers in this generation are CAD patients; (2) LRP6 has a broad range of functions, and whether other signal pathways are involved in the pathogenic mechanism of this family cannot be excluded. For example, LRP6 is a co-receptor for multiple fibrogenic signaling pathways in pericytes and myofibroblasts [41]. It is not clear whether or not these pathways contribute to CAD associated with the LRP6 mutations; and (3) although Wang et al. identified *MEF2A* as a causal gene for CAD, we did not find any mutation in this gene during our first screening. Similar to our finding, Lieb et al. suggested the lack of association between the *MEF2A* gene and myocardial infarction [42]. However, limited by the modest sample number, we cannot rule out the role of *MEF2A* in CAD.

In conclusion, we identified a mutation (Y418H) in the YWTD domain of LRP6 that co-segregated with normolipidemic CAD in a Han Chinese family that impaired endothelial cell functions, implying that endothelial dysfunctions associated with a genetic mutation play an important role in normolipidemic CAD.

4. Materials and Methods

4.1. Study Subjects

We recruited 40 Chinese Han families with CAD that were ascertained through probands and included more than two early-onset CAD/ myocardial infarction (MI) patients (less than 50 years old for males or 55 years old for females). Blood pressure, glucose, hypertension, and diabetes mellitus were measured or defined [43]. Hyperlipidemia or normolipidemia were defined based on clinical diagnosis. 1025 unrelated Han Chinese controls were general healthy donors [44]. Written informed consent was obtained from all participants. The study was conducted in agreement with the principles outlined in the Declaration of Helsinki and approved by the Institutional Review Board, Institute of Molecular Medicine at Peking University.

4.2. Cell Culture

Primary human umbilical vein endothelial cells (HUVECs) were isolated from fresh human umbilical veins, cultured in complete Endothelial Cell Medium (ECM, ScienCell), and maintained at 37 °C in 5% CO₂. The informed consents were signed by babies' fathers. The study was conducted in agreement with the principles outlined in the Declaration of Helsinki and approved by the Institutional Review Board, Institute of Molecular Medicine at Peking University.

4.3. Mutational Screening

Human genomic DNA was isolated as described previously [44]. The exons of the target genes and their flanking exon-intron boundaries were amplified by PCR using specific primers listed in Tables S2 and S3. The amplified DNA fragments were purified and subjected to direct sequencing on ABI 3130XL according to the manual description of BigDye v3.1 kit.

4.4. Wnt Signaling Analysis

cDNA clone of LRP6 (pCR-XL-TOPO-LRP6) was purchased from FulenGen. cDNA sequence was validated by sequencing and inserted into pShuttle-IRES-hrGFP-1 vector. Mutations (Y418H and R611C, a previously reported mutation [12]) were introduced by PCR-based mutagenesis, respectively. The mutations were verified by DNA sequencing. HUVEC was electric transfected with equal amount of plasmids expressing wild-type (LRP6wt) and mutant LRP6 (LRP6R611C or LRP6Y418H), respectively. A Wnt pathway reporter system was utilized as previously described [12]. Briefly, plasmids encoding wild-type LRP6 or mutants, LEF-1, firefly luciferase, and renilla luciferase were introduced into cells by transfection. After 24 h, cells were lysed and luciferase reporter activity indicating the extent of Wnt signal activation was measured in accordance with the dual luciferase assay specifications (Promega, Hollow Road Madison, WI, USA).

4.5. Quantitative Real-Time PCR

Total RNA was extracted using Trizol reagent (Invitrogen, Waltham, MA, USA). Reverse transcription and quantitative real-time PCR were performed as previously described [45]. Information of specific primers is listed in Table S6. Results were normalized to 18S rRNA.

4.6. Western Blot Analysis of LRP6

Total and membrane protein were extracted using kit from Beyotime Biotechnology. Western blot was performed to detect the wild type and mutant LRP6 protein (primary antibody for LRP6: sc-25317, Santa Cruz, Dallas, TX, USA) based on the protocol previously reported [46]. GAPDH was used as a loading control.

4.7. HUVEC Proliferation, Migration, and Apoptosis Analysis

For overexpression wild-type LRP6 or mutants in HUVECs, infection was performed with adenovirus that constructed following manufacturer's protocol for AdEasy system (Stratagene, Santa Clara, CA, USA) [47]. We controlled the same over-expressions level among different groups by adjusting the amount of virus added. Proliferation was evaluated using MTT (Sigma, St. Louis, MO, USA) assay and actual cell number count, and migration was evaluated Boyden Chamber assay [48]. To avoid the effect of proliferation, we controlled the migration time within 12 h. Apoptosis was presented by both DNA ladder gel electrophoresis [49] and FACS analysis (BD Biosciences Clontech Kit, San Jose, CA, USA).

4.8. Dil-LDL Uptake

HUVECs were placed in a six-well plate containing 20 µg/dL cholesterol and 2 µg/mL 25-hydroxycholesterol to down-regulate the endogenous LDLR (Supplementary Figure S2). After 24 h, 10 µg/mL Dil-LDL was added and incubated at 37 °C for six hours. Cells were washed three times with PBS containing 1% FBS and were fixed in 4% paraformaldehyde. Specimens were then examined by confocal microscope.

4.9. Statistic Analysis

Results are expressed as mean ± SD as indicated in the legends for measurement data. Comparisons were performed using one-way ANOVA with post-hoc in SPSS software. $p < 0.05$ was considered statistically significant.

Supplementary Materials: Supplementary materials can be found at <http://www.mdpi.com/1422-0067/17/7/1173/s1>.

Acknowledgments: We thank all the participants in our population study. This work was supported by the National Basic Research Program of the Chinese Ministry of Science and Technology (973 program) (Grant

No. 2013CB530700 and 2007CB512103); and the National Natural Science Foundation of China (NSFC Grant No. 81130003 and 81070262).

Author Contributions: Xiao-Li Tian supervised the study. Xiao-Li Tian, Yi-Hong Ren, Dao Wen Wang, Jie Du, Jian Guo and Yang Li participated in the study design. Yi-Hong Ren, Zhijun Sun and Yujun Xu performed sample collection and data management. Jian Guo and Yang Li conceived and designed the experiments; Jian Guo, Yang Li, Jie Dong, Han Yan, and Gu-Yan Zheng performed the experiments. Xiao-Li Tian, Jian Guo and Yang Li analyzed the data and wrote the manuscript. All authors read and contributed to the manuscript.

Conflicts of Interest: The authors declare no conflict of interest.

References

- Watkins, H.; Farrall, M. Genetic susceptibility to coronary artery disease: From promise to progress. *Nat. Rev. Genet.* **2006**, *7*, 163–173. [CrossRef] [PubMed]
- Hansson, G.K. Inflammation, atherosclerosis, and coronary artery disease. *N. Engl. J. Med.* **2005**, *352*, 1685–1695. [CrossRef] [PubMed]
- Tian, X.L.; Li, Y. Endothelial cell senescence and age-related vascular diseases. *J. Genet. Genom.* **2014**, *41*, 485–495. [CrossRef] [PubMed]
- Go, A.S.; Mozaffarian, D.; Roger, V.L.; Benjamin, E.J.; Berry, J.D.; Blaha, M.J.; Dai, S.; Ford, E.S.; Fox, C.S.; Franco, S.; et al. Heart disease and stroke statistics—2014 update: A report from the American Heart Association. *Circulation* **2014**, *129*. [CrossRef] [PubMed]
- Ford, E.S.; Ajani, U.A.; Croft, J.B.; Critchley, J.A.; Labarthe, D.R.; Kottke, T.E.; Giles, W.H.; Capewell, S. Explaining the decrease in U.S. deaths from coronary disease, 1980–2000. *N. Engl. J. Med.* **2007**, *356*, 2388–2398. [CrossRef] [PubMed]
- Schunkert, H.; Konig, I.R.; Kathiresan, S.; Reilly, M.P.; Assimes, T.L.; Holm, H.; Preuss, M.; Stewart, A.F.R.; Barbalic, M.; Gieger, C.; et al. Large-scale association analysis identifies 13 new susceptibility loci for coronary artery disease. *Nat. Genet.* **2011**, *43*, 333–338. [CrossRef] [PubMed]
- Wang, F.; Xu, C.Q.; He, Q.; Cai, J.P.; Li, X.C.; Wang, D.; Xiong, X.; Liao, Y.H.; Zeng, Q.T.; Yang, Y.-Z.; et al. Genome-wide association identifies a susceptibility locus for coronary artery disease in the Chinese Han population. *Nat. Genet.* **2011**, *43*, 345–349. [CrossRef] [PubMed]
- Lu, X.; Wang, L.; Chen, S.; He, L.; Yang, X.; Shi, Y.; Cheng, J.; Zhang, L.; Gu, C.C.; Huang, J.; et al. Genome-wide association study in Han Chinese identifies four new susceptibility loci for coronary artery disease. *Nat. Genet.* **2012**, *44*, 890–894. [CrossRef] [PubMed]
- Lieb, W.; Vasan, R.S. Genetics of coronary artery disease. *Circulation* **2013**, *128*, 1131–1138. [CrossRef] [PubMed]
- Roberts, R. Genetics of coronary artery disease. *Circ. Res.* **2014**, *114*, 1890–1903. [CrossRef] [PubMed]
- Wang, L.; Fan, C.; Topol, S.E.; Topol, E.J.; Wang, Q. Mutation of MEF2A in an inherited disorder with features of coronary artery disease. *Science* **2003**, *302*, 1578–1581. [CrossRef] [PubMed]
- Mani, A.; Radhakrishnan, J.; Wang, H.; Mani, A.; Mani, M.A.; Nelson-Williams, C.; Carew, K.S.; Mane, S.; Najmabadi, H.; Wu, D.; et al. *LRP6* mutation in a family with early coronary disease and metabolic risk factors. *Science* **2007**, *315*, 1278–1282. [CrossRef] [PubMed]
- Kannel, W.B.; Dawber, T.R.; Kagan, A.; Revotskie, N.; Stokes, J., 3rd. Factors of risk in the development of coronary heart disease—Six year follow-up experience. The Framingham Study. *Ann. Intern. Med.* **1961**, *55*, 33–50. [CrossRef] [PubMed]
- Thaker, A.M.; Frishman, W.H. Sortilin: The mechanistic link between genes, cholesterol, and coronary artery disease. *Cardiol. Rev.* **2014**, *22*, 91–96. [CrossRef] [PubMed]
- Expert Panel on Detection, Evaluation, and Treatment of High Blood Cholesterol in Adults. Executive Summary of the Third Report of the National Cholesterol Education Program (NCEP) Expert Panel on Detection, Evaluation, and Treatment of High Blood Cholesterol in Adults (Adult Treatment Panel III). *J. Am. Med. Assoc.* **2001**, *285*, 2486–2497.
- Grundy, S.M.; Cleeman, J.I.; Merz, C.N.; Brewer, H.B., Jr.; Clark, L.T.; Hunninghake, D.B.; Pasternak, R.C.; Smith, S.C.; Stone, N.J. Implications of recent clinical trials for the National Cholesterol Education Program Adult Treatment Panel III guidelines. *Circulation* **2004**, *110*, 227–239. [CrossRef] [PubMed]

17. Chernobelsky, A.; Ashen, M.D.; Blumenthal, R.S.; Coplan, N.L. High-density lipoprotein cholesterol: A potential therapeutic target for prevention of coronary artery disease. *Prev. Cardiol.* **2007**, *10*, 26–30. [CrossRef] [PubMed]
18. Ding, D.; Li, X.; Qiu, J.; Li, R.; Zhang, Y.; Su, D.; Li, Z.; Wang, M.; Lv, X.; Wang, D.; et al. Serum lipids, apolipoproteins, and mortality among coronary artery disease patients. *BioMed. Res. Int.* **2014**, *2014*, 709756. [CrossRef] [PubMed]
19. Rubins, H.B.; Robins, S.J.; Collins, D.; Iranmanesh, A.; Wilt, T.J.; Mann, D.; Mayo-Smith, M.; Faas, F.H.; Elam, M.B.; Rutan, G.H.; et al. Distribution of lipids in 8500 men with coronary artery disease. Department of Veterans Affairs HDL Intervention Trial Study Group. *Am. J. Cardiol.* **1995**, *75*, 1196–1201. [CrossRef]
20. Igurim-Souissi, I.; Jelassi, A.; Hrira, Y.; Najah, M.; Slimani, A.; Addad, F.; Hassine, M.; Hamda, K.B.; Maatouk, F.; Rouis, M.; et al. +294T/C polymorphism in the PPAR-delta gene is associated with risk of coronary artery disease in normolipidemic Tunisians. *Genet. Mol. Res.* **2010**, *9*, 1326–1333. [CrossRef] [PubMed]
21. Xu, Y.; Gong, W.; Peng, J.; Wang, H.; Huang, J.; Ding, H.; Wang, D.W. Functional analysis LRP6 novel mutations in patients with coronary artery disease. *PLoS ONE* **2014**, *9*, e84345. [CrossRef] [PubMed]
22. Singh, R.; Smith, E.; Fathzadeh, M.; Liu, W.; Go, G.W.; Subrahmanyam, L.; Faramarzi, S.; McKenna, W.; Mani, A. Rare nonconservative LRP6 mutations are associated with metabolic syndrome. *Hum. Mutat.* **2013**, *34*, 1221–1225. [CrossRef] [PubMed]
23. Reidy, M.A.; Schwartz, S.M. Endothelial injury and regeneration. IV. Endotoxin: A nondenuding injury to aortic endothelium. *Lab. Investig.* **1983**, *48*, 25–34. [PubMed]
24. Caplan, B.A.; Schwartz, C.J. Increased endothelial cell turnover in areas of in vivo Evans Blue uptake in the pig aorta. *Atherosclerosis* **1973**, *17*, 401–417. [CrossRef]
25. Hansson, G.K.; Chao, S.; Schwartz, S.M.; Reidy, M.A. Aortic endothelial cell death and replication in normal and lipopolysaccharide-treated rats. *Am. J. Pathol.* **1985**, *121*, 123–127. [PubMed]
26. Langille, B.L.; Reidy, M.A.; Kline, R.L. Injury and repair of endothelium at sites of flow disturbances near abdominal aortic coarctations in rabbits. *Arteriosclerosis* **1986**, *6*, 146–154. [CrossRef] [PubMed]
27. Cines, D.B.; Pollak, E.S.; Buck, C.A.; Loscalzo, J.; Zimmerman, G.A.; McEver, R.P.; Pober, J.S.; Wick, T.M.; Konkle, B.A.; Schwartz, B.S.; et al. Endothelial cells in physiology and in the pathophysiology of vascular disorders. *Blood* **1998**, *91*, 3527–3561. [PubMed]
28. Walter, D.H.; Dimmeler, S. Endothelial progenitor cells: Regulation and contribution to adult neovascularization. *Herz* **2002**, *27*, 579–588. [CrossRef] [PubMed]
29. Iwakura, A.; Luedemann, C.; Shastry, S.; Hanley, A.; Kearney, M.; Aikawa, R.; Isner, J.M.; Asahara, T.; Losordo, D.W. Estrogen-mediated, endothelial nitric oxide synthase-dependent mobilization of bone marrow-derived endothelial progenitor cells contributes to reendothelialization after arterial injury. *Circulation* **2003**, *108*, 3115–3121. [CrossRef] [PubMed]
30. Werner, N.; Junk, S.; Laufs, U.; Link, A.; Walenta, K.; Bohm, M.; Nickenig, G. Intravenous transfusion of endothelial progenitor cells reduces neointima formation after vascular injury. *Circ. Res.* **2003**, *93*, e17–e24. [CrossRef] [PubMed]
31. Porto, I.; Leone, A.M.; De Maria, G.L.; Hamilton Craig, C.; Tritarelli, A.; Camaioni, C.; Natale, L.; Niccoli, G.; Biasucci, L.M.; Crea, F. Are endothelial progenitor cells mobilized by myocardial ischemia or myocardial necrosis? A cardiac magnetic resonance study. *Atherosclerosis* **2011**, *216*, 355–358. [CrossRef] [PubMed]
32. He, X.; Semenov, M.; Tamai, K.; Zeng, X. LDL receptor-related proteins 5 and 6 in Wnt/beta-catenin signaling: Arrows point the way. *Development* **2004**, *131*, 1663–1677. [CrossRef] [PubMed]
33. Cheng, Z.; Biechele, T.; Wei, Z.; Morrone, S.; Moon, R.T.; Wang, L.; Xu, W. Crystal structures of the extracellular domain of LRP6 and its complex with DKK1. *Nat. Struct. Mol. Biol.* **2011**, *18*, 1204–1210. [CrossRef] [PubMed]
34. Liu, W.; Mani, S.; Davis, N.R.; Sarrafzadegan, N.; Kavathas, P.B.; Mani, A. Mutation in EGFP domain of LDL receptor-related protein 6 impairs cellular LDL clearance. *Circ. Res.* **2008**, *103*, 1280–1288. [CrossRef] [PubMed]
35. Go, G.W.; Srivastava, R.; Hernandez-Ono, A.; Gang, G.; Smith, S.B.; Booth, C.J.; Ginsberg, H.N.; Mani, A. The combined hyperlipidemia caused by impaired Wnt-LRP6 signaling is reversed by Wnt3a rescue. *Cell Metab.* **2014**, *19*, 209–220. [CrossRef] [PubMed]

36. Brown, S.D.; Twells, R.C.; Hey, P.J.; Cox, R.D.; Levy, E.R.; Soderman, A.R.; Metzker, M.L.; Caskey, C.T.; Todd, J.A.; Hess, J.F. Isolation and characterization of LRP6, a novel member of the low density lipoprotein receptor gene family. *Biochem. Biophys. Res. Commun.* **1998**, *248*, 879–888. [CrossRef] [PubMed]
37. Bafico, A.; Liu, G.; Yaniv, A.; Gazit, A.; Aaronson, S.A. Novel mechanism of Wnt signalling inhibition mediated by Dickkopf-1 interaction with LRP6/Arrow. *Nat. Cell Biol.* **2001**, *3*, 683–686. [CrossRef] [PubMed]
38. Samarzija, I.; Sini, P.; Schlaege, T.; Macdonald, G.; Hynes, N.E. Wnt3a regulates proliferation and migration of HUVEC via canonical and non-canonical Wnt signaling pathways. *Biochem. Biophys. Res. Commun.* **2009**, *386*, 449–454. [CrossRef] [PubMed]
39. Okumura, N.; Nakamura, T.; Kay, E.P.; Nakahara, M.; Kinoshita, S.; Koizumi, N. R-spondin1 regulates cell proliferation of corneal endothelial cells via the Wnt3a/β-catenin pathway. *Investig. Ophthalmol. Vis. Sci.* **2014**, *55*, 6861–6869. [CrossRef] [PubMed]
40. De Jesus Perez, V.A.; Alastalo, T.P.; Wu, J.C.; Axelrod, J.D.; Cooke, J.P.; Amieva, M.; Rabinovitch, M. Bone morphogenetic protein 2 induces pulmonary angiogenesis via Wnt-beta-catenin and Wnt-RhoA-Rac1 pathways. *J. Cell Biol.* **2009**, *184*, 83–99. [CrossRef] [PubMed]
41. Ren, S.; Johnson, B.G.; Kida, Y.; Ip, C.; Davidson, K.C.; Lin, S.L.; Kobayashi, A.; Lang, R.A.; Hadjantonakis, A.-K.; Moon, R.T.; et al. LRP-6 is a coreceptor for multiple fibrogenic signaling pathways in pericytes and myofibroblasts that are inhibited by DKK-1. *Proc. Natl. Acad. Sci. USA* **2013**, *110*, 1440–1445. [CrossRef] [PubMed]
42. Lieb, W.; Mayer, B.; Konig, I.R.; Borwitzky, I.; Gotz, A.; Kain, S.; Hengstenberg, C.; Linsel-Nitschke, P.; Fischer, M.; Döring, A.; et al. Lack of association between the MEF2A gene and myocardial infarction. *Circulation* **2008**, *117*, 185–191. [CrossRef] [PubMed]
43. Jiang, F.; Dong, Y.; Wu, C.; Yang, X.; Zhao, L.; Guo, J.; Li, Y.; Dong, J.; Zheng, G.-Y.; Cao, H.; et al. Fine mapping of chromosome 3q22.3 identifies two haplotype blocks in ESYT3 associated with coronary artery disease in female Han Chinese. *Atherosclerosis* **2011**, *218*, 397–403. [CrossRef] [PubMed]
44. Li, Y.; Wang, W.J.; Cao, H.; Lu, J.; Wu, C.; Hu, F.Y.; Guo, J.; Zhao, L.; Yang, F.; Zhang, Y.-X.; et al. Genetic association of FOXO1A and FOXO3A with longevity trait in Han Chinese populations. *Hum. Mol. Genet.* **2009**, *18*, 4897–4904. [CrossRef] [PubMed]
45. Yang, F.; Zhou, L.; Wang, Q.; You, X.; Li, Y.; Zhao, Y.; Han, X.; Chang, Z.; He, X.; Cheng, C.; et al. NEXN inhibits GATA4 and leads to atrial septal defects in mice and humans. *Cardiovasc. Res.* **2014**, *103*, 228–237. [CrossRef] [PubMed]
46. Tian, X.L.; Paul, M. Species-specific splicing and expression of angiotensin converting enzyme. *Biochem. Pharmacol.* **2003**, *66*, 1037–1044. [CrossRef]
47. Hu, F.Y.; Wu, C.; Li, Y.; Xu, K.; Wang, W.J.; Cao, H.; Tian, X.-L. AGGF1 is a novel anti-inflammatory factor associated with TNF-α-induced endothelial activation. *Cell Signal.* **2013**, *25*, 1645–1653. [CrossRef] [PubMed]
48. Yan, G.; Chen, S.; You, B.; Sun, J. Activation of sphingosine kinase-1 mediates induction of endothelial cell proliferation and angiogenesis by epoxyeicosatrienoic acids. *Cardiovasc. Res.* **2008**, *78*, 308–314. [CrossRef] [PubMed]
49. Matsuda, N.; Takano, Y.; Kageyama, S.; Hatakeyama, N.; Shakunaga, K.; Kitajima, I.; Yamazaki, M.; Hattori, Y. Silencing of caspase-8 and caspase-3 by RNA interference prevents vascular endothelial cell injury in mice with endotoxic shock. *Cardiovasc. Res.* **2007**, *76*, 132–140. [CrossRef] [PubMed]



© 2016 by the authors. Licensee MDPI, Basel, Switzerland. This article is an open access article distributed under the terms and conditions of the Creative Commons Attribution (CC BY) license (<http://creativecommons.org/licenses/by/4.0/>).



Article

Cerebral Hyperperfusion after Revascularization Inhibits Development of Cerebral Ischemic Lesions Due to Artery-to-Artery Emboli during Carotid Exposure in Endarterectomy for Patients with Preoperative Cerebral Hemodynamic Insufficiency: Revisiting the “Impaired Clearance of Emboli” Concept

Kentaro Fujimoto ¹, Yoshiyasu Matsumoto ¹, Kohki Oikawa ¹, Jun-ichi Nomura ¹, Yasuyoshi Shimada ¹, Shunrou Fujiwara ¹, Kazunori Terasaki ², Masakazu Kobayashi ¹, Kenji Yoshida ¹ and Kuniaki Ogasawara ^{1,*}

¹ Department of Neurosurgery, School of Medicine, Iwate Medical University, 19-1 Uchmaru, 020-8505 Morioka, Japan; norimori@iwate-med.ac.jp (K.F.); yoshiyasu.matumoto@gmail.com (Y.M.); hchrt770@yahoo.co.jp (K.O.); pbx1vfuj@yahoo.co.jp (J.-i.N.); khata@iwate-med.ac.jp (Y.S.); shunfaji@iwate-med.ac.jp (S.F.); kobamasa@iwate-med.ac.jp (M.K.); kenyoshi@iwate-med.ac.jp (K.Y.)

² Cyclotron Research Center, School of Medicine, Iwate Medical University, 19-1 Uchmaru, 020-8505 Morioka, Japan; ktera@iwate-med.ac.jp

* Correspondence: kuogasa@iwate-med.ac.jp; Tel.: +81-19-651-5111; Fax: +81-19-625-8799

Academic Editor: Michael Henein

Received: 1 June 2016; Accepted: 25 July 2016; Published: 3 August 2016

Abstract: The purpose of the present study was to determine whether cerebral hyperperfusion after revascularization inhibits development of cerebral ischemic lesions due to artery-to-artery emboli during exposure of the carotid arteries in carotid endarterectomy (CEA). In patients undergoing CEA for internal carotid artery stenosis ($\geq 70\%$), cerebral blood flow (CBF) was measured using single-photon emission computed tomography (SPECT) before and immediately after CEA. Microembolic signals (MES) were identified using transcranial Doppler during carotid exposure. Diffusion-weighted magnetic resonance imaging (DWI) was performed within 24 h after surgery. Of 32 patients with a combination of reduced cerebrovascular reactivity to acetazolamide on preoperative brain perfusion SPECT and MES during carotid exposure, 14 (44%) showed cerebral hyperperfusion (defined as postoperative CBF increase $\geq 100\%$ compared with preoperative values), and 16 (50%) developed DWI-characterized postoperative cerebral ischemic lesions. Postoperative cerebral hyperperfusion was significantly associated with the absence of DWI-characterized postoperative cerebral ischemic lesions (95% confidence interval, 0.001–0.179; $p = 0.0009$). These data suggest that cerebral hyperperfusion after revascularization inhibits development of cerebral ischemic lesions due to artery-to-artery emboli during carotid exposure in CEA, supporting the “impaired clearance of emboli” concept. Blood pressure elevation following carotid declamping would be effective when embolism not accompanied by cerebral hyperperfusion occurs during CEA.

Keywords: artery-to-artery embolism; carotid endarterectomy; cerebral hemodynamic insufficiency; cerebral hyperperfusion; ischemic lesion

1. Introduction

It has been previously reported that hemodynamic and embolic mechanisms are closely linked, and they may act together to cause cerebral ischemia [1,2]. The authors suggested that clearance of emboli from a proximal lesion may be decreased by low blood flow velocity in a cerebral artery, which may lead to ischemia from emboli in poorly perfused areas of the brain. In support of this, several previous studies showed that there was a relationship between embolic and hemodynamic mechanisms, particularly in border zone regions having impaired wash-out due to artery-to-artery embolism in cases of middle cerebral artery stenosis [3,4] or in new postoperative neurological deficits caused by emboli developing during carotid artery stenting associated with intraprocedural lower middle cerebral artery blood flow velocity [5].

More than 70% of the intraoperative procedure-related strokes that occur during carotid endarterectomy (CEA) are due to surgical site embolisms [6]. When intraoperative transcranial Doppler (TCD) is used to monitor the middle cerebral artery (MCA), more than 90% of patients undergoing CEA are found to have microembolic signals (MES) [6–8]. However, the stage of CEA determines the quality and quantity of MES that are detected [6,8,9]. When the carotid arteries are being exposed, plaque that has not been removed is exposed to blood flow and can be a source of emboli. In such cases, emboli can be dislodged from the surgical site into the intracranial arteries during manipulation of the carotid arteries [8]. In addition, the MES that are detected are considered to represent solid masses, because the target vessel is closed while the vessel is being exposed [10]. However, once the carotid artery walls are incised for the endarterectomy, many harmless gaseous MES may be seen during carotid declamping as air enters the arterial lumina [8,11]. MES detection while the artery is being exposed has been shown to be correlated with the development of post-CEA cerebral ischemic lesions on diffusion-weighted imaging (DWI) [7–9,11–13]. Furthermore, these ischemic lesions that are related to the emboli generated during carotid artery exposure have been shown to be related to preoperative hemodynamic cerebral compromise, such as reduced cerebrovascular reactivity (CVR) to acetazolamide [14], providing support for the concept of “impaired clearance of emboli”.

Cerebral hyperperfusion is defined as a major increase in ipsilateral cerebral blood flow (CBF) after surgical repair of carotid stenosis that is well above the metabolic demands of the brain tissue; it is another adverse event following CEA [15]. It occasionally evolves into cerebral hyperperfusion syndrome, whose characteristic manifestations include face and eye pain, unilateral headache, seizure, focal neurological symptoms, and disturbance of consciousness secondary to intracerebral hemorrhage or cerebral edema [15–18]. Impairment of the cerebral hemodynamic reserve before surgery may be related to post-CEA hyperperfusion, and quick normalization of perfusion pressure after CEA may produce hyperperfusion in brain regions with diminished autoregulation from chronic ischemia [17,18]. This hypothesis is consistent with the observation that reduced CVR to acetazolamide prior to surgery is a significant predictor of hyperperfusion after CEA [19–21].

Thus, both cerebral ischemic lesions due to artery-to-artery embolism and cerebral hyperperfusion may develop simultaneously during CEA in patients with preoperative cerebral hemodynamic impairment. When broadening the interpretation of the “impaired clearance of emboli” concept, blood flow greater than the normal level can inhibit development of ischemic lesions due to emboli in the brain, and research regarding the influence of cerebral hyperperfusion on the development of cerebral ischemic lesions due to artery-to-artery embolism seems interesting from the standpoint of this concept.

The aim of the present study was to determine whether broadening the interpretation of the “impaired clearance of emboli” concept is correct, namely cerebral hyperperfusion after revascularization inhibits development of cerebral ischemic lesions due to intraoperative artery-to-artery emboli. In order to do this, the relationship between development of DWI-characterized postoperative cerebral ischemic lesions and cerebral hyperperfusion was investigated in patients with a combination of preoperatively reduced CVR to acetazolamide on brain perfusion single-photon emission computed tomography (SPECT) and MES on TCD during carotid artery exposure in CEA.

2. Results

2.1. Trial Profile

Figure 1 shows the patient flow chart for this study. Six hundred and thirty patients with ipsilateral internal carotid artery (ICA) stenosis $\geq 70\%$ and useful residual function were scheduled for CEA and consented to participate in the present study. Of these 630 patients, 190 were defined as having reduced CVR to acetazolamide. Of these 190 patients, five did not undergo CEA and were excluded from the analysis. Of the 185 patients who underwent CEA, 23 did not show reliable TCD monitoring during carotid exposure because of failure to obtain an adequate bone window, and 26 showed electroencephalography (EEG)-defined hemispheric ischemia during ICA clamping; these 47 patients (two had both conditions) were excluded from the analysis. Of the remaining 138 patients, 32 had MES during exposure of the carotid arteries and were finally analyzed. Data acquisition with brain perfusion SPECT was completed within 3 h after declamping of the ICA in all these 32 patients. They all underwent DWI 24 h after surgery.

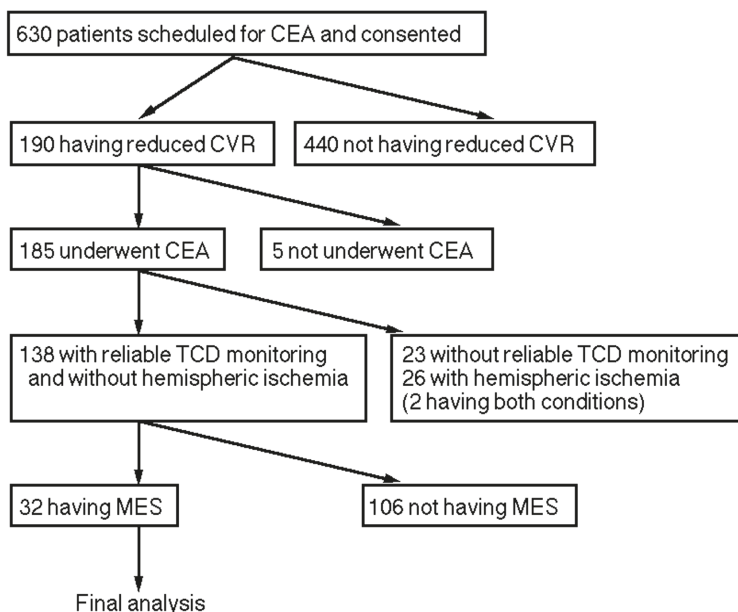


Figure 1. Trial profile showing the flow chart of patient numbers from initial screening to final analysis. Patients who did not have preoperative reduced cerebrovascular reactivity (CVR), did not undergo carotid endarterectomy (CEA), did not have reliable intraoperative transcranial Doppler (TCD) monitoring, had hemispheric ischemia during carotid clamping, and did not have microembolic signals (MES) during carotid exposure were excluded from the study.

2.2. Clinical Characteristics

The mean age of the 32 patients (29 men, three women) was 71.7 ± 4.5 (mean \pm standard deviation (SD)) years (range of 63–85 years). Twenty-six patients had preoperative hypertension, and 23 patients received antihypertensive drugs (calcium antagonist alone for five, angiotensin receptor blocker alone for 13 and both for five). Thirteen patients had preoperative diabetes mellitus, and all these patients received antidiabetic drugs. Fifteen patients had preoperative dyslipidemia, and 12 patients received a statin (strong statin for six). Seven patients had ischemic heart or valvular disease that did not satisfy the criteria for high-risk factors for CEA in the Stenting and Angioplasty with Protection in

Patients at High Risk for Endarterectomy (SAPPHIRE) study (congestive heart failure, abnormal stress test, or need for open-heart surgery) [22]. None of the 32 patients had atrial fibrillation. Twenty-five patients had ipsilateral carotid territory symptoms, and seven patients had asymptomatic ICA stenosis. The overall average degree of ICA stenosis was $85.4\% \pm 8.8\%$ (range, 70%–99%), with nine patients showing >70% stenosis or occlusion in the contralateral ICA. Preoperative CBF and CVR to acetazolamide were $33.1 \pm 6.1 \text{ mL}/100 \text{ g}/\text{min}$ (range of 22.6 – $44.5 \text{ mL}/100 \text{ g}/\text{min}$) and $8.6\% \pm 6.9\%$ (range of –8.3%–18.0%), respectively. Preoperative systolic blood pressure was $133.6 \pm 11.7 \text{ mmHg}$ (range of 111 – 156 mmHg). The number of MES ranged from one to 14 (4.3 ± 3.9). The interval from the first MES to ICA declamping ranged from 34 to 59 min (45.3 ± 6.4 min). The interval from the last MES to ICA declamping ranged from 35 to 65 min (46.8 ± 6.6 min). Mean systolic blood pressure during carotid exposure was $113.8 \pm 10.7 \text{ mmHg}$ (range of 95 – 138 mmHg). Mean duration of ICA clamping was 36.0 ± 5.7 min (range of 28 – 47 min). Mean systolic blood pressure in the post-carotid declamping period in surgery was $121.4 \pm 11.9 \text{ mmHg}$ (range of 105 – 141 mmHg). Mean systolic blood pressure in the postoperative period (within 24 h after surgery) was $127.8 \pm 12.6 \text{ mmHg}$ (range of 109 – 147 mmHg). The mean rate of blood pressure–measured points with successfully controlled blood pressure to all measured points in the post-carotid declamping period in surgery was $85.9\% \pm 3.9\%$ (range of 72%–93%). The mean rate of blood pressure–measured points with successfully controlled blood pressure to all the measured points in the postoperative period was $76.1\% \pm 4.9\%$ (range of 67%–92%).

2.3. Postoperative Events

In the 32 patients studied, postoperative CBF was $52.9 \pm 17.5 \text{ mL}/100 \text{ g}/\text{min}$ (range of 35.8 – $90.5 \text{ mL}/100 \text{ g}/\text{min}$); 14 patients (44%) met CBF criteria for cerebral hyperperfusion. Sixteen patients (50%) developed new postoperative ischemic lesions on DWI 24 h after surgery in the cortex and/or white matter in the cerebral hemisphere ipsilateral to CEA. All new ischemic lesions were spotty, and their diameters were 1 cm or less. Five (16%) of 32 patients studied developed new neurological deficits after recovery from general anesthesia. All deficits included slight hemiparesis contralateral to the CEA. These deficits resolved completely within 12 h in these five patients, and they underwent additional DWI between 6 and 8 h after surgery and had new postoperative ischemic lesions on both the first (6 to 8 h after surgery) and second (24 h after surgery) postoperative DWI examinations.

2.4. Postoperative Cerebral Hyperperfusion vs. Diffusion-Weighted Imaging (DWI)-Characterized Postoperative Cerebral Ischemic Lesions

Results of univariate analyses of factors related to the development of DWI-characterized postoperative cerebral ischemic lesions are shown in Table 1. The postoperative CBF and the incidence of postoperative cerebral hyperperfusion were significantly higher in patients without than in those with DWI-characterized postoperative cerebral ischemic lesions. Other variables were not significantly associated with DWI-characterized postoperative cerebral ischemic lesions. After eliminating variables that were closely related, the following items with values of $p < 0.2$ in univariate analyses were adopted as confounders in the logistic regression model for multivariate analysis: degree of ICA stenosis and postoperative CBF or postoperative cerebral hyperperfusion (since the latter two interacted, each item was adopted individually). This analysis showed that greater postoperative CBF (95% confidence interval, 0.616 – 0.938 ; $p = 0.0104$) or postoperative cerebral hyperperfusion (95% confidence interval, 0.001 – 0.179 ; $p = 0.0009$) was significantly associated with the absence of DWI-characterized postoperative cerebral ischemic lesions.

Figure 2 shows the relationships between the number of MES, postoperative CBF, cerebral hyperperfusion, and the development of DWI-characterized postoperative cerebral ischemic lesions. Postoperative CBF in patients with cerebral hyperperfusion ranged from mean + 3.9 SD to mean + 11.8 SD of the control value. Whereas 15 (83%) of 18 patients without postoperative cerebral hyperperfusion showed DWI-characterized postoperative cerebral ischemic lesions, only one (7%) of 14 patients with hyperperfusion had these ischemic lesions.

Table 1. Univariate analysis of factors related to development of diffusion-weighted imaging (DWI)-characterized postoperative cerebral ischemic lesions.

Variable	DWI-Characterized Ischemic Lesions		<i>p</i>
	Yes (n = 16)	No (n = 16)	
Age (years, mean ± SD)	72.8 ± 5.4	70.7 ± 3.2	0.2557
Male sex	15 (94%)	14 (88%)	>0.9999
Hypertension	12 (75%)	14 (88%)	0.6539
Preoperative antihypertensive drugs	10 (63%)	13 (81%)	0.4331
Preoperative calcium antagonist	5 (31%)	5 (31%)	>0.9999
Preoperative angiotensin receptor blocker	8 (50%)	10 (63%)	0.7224
Diabetes mellitus	6 (38%)	7 (44%)	>0.9999
Preoperative antidiabetic drugs	6 (38%)	7 (44%)	>0.9999
Dyslipidemia	7 (44%)	8 (50%)	>0.9999
Preoperative statins	5 (31%)	7 (44%)	0.7160
Preoperative strong statins *	2 (12%)	4 (25%)	0.6539
Preoperative aspirin	6 (38%)	4 (25%)	0.7043
Preoperative clopidogrel	10 (63%)	12 (75%)	0.7043
Ischemic heart or valvular disease	3 (19%)	4 (25%)	>0.9999
Symptomatic lesion	14 (88%)	11 (69%)	0.3944
Degree of ICA stenosis (%), mean ± SD)	83.1 ± 9.0	87.7 ± 8.2	0.1258
Bilateral lesions	4 (25%)	5 (31%)	>0.9999
Preoperative CBF (mL/100 g/min, mean ± SD)	31.9 ± 5.8	34.4 ± 6.4	0.2581
Preoperative CVR to acetazolamide (%), mean ± SD)	8.7 ± 5.9	8.6 ± 8.0	0.6783
Preoperative systolic blood pressure (mmHg, mean ± SD)	134.5 ± 15.8	132.5 ± 14.2	0.9254
Number of MES (mean ± SD)	4.6 ± 4.3	4.0 ± 3.6	0.8932
Interval from first MES to ICA declamping (min, mean ± SD)	46.1 ± 6.8	44.4 ± 6.1	0.4848
Interval from last MES to ICA declamping (min, mean ± SD)	47.2 ± 7.9	46.3 ± 5.2	0.8353
Mean systolic blood pressure during carotid exposure (mmHg, mean ± SD)	114.2 ± 14.8	113.4 ± 13.0	0.9849
Duration of ICA clamping (min, mean ± SD)	37.2 ± 5.6	34.8 ± 5.6	0.2191
Mean systolic blood pressure after carotid declamping (mmHg, mean ± SD)	122.2 ± 15.1	120.7 ± 13.1	0.9049
Successfully controlled blood pressure after carotid declamping ** (%) , mean ± SD)	84.6 ± 5.3	87.2 ± 6.8	0.8954
Mean systolic blood pressure in postoperative period (mmHg, mean ± SD)	128.8 ± 16.8	127.1 ± 17.0	0.9241
Successfully controlled blood pressure in postoperative period *** (%) , mean ± SD)	74.5 ± 6.8	78.3 ± 7.8	0.8037
Postoperative CBF (mL/100 g/min, mean ± SD)	39.6 ± 4.8	66.3 ± 15.0	<0.0001
Cerebral hyperperfusion	1 (6%)	13 (81%)	<0.0001

SD, Standard deviation; ICA, Internal carotid artery; CBF, Cerebral blood flow; CVR, Cerebrovascular reactivity; MES, Microembolic signal; *, Including atorvastatin, pitavastatin, and rosuvastatin; **, Rate of blood pressure-measured points with systolic blood pressure <90% of the preoperative value in the post-carotid declamping period in surgery; ***, Rate of blood pressure-measured points with systolic blood pressure <90% of the preoperative value in the postoperative period (within 24 h after surgery).

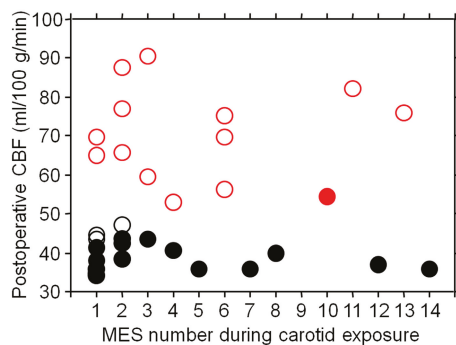


Figure 2. Relationships between the number of microembolic signals (MES), postoperative CBF (cerebral blood flow), cerebral hyperperfusion, and the development of diffusion-weighted imaging (DWI)-characterized postoperative cerebral ischemic lesions. Closed and open circles indicate patients with and without DWI-characterized postoperative cerebral ischemic lesions, respectively. Red and black circles indicate patients with and without postoperative cerebral hyperperfusion (defined as postoperative CBF increase $\geq 100\%$ compared with preoperative values), respectively. Whereas 15 (83%) of 18 patients without postoperative cerebral hyperperfusion showed DWI-characterized postoperative cerebral ischemic lesions, only one (7%) of 14 patients with hyperperfusion had these ischemic lesions.

2.5. Case Presentation

Figure 3 shows images of brain perfusion SPECT, TCD, and DWI in a 74-year-old man with symptomatic ICA stenosis (90%) showing DWI-characterized postoperative cerebral ischemic lesions due to MES during exposure of the carotid arteries despite development of cerebral hyperperfusion after left CEA.

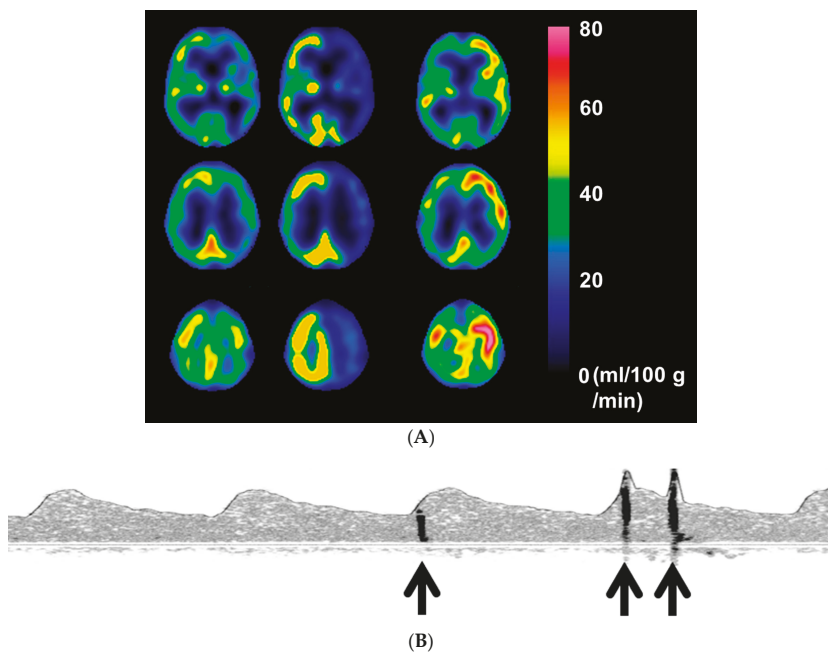


Figure 3. Cont.

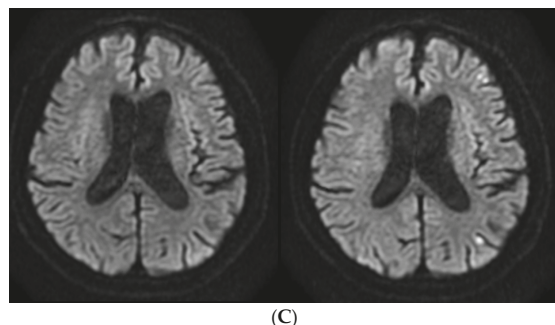


Figure 3. (A) Preoperative brain perfusion single-photon emission computed tomography in a 74-year-old man with symptomatic left internal carotid artery stenosis (90%) shows reduced cerebral blood flow (**left**) and reduced cerebrovascular reactivity to acetazolamide (**center**) in the left cerebral hemisphere where hyperperfusion develops immediately after surgery (**right**); (B) Transcranial Doppler recording during exposure of the carotid arteries in the patient of Figure 3A shows three microembolic signals (**arrows**) in the power spectrum display of left middle cerebral artery blood flow. This patient had a total of 10 microembolic signals during exposure of the carotid arteries; (C) A diffusion-weighted image 6 h after surgery in the patient of Figure 3A,B shows development of new postoperative multiple high-intensity lesions in the left cerebral hemisphere (**right**) when compared with a preoperative image (**left**). These lesions did not change on diffusion-weighted imaging 24 h after surgery. This patient suffered slight motor weakness in the right upper extremity after recovery from general anesthesia, and this deficit resolved completely within 12 h.

3. Discussion

3.1. Findings

The present study demonstrated that cerebral hyperperfusion after revascularization inhibits the development of cerebral ischemic lesions due to artery-to-artery emboli during carotid exposure in CEA for patients with preoperatively impaired cerebral hemodynamics, supporting the “impaired clearance of emboli” concept when broadening its interpretation.

3.2. Reason of Patient Exclusion

Hemodynamic cerebral ischemia due to hemispheric cerebral hypoperfusion during ICA clamping, as well as emboli from the surgical site, plays a significant role in the development of new ischemic lesions after CEA [11,23]. Intraoperative EEG monitoring is the most widely used and best documented method for the detection of hemispheric cerebral hypoperfusion due to carotid clamping [24]. To investigate the development of cerebral ischemic lesions caused by MES rather than by hemispheric cerebral hypoperfusion during ICA clamping, patients with EEG-defined hemispheric ischemia during ICA clamping were excluded from the present study.

3.3. Data Interpretation

In the present study, 44% of patients with preoperatively reduced CVR to acetazolamide showed cerebral hyperperfusion immediately after surgery. This incidence was comparable to a previous study [19–21]. All postoperative ischemic lesions on DWI that were newly developed in the cortex and/or white matter in the cerebral hemisphere ipsilateral to CEA were spotty, and their diameters were 1 cm or less. Furthermore, the duration of ICA clamping did not differ between patients with and without DWI-characterized postoperative cerebral ischemic lesions. Thus, these ischemic lesions were possibly due to artery-to-artery embolism rather than cerebral hemispheric ischemia during ICA clamping. More than 80% of patients with a combination of preoperatively reduced

CVR to acetazolamide and MES during carotid exposure, when they did not exhibit postoperative cerebral hyperperfusion, developed DWI-characterized postoperative cerebral ischemic lesions, which corresponded with previous findings [14].

In the present study, preoperative CBF, preoperative CVR to acetazolamide, mean systolic blood pressure during carotid exposure, and interval from the first or last MES to ICA declamping did not differ between patients with and without DWI-characterized postoperative cerebral ischemic lesions. Thus, perfusion in the cerebral hemisphere ipsilateral to surgery during carotid exposure and the duration of cerebral ischemia caused by emboli until ICA declamping might be equivalent between these two subgroups of patients. The duration of ICA clamping also did not differ between them. Nevertheless, greater postoperative CBF or postoperative cerebral hyperperfusion (postoperative CBF \geq mean + 3.9 SD of the control value) was associated with the absence of DWI-characterized postoperative cerebral ischemic lesions, and only 7% of patients with a combination of MES during carotid exposure and postoperative cerebral hyperperfusion developed these lesions. These findings suggested that blood flow that increased far beyond the normal level might clear cerebral emboli generated from the surgical site, inhibiting the development of ischemic lesions. These support the “impaired clearance of emboli” concept if the interpretation of this concept is broadened.

We have another hypothesis regarding the correlation between postoperative cerebral hyperperfusion and the development of ischemic lesions by emboli in patients with reduced CVR to acetazolamide. Reduced CVR to acetazolamide implies a chronic reduction in cerebral perfusion pressure and poor collateral blood flow [25–27]. When emboli generated from a lesion in the ICA acutely disturb blood flow in the cerebral artery, cerebral blood flow may be further decreased in the affected vascular territory with the pre-existing chronic reduction in cerebral perfusion pressure. However, if cerebral ischemic lesions have not yet formed between the onset of emboli and ICA declamping (the interval ranged from approximately 30 min to 60 min in the present study), hyperperfusion after ICA declamping may lead to an extreme increase in collateral blood flow to the affected vascular territory, inhibiting the postoperative development of new cerebral ischemic lesions.

3.4. Future Directions

The present study suggests that CBF greater than the normal level after declamping of the ICA can inhibit development of cerebral ischemic lesions due to emboli from the surgical site during exposure of the carotid arteries. On the other hand, postoperative cerebral hyperperfusion, which is defined as a postoperative CBF increase of $\geq 100\%$ when compared to preoperative values, occasionally evolves into cerebral hyperperfusion syndrome, leading to intracerebral hemorrhage [15–18]. Strict postoperative control of blood pressure (systolic blood pressure < 90 mmHg) reportedly prevents the development of intracerebral hemorrhage [16,20]. Further, intraoperative monitoring of MCA flow velocity using TCD or regional cerebral oxygen saturation using near-infrared spectroscopy are reliable methods of identifying patients with cerebral hyperperfusion following declamping of the ICA during CEA [28,29]. On the basis of these findings, we propose a practical clinical algorithm to prevent development of embolic ischemic events and hyperperfusion-related hemorrhage in CEA: when the intraoperative monitoring suggests development of cerebral hyperperfusion following declamping of the ICA, the blood pressure should then be reduced; when the intraoperative monitoring suggests development of embolism from the surgical site during carotid exposure that is not accompanied by cerebral hyperperfusion, the blood pressure should be elevated above the preoperative value following declamping of the ICA. Further investigation to determine whether the latter procedure prevents development of cerebral ischemic lesions would be of benefit, although, in the present study, blood pressure was reduced for all patients regardless of the presence or absence of cerebral hyperperfusion after declamping of the ICA.

3.5. Study Limitations

Although TCD detects emboli generated from the surgical site of the carotid arteries as MES, it cannot provide information about the size and characteristics of each embolus, which may affect the

development of postoperative cerebral ischemic lesions. The present results did not take into account these two factors.

4. Materials and Methods

4.1. Subjects

The present study was designed as a prospective, observational study. This study was approved by the Regional Ethical Board in Iwate Medical University (H22-3) and was in compliance with the Helsinki Declaration, and written, informed consent was obtained from all patients or their next of kin prior to participation.

Of symptomatic or asymptomatic patients with ipsilateral ICA stenosis $\geq 70\%$, as per the North American Symptomatic Carotid Endarterectomy Trial [30], on angiography/arterial catheterization, and useful residual function (modified Rankin scale score 0, 1, or 2) who were scheduled for CEA of the carotid bifurcation, those who satisfied the following inclusion criteria were prospectively selected for the present study: having preoperatively reduced CVR to acetazolamide according to the methods described below (see “4.2. CBF Measurements” section); undergoing CEA; and having MES during exposure of the carotid arteries under reliable TCD monitoring according to the methods described below (see “4.3. TCD Monitoring” section). Patients who showed electroencephalography (EEG)-defined cerebral hemispheric ischemia during ICA clamping according to the methods described below (see “4.5. Preoperative, Intraoperative, and Postoperative Management” section) were excluded from the present study.

4.2. CBF Measurements

CBF was assessed using [^{123}I]N-isopropyl-*p*-iodoamphetamine (IMP) and SPECT with a ring-type scanner (Headtome-SET 080; Shimadzu, Kyoto, Japan) within 14 days before and immediately after CEA. CBF measurement with acetazolamide challenge was also performed before CEA. The [^{123}I]IMP SPECT study with and without acetazolamide challenge was performed as described previously [31,32]. After a 1 min intravenous infusion of 222 MBq of [^{123}I]IMP (5 mL volume) at a constant rate of 5 mL/min and a 1 min infusion of physiologic saline at the same rate, data acquisition was performed at a midscan time of 30 min after the [^{123}I]IMP administration for a scan duration of 20 min. At 10 min after the beginning of the [^{123}I]IMP infusion, arterial blood (1 mL) was taken from the brachial artery. The whole-blood radioactivity of each blood sample obtained was measured using a well counter that was cross-calibrated to the SPECT scanner. All reconstructed SPECT images were corrected for the radioactive decay of ^{123}I back to the [^{123}I]IMP injection start time, normalized by the data collection time and cross-calibrated to the well counter system. The CBF images were calculated according to the [^{123}I]IMP-autoradiography method [31,32]. The whole-blood radioactivity counts of the single blood sample were referred to the standard input function.

All SPECT images were transformed into standard brain size and shape by linear and nonlinear transformations using statistical parametric mapping 2 software for anatomical standardization [33]. A three-dimensional stereotactic region-of-interest (ROI) template was used to automatically place 318 constant ROIs in both cerebral and cerebellar hemispheres [34]. ROIs were grouped into 10 segments (callosomarginal, pericallosal, precentral, central, parietal, angular, temporal, posterior, hippocampal, and cerebellar) in each hemisphere according to the arterial supply. Five (precentral, central, parietal, angular, and temporal) of these 10 segments were combined and defined as an ROI perfused by the middle cerebral artery (MCA) (Figure 4).

The mean value of all pixels in the MCA ROI in the cerebral hemisphere ipsilateral to CEA was calculated. Preoperative CVR to acetazolamide in the cerebral hemisphere ipsilateral to CEA was calculated as follows: CVR (%) = [(CBF with acetazolamide challenge – CBF at the resting state)/CBF at the resting state] $\times 100$. For CBF in the resting state and CVR to acetazolamide, data described previously ((mean \pm SD), 35.9 ± 4.4 mL/100 g/min and $36.8\% \pm 9.2\%$, respectively) were used as

control values, and decreased CVR to acetazolamide was defined as less than mean – 2 SD of the control value (18.4%) [31]. In each patient, cerebral hyperperfusion was defined as a postoperative CBF increase of $\geq 100\%$ (i.e., a doubling) when compared to preoperative values in the MCA ROI ipsilateral to the side of surgery [20].



Figure 4. Diagrams show the regions of interests (ROIs) for a three-dimensional, stereotactic ROI template to automatically place constant ROIs on brain perfusion single-photon emission computed tomography images. White ROIs indicate middle cerebral artery territories (precentral, central, parietal, angular, and temporal).

4.3. Transcranial Doppler (TCD) Monitoring

TCD was performed using a PIONEER TC2020 system (EME, Überlingen, Germany; software version 2.50, 2 MHz probe; diameter, 1.5 cm; insonation depth, 40–66 mm; scale, –100 and +150 cm/s; sample volume, 2 mm; 64 point fast Fourier transform; fast Fourier transform length, 2 mm; fast Fourier transform overlap, 60%; high-pass filter, 100 Hz; detection threshold, 9 dB; minimum increase time, 10 ms) for insonation of the MCA ipsilateral to the carotid artery undergoing CEA. TCD data were stored on a hard disk using a coding system and later analyzed manually by a clinical neurophysiologist who was blinded to patient information. MES were identified during exposure of the carotid arteries (from skin incision to ICA clamping) according to the recommended guidelines [35].

4.4. Magnetic Resonance Imaging

DWI was performed using a 1.5 T whole-body imaging system (Signa MR/I; GE Healthcare, Milwaukee, WI, USA) within three days before and 24 h after surgery.

A neuroradiologist who was blinded to patient clinical information analyzed the images and determined whether new ischemic lesions had developed postoperatively.

4.5. Preoperative, Intraoperative, and Postoperative Management

Blood pressure was measured at the upper arm using an automatic sphygmomanometer with the oscillometric method, and mean systolic blood pressure in the morning for the three days before surgery was defined as the preoperative value for each patient. Patients received medications including antihypertensive and antidiabetic drugs and statins until the evening of the day before CEA was performed. All patients received a single antiplatelet drug until the morning of the day on which CEA was performed. For all patients, surgery was conducted under general anesthesia, which was induced with etomidate/fentanyl and maintained with O₂/propofol. A bolus of heparin (5000 international units) was given prior to ICA clamping. Blood pressure was measured in the same fashion as preoperatively every 5 min throughout surgery. The EEG was recorded, and a clinical neurophysiologist monitored the recordings continuously during the surgical procedure. The presence of unilateral or bilateral decreases of alpha and beta activity during ICA clamping, with or without simultaneous increases of theta or delta activity, was defined as development of cerebral hemispheric ischemia by the clinical neurophysiologist [24]. In this situation, an intraluminal shunt was introduced. From declamping of the ICA to the third postoperative day, attempts were made to reduce systolic blood pressure to below 90% of the preoperative value using intravenous injection of the calcium antagonist nicardipine. Blood pressure was measured in the same fashion as preoperatively every 1 h until 24 h after surgery. When systolic blood pressure was <90% of the preoperative value at a blood pressure-measured point, the point was defined as having successfully controlled blood pressure. Patients received the same drugs as preoperative medications from the second postoperative day.

4.6. Statistical Analysis

Data are expressed as means \pm SD. The relationship between each variable and DWI-characterized postoperative cerebral ischemic lesions was evaluated by univariate analysis using the Mann-Whitney U test or the χ^2 test. Hypertension was defined as preoperative systolic blood pressure ≥ 140 mmHg, preoperative diastolic blood pressure ≥ 90 mmHg or preoperatively receiving antihypertensive drugs; diabetes mellitus was defined as preoperative hemoglobin A1c $\geq 6.5\%$ or preoperatively receiving antidiabetic drugs; dyslipidemia was defined as preoperative plasma low density lipoprotein (LDL) cholesterol ≥ 140 mg/dL, preoperative plasma high density lipoprotein (HDL) cholesterol <40 mg/dL, preoperative plasma triglyceride ≥ 150 mg/dL, or preoperatively receiving statins. Multivariate statistical analysis of factors related to DWI-characterized postoperative cerebral ischemic lesions was also performed using a logistic regression model. Variables with $p < 0.2$ on univariate analyses were selected for analysis in the final model. Differences were deemed significant for values of $p < 0.05$.

5. Conclusions

The present study demonstrated that cerebral hyperperfusion after revascularization inhibits the development of cerebral ischemic lesions due to artery-to-artery emboli during carotid exposure in CEA for patients with preoperatively impaired cerebral hemodynamics, supporting the “impaired clearance of emboli” concept when its interpretation is broadened.

Acknowledgments: The author (Kuniaki Ogasawara) disclosed receipt of the following financial support for the research, authorship, and/or publication of this article: Strategic Medical Science Research from the Ministry of Education, Culture, Sports, Science and Technology of Japan, Grant Number S1491001; Scientific Research from Japan Society for the Promotion of Science, Grant Number JP15K10313.

Author Contributions: Kentaro Fujimoto and Kuniaki Ogasawara conceived and designed the study; Yoshiyasu Matsumoto, Kohki Oikawa and Kazunori Terasaki performed measurements and analyses of brain perfusion; Masakazu Kobayashi performed measurements and analyses of microembolic signals on transcranial Doppler; Shunrou Fujiwara statically analyzed the data; Jun-ichi Nomura, Yasuyoshi Shimada and Kenji Yoshida critically revised the manuscript and helped with results interpretation. Kentaro Fujimoto and Kuniaki Ogasawara wrote the paper.

Conflicts of Interest: The author (Kuniaki Ogasawara) declared the following potential conflicts of interest with respect to the research, authorship, and/or publication of this article: Consigned research fund (3,150,000 yen) from Nihon Medi-Physics Co., Ltd.

Abbreviations

CEA	Carotid endarterectomy
TCD	Transcranial Doppler
MCA	Middle cerebral artery
MES	Microembolic signals
DWI	Diffusion-weighted imaging
CVR	Cerebrovascular reactivity
CBF	Cerebral blood flow
SPECT	Single-photon emission computed tomography
ICA	Internal carotid artery
EEG	Electroencephalography
IMP	[¹²³ I]N-isopropyl-p-iodoamphetamine
ROI	Region-of-interest
SD	Standard deviation

References

- Caplan, L.R.; Hennerici, M. Impaired clearance of emboli (washout) is an important link between hypoperfusion, embolism, and ischemic stroke. *Arch. Neurol.* **1998**, *55*, 1475–1482. [CrossRef]
- Caplan, L.R.; Wong, K.S.; Gao, S.; Hennerici, M.G. Is hypoperfusion an important cause of strokes? If so, how? *Cerebrovasc. Dis.* **2006**, *21*, 145–153. [CrossRef] [PubMed]
- Wong, K.S.; Gao, S.; Chan, Y.L.; Hansberg, T.; Lam, W.W.; Droste, D.W.; Kay, R.; Ringelstein, E.B. Mechanisms of acute cerebral infarctions in patients with middle cerebral artery stenosis: A diffusion-weighted imaging and microemboli monitoring study. *Ann. Neurol.* **2002**, *52*, 74–81. [CrossRef] [PubMed]
- Schreiber, S.; Serdaroglu, M.; Schreiber, F.; Skalej, M.; Heinze, H.J.; Goertler, M. Simultaneous occurrence and interaction of hypoperfusion and embolism in a patient with severe middle cerebral artery stenosis. *Stroke* **2009**, *40*, e478–e480. [CrossRef] [PubMed]
- Orlandi, G.; Fanucchi, S.; Gallerini, S.; Sonnoli, C.; Cosottini, M.; Puglioli, M.; Sartucci, F.; Murri, L. Impaired clearance of microemboli and cerebrovascular symptoms during carotid stenting procedures. *Arch. Neurol.* **2005**, *62*, 1208–1211. [CrossRef] [PubMed]
- Spencer, M.P. Transcranial Doppler monitoring and causes of stroke from carotid endarterectomy. *Stroke* **1997**, *28*, 685–691. [CrossRef] [PubMed]
- Ackerstaff, R.G.; Moons, K.G.; van de Vlasakker, C.J.; Moll, F.L.; Vermeulen, F.E.; Algra, A.; Spencer, M.P. Association of intraoperative transcranial doppler monitoring variables with stroke from carotid endarterectomy. *Stroke* **2000**, *31*, 1817–1823. [CrossRef] [PubMed]
- Wolf, O.; Heider, P.; Heinz, M.; Poppert, H.; Sander, D.; Greil, O.; Weiss, W.; Hanke, M.; Eckstein, H.H. Microembolic signals detected by transcranial Doppler sonography during carotid endarterectomy and correlation with serial diffusion-weighted imaging. *Stroke* **2004**, *35*, e373–e375. [CrossRef] [PubMed]
- Gavrilescu, T.; Babikian, V.L.; Cantelmo, N.L.; Rosales, R.; Pochay, V.; Winter, M. Cerebral microembolism during carotid endarterectomy. *Am. J. Surg.* **1995**, *170*, 159–164. [CrossRef]
- Rothwell, P.M.; Eliasziw, M.; Gutnikov, S.A.; Fox, A.J.; Taylor, D.W.; Mayberg, M.R.; Warlow, C.P.; Barnett, H.J. Analysis of pooled data from the randomised controlled trials of endarterectomy for symptomatic carotid stenosis. *Lancet* **2003**, *361*, 107–116. [CrossRef]

11. Verhoeven, B.A.; de Vries, J.P.; Pasterkamp, G.; Ackerstaff, R.G.; Schoneveld, A.H.; Velema, E.; de Kleijn, D.P.; Moll, F.L. Carotid atherosclerotic plaque characteristics are associated with microembolization during carotid endarterectomy and procedural outcome. *Stroke* **2005**, *36*, 1735–1740. [CrossRef] [PubMed]
12. Gaunt, M.E.; Martin, P.J.; Smith, J.L.; Rimmer, T.; Cherryman, G.; Ratliff, D.A.; Bell, P.R.; Naylor, A.R. Clinical relevance of intraoperative embolization detected by transcranial Doppler ultrasonography during carotid endarterectomy: A prospective study of 100 patients. *Br. J. Surg.* **1994**, *81*, 1435–1439. [CrossRef] [PubMed]
13. Jansen, C.; Ramos, L.M.; van Heesewijk, J.P.; Moll, F.L.; van Gijn, J.; Ackerstaff, R.G. Impact of microembolism and hemodynamic changes in the brain during carotid endarterectomy. *Stroke* **1994**, *25*, 992–997. [CrossRef] [PubMed]
14. Aso, K.; Ogasawara, K.; Sasaki, M.; Kobayashi, M.; Suga, Y.; Chida, K.; Otawara, Y.; Ogawa, A. Preoperative cerebrovascular reactivity to acetazolamide measured by brain perfusion SPECT predicts development of cerebral ischemic lesions caused by microemboli during carotid endarterectomy. *Eur. J. Nucl. Med. Mol. Imaging* **2009**, *36*, 294–301. [CrossRef] [PubMed]
15. Bernstein, M.; Fleming, J.F.; Deck, J.H. Cerebral hyperperfusion after carotid endarterectomy: A cause of cerebral hemorrhage. *Neurosurgery* **1984**, *15*, 50–56. [CrossRef] [PubMed]
16. Ogasawara, K.; Sakai, N.; Kuroiwa, T.; Hosoda, K.; Iihara, K.; Toyoda, K.; Sakai, C.; Nagata, I.; Ogawa, A. Intracranial hemorrhage associated with cerebral hyperperfusion syndrome following carotid endarterectomy and carotid artery stenting: Retrospective review of 4494 patients. *J. Neurosurg.* **2007**, *107*, 1130–1136. [CrossRef] [PubMed]
17. Piepgras, D.G.; Morgan, M.K.; Sundt, T.M., Jr.; Yanagihara, T.; Mussman, L.M. Intracerebral hemorrhage after carotid endarterectomy. *J. Neurosurg.* **1988**, *68*, 532–536. [CrossRef] [PubMed]
18. Sundt, T.M., Jr.; Sharbrough, F.W.; Piepgras, D.G.; Kearns, T.P.; Messick, J.M., Jr.; O'Fallon, W.M. Correlation of cerebral blood flow and electroencephalographic changes during carotid endarterectomy, with results of surgery and hemodynamics of cerebral ischemia. *Mayo Clin. Proc.* **1981**, *56*, 533–543. [CrossRef] [PubMed]
19. Hosoda, K.; Kawaguchi, T.; Shibata, Y.; Kamei, M.; Kidoguchi, K.; Koyama, J.; Fujita, S.; Tamaki, N. Cerebral vasoreactivity and internal carotid artery flow help to identify patients at risk for hyperperfusion after carotid endarterectomy. *Stroke* **2001**, *32*, 1567–1573. [CrossRef] [PubMed]
20. Ogasawara, K.; Yukawa, H.; Kobayashi, M.; Mikami, C.; Konno, H.; Terasaki, K.; Inoue, T.; Ogawa, A. Prediction and Monitoring of cerebral hyperperfusion after carotid endarterectomy by using single-photon emission computerized tomography scanning. *J. Neurosurg.* **2003**, *99*, 504–510. [CrossRef] [PubMed]
21. Yoshimoto, T.; Houkin, K.; Kuroda, S.; Abe, H.; Kashiwaba, T. Low cerebral blood flow and perfusion reserve induce hyperperfusion after surgical revascularization: Case reports and analysis of cerebral hemodynamics. *Surg. Neurol.* **1997**, *48*, 132–139. [CrossRef]
22. Yadav, J.S.; Wholey, M.H.; Kuntz, R.E.; Fayad, P.; Katzen, B.T.; Mishkel, G.J.; Bajwa, T.K.; Whitlow, P.; Strickman, N.E.; Jaff, M.R.; et al. Protected carotid-artery stenting versus endarterectomy in high-risk patients. *N. Engl. J. Med.* **2004**, *351*, 1493–1501. [CrossRef] [PubMed]
23. Van der Schaaf, I.C.; Horn, J.; Moll, F.L.; Ackerstaff, R.G. Transcranial Doppler monitoring after carotid endarterectomy. *Ann. Vasc. Surg.* **2005**, *19*, 19–24. [CrossRef] [PubMed]
24. Rutgers, D.R.; Blankensteijn, J.D.; van der Grond, J. Preoperative MRA flow quantification in CEA patients: Flow differences between patients who develop cerebral ischemia and patients who do not develop cerebral ischemia during cross-clamping of the carotid artery. *Stroke* **2000**, *31*, 3021–3028. [CrossRef] [PubMed]
25. Grubb, R.L., Jr.; Derdeyn, C.P.; Fritsch, S.M.; Carpenter, D.A.; Yundt, K.D.; Videen, T.O.; Spitznagel, E.L.; Powers, W.J. Importance of hemodynamic factors in the prognosis of symptomatic carotid occlusion. *JAMA* **1998**, *280*, 1055–1060. [CrossRef] [PubMed]
26. Kuroda, S.; Houkin, K.; Kamiyama, H.; Mitsumori, K.; Iwasaki, Y.; Abe, H. Long-term prognosis of medically treated patients with internal carotid or middle cerebral artery occlusion: Can acetazolamide test predict it? *Stroke* **2001**, *32*, 2110–2116. [CrossRef] [PubMed]
27. Schmiedek, P.; Piepgras, A.; Leinsinger, G.; Kirsch, C.M.; Einhäupl, K. Improvement of cerebrovascular reserve capacity by EC-IC arterial bypass surgery in patients with ICA occlusion and hemodynamic cerebral ischemia. *J. Neurosurg.* **1994**, *81*, 236–244. [CrossRef] [PubMed]
28. Ogasawara, K.; Konno, H.; Yukawa, H.; Endo, H.; Inoue, T.; Ogawa, A. Transcranial regional cerebral oxygen saturation monitoring during carotid endarterectomy as a predictor of postoperative hyperperfusion. *Neurosurgery* **2003**, *53*, 309–315. [CrossRef] [PubMed]

29. Ogasawara, K.; Inoue, T.; Kobayashi, M.; Endo, H.; Yoshida, K.; Fukuda, T.; Terasaki, K.; Ogawa, A. Cerebral hyperperfusion following carotid endarterectomy: Diagnostic utility of intraoperative transcranial Doppler ultrasonography compared with single-photon emission computed tomography study. *AJNR Am. J. Neuroradiol.* **2005**, *26*, 252–257. [PubMed]
30. North American Symptomatic Carotid Endarterectomy Trial Collaborators. Beneficial effect of carotid endarterectomy in symptomatic patients with high-grade carotid stenosis. *N. Engl. J. Med.* **1991**, *325*, 445–453.
31. Ogasawara, K.; Ito, H.; Sasoh, M.; Okuguchi, T.; Kobayashi, M.; Yukawa, H.; Terasaki, K.; Ogawa, A. Quantitative measurement of regional cerebrovascular reactivity to acetazolamide using ^{123}I -N-isopropyl-p-iodoamphetamine autoradiography with SPECT: Validation study using H_2^{15}O with PET. *J. Nucl. Med.* **2003**, *44*, 520–525. [PubMed]
32. Iida, H.; Itoh, H.; Nakazawa, M.; Hatazawa, J.; Nishimura, H.; Onishi, Y.; Uemura, K. Quantitative mapping of regional cerebral blood flow using iodine-123-IMP and SPECT. *J. Nucl. Med.* **1994**, *35*, 2019–2030. [PubMed]
33. Nishimiya, M.; Matsuda, H.; Imabayashi, E.; Kuji, I.; Sato, N. Comparison of SPM and NEUROSTAT in voxelwise statistical analysis of brain SPECT and MRI at the early stage of Alzheimer’s disease. *Ann. Nucl. Med.* **2008**, *22*, 921–927. [CrossRef] [PubMed]
34. Takeuchi, R.; Matsuda, H.; Yoshioka, K.; Yonekura, Y. Cerebral blood flow SPET in transient global amnesia with automated ROI analysis by 3DSRT. *Eur. J. Nucl. Med. Mol. Imaging* **2004**, *31*, 578–589. [CrossRef] [PubMed]
35. Consensus Committee of the Ninth International Cerebral Hemodynamic Symposium. Basic identification criteria of Doppler microembolic signals. *Stroke* **1995**, *26*, 1123. [CrossRef]



© 2016 by the authors. Licensee MDPI, Basel, Switzerland. This article is an open access article distributed under the terms and conditions of the Creative Commons Attribution (CC BY) license (<http://creativecommons.org/licenses/by/4.0/>).



Review

Diabetes and Hypertension Consistently Predict the Presence and Extent of Coronary Artery Calcification in Symptomatic Patients: A Systematic Review and Meta-Analysis

Rachel Nicoll ¹, Ying Zhao ², Pranvera Ibrahim ¹, Gunilla Olivecrona ³ and Michael Henein ^{1,*}

¹ Department of Public Health and Clinical Medicine, Umea University and Heart Centre, Umea SE-901-87, Sweden; rachelnicoll25@gmail.com (R.N.); pranvera_i86@hotmail.com (P.I.)

² Department of Ultrasound, Beijing Anzhen Hospital, Capital Medical University, Beijing 100029, China; yingzhaoecho@163.com

³ Department of Medical Biosciences, Umea University, Umea SE-901-87, Sweden; gunilla.olivecrona@medbio.umu.se

* Correspondence: michael.henein@umu.se; Tel.: +44-7956-386237

Academic Editor: Joseph Moxon

Received: 4 June 2016; Accepted: 22 August 2016; Published: 6 September 2016

Abstract: Background: The relationship of conventional cardiovascular risk factors (age, gender, ethnicity, diabetes, dyslipidaemia, hypertension, obesity, exercise, and the number of risk factors) to coronary artery calcification (CAC) presence and extent has never before been assessed in a systematic review and meta-analysis. Methods: We included only English language studies that assessed at least three conventional risk factors apart from age, gender, and ethnicity, but excluded studies in which all patients had another confirmed condition such as renal disease. Results: In total, 10 studies, comprising 15,769 patients, were investigated in the systematic review and seven studies, comprising 12,682 patients, were included in the meta-analysis, which demonstrated the importance of diabetes and hypertension as predictors of CAC presence and extent, with age also predicting CAC presence. Male gender, dyslipidaemia, family history of coronary artery disease, obesity, and smoking were overall not predictive of either CAC presence or extent, despite dyslipidaemia being a key risk factor for coronary artery disease (CAD). Conclusion: Diabetes and hypertension consistently predict the presence and extent of CAC in symptomatic patients.

Keywords: meta-analysis; systematic review; coronary calcification; risk factors

1. Introduction

The presence of conventional cardiovascular (CV) risk factors (hypertension, diabetes, dyslipidaemia, smoking, obesity, and family history of coronary artery disease) have been shown to predict the 10-year coronary event risk [1–3]. In patients at intermediate risk, coronary artery calcification (CAC) is described as a subclinical form of atherosclerosis, often occurring as calcified atheroma or spotty calcification within a lipid core. Its measurement is commonly used clinically to avoid an invasive angiogram or as a marker for atherosclerosis in studies [4]. Similarly, the conventional CV risk factors may be used clinically to assess the likelihood of coronary calcification. Since both the CV risk factors and the presence and extent of CAC are predictive of coronary event risk [5,6], we investigated for the first time, in a systematic review and meta-analysis, whether conventional risk factors were also predictive of CAC presence, extent or progression in symptomatic patients. We hoped this would also throw more light on the phenomenon of coronary calcification, which in severe form could represent a clinical challenge as patients tend not to respond to conventional anti-anginal

therapy [7]. Furthermore, as there is currently no specific treatment for arterial calcification, with atherosclerosis therapy such as statins and vasodilators having little effect [8], we hope that identifying specific predictive risk factors may point the way towards a remedy which could help prevent or even slow the process of coronary calcification.

2. Methods

The methodology for this systematic review and meta-analysis conforms to the Preferred Reporting Items for Systematic Reviews and Meta-Analyses statement [9].

2.1. Information Search and Data Collection

We systematically searched electronic databases (PubMed, MEDLINE, EMBASE, and Cochrane Centre Register) for observational human studies, assessing CAC and conventional CV risk factors. Articles were selected if the title or abstract indicated that the paper analysed original associations between CAC and CV risk factors using different combinations of the Medical Subject Headings (MeSH): “coronary calcification” or “coronary calcium” and “risk factors”, “hypertension”, “dyslipidaemia”, “hyperlipidaemia obesity”, “diabetes”, “smoking”, “family history”, “exercise” or “physical activity”. No date limit was applied to article selection. Since computed tomographic scanning for CAC was first introduced in the early 1990s, the study dates range from then to the present date. Two researchers performed the literature search, study selection and data extraction independently of each other, with the results placed in a spreadsheet; disagreements were resolved by discussion between the two researchers and a third adjudicated in case of disagreement. The selected reports were manually searched and other relevant articles, obtained from the reference lists, were retrieved. We also performed a quality assessment of each study included in the meta-analysis.

2.2. Study Eligibility Criteria

Any clinical studies that reported the presence, extent, new development or progression of CAC, assessed by electron beam computed tomography (EBCT), multi-detector computed tomography (MDCT), or coronary angiography, were eligible, regardless of whether or not the study objective was an assessment of the association of risk factors with CAC.

Study inclusion criteria were:

- (a) English language articles published in peer-reviewed journals;
- (b) In addition to age, gender, and ethnicity (where applicable), the study must include assessment of at least three risk factors out of dyslipidaemia, hypertension, obesity, diabetes, smoking, family history of premature CVD, or exercise. In some cases surrogate markers were used to indicate the presence of a risk factor, such as elevated low density lipoprotein (LDL) cholesterol to indicate hyperlipidaemia or elevated systolic blood pressure (SBP) consistent with hypertension. Any differences in risk factor criteria between studies are discussed in the narrative;
- (c) The ability of risk factors to predict CAC presence, extent, new development, or progression must be displayed in a table rather than as a narrative. This criterion was included because narrative results in some studies did not adequately reflect the tabular results, for example, where a risk factor shown as significant in a table was not mentioned in the narrative. Studies also varied in their treatment of a *p*-value of 0.05, with some taking it as borderline and others as significant but the exact *p*-value may not be shown in the narrative; for our purposes only *p* < 0.05 is taken as significant;
- (d) The patients must be symptomatic (complaining of chest pain or any other typical or atypical angina symptoms); and
- (e) For the systematic review only, the study results must show risk factors as multivariate predictors of CAC presence, extent, or progression.

Study exclusion criteria were:

Those involving patients with a specific diagnosis, such as Type 1 diabetes or renal disease, which had no healthy control group.

There were no specified requirements for the control groups, where applicable.

2.3. Statistical Analysis

The data was extracted from each study and analysed using the Revman software 5.3 (Copenhagen, Denmark: The Nordic Cochrane Centre, The Cochrane Collaboration, 2014). The publication bias was tested using Egger's regression interception test and funnel plot by comprehensive meta-analysis software. The unadjusted odds ratios (ORs) of each risk factors were estimated from the exposure distributions for CAC presence or absence. The ORs and 95% confidence intervals (CIs) were converted into Log OR and standard error (SE) using the calculator and the Revman software in order to obtain the forest plots for each risk factor. The statistical heterogeneity was evaluated using the I^2 statistical test. When the I^2 was greater than 50%, the analysis was considered significantly heterogeneous and the random effect model was applied. When the I^2 was less than 50%, the analysis was considered not heterogeneous and the fixed effect meta-analysis model was applied. A p -value of <0.05 was regarded as significant.

3. Results

3.1. Data Extraction

A total of 884 studies were identified. After exclusion of duplicates and review of the retrieved papers for the above criteria (the selection process is shown in Figure 1), 10 studies comprising 15,769 symptomatic patients [10–19] were eligible for inclusion in the systematic review, while seven studies comprising 12,682 patients [10–12,14,16–18] were eligible for inclusion in the meta-analysis. All are listed in Table 1. A risk factor was included in the meta-analysis when at least three papers had provided data on that risk factor. The papers were then divided according to CAC assessment type (i.e., CAC presence, extent or progression). One study, Lai et al. [10], assessed both CAC presence and extent and is, consequently, shown twice in both the systematic review and meta-analysis, while studies by Mayer et al. [11] and Mitsutake et al. [12] could be used for both CAC presence and extent in the meta-analysis but were used only for CAC extent in the systematic review.

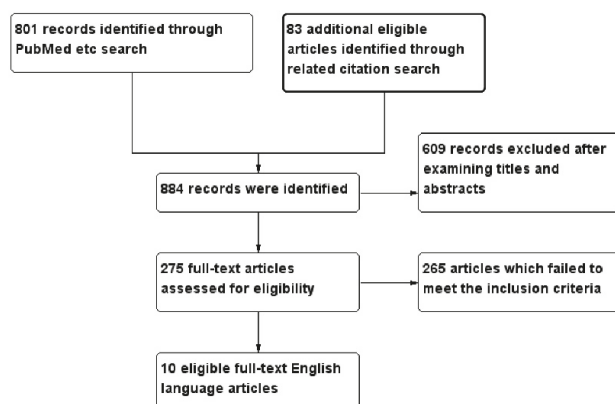


Figure 1. Flowchart showing selection of eligible studies.

Table 1. Study characteristics.

CAC Measurement	Author Year	Reference No.	Study Population CAC = 0	CAC > 0 or Total Population If No Data Provided	Mean Age (Years)	Means of CAC Assessment	Notable Patient Characteristics
CAC Extent	Lai et al., 2015 as above	[10]	91	120	71.1	64-slice GE scanner	Chinese ethnicity, males aged ≥ 65
	Mayer et al., 2007	[11]	333	544	59.7	Angiographic, CAC observed in the coronary vessels could be none, mild-moderate or severe.	Males
	Mitsutake et al., 2007	[12]	245	290	64	16- or 64-slice Toshiba CT scanner	Japanese ethnicity
	Tanaka et al., 2012	[13]	1363		68	64-slice Toshiba CT scanner	Japanese ethnicity
	Atar et al., 2013	[14]	362	60	53.6	64-slice Phillips CT scanner	Turkish ethnicity
CAC Presence	Greif et al., 2013	[15]	Males	1123	55.4	16-slice Siemens CT scanner	European ethnicity
	Kovacic et al., 2012	[16]	Females	437	63.2		
	Lai et al., 2015	[10]	8553	1440	66.6	Angiographic, CAC on stenotic lesion undergoing PCI, could be none, mild, moderate or severe.	All with coronary stenosis ≥ 60%
	Maragiannis et al., 2015	[17]	91	120	71.1	64-slice GE scanner	Chinese ethnicity, males aged ≥ 65
	Qing et al., 2015	[18]	65	49	56.1	16-slice Phillips CT scanner	US study
CAC Progression	Okada et al., 2013	[19]	146	364	56.0	64-slice GE CT scanner	Chinese ethnicity
			164 (all with CAC > 0)		68.7	64-slice Toshiba CT scanner	Japanese ethnicity

All studies of CAC presence and extent were case-control studies, while the one study of CAC progression (Okada et al. [19]) was a cohort study.

CAC presence was defined as any CAC score >0. CAC extent was defined as the amount of the CAC score in studies which did not use a CAC score threshold or, in studies which did use a CAC score threshold, CAC extent was defined as any CAC score >100 compared to CAC = 0; any study with a CAC score threshold ≤ 100 was taken as a study of CAC presence. Similarly in angiographic studies, where moderate/severe calcification was compared with mild/no calcification, this was also taken as a study of CAC presence. CAC progression was defined as an increase in the CAC score over time.

Ten studies fitted our inclusion criteria [10–19], comprising 15,769 symptomatic patients, as outlined in Table 1. The number of patients ranged from 114 in Maragiannis et al. [17], to 1560 in Greif et al. [15], with one study of CAC presence by Kovacic et al. [16] comprising 9993 patients; due to the large numbers in this study, it will be separately mentioned in the analysis unless its results conform to those of all other studies. Three studies had a solely Japanese population [12,13,19], two studies were Chinese [10,18], while one was Turkish [14]. All studies were mixed gender, except for Lai et al. [10] and Mayer et al. [11], which investigated exclusively male patients. One study, Greif et al. [15], separately investigated males and females and, consequently, this was treated as two separate studies [15] in the analysis. All studies investigated a wide age range except Lai et al. [10], whose patients were aged ≥ 65 . All patients in the study by Kovacic et al. [16] had coronary stenosis $\geq 60\%$, while those in the study by Mayer et al. [11] had CAD and a close relative who had suffered a myocardial infarction before the age of 60 years. Eight of the 10 studies had CAC assessed by CT scanner, either 16- or 64-slice, but the remaining two were investigated angiographically. Kovacic et al. [16] assessed the extent of CAC on the stenotic lesion undergoing percutaneous coronary intervention (PCI), with CAC being graded as none, mild, moderate or severe, while Mayer et al. [11] assessed the CAC observed in the coronary vessels as none, mild-moderate, or severe. Kovacic et al. [16] assessed predictors for calcification as moderate-severe calcification compared to no calcification; we have included this in the analysis as a study of CAC presence rather than CAC extent.

3.1.1. Systematic Review

We analysed the following numbers of studies in each category:

CAC presence cross-sectional	six studies	12,830 patients
CAC extent cross-sectional	four studies	2986 patients
CAC progression	one study	164 patients
Total symptomatic patients	15,980 patients	

However, Lai et al. [10], with 211 patients, was included in both CAC presence and extent.

3.1.2. Meta-Analyses

We analysed the following numbers of studies in each category, with three studies providing data for both CAC presence and extent:

CAC presence cross-sectional	seven studies	12,682 patients
CAC extent cross-sectional	three studies	1623 patients

The unadjusted ORs of each risk factors were estimated from the exposure distributions for CAC presence or absence [20,21], with the exception of the ORs from the study by Kovacic et al. [16], which directly showed the univariate ORs in the results. Since age was a continuous parameter, the OR for age was pooled from multivariate results. For the remaining risk factors, few papers provided the multivariate ORs, so consequently the pooled ORs from multivariate results were not analysed. In the three papers which provided the ORs for both CAC presence and extent [10–12], we extracted the exposure distributions for moderate and severe CAC and combined them as CAC presence. In these three papers, the ORs for the comparison between mild to moderate CAC and zero CAC and the comparison between severe CAC and zero CAC were pooled from the exposure distribution separately to assess the risk factors which predicted CAC extent.

3.2. Systematic Review

The papers were then analysed by age, gender, ethnicity, diabetes, dyslipidaemia, family history, hypertension, obesity, and smoking (Table 2). In none of the studies was physical activity assessed. In several studies the definition of the risk factor comprised multiple components for example, dyslipidaemia could include any of elevated total, LDL cholesterol or the total/HDL cholesterol ratio, or decreased HDL cholesterol. For the purposes of analysis for the systematic review, a risk factor was assessed if any one of its components was present (so dyslipidaemia was predictive if only LDL cholesterol was elevated and all other components were in normal range). Analysis of the precise risk factor components is also provided in each relevant section, where any modifying effect of age is also considered.

Table 2. Systematic Review: analysis of the number and type of studies investigating risk factors for CAC.

Risk Factors	CAC Presence		CAC Extent		CAC Progression	
	Predictive	Not Predictive	Predictive	Not Predictive	Predictive	Not Predictive
Age	5	1	3	1	0	1
Gender	2	2	2	0	0	0
Ethnicity	1	0	0	0	0	0
Diabetes	3	4	1	3	1	0
Dyslipidaemia	3	4	1	3	0	1
Hypertension	2	5	3	1	1	0
Family history	0	1	1	1	0	0
Obesity	1	5	0	3	0	1
Smoking	1	5	0	4	0	0

Age: There are five studies showing that age is predictive of CAC presence [14–18], compared to one which is not predictive [10], although in this study all patients were as ≥ 65 . Three studies showed that age was predictive of CAC extent [11–13] and the same study of patients aged ≥ 65 found age not to be predictive [10]. The only study of CAC progression found that age was not predictive [19].

Male gender: two studies of CAC presence showed that gender was not predictive [14,16], including the angiographic study of 9993 patients [16], although in two studies of CAC presence [17,18] and two studies of CAC extent it was predictive [12,13].

Ethnicity: The study of 9993 patients was the only one to consider ethnicity and this found that being white was predictive of CAC presence [16].

Diabetes mellitus: The two Greif et al. studies [15] and the angiographic study of 9993 patients [16] found diabetes to be predictive of CAC presence, although four smaller studies showed that it is not [10,14,17,18]. Although one study of 1363 patients found diabetes to be predictive of CAC extent [13], three studies with a total of 1623 patients showed that it was not predictive [10–12]. The only study of CAC progression showed that diabetes was predictive [19].

When the studies are analysed by markers for diabetes:

- Blood glucose was not predictive of CAC presence [14] or extent [12].
- Insulin was not predictive in one study of CAC presence and extent [10].
- HbA1c was not predictive of CAC presence [15,18] or extent [11,12], although it did show predictive ability for CAC progression [19].
- Oral hypoglycaemic medication was not predictive in one study of CAC presence and extent [10].
- Homeostatic Model Assessment-Insulin Resistance (HOMA-IR) was not predictive of CAC presence [15].

Dyslipidaemia: Three studies showed that dyslipidaemia was predictive of CAC presence [15,18], while four studies, including the study of 9333 patients, shows that it is not predictive [10,14,16,17]. For CAC extent, however, one study showed that dyslipidaemia was predictive [11] but three studies,

with more than twice as many patients, found it not to be predictive [10,12,13]. The one study of CAC progression [19] showed that it was not predictive.

When the studies are analysed by markers and biomarkers for dyslipidaemia:

- Elevated LDL cholesterol was not predictive in all four studies of CAC presence [14–16] and in two studies of CAC extent [11,12].
- Elevated total cholesterol was not predictive in two studies of CAC presence [14,18], two studies of CAC extent [11,12], and one study of CAC progression [19].
- Decreased HDL was not predictive in three studies of CAC presence [14,15] and one study of CAC extent [12], but was predictive of severe CAC extent in one study [11].
- Lipid-lowering medication was predictive in three studies of CAC presence [15,18], but was not predictive in one study of CAC presence [10] and two studies of CAC extent [10,12].

Hypertension: Although two studies, including the study of 9993 patients, [16,17] found that hypertension was predictive of CAC presence, the remaining studies showed that it had no predictive ability for CAC presence [10,13,15,18]. Three studies of CAC extent found that it was predictive [11–13], but one study found it not to be predictive [10]; the one study of CAC progression was also predictive [19].

When the studies are analysed by markers for hypertension:

- Systolic blood pressure (SBP) was not predictive in three studies of CAC presence [10,15] and two studies of CAC extent [10,12] but one angiographic study showed it was predictive of severe CAC extent [11]. SBP was also predictive of CAC progression [19].
- Diastolic blood pressure (DBP) was not predictive in three studies of CAC presence [10,15] and three studies of CAC extent [10–12].
- Antihypertensive medications were not predictive in four studies of CAC presence [10,15,18] and one of CAC extent [10].
- Pulse pressure was not predictive in one study of CAC extent [11] and the study of CAC progression [19].

Family history of premature CHD: The only study to assess predictive ability for CAC presence was the study of 9993 patients [16], which found it was not predictive. Among those investigating CAC extent, one was predictive, with 877 patients, [11] but another was not, with 535 patients [12]. The one predictive study of CAC extent was angiographic and investigated a family history of CAC since the population was preselected to comprise males with a family history of CAD [11].

Obesity: Five studies found no ability for obesity to predict CAC presence [10,15,17,18], although the large study by Kovacic et al. found that there was an inverse predictive ability between obesity and CAC presence, making obesity protective against CAC [16]. No study of CAC extent, found that obesity was predictive [10–12]. The only study of CAC progression did not find obesity to be predictive [19].

When the studies are analysed by markers for obesity:

- Body mass index (BMI) was inversely predictive in the angiographic study of CAC presence involving 9993 patients [16], but not in a further three studies of CAC presence [10,17,18] and one of CAC extent [10]. BMI was not predictive in one study of CAC progression [19].
- Weight was not predictive in one study of CAC extent [16].

Smoking: With respect to CAC presence, only one small study found it to be predictive [14], while the remainder, including the study of 9993 patients, found that smoking was not predictive of CAC presence [10,15,16,18]. None of the four studies of CAC extent [10–13] found smoking to be predictive.

When the studies are analysed by markers for smoking, current smoking was not predictive in two studies of CAC presence [15].

3.3. Meta-Analysis

Out of the ten papers that were eligible for the systematic review [10–19], seven were also suitable for the meta-analysis: Lai et al. [10], Mayer et al. [11], Mitsutake et al. [12], Atar et al. [14], Kovacic et al. [16], Maragiannis et al. [17], and Qing et al. [18].

The meta-analysis investigated the predictive ability of age, male gender, diabetes, dyslipidaemia, hypertension, and smoking for CAC presence and extent (Supplementary Materials, Figure S1). It was not possible to include ethnicity, obesity, exercise, or number of risk factors, although family history of CAD was not predictive; since no other study assessed these two risk factors, they have not been entered in the meta-analysis. As mentioned above, data from three studies investigating CAC extent in the systematic review (Lai et al. [10], Mayer et al. [11], and Mitsutake et al. [12]) have been re-analysed to identify potential risk factor predictors of CAC presence in the meta-analysis.

3.3.1. Predictors of CAC Presence

Table 3 gives the pooled results from the meta-analysis. The predictors of CAC presence in order of importance were hypertension (OR = 1.71, $p < 0.00001$), male gender (OR = 1.47, $p = 0.02$), diabetes (OR = 1.34, $p = 0.03$), and age (OR = 1.07, $p = 0.04$). Smoking and dyslipidaemia were not predictive of CAC presence. The Egger's regression interception test was not significant suggesting no significant publication bias (Table 3). Age, being a continuous variable, could not be entered into the Egger test. The funnel plots for each risk factor are provided in the supplementary Figure S2 and, similarly, show no publication bias.

Table 3. Meta-analysis: pooled risk factors and their ORs predicting CAC presence.

Risk Factors	Pooled or (95% CI)	<i>p</i> for Overall Effect	Studies	Patient Numbers	Egger's Test		
					Intercept	<i>t</i> -Value	<i>p</i> -Value
Age (years)	1.07 (1.00–1.04)	0.04	[10,14,18]	11,63			
Male gender	1.47 (1.05–2.06)	0.02	[12,14,16–18]	11,594	2.29	2.42	0.09
Hypertension	1.71 (1.51–1.94)	<0.00001	[10–12,14,16–18]	12,682	0.94	0.78	0.47
Diabetes mellitus	1.34 (1.02–1.75)	0.03	[10–12,14,16–18]	12,682	0.81	0.83	0.44
Smoking	1.42 (0.90–2.22)	0.13	[10–12,14,16–18]	12,682	3.39	1.84	0.12
Dyslipidaemia	1.25 (0.81–1.94)	0.31	[10,12,16,17]	10,853	1.09	0.64	0.59

Due to the disproportionately large number of patients in the study by Kovacic et al. [16], we repeated the meta-analysis after excluding this paper (shown in the supplementary data, Table S1). This slightly increased the ORs for hypertension to 1.89 ($p < 0.00001$), male gender to 1.74 ($p < 0.00001$), diabetes to 1.45 ($p < 0.00001$). Smoking and dyslipidaemia were still not significant.

3.3.2. Predictors of CAC Extent

Only three studies (Lai et al. [10], Mayer et al. [11], and Mitsutake et al. [12]) analysed the predictors of CAC extent, among which Mayer et al. was an angiographic study classifying CAC as either “no calcification”, “mild to moderate calcification”, or “severe calcification”. Mitsutake et al. [12] used CAC scoring and classified the lowest group (taken to be CAC = 0) as a CAC score of 0–12, the mild-moderate group as a CAC score of 13–445, and the severe calcification group as a CAC score of >445, while Lai et al. [10] used a threshold CAC score of ≥ 400 . The results are shown in Table 4.

Table 4. Meta-analysis: pooled risk factors and their ORs predicting CAC extent.

Risk Factors	Mild to Moderate CAC or CACS 13–445 vs. CACS = 0		Severe CAC or CACS > 445 vs. CACS = 0		Patient Numbers
	OR	p-Value	OR	p-Value	
Hypertension	1.61 (1.28–2.03)	<0.0001	2.09 (1.09–4.03)	0.0100	1623
Diabetes mellitus	1.22 (0.93–1.60)	0.1600	1.55 (1.14–2.10)	0.0050	1623
Dyslipidaemia	0.75 (0.52–1.00)	0.1300	1.03 (0.65–1.63)	0.9000	746
Smoking	0.93 (0.72–1.20)	0.6000	1.07 (0.68–1.67)	0.7700	1623

CACS = Coronary artery calcification score; Studies used in CAC extent meta-analysis: Lai et al. [10], Mayer et al. [11], and Mitsutake et al. [12]. Lai et al. [10], a study using a threshold of >400, was included as severe CAC.

The presence of mild-moderate CAC, compared with zero CAC, was independently predicted only by hypertension (OR 1.61, $p < 0.0001$), with diabetes, dyslipidaemia, and smoking proving not to be predictive of mild-moderate CAC. The presence of severe CAC, compared with zero CAC, was predicted by hypertension (OR 2.09, $p = 0.01$) and diabetes (OR 1.55, $p = 0.005$); dyslipidaemia and smoking were not independently predictive of severe CAC. It was not possible to analyse age or male gender as predictors of CAC extent.

A summary of the studies showing the predictive ability of the risk factors from the systematic review and meta-analysis are shown at Table 5.

Table 5. Summary of studies showing risk factor predictive ability for CAC presence, extent, or progression.

Risk Factors	SYSTEMATIC REVIEW References			Meta-Analysis References	
	CAC Presence	CAC Extent	CAC Progression	CAC Presence	CAC Extent
Age	[10,14–18]	10, 11–13	19	[10,14,18]	Not assessed
Male gender	[14,16–18]	12, 13	Not assessed	[12,14,16–18]	Not assessed
Ethnicity	[16]	Not assessed	Not assessed	Not assessed	Not assessed
Diabetes	[10,14–18]	13–10	19	[10–12,14,16–18]	10; 11
Dyslipidaemia	[10,14–18]	13–10	19	[10,12,16,17]	10; 11
Hypertension	[10,13,15–18]	13–10	19	[10–12,14,16–18]	10; 11
Family history	[16]	11,12	Not assessed	Not assessed	Not assessed
Obesity	[10,15–18]	12–10	19	Not assessed	Not assessed
Smoking	[10,14–16,18]	13–10	Not assessed	[10–12,14,16–18]	10; 11

Reference key: [10]: Lai et al., 221 Chinese males aged ≥ 65 ; [11]: Mayer et al., 877 males with CAD, angiographic study; [12]: Mitsutake et al., 535 patients, Japanese ethnicity; [13]: Tanaka et al., 1363 patients, Japanese ethnicity; [14]: Atar et al., 442 patients, Turkish ethnicity; [15]: Greif et al., 1123 males, European ethnicity; [15]: Greif et al., 437 females, European ethnicity; [16]: Kovacic et al., 9993 patients, angiographic study; [17]: Maragianis et al., 114 patients, US study; [18]: Qing et al., 510 patients, Chinese ethnicity; [19]: Okada et al., 164 patients with CAC, Japanese ethnicity.

3.3.3. Quality Assessment

We carried out a MINORS evaluation of the studies included in the meta-analysis, as shown at Table 6. The items are scored 0 (not reported), 1 (reported but inadequate), or 2 (reported and adequate), with the global ideal score being 16 for non-comparative studies. Most studies scored 2 for all parameters, except follow-up data and prospectivity, which were obviously not in the design for our case-control studies. These results were considered quite satisfactory.

Table 6. Quality assessment of studies included in the meta-analysis.

Study	Clearly Stated Aim	Consecutive Patients Inclusion	Prospective Collection of Data	Endpoints Appropriate	Unbiased Assessment of the Study Endpoint	Follow-up Period Appropriate to the Aim of the Study	Loss to Follow up Less than 5%	Prospective Calculation of the Study Size	Total Score
Atar et al., 2013 [14]	2	2	2	2	2	2	0	0	10
Greif et al., 2013 [15]	2	2	2	2	2	2	0	0	10
Kovacic et al., 2012 [16]	1	2	0	1	2	0	0	0	6
Mayer et al., 2007 [11]	2	2	2	2	2	0	0	0	10
Mitsutake et al., 2007 [12]	2	2	2	2	2	0	0	0	10
Okada et al., 2013 [19]	2	2	2	2	2	2	1	0	13
Tanaka et al., 2012 [13]	2	2	2	2	2	0	0	0	10
Lai et al., 2015 [10]	2	2	2	2	2	0	0	0	10
Maragiamnis et al., 2015 [17]	2	1	2	2	2	0	0	0	9
Qing et al., 2015 [18]	2	2	2	2	2	0	0	0	10

Evaluation of meta-analysis studies using the Methodological Index for Non-Randomized Studies (MINORS) [22]. Elements are scored 0 (not reported), 1 (reported but inadequate), or 2 (reported and adequate).

4. Discussion

4.1. Findings

In the Systematic Review, age was strongly predictive of both CAC presence and extent, but not of CAC progression. The results for other risk factors for CAC presence are not as clear cut, largely due to the Kovacic et al. [16] study of 9993 patients, which overwhelmed the analysis. This study found that white ethnicity, diabetes, hypertension, and obesity were predictive of CAC presence, but not male gender, dyslipidaemia, family history, or smoking. These results do not necessarily accord with the totality of the studies, in which a broadly equal number showed that male gender, diabetes, and dyslipidaemia were predictive of CAC presence as not predictive. Only two studies (including Kovacic et al. [16]) found that hypertension was predictive of CAC presence, compared to five studies finding that it was not predictive, while only Kovacic et al. [16] found that obesity was predictive (albeit inversely), whereas five studies found that it was not predictive of CAC presence. Smoking was, overall, not predictive. No study of CAC presence, other than Kovacic et al. [16], assessed ethnicity (predictive) or family history of CAD (not predictive). With respect to CAC extent, male gender, hypertension, and possibly a family history of CAC were predictive, but diabetes, dyslipidaemia, obesity, and smoking were, overall, not predictive. For diabetes there were an almost equal amount of patient numbers in the three studies which found diabetes to be predictive as not predictive of CAC extent. In the one study of CAC progression, diabetes and hypertension were predictive, but not age, dyslipidaemia, or obesity.

Among the risk factor markers, only use of lipid-lowering medication and higher BMI were broadly predictive of CAC presence, with possibly decreased HDL and increased SBP being predictive of CAC extent, although these results were found in only one study. In the single study of CAC progression, HbA1c and SBP were predictive.

The meta-analysis included seven studies, rather than the ten in the systematic review, although two studies of CAC extent also provided sufficient statistical data to be used to assess CAC presence, while another study provided data for both CAC presence and extent. This analysis shows that hypertension followed by male gender, diabetes, and age were predictive of CAC presence, while smoking and dyslipidaemia were not predictive. For CAC extent, however, mild-moderate CAC was predicted by hypertension alone, whereas severe CAC was predicted by hypertension followed by diabetes. The MINORS scores were quite satisfactory for all included studies which adds to the strength of the data analysis.

4.2. Areas of Difference between Results from the Systematic Review and Meta-Analysis

The most striking difference between the results from the systematic review and the meta-analysis is the minimal importance of age as a predictor of CAC in the meta-analysis, whereas it is a consistent predictor of both CAC presence and extent in the systematic review. However, this may largely be accounted for, firstly, by the fact that age is a continuous variable and, secondly, that a different mix of studies of CAC presence were used for the systematic review and meta-analysis. We have previously shown the important predictive value of age in a large cohort of symptomatic patients [23].

With respect to CAC presence, there were no other clear predictive risk factors based on the numbers of studies but when considering numbers of patients then the Kovacic et al. [16] study of 9993 patients, which found that diabetes and hypertension were predictive, was broadly in agreement with the meta-analysis. In the systematic review, CAC extent was predicted by male gender and hypertension, whereas in the meta-analysis CAC extent was predicted by hypertension and diabetes; this can be explained by the different mix of studies between the two methods. The main limitation of the systematic review is its qualitative analysis with many contributory factors, such as the power of the study, the number of studies, and the number of patients. These limitations are overcome by the quantitative pooling of the meta-analysis.

4.3. Comparison with Other Studies

Although we have found that in symptomatic patients the predictive risk factors for CAC presence, extent, and progression are hypertension and diabetes, this is not the case in asymptomatic subjects where dyslipidaemia, smoking, obesity, and family history of CAD have also been shown to be predictive of CAC presence and progression in large population studies, such as the Multi-Ethnic Study of Atherosclerosis and Heinz Nixdorf Recall [24,25]. No systematic review or meta-analysis of risk factor predictors for CAC in asymptomatic subjects has been carried out. Although the two conditions, hypertension and diabetes, are different in their clinical presentation and means of treatment, their effect on the arterial wall seems to be phenotypically similar, suggesting a shared mechanism such as oxidative stress [26,27]. Arterial calcification represents segmental ossification which is known to be progressive even after controlling risk factors, thus suggesting a perpetual effect, through a biochemical and/or histopathological mechanism, of those risk factors rather than just a triggering effect that subsides with their optimum control. Nevertheless, there is no inherent reason why the conventional CV risk factors, which were identified as predictors of 10-year coronary event risk [28,29], should predict CAC presence or extent, merely because CAC can also predict the 10-year event risk [3].

Curiously, the expected predictive risk of dyslipidaemia did not feature strongly in either the systematic review or the meta-analysis. While some studies have shown that dyslipidaemia can be predictive of arterial calcification presence or extent in asymptomatic subjects, this is not always the case, previously seen in a systematic review and meta-analysis of predictors of breast arterial calcification which found no relationship with dyslipidaemia [30]. In addition, dyslipidaemia is a particularly Caucasian problem [31] and it may be that the high number of studies with a Chinese or Japanese population included in the meta-analysis has impacted the results. Nevertheless, we have previously found that lipid-lowering medication has no effect on reducing coronary or aortic valve calcification [32,33], while other studies have found that rather than the treatment group, it is the placebo group that has less calcium progression [22,34]. It may, however, be the case that by the time calcification is established, the association with dyslipidaemia has been lost.

4.4. Limitations

A number of limitations deserve mention. Firstly, although we attempted to identify and include all relevant studies, there will inevitably be some that we have overlooked. Secondly, our search was restricted to studies in English, so it may be possible that some studies in other languages have been missed. Thirdly, the studies included in this systematic review and meta-analysis varied in design, population (e.g., eligibility by age), definition and duration of risk factor, and year of publication. As expected, we observed considerable heterogeneity between studies, so it is arguable whether a summary estimate should be presented. However, our objective was not to provide this but rather to present a general approximation of the prevalence of these risk factors to facilitate the message. In particular, two studies assessed CAC angiographically, which is not sensitive to CAC detection, while the remainder used 16- or 64-slice CT scanning. Fourthly, analysis of studies of CAC presence was overwhelmed by the study of 9333 patients, while the next largest study had only 1560. Fifthly, the lack of standardisation of definitions of risk factors limits our ability to provide summary estimates and we had no information on the duration of risk factors, which might have impacted the analysis. Sixthly, we were confined to those risk factors commonly measured in a clinical setting and, inevitably, there are others which might have been relevant.

5. Conclusions

Our meta-analysis showed that hypertension followed by diabetes were the most important risk factors for prediction of CAC presence and extent, with age and male gender also showing predictive ability for CAC presence. The results from the systematic review were more equivocal,

but the two forms of analysis were in general agreement that dyslipidaemia, obesity, and smoking were not predictive of CAC presence or extent. Irrespective of the mechanism for arterial endothelial damage, hypertension and diabetes seem to result in a common phenotypic arterial wall damage in the form of calcification. Finally, despite CAC and the conventional CV risk factors both being predictive of 10-year coronary event risk, only a few of the CV risk factors appear predictive of CAC.

Supplementary Materials: Supplementary materials can be found at www.mdpi.com/1422-0067/17/9/1481/s1.

Conflicts of Interest: The authors declare no conflict of interest.

References

1. Assmann, G.; Cullen, P.; Schulte, H. Simple scoring scheme for calculating the risk of acute coronary events based on the 10-year follow-up of the Prospective Cardiovascular Muenster (PROCAM) study. *Circulation* **2002**, *105*, 310–315. [CrossRef] [PubMed]
2. The Second Joint Task Force of European and Other Societies. Prevention of coronary heart disease in clinical practice. Recommendations of the Second Joint Task Force of European and other Societies on Coronary Prevention. *Eur. Heart J.* **1998**, *19*, 1434–1503.
3. Grundy, S.M.; Cleeman, J.I.; Merz, C.N.; Brewer, H.B., Jr.; Clark, L.T.; Huntinghake, D.B.; Pasternak, R.C.; Smith, S.C., Jr.; Stone, N.J.; National Heart, Lung, and Blood Institute; et al. Implications of recent clinical trials for the National Cholesterol Education Program Adult Treatment Panel III guidelines. *Circulation* **2004**, *13*, 227–239. [CrossRef] [PubMed]
4. Rumberger, J.A.; Simons, D.B.; Fitzpatrick, L.A.; Sheedy, P.F.; Schwartz, R.S. Coronary artery calcium area by electron-beam computed tomography and coronary atherosclerotic plaque area. A histopathologic correlative study. *Circulation* **1995**, *92*, 2157–2162. [CrossRef] [PubMed]
5. National Cholesterol Education Program (NCEP) Expert Panel on Detection, Evaluation, and Treatment of High Blood Cholesterol in Adults (Adult Treatment Panel III). Third Report of the National Cholesterol Education Program (NCEP) Expert Panel on Detection, Evaluation, and Treatment of High Blood Cholesterol in Adults (Adult Treatment Panel III) final report. *Circulation* **2002**, *106*, 3143–3421.
6. Zeb, I.; Budoff, M. Coronary Artery Calcium Screening: Does it Perform Better than Other Cardiovascular Risk Stratification Tools? *Int. J. Mol. Sci.* **2015**, *16*, 6606–6620. [CrossRef] [PubMed]
7. Henein, M.; Nicoll, R. Atherosclerosis and extensive arterial calcification: The same condition? *Int. J. Cardiol.* **2010**, *141*, 1–2. [CrossRef] [PubMed]
8. Henein, M.; Owen, A. Statins moderate coronary atheroma but not coronary calcification: Results from meta-analyses. *Scand. Cardiovasc. J.* **2010**, *44*. [CrossRef]
9. Liberati, A.; Altman, D.G.; Tetzlaff, J.; Mulrow, C.; Gøtzsche, P.C.; Ioannidis, J.P.A.; Clarke, M.; Devereaux, P.J.; Kleijnen, J.; Moher, D. The PRISMA statement for reporting systematic reviews and meta-analyses of studies that evaluate health care interventions: Explanation and elaboration. *Ann. Intern. Med.* **2009**, *151*, W65–W94. [CrossRef] [PubMed]
10. Lai, J.; Ge, Y.; Shao, Y.; Xuan, T.; Xia, S.; Li, M. Low serum testosterone level was associated with extensive coronary artery calcification in elderly male patients with stable coronary artery disease. *Coron. Artery Dis.* **2015**, *26*, 437–441. [CrossRef] [PubMed]
11. Mayer, B.; Lieb, W.; Radke, P.W.; Götz, A.; Fischer, M.; Bässler, A.; Doehring, L.C.; Aherrahrou, Z.; Liptau, H.; Erdmann, J. Association between arterial pressure and coronary artery calcification. *J. Hypertens.* **2007**, *25*, 1731–1738. [CrossRef] [PubMed]
12. Mitsutake, R.; Miura, S.; Saku, K. Association between coronary artery calcification score as assessed by multi-detector row computed tomography and upstroke time of pulse wave. *Intern. Med.* **2007**, *46*, 1833–1836. [CrossRef] [PubMed]
13. Tanaka, M.; Fukui, M.; Tomiyasu, K.; Akabame, S.; Nakano, K.; Yamasaki, M.; Hasegawa, G.; Oda, Y.; Nakamura, N. Eosinophil count is positively correlated with coronary artery calcification. *Hypertens. Res.* **2012**, *35*, 325–328. [CrossRef] [PubMed]

14. Atar, A.I.; Yilmaz, O.C.; Akin, K.; Selçoki, Y.; Er, O.; Eryonucu, B. Serum uric acid level is an independent risk factor for presence of calcium in coronary arteries: An observational case-controlled study. *Anadolu Kardiyol. Derg.* **2013**, *13*, 139–145. [CrossRef] [PubMed]
15. Greif, M.; Arnoldt, T.; von Ziegler, F.; Ruemmler, J.; Becker, C.; Wakili, R.; D’Anastasi, M.; Schenzle, J.; Leber, A.W.; Becke, A. Lipoprotein(a) is independently correlated with coronary artery calcification. *Eur. J. Intern. Med.* **2013**, *24*, 75–79. [CrossRef] [PubMed]
16. Kovacic, J.C.; Lee, P.; Baber, U.; Karajgikar, R.; Evrard, S.M.; Moreno, P.; Mehran, R.; Fuster, V.; Dangas, G.; Sharma, S.K.; et al. Inverse relationship between body mass index and coronary artery calcification in patients with clinically significant coronary lesions. *Atherosclerosis* **2012**, *221*, 176–182. [CrossRef] [PubMed]
17. Maragiannis, D.; Schutt, R.C.; Gramze, N.L.; Chaikriangkrai, K.; McGregor, K.; Chin, K.; Nabi, F.; Little, S.H.; Nagueh, S.F.; Chang, S.M. Association of Left Ventricular Diastolic Dysfunction with Subclinical Coronary Atherosclerotic Disease Burden Using Coronary Artery Calcium Scoring. *J. Atheroscler. Thromb.* **2015**, *22*, 1278–1286. [CrossRef] [PubMed]
18. Qing, P.; Li, X.L.; Zhang, Y.; Li, Y.L.; Xu, R.X.; Guo, Y.L.; Li, S.; Wu, N.Q.; Li, J.J. Association of Big Endothelin-1 with Coronary Artery Calcification. *PLoS ONE* **2015**, *10*, e0142458. [CrossRef] [PubMed]
19. Okada, H.; Fukui, M.; Tanaka, M.; Matsumoto, S.; Mineoka, Y.; Nakanishi, N.; Tomiyasu, K.; Nakano, K.; Hasegawa, G.; Nakamura, N. Visit-to-visit variability in systolic blood pressure is a novel risk factor for the progression of coronary artery calcification. *Hypertens. Res.* **2013**, *36*, 996–999. [CrossRef] [PubMed]
20. Greenland, S.; Longnecker, M.P. Methods for trend estimation from summarised dose-response data, with applications to meta-analysis. *Am. J. Epidemiol.* **1992**, *135*, 1301–1309. [PubMed]
21. Hamling, J.; Lee, P.; Weitkunat, R.; Ambuhl, M. Facilitating meta-analyses by deriving relative effect and precision estimates for alternative comparisons from a set of estimates presented by exposure level or disease category. *Stat. Med.* **2008**, *27*, 954–970. [CrossRef] [PubMed]
22. Slim, K.; Nini, E.; Forestier, D.; Kwiatkowski, F.; Panis, Y.; Chipponi, J. Methodological index for non-randomized studies (minors): Development and validation of a new instrument. *ANZ J. Surg.* **2003**, *73*, 712–716. [CrossRef] [PubMed]
23. Nicoll, R.; Wiklund, U.; Zhao, Y.; Diederichsen, A.; Mickley, H.; Ovrehus, K.; Zamorano, J.; Gueret, P.; Schermund, A.; Maffei, E.; et al. Gender and age effects on risk factor-based prediction of coronary artery calcium in symptomatic patients: A Euro-CCAD study. *Atherosclerosis* **2016**, in press. [CrossRef] [PubMed]
24. Kronmal, R.A.; McClelland, R.L.; Detrano, R.; Shea, S.; Lima, J.A.; Cushman, M.; Bild, D.E.; Burke, G.L. Risk factors for the progression of coronary artery calcification in asymptomatic subjects: Results from the Multi-Ethnic Study of Atherosclerosis (MESA). *Circulation* **2007**, *115*, 2722–2730. [CrossRef] [PubMed]
25. Schermund, A.; Lehmann, N.; Bielak, L.F.; Yu, P.; Sheedy, P.F.; Cassidy-Bushrow, A.E.; Turner, S.T.; Moebus, S.; Möhlenkamp, S.; Stang, A.; et al. Comparison of subclinical coronary atherosclerosis and risk factors in unselected populations in Germany and US-America. *Atherosclerosis* **2007**, *195*, e207–e216. [CrossRef] [PubMed]
26. Harvey, A.; Montezano, A.C.; Touyz, R.M. Vascular biology of ageing—Implications in hypertension. *J. Mol. Cell. Cardiol.* **2015**, *83*, 112–121. [CrossRef] [PubMed]
27. Gross, M.; Steffes, M.; Jacobs, D.R., Jr.; Yu, X.; Lewis, L.; Lewis, C.E.; Loria, C.M. Plasma F2-isoprostanes and coronary artery calcification: The CARDIA Study. *Clin. Chem.* **2005**, *51*, 125–131. [CrossRef] [PubMed]
28. Erbel, R.; Möhlenkamp, S.; Moebus, S.; Schermund, A.; Lehmann, N.; Stang, A.; Dragano, N.; Grönemeyer, D.; Seibel, R.; Kälsch, H.; et al. Coronary risk stratification, discrimination, and reclassification improvement based on quantification of subclinical coronary atherosclerosis: The Heinz Nixdorf Recall study. *J. Am. Coll. Cardiol.* **2010**, *56*, 1397–1406. [CrossRef] [PubMed]
29. Polonsky, T.S.; McClelland, R.L.; Jorgensen, N.W.; Bild, D.E.; Burke, G.L.; Guerci, A.D.; Greenland, P. Coronary artery calcium score and risk classification for coronary heart disease prediction. *JAMA* **2010**, *303*, 1610–1616. [CrossRef] [PubMed]
30. Hendriks, E.J.; de Jong, P.A.; van der Graaf, Y.; Mali, W.P.; van der Schouw, Y.T.; Beulens, J.W. Breast arterial calcifications: A systematic review and meta-analysis of their determinants and their association with cardiovascular events. *Atherosclerosis* **2015**, *239*, 11–20. [CrossRef] [PubMed]
31. Budoff, M.J.; Nasir, K.; Mao, S.; Tseng, P.H.; Chau, A.; Liu, S.T.; Flores, F.; Blumenthal, R.S. Ethnic differences of the presence and severity of coronary atherosclerosis. *Atherosclerosis* **2006**, *187*, 343–350. [CrossRef] [PubMed]

32. Henein, M.Y.; Owen, A. Statins moderate coronary stenoses but not coronary calcification: Results from meta-analyses. *Int. J. Cardiol.* **2011**, *153*, 31–35. [CrossRef] [PubMed]
33. Zhao, Y.; Nicoll, R.; He, Y.H.; Henein, M.Y. The effect of statins on valve function and calcification in aortic stenosis: A meta-analysis. *Atherosclerosis* **2016**, *246*, 318–324. [CrossRef] [PubMed]
34. McCullough, P.A.; Chinnaian, K.M. Annual progression of coronary calcification in trials of preventive therapies: A systematic review. *Arch. Intern. Med.* **2009**, *169*, 2064–2070. [CrossRef] [PubMed]



© 2016 by the authors. Licensee MDPI, Basel, Switzerland. This article is an open access article distributed under the terms and conditions of the Creative Commons Attribution (CC BY) license (<http://creativecommons.org/licenses/by/4.0/>).



Review

Molecular Imaging of Vulnerable Atherosclerotic Plaques in Animal Models

Sara Gargiulo, Matteo Gramanzini and Marcello Mancini *

Institute of Biostructure and Bioimaging, National Research Council, Via T. De Amicis 95, 80145 Naples, Italy; sara.gargiulo@ibb.cnr.it (S.G.); matteo.gramanzini@ibb.cnr.it (M.G.)

* Correspondence: marcello.mancini@ibb.cnr.it; Tel.: +39-081-2203411

Academic Editor: Michael Henein

Received: 26 July 2016; Accepted: 31 August 2016; Published: 9 September 2016

Abstract: Atherosclerosis is characterized by intimal plaques of the arterial vessels that develop slowly and, in some cases, may undergo spontaneous rupture with subsequent heart attack or stroke. Currently, noninvasive diagnostic tools are inadequate to screen atherosclerotic lesions at high risk of acute complications. Therefore, the attention of the scientific community has been focused on the use of molecular imaging for identifying vulnerable plaques. Genetically engineered murine models such as ApoE^{-/-} and ApoE^{-/-}Fbn1C1039G⁺⁻ mice have been shown to be useful for testing new probes targeting biomarkers of relevant molecular processes for the characterization of vulnerable plaques, such as vascular endothelial growth factor receptor (VEGFR)-1, VEGFR-2, intercellular adhesion molecule (ICAM)-1, P-selectin, and integrins, and for the potential development of translational tools to identify high-risk patients who could benefit from early therapeutic interventions. This review summarizes the main animal models of vulnerable plaques, with an emphasis on genetically altered mice, and the state-of-the-art preclinical molecular imaging strategies.

Keywords: atherosclerosis; vulnerable plaques; animal models; genetically modified mice; molecular imaging

1. Introduction

Atherosclerosis is the primary cause of myocardial ischemia, stroke and lower limb amputation. It is a chronic disease that occurs predominantly at sites of disturbed laminar flow (arterial branches and bifurcations), which are characterized by the focal subendothelial accumulation of apolipoprotein B-containing lipoproteins and inflammatory cells (monocytes, macrophages, T cells, and mast cells) on injured intima, leading to the thickening of the arterial wall and formation of atherosclerotic plaques. The majority of atherosclerotic plaques remain clinically silent [1], but, in some cases, a plaque can become symptomatic via two mechanisms: (a) a gradual reduction of the vessel lumen leading to reduced blood flow, with the appearance of ischemic symptoms in conditions of high oxygen demand (stable angina pectoris, intermittent claudication); (b) erosion and rupture of the fibrous cap of the plaque with complete thrombosis of the lumen and/or embolization of the distal territory (heart attack or stroke) [2]. The broadest definition of a vulnerable plaque was proposed from a consensus document of the American Heart Association (AHA) in 2003: “The term ‘vulnerable plaque’ defines plaques susceptible to complications, and identifies all thrombosis-prone plaques and ones with a high probability of undergoing rapid progression, thus becoming culprit plaques” [3]. The term “vulnerable plaque” refers to often modestly stenotic lesions with a specific morphological presentation [4]: a large core of lipid deposits, necrotic cell debris and macrophages producing matrix-degrading enzymes such as metalloproteinases, with thinning of the fibrous cap.

These lesions are prone to rupture and may cause the above clinical complications [5]. The mechanisms underlying the transition of stable plaques to clinically significant lesions are

currently not fully clear, but they involve a complex interplay of several biological processes, including inflammation, matrix remodeling, angiogenesis and apoptosis.

The present clinical and diagnostic tools are inadequate for the early identification of atherosclerosis and lesions that have a high probability to determine an acute event. Using a predictive model of risk assessment such as the Framingham risk score, it is impossible to accurately identify patients who will develop events and who would require immediate and aggressive therapeutic intervention. Therefore, the attention of the scientific community has focused on the development of new tools that provide higher sensitivity and specificity for the detection of vulnerable plaques. Molecular imaging can reveal specific biological pathways or cellular processes for a better understanding of the molecular events responsible for plaque destabilization. Moreover, the identification of novel imaging biomarkers may aid in risk stratification, with the potential to optimize preventive interventions that would reduce disease progression and cardiovascular events.

In vivo studies with experimental systems are essential to gain detailed insight into the molecular mechanisms of atherosclerotic plaque vulnerability and to develop better diagnostic and therapeutic tools. Animal models may enable us to study noninvasive imaging strategies to improve the ability to predict future risks of plaque rupture and to reduce the incidence of acute events. Although a variety of small and large animal models have been used for research on atherosclerosis, no model is currently considered ideal, and each has its own advantages and limitations with respect to the study of atherogenesis and modeling of the vulnerable plaque [6].

Until recently, useful large animal models have included nonhuman primates, pigs, and rabbits. Lesions in primates [7–11] and pigs [12–14] most closely resemble human lesions morphologically at all stages of the disease, and therefore they would be ideal models. In particular, the pig has a human-like lipoprotein profile and develops lesions in the coronary arteries [15,16], and porcine models of familial hypercholesterolemia have been shown to develop complex atherosclerotic lesions [17].

Rabbits have also been extensively used in atherosclerosis research, and some strains that exhibit familial hypercholesterolemia [18,19], such as the well-established Watanabe rabbit [20], develop coronary atherosclerosis. These models have certainly provided invaluable insight for defining the primary cellular events in the initiation and development of atherosclerotic lesions. Nevertheless, larger animals are more expensive to purchase, feed, handle and house in conditions appropriate to modern animal husbandry. Moreover, overall, large animals do not lend themselves to the ease and types of genetic manipulation that are possible in other species, such as mice [21]. At present, spontaneous plaque rupture in these models occurs only sporadically, after a long period of time, or depends on an additional trigger such as mechanical injury [22–24] or pharmacological treatment [25]. Additionally, the slow progression of complex atherosclerotic lesions, the long generation time, and ethical issues hinder the use of these species in preclinical molecular imaging research [26–31].

Although not all aspects are comparable to humans, the laboratory mouse (*Mus musculus*) is currently the most favored species to better understand the biology and pathology of atherosclerosis. The main advantages of this model include a well-known genetic background, a proportion of approximately 80% of genes in homology with humans [32], ease of breeding and low cost of maintenance. Moreover, the small size of mice facilitates the use of representative samples, which is a relevant issue for studying atherosclerotic lesions characterized by a large inherent variability.

In particular, murine models are recommended due to the relatively short time frame in which they develop atherosclerosis and due to their relative ease of genetic manipulation. Among these animal models, the genetically altered apolipoprotein-E-knockout ($ApoE^{-/-}$) mice have been used extensively for the following reasons: they develop spontaneous atherosclerosis; the rate of atherogenesis can be notably accelerated by feeding the mice a high-fat, western-type diet (WTD); they exhibit various phases of the disease, including the early stage of fatty streaks, the accumulation of foam cells, and the development of a fibrous cap [33,34]; and they exhibit advanced stages of the disease characterized by relevant complications such as fissures, hemorrhage, plaque rupture and thrombosis [35].

Furthermore, depending on the experimental design, atherosclerotic lesions in this model may resemble the stable or unstable atherosclerotic lesions of humans [36–38]. Finally, ApoE^{−/−} mice have also been used to generate other relevant mouse models of atherosclerosis through breeding strategies [39–41]. Recently, a new genetically altered murine model of vulnerable plaques was established by crossbreeding ApoE^{−/−} mice with mice carrying a heterozygous mutation (C1039^{+/−}) in the fibrillin-1 (Fbn1) gene [42]. Fbn1 is the major structural component of the extracellular microfibrils in the vessel wall, and the heterozygous C1039^{+/−} mutation led to fragmentation of the elastic fibers. Furthermore, it has been reported that ApoE^{−/−}–Fbn1C1039G^{+/−} mice seem to be associated with a more unstable plaque phenotype compared to ApoE^{−/−} mice because they develop acute plaque rupture, with subsequent myocardial infarction, neurological symptoms (head tilt, disorientation and motor disturbances), and sudden death. For these features, at the moment, transgenic ApoE^{−/−} mice are successfully being used as a model of stable atherosclerotic plaques, whereas ApoE^{−/−}–Fbn1C1039G^{+/−} mice could be considered to be a model for the study of the mechanisms of plaque rupture and for investigating theranostic tools.

Although the small size of the mouse could complicate the analysis of atherosclerotic vessels, recent technological advances in the field of high-resolution preclinical imaging such as magnetic resonance imaging (MRI) and contrast-enhanced ultrasound (CEUS) allow for the quantification of parameters of interest with high accuracy to monitor disease progression and may reduce the number of animals needed for research.

Both ApoE^{−/−} and ApoE^{−/−}–Fbn1C1039G^{+/−} mice have been shown to be useful tools for testing new imaging probes targeted for molecular markers of relevant biological processes such as VEGFR-1, VEGFR-2, ICAM-1, P-selectin and integrins. In this way, it is possible to noninvasively monitor the molecular pathways involved in the development of atherosclerotic plaques *in vivo* in these mice for comparison with those molecular pathways currently highlighted in humans, in a manner that is complementary to the use of molecular and cellular biology.

Very recently, the ApoE^{−/−}–Fbn1C1039G^{+/−} mouse model has been studied *in vivo* using gold nanoparticle-enhanced micro-computed tomography (microCT) to evaluate macrophage infiltration in atherosclerotic plaques at the level of the carotid bifurcation, with ex-vivo validation [43]. Genetically modified murine models such as ApoE^{−/−} and ApoE^{−/−}–Fbn1C1039G^{+/−} could offer promising avenues for testing innovative molecular imaging strategies as potential translational tools able to identify high-risk patients who could benefit from early therapeutic interventions.

2. Murine Models of Atherosclerosis and Molecular Imaging Targets

2.1. Murine Models of Atherosclerosis and Vulnerable Plaques

The study of atherosclerosis progression in humans is hindered by the complexity and chronicity of the disease process, by the difficulty to longitudinally monitor the changes of the plaques in an individual patient and by deficiency of the noninvasive detection modalities that provide limited information on the composition of the lesions.

The investigation of pathological changes in the arteries of humans is restricted to studies in the cross-sections of autopic or surgical samples. Therefore, there has been a reliance on animal models, and, since 1992, the mouse has become an excellent system for the study of atherosclerosis, progressively replacing the use of large animals [44,45], in particular due to the ability to easily over- or under-express specific genes in this species. A number of recent reviews have extensively discussed the various mouse models of atherosclerosis available [46–49].

This review summarizes the relevant characteristics of the above experimental systems, with an emphasis on the currently available mouse models of vulnerable atherosclerotic plaques, comparing the pattern of their lesions to those in humans.

2.1.1. Murine Models of Atherosclerosis: General Considerations

Unlike humans, in general, mice have high levels of antiatherosclerotic high-density lipoprotein (HDL) and low levels of proatherogenic low-density lipoprotein (LDL) and very low-density lipoprotein (VLDL) [46–49]. However, mice with specific genetic backgrounds can develop atherosclerosis on particular diets that promote an increase in the VLDL fraction, and the inbred strain C57BL/6 has been shown to be the most susceptible [46–50]. The earliest mouse model of atherosclerosis was induced in C57BL/6 mice with a special diet containing 30% fat, 5% cholesterol, and 2% cholic acid. However, this diet induced weight loss and often led to respiratory infections [46–49]. Therefore, subsequent studies have predominantly used C57BL/6 mice fed a diet supplemented with 15% fat, 1.25% cholesterol, and 0.5% cholic acid, commonly referred to as the “Paigen diet” [50].

Although this last model has been widely used in the study of atherosclerosis, unfortunately, the type of lesions did not resemble those in humans. In fact, the atherosclerotic plaques, which developed in these mice at four to five months of age, were very small (on the order of 200 to 1000 square microns) and were limited to the aortic root when the mice were fed the “Paigen diet” for periods of 14 weeks to nine months. Moreover, atherosclerotic lesions in this model were largely limited to the fatty streak stage, usually consisting mainly of macrophage foam cells and few smooth muscle cells (SMCs), and they did not progress to intermediate stages as in humans. Finally, the “Paigen diet” appeared to be unphysiological with regard to its extremely high cholesterol content and the presence of cholic acid, and it exhibited inflammatory properties [51].

To overcome these limitations, wild-type C57BL/6 mice are no longer used, and the current murine models for atherosclerosis have been primarily developed by genetic manipulations of and backcrossing onto C57BL/6, resulting in perturbations of the lipoprotein metabolism through adequate dietary modification or endogenous hyperlipidemia.

These genetically modified strains have the advantage of exhibiting extensive lesions at various stages of the disease, phenotypes of stable and vulnerable plaques and relevant complications such as plaque rupture and thrombosis. Although the current mouse models more closely represent human atherosclerosis, the choice should be based on the investigator’s specific needs as each model has distinctive features and some limitations. Several studies have demonstrated the feasibility of these models. In contemporary research on atherosclerosis, the most extensively characterized strains are those deficient in apolipoprotein E ($ApoE^{-/-}$) and low-density lipoprotein ($LDL^{-/-}$) receptors [52–54]. The introduction of these gene-targeted mice has revolutionized the study of atherogenic processes and has ensured that the mouse quickly became the most popular mammalian model of atherosclerosis to date. A specific allele is deleted, permitting the precise definition of a protein’s activities. These two murine models have several advantages as follows: they are readily commercially available, they breed well, and their lesions have been documented in detail within a well-defined time frame and appear morphologically comparable to those found in humans [33,34,55].

In $ApoE^{-/-}$ mice, the normal gene coding for apolipoprotein E is replaced by a mutated gene that does not produce this molecule, leading to elevation of cholesterol-enriched chylomicrons and very low-density lipoprotein (VLDL)-sized particles. The first mouse model with a switched-off gene for apolipoprotein E was generated almost contemporaneously in two laboratories in the United States [56,57], and shortly thereafter this model was described as “the best animal model of atherosclerosis” available at that time [58]. In contrast to previous animal models, this mouse is able to develop atherosclerosis spontaneously [59], and it is possible to accelerate the development of the disease using a high-fat diet similar in composition to an average American diet (21% fat, 0.15% cholesterol), called a “western-type” diet [55]. Gender- and age-related differences in cardiovascular aging have been demonstrated in this genetically modified mouse, since hypercholesterolemia and male gender additively aggravate the entity of lipid deposition and vascular senescence in $ApoE^{-/-}$ mice of advanced age [60].

In $LDL^{-/-}$ mice, the deletion of the LDL receptor mimics the homozygous form of genetic hypercholesterolemia found in humans; however, these mice exhibit only modest hyperlipidemia

when fed a normal diet, whereas they are susceptible to the formation of atherosclerotic lesions when fed a high-fat diet.

Because this review is intended to highlight the use of murine models to study the process of atherogenesis and, in particular, vulnerable plaques, a brief description of the morphological features of the six stages of atherosclerotic lesions in $\text{ApoE}^{-/-}$ and $\text{LDL}^{-/-}$ mice, based on the human scale of AHA, is provided (as shown in Figure 1) [48,61].

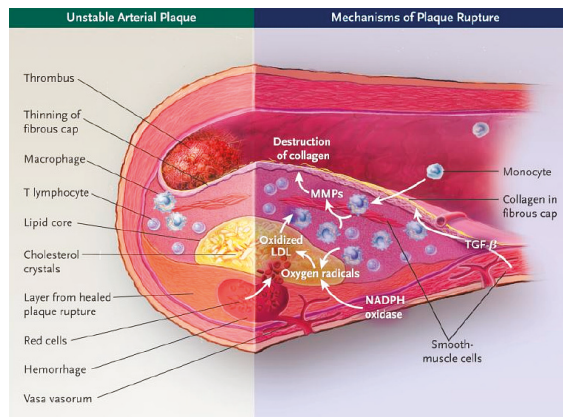


Figure 1. Pathogenesis of atherosclerosis and the mechanisms of plaque rupture. Unstable plaque has a thin fibrous cap, may be thrombotic, and is characterized by many inflammatory cells and a large lipid core. Accumulation of macrophages and T lymphocytes in plaques leads to the release of matrix metalloproteinases (MMPs), which digest collagen and cause thinning of the fibrous cap. The necrotic lipid core grows as a result of the accumulation of lipids in the extracellular matrix, the death of lipid-laden macrophages, and perhaps the accumulation of erythrocyte membranes after intraplaque hemorrhage from the vasa vasorum. Oxygen radicals, generated mainly from NADPH oxidase and inflammatory cells, oxidize low-density lipoproteins (LDL) and cause necrosis of cells. (Reprinted from Reference [61]. Copyright with permission from © 2003, Massachusetts Medical Society.)

Stage I lesions consist of the focal accumulation of lipids with slight intimal thickening. The progression to stage II involves the infiltration of lymphocytes and macrophages, with the latter referred to as “foam cells”, due to the intracytoplasmic lipidic inclusions. This type of lesion, defined as a “fatty streak”, appears as a yellowish stripe on the intimal surface and is a common feature in the aortas of both $\text{ApoE}^{-/-}$ and $\text{LDL}^{-/-}$ mice. The accumulation of extracellular lipids is detected in lesions that undergo progression to stage III. The first lesion considered advanced by histological criteria is stage IV, presenting a further increase and convergence of extracellular lipids to form a “lipid core” covered with foam cells. Afterwards, a “cap” of fibrous tissue progressively develops, and thus the stage V lesions are defined as “fibrous plaques”. Macrophage-derived foam cells and lymphocytes are generally found densely concentrated along the periphery of the lipid core of both stage IV and V lesions [62,63]. Stage IV and V lesions are capable of developing fissures, hematomas, and/or thrombi and, for this reason, are clinically relevant in terms of morbidity and mortality in humans. Finally, plaques called “complicated” correspond to stage VI, because these lesions are characterized by ulcerations, hematomas, hemorrhages or thrombi, and may generate acute events.

Although both mouse models develop atherosclerotic plaques at the level of the aorta after being fed a high-fat diet which closely resemble the morphological features of human atherosclerotic plaques, $\text{ApoE}^{-/-}$ mice develop more extended lesions in a shorter time frame [55,57,64].

Moreover, the atherosclerotic plaques have been described in $\text{ApoE}^{-/-}$ mice not only in the aortic root but throughout the entire aorta (descending thoracic and lower abdominal aorta, aortic

bifurcation and common iliac vascular tracts) and its principal branches (brachiocephalic and right common carotid arteries). With a standard diet, fatty streaks were first observed in the proximal aortas of three-month-old ApoE^{-/-} mice, and foam cell lesions were seen at 10 weeks of age [55]. Intermediate lesions containing foam cells and SMCs appeared at 15 weeks, and fibrous plaques at 20 weeks of age. The western diet markedly increases plasmatic VLDL and chylomicrons [56,57] and accelerates the atherogenic process, resulting in the detection of fatty streaks by eight weeks of age and the appearance of complications such as intraleisional calcifications [55,65]. In comparison, LDL^{-/-} mice fed a regular chow diet display high individual variability in lesion development, whereas those subjected to a high-fat diet develop atherosclerotic lesions specifically in the aortic root and innominate artery at approximately three months of age. Lesions extended to the thoracic aorta at six months and the abdominal aorta at nine months [66]. Moreover, plaques formed in LDL^{-/-} mice are representative only of the I–III phases, consisting predominantly of macrophage foam cells, while advanced lesions develop solely after prolonged exposure to a fat-enriched diet and do not progress beyond stage IV of the AHA-defined scale of human atherosclerosis [33,34,64]. Conversely, at 45–54 weeks of age in ApoE^{-/-} mice that are fed an atherogenic diet for a prolonged period of time (14 to 20 weeks), lesions classified as stage VI are observed, but only in the innominate artery [35,67], while they have never been documented in the aortic root or along the aortic tree [55,68].

In particular, lesions in the innominate artery may provide valuable insight because they more frequently exhibit complex features comparable to vulnerable plaques in humans, including an acellular necrotic core, erosion of the necrotic mass through to the lumen or intraplaque hemorrhage [35], and, although its small size provides some technical challenges, this site will likely become more popular with time. LDL^{-/-} mice have been found to be most suitable for studying the genetics of primary or secondary dyslipidemias, while ApoE^{-/-} mice have been established as the best murine model for characterizing the cytological and molecular aspects of stable and vulnerable plaques. Atherosclerotic plaques with visible defects of the fibrous cap and hemorrhage have been described in the innominate arteries of 37- to 59-week-old ApoE^{-/-} mice fed a high-fat diet for approximately two months [69] or in younger mice at eight to 16 weeks of age [70], but acute events have occurred rarely [71,72], or without sufficiently reliability, after prolonged feeding of a western diet (10 months) [70].

Some groups use the transgenic ApoE*Leiden mice, which are knock-in mice expressing the human apolipoprotein E3 isoform with low affinity for the LDL receptor. These mice are less hyperlipidemic than ApoE^{-/-} mice, spontaneously develop atherosclerosis when fed the atherogenic diet, and are suitable for exploring the mechanisms by which apolipoprotein E isoforms influence hepatic VLDL metabolism in atherosgenesis [73].

2.1.2. Murine Models of Vulnerable Atherosclerotic Plaques

The study of destabilized lesions appeared to be difficult and to require a long observation time in these murine models, thus stimulating the improvement of their efficiency and reproducibility regarding the salient features of spontaneous rupture of plaques in humans. Therefore, in the last decade, several strategies have been proposed in ApoE^{-/-} mice to generate models in which plaque rupture occurs in a reasonably short period of time that allows for the observation of the rupture of plaques and for testing diagnostic and therapeutic interventions. While a stable atheromatous plaque is most commonly covered with a fairly thick fibrous layer, protecting the lipid nucleus from contact with the blood, vulnerable plaques are characterized by a large lipid-rich core covered by a thin fibrous cap, with extensive macrophage infiltration, but very few SMCs [3,74]. These unstable plaques may undergo erosions, which is a loss of endothelium leading to thrombus formation [75] or rupture, defined as disruption of the fibrous cap accompanied by intrusion of erythrocytes into the lesion itself [67].

The first mouse models of destabilized plaques were mainly generated from the ApoE^{-/-} strain using microsurgical procedures, such as compressive injury using blunt forceps applied to atheromatous lesions in the abdominal aorta [76] or disruption of the fibrous cap in advanced plaques using a needle [77]. These experimental systems have primarily been a valuable model for studying

post-rupture thrombosis, but they have not provided a tool for investigating the spontaneous rupture of atherosclerotic plaques.

Further invasive approaches to develop unstable plaques were aimed at generating hemodynamic changes both in ApoE^{-/-} mice fed a high-fat diet, for example by placing a perivascular device [36,78] or introducing a tandem stenosis in the carotid arteries [38], and in ApoE^{-/-} mice fed a standard diet, using two different interventions (ligation plus cuff positioning) on common carotid arteries [79,80] or using ligation of external and internal carotid arteries and part of the renal artery to induce hypertension [81]. A model of cuff-induced thrombosis, produced by placing a silastic collar around the left common carotid artery in ApoE^{-/-} mice fed a normal chow, was used to evaluate the efficacy of intravenous administration of mononuclear cells, demonstrating the attenuation of the progression of atherosclerosis, reducing endothelial dysfunction, formation of thrombi, oxidative stress and apoptosis [82]. However, the induced biomechanical alterations might not reflect the pathogenesis of spontaneous plaque rupture in humans and could call into question the interpretations of the experimental results in these models [83,84]; additionally, the invasive nature of the procedures could represent a limitation for both ethical and practical reasons. The incidence of plaque rupture in ApoE^{-/-} mice with collar-induced lesions in carotid arteries was also increased by adenovirus-mediated over-expression of p53, a pro-apoptotic stimulus for intraleisional SMCs producing a cap thinning, combined with phenylephrine injection, a defined hemodynamic stimulus [85]. Nevertheless, the requirements for both survival surgery and carotid viral transfection may not be readily available for high-throughput experimental protocols in all laboratories.

Different biological approaches have also been described in the literature on the ApoE^{-/-} strain to generate mouse models reminiscent of human vulnerable plaques. Such interventions have included: alterations of transforming growth factor- β signaling, which produced thinning of fibrous caps, large lipid cores, intraplaque hemorrhage and disruption of the endothelium [86,87]; deletion or inhibition of Gas6, a platelet-response amplifier, which induced large intraplaque hemorrhages in the absence of fibrous cap fissuring [88,89]; and a null mutation for high-density lipoprotein receptor SR-BI, resulting in severe occlusive coronary atherosclerotic lesions leading to myocardial infarctions [90]. Gough et al. [91] induced molecular weakening of the fibrous cap by transfection of ApoE^{-/-} mice with hematopoietic stem cells over-expressing matrix metalloproteinase (MMP) 9. Fundamentally, degradation of collagen reduces the strength of the fibrous cap and, therefore, enhances the risk of its rupture. Another study combined collar placement on the carotid artery and short-term lipopolysaccharide (LPS) administration together with phenylephrine treatment and cold [92]. LPS leads to an increase in Th17 cells, which, through IL17, induces apoptosis of SMCs, potentially decreasing collagen content in the plaque, while phenylephrine, a vasoconstrictor, leads to increased blood pressure. Also, in these models, the complex experimental methods and specialized expertise required to induce plaque rupture may represent a limitation for their extensive use.

Recent evidence both in humans and mouse models [93] has indicated that angiotensin II (Ang II) plays a pivotal role in atherogenesis. The pro-atherosclerotic actions of Ang II are mediated by the AT1 receptor, which is expressed in a variety of organs, blood vessels, and bone marrow-derived cells, such as macrophages and T cells [94,95]. Therefore, subcutaneous and chronic infusion of Ang II has recently emerged as a practical and reproducible stimulus to spontaneously induce the development of vulnerable plaques in ApoE^{-/-} mice, both in the aorta and in its branches, especially the innominate artery [96–99], even after discontinuation [37]. Ang II likely promotes the destabilization of plaques through multifactorial mechanisms, including hypertension, chemotaxis of monocytes, activation of macrophages, altered sympathetic regulation of vascular tone, altered secretion of aldosterone and prostaglandin, generation of reactive oxygen species and over-expression of monocyte chemoattractant protein-1 (MCP-1) in vascular SMCs. Overall, these events are responsible for intraleisional neovascularization, hemorrhages, inflammation and remodeling of plaque [100,101]. Occlusive vascular events are not described in this model, most likely due to differences in clotting mechanisms between mice and humans, but, in reality, not all thrombotic events lead to clinically

relevant occlusive events, and thus the model lends itself easily to the study of the process of plaque destabilization in various stages of evolution. Ang II infusion may be implemented in mice through the use of different models of osmotic pumps, subcutaneously implanted, which provide a constant release of Ang II over time and differ in dosage and duration of treatment. Several protocols are described in the literature, and the most accredited involves the administration of Ang II at a dose of 0.7 mg/kg/day for four to eight weeks, four weeks from the start of the high-fat diet at eight weeks of age [97].

Diabetes is well recognized as a prevalent risk factor for atherosclerosis, and cardiovascular incidents as a consequence of plaque rupture are significantly increased in diabetic patients [102,103]. Diabetes triggers endothelial cell dysfunction and lipid abnormalities, promoting the expression of adhesion molecules, chemokines and other proinflammatory mediators. Moreover, atherosclerotic plaques in diabetics exhibit reduced collagen synthesis and increased breakdown of collagen, which predispose these patients to plaque rupture and a higher risk of thrombus formation [104]. In fact, hyperglycemia leads to the formation of oxidized glycated LDLs, which in turn induce vascular SMC apoptosis and reduced collagen content within plaques and may enhance thrombogenesis by activating platelets and reducing the production of endogenous platelet inhibitors [105].

This evidence has highlighted the importance of studying the mechanistic link between diabetes and atherosclerosis. In the past decade, several diabetic atherosclerosis mouse models have been established, and, despite their limitations, they currently have a leading role for these purposes. Convenient models are nontransgenic or transgenic mice. One of the first mouse models of diabetic atherosclerosis was the diet-induced obese (DIO) C57Bl/6J mouse, but only 40% of these mice developed small lipid deposits in the aortic sinus after 14 weeks of a diabetogenic diet (DD, 35.5% energy from fat); therefore, this appeared to be a poor model for the study of atherosclerotic complications in diabetes [106]. The genetically modified mouse models ApoE^{-/-} (King 2010; Canizzo 2012) [107,108] and LDL^{-/-} [109,110] also failed as pure diet-induced diabetic atherosclerosis models, because they have exhibited inconsistent effects on blood glucose or insulin levels or on the development of insulin resistance, and the variable increment of plaques would mainly be related to hyperlipidemia rather than to alterations in glucose metabolism.

The most common mouse models that closely resemble human diabetic atherosclerosis have been produced using two different approaches, alternative or complementary to the manipulation of diet: chemical toxins or additional genetic manipulation in dyslipidemic atherosclerosis-prone strains. Streptozotocin (STZ) is a toxic glucose analogue that accumulates in pancreatic β -cells and causes cell death leading to type 1 diabetes (T1D) with hyperglycemia. Induction of diabetes with STZ has been performed in different atherosclerosis models, and especially in ApoE^{-/-} mice [111]. Diabetic ApoE^{-/-} mice exhibited a significant increase in plaque area at the level of the aortic arch and the proximal aorta compared to controls [112–114], but it is difficult to discriminate whether the accelerated atherosclerosis is due to hyperglycemia or dyslipidemia. However, deranged carbohydrate and lipid metabolism is a common feature in human diabetic patients, thus highlighting the relevance of such available murine models.

Interestingly, Veerman et al. [115] found that STZ-induced hyperglycemia in ApoE^{-/-} mice was associated with low density of the vasa vasorum and under-expression of VEGF-R2. The use of STZ has the advantage of a standardized protocol, onset and development of diabetes, but does not fully replicate T1D as it usually does not induce ketosis and does not necessitate insulin therapy. Moreover, although it has been reported that diabetes accelerates atherosclerosis in these mouse models, a potential problem with STZ treatment is the toxic effect in many organs. The issue of high plasmatic levels of lipids in the widely used models of atherosclerosis has been overcome by crossing mice expressing human aldose reductase (hAR) with LDLR^{-/-}. In fact, hAR-LDLR mice are a model of accelerated atherosclerosis that does not exhibit hyperlipidemia [116]. This mouse model has confirmed that AR expression influences atherosclerosis development and that hyperglycemia alone, in conjunction with a particular genetic background, may accelerate the progression of this disease.

Recently, genetically modified models of diabetic atherosclerosis have been developed using Ins2AKITA (or Akita) mice on ApoE^{-/-} or LDLR^{-/-} backgrounds. Akita mice have a mutation in the insulin 2 gene (Cys96Tyr), leading to a misfolding of the proinsulin 2 protein, beta cell apoptosis, and T1D. Akita mice crossbred to ApoE^{-/-} [117] and LDLR^{-/-} [118,119] have a three-fold increase in non-HDL cholesterol and triglyceride levels and an accumulation of inflammatory cells in plaques. Wang et al. [120] induced T1D with STZ in ApoE^{-/-}/LDL^{-/-} mice fed a WTD and found that they displayed a more unstable phenotype of atherosclerotic plaques than nondiabetic controls fed a normal diet. They also found that the amelioration of insulin resistance through the silencing of Tribbles homolog 3 (TRIB3), an inhibitor of the Akt phosphorylation proatherogenic pathway, was able to improve plaque stability. Wu et al. [121] crossed ApoE^{-/-} mice with db/db mice to generate a type 2 diabetic (T2D) atherosclerosis model. ApoE^{-/-}/db/db mice exhibited significantly accelerated atherosclerosis in the aorta, and Wendt et al. [122] found that ApoE^{-/-}/db/db mice display enhanced expression of VCAM-1 and MMP-9 in the aorta.

Arterial calcification has emerged as a significant marker of advanced atherosclerosis, and calcium score is a well-established clinical predictor of cardiovascular risk [123,124]. However, the link between intimal calcification and plaque vulnerability is still controversial, and several factors such as morphology, size and location, in relation to the amount of calcium deposits, may affect lesion stability [125]. It is reported that large calcifications, easily detected with coronary computed tomography, do not appear to increase plaque vulnerability [126], whereas small calcifications within the fibrous cap can lead to biomechanical stress that can cause plaque rupture. Therefore, microcalcifications are recognized to play a role in destabilizing atherosclerotic plaques [127,128], and murine models of atherosclerotic calcification have been developed to better understand its pathological role and to test the effects of new therapies on this prognostic factor.

Several inbred mouse strains, including C57BL/6, Balb/C, C3H/HeJ, DBA/2J, and SM/J, develop spontaneous artery wall calcification with different occurrence, particularly when fed a high-fat/high-cholesterol diet [129,130], indicating genetic regulation of this phenomenon. Vascular calcification occurs spontaneously in genetically modified ApoE^{-/-} mice, which were shown to have marked cartilaginous metaplasia in the brachiocephalic artery [35,131], and is accentuated by osteopontin deficiency [132,133]. Debernardi et al. [134] investigated the presence of microcalcifications in mechanical-induced atherosclerotic lesions of the carotid artery in ApoE^{-/-} mice, and they proposed the use of this mouse model to investigate the pathophysiological significance of accumulation of elements such as calcium, iron and zinc during the atherosclerotic process. Moreover, Towler et al. [135] demonstrated that vascular calcification occurs in response to a high-fat, diabetogenic diet in LDL^{-/-} mice.

Unraveling the mechanisms underlying cardiovascular calcification may be an important step towards future strategies. Interestingly, research has demonstrated that dyslipidemia and inflammation may link reduced bone mineral density and vascular calcification: it has been reported that patients with low bone density have more pronounced atherosclerotic plaque calcification [136,137], and different preclinical studies have suggested that hyperlipidemia promotes both arterial calcification and bone loss in the ApoE^{-/-} model [138–140]. Very recently, Li et al. [141] tested the effects of simvastatin treatment in the ApoE^{-/-} model and showed a significant reduction of microcalcification in atherosclerotic plaques.

A recent model has investigated the effect of impaired fibrillin-1 function on atherosclerosis in ApoE^{-/-}/C1039G^{+/+} double-knockout mice on a western-type diet. Mice with a heterozygous mutation in the fibrillin-1 gene (Fbn1C1039G^{+/+}) develop fragmentation of the elastic fibers and were crossbred with ApoE^{-/-} mice to generate reduced levels of elastin in their vessel walls and, consequently, stiffer vessels [142]. The loss of elastin would result in exposure of the fibrous cap of the atherosclerotic plaques to increased biomechanical stress. Indeed, after 10–20 weeks of high-fat diet, these mice developed larger plaques with features of vulnerability, such as a decrease in collagen content, increased apoptosis of SMCs, large necrotic cores, an increase in macrophage infiltration, and numerous buried caps, not only at the level of the aortic valves but also in the brachiocephalic artery and in different tracts of the aorta. Furthermore, after being fed a western-type diet for up

to 35 weeks, a large number of the mice showed coronary plaques fissured with thrombi [42], and spontaneous acute plaque disruption was reported [143] and described in a large percentage of the mice in combination with symptoms of myocardial infarction, stroke or sudden death [42,142,144] (as shown in Figure 2).

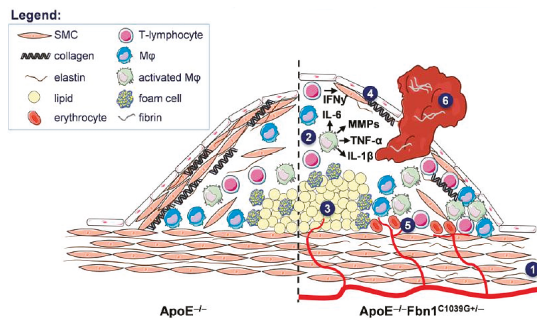


Figure 2. Mechanisms leading to the formation of vulnerable plaques, plaque rupture, myocardial infarction, stroke, and sudden death in $\text{ApoE}^{-/-}\text{Fbn1C1039G}^{+/-}$ mice. In $\text{ApoE}^{-/-}\text{Fbn1C1039G}^{+/-}$ mice, elastin fragmentation (1) and arterial stiffness lead to the development of large plaques with a highly unstable phenotype, characterized by enhanced inflammation (2), large necrotic cores (NC) (3) and a thin fibrous cap (FC) (4). Additionally, in the brachiocephalic and carotid arteries intraplaque neovascularization and hemorrhage (IPH) are abundantly present (5). Due to the elevated pulse pressure and extensive aortic dilatation (especially in the ascending aorta), the mechanical stress on plaques is increased, leading to rupture and subsequent thrombus formation (6). Plaque rupture with thrombosis as well as hypoperfusion of the heart and brain most likely result in myocardial infarction, stroke, and eventually sudden death. (Reprinted from Reference [42]. Copyright with permission from © 2014, Oxford University Press on behalf of the European Society of Cardiology.)

The level of macrophage infiltration was highlighted as one indicator of plaque vulnerability in the $\text{ApoE}^{-/-}\text{C1039G}^{+/-}$ mouse model and was quantified *in vivo* by gold nanoparticle-enhanced microCT at the level of the common, external, and internal carotid arteries, demonstrating a more rapid development and a larger extent of plaques in the $\text{ApoE}^{-/-}\text{C1039G}^{+/-}$ mice compared to the $\text{ApoE}^{-/-}$ mice [43]. Very recently, a new mouse model was introduced with an inducible adenovirus-mediated gain-of-function mutation, D374Y, in the proprotein convertase subtilisin/kexin type 9 (PCSK9) gene, which is another important factor that regulates lipid homeostasis like the ApoE and LDL proteins [145]. This PCSK9^{DY} mutation in $\text{ApoE}^{-/-}$ mice mimics a genetic condition of hypercholesterolemia in patients, and it showed a synergistic effect in combination with ApoE deficiency, resulting in a strong increase in serum low-density lipoprotein, accelerated plaque growth and doubling of lesion size compared to wild-type $\text{ApoE}^{-/-}$ mice. Therefore, intravenous administration of an adenoviral vector for stable transfection of the PCSK9^{DY} mutated gene in $\text{ApoE}^{-/-}$ mice has been described as a promising approach to study the development of advanced atherosclerotic plaques related to the interaction of different genetic mutations, without time-consuming backcrosses, and further long-term studies to well characterize this model are expected to be published [146].

Finally, as not the least-relevant aspect, it is known that although some features of plaque instability have been reproduced in genetically modified mouse models, atherothrombosis induction is difficult. In a recent work by Liu et al. [147], murine prothrombin was over-expressed via adenovirus-mediated gene transfer in an $\text{ApoE}^{-/-}$ mouse model of plaque destabilization [148]. This approach produces features of plaques that are found in human coronary arteries including fibrous cap disruption, plaque hemorrhage and luminal thrombosis in 70% of the animals, suggesting that blood coagulation is critical to consistently reproduce atherothrombosis in the mouse model.

The major mouse models of atherosclerosis are briefly summarized in Table 1.

Table 1. Summary of major mouse models of atherosclerosis with features of vulnerability (highlighted in blue).

Model	Mouse Strain	Stage of Lesion Formed (I–VI)	Lesion Characteristics	Area of Lesion Characterization	Modified Diet Required	Commercial Availability of Strain
Diet-induced	C57Bl/6j	I	Predominantly lipid-laden foam cells	Aortic root, aorta	Yes	Jackson, Taconic, Charles River
Genetically modified	LDL ^{-/-} [64]	I–IV	Progression from predominantly lipid-laden foam cells to lesions with necrotic core and fibrous caps	Aortic root, aorta	Yes	Jackson
Genetically modified	ApoE ^{-/-} [56,57]	I–V	Progression from predominantly lipid-laden foam cells to lesions with necrotic core and fibrous caps	Aortic root, aorta; rare vulnerable plaques in innominate artery	No; fat diet accelerates atherosclerosis	Jackson
Genetically modified	ApoE ^{-/-} Fbn(C1039G) ^{+/+} [42]	I–VI	Development of vulnerable plaques prone to rupture (acute cardiovascular events (stroke, myocardial infarction))	Aortic root, aorta, innominate artery	No; fat diet accelerates atherosclerosis	Jackson for ApoE ^{-/-} and Fbn(C1039G) ^{+/+} breeders
Genetically modified	ApoE ^{3-Leiden} [73]	I–IV	Progression from predominantly lipid-laden foam cells to lesions with necrotic core and fibrous caps	Aortic root, aorta, common carotid arteries	No; fat diet accelerates atherosclerosis	Jackson
Collar-induced	ApoE ^{-/-}	I–VI	Development of vulnerable plaques for biomechanical alterations	Common carotid arteries	No; fat diet accelerates atherosclerosis	Jackson
Tandem stenosis	ApoE ^{-/-}	I–VI	Development of vulnerable plaques for biomechanical alterations	Common carotid arteries	No; fat diet accelerates atherosclerosis	Jackson
Collar + Ad-p53 + phenylephrine-induced	ApoE ^{-/-}	I–VI	Development of vulnerable plaques for SMCs and hypertension	Common carotid arteries	No; fat diet accelerates atherosclerosis	Jackson
Ligation plus cuff	ApoE ^{-/-}	I–VI	Development of vulnerable plaques for biomechanical alterations	Common carotid arteries	No; fat diet accelerates atherosclerosis	Jackson
Partial ligation of carotid and renal arteries	ApoE ^{-/-}	I–VI	Development of vulnerable plaques for biomechanical alterations and hypertension	Common carotid arteries, renal arteries	No; fat diet accelerates atherosclerosis	Jackson
Angiotensin II	ApoE ^{-/-}	I–VI	Development of vulnerable plaques with neovascularization, hemorrhages and inflammation	Aortic root, aorta, innominate artery	No; fat diet accelerates atherosclerosis	Jackson
Adenovirus-induced gene mutation	ApoE ^{-/-}	I–VI	FcSK9 ^{DP} mutation; prothrombin overexpression; fibrous cap disruption, hemorrhages and thrombosis	Aortic root, aorta, innominate artery	No; fat diet accelerates atherosclerosis	Jackson

2.2. Molecular Biomarkers of Atherosclerotic Plaques in Humans and Murine Models

The characterization of molecular markers expressed both in humans and in murine models is relevant to promote the translation of novel noninvasive diagnostic and therapeutic approaches for vulnerable plaques from preclinical research to the clinic (as shown in Figure 3) [149].

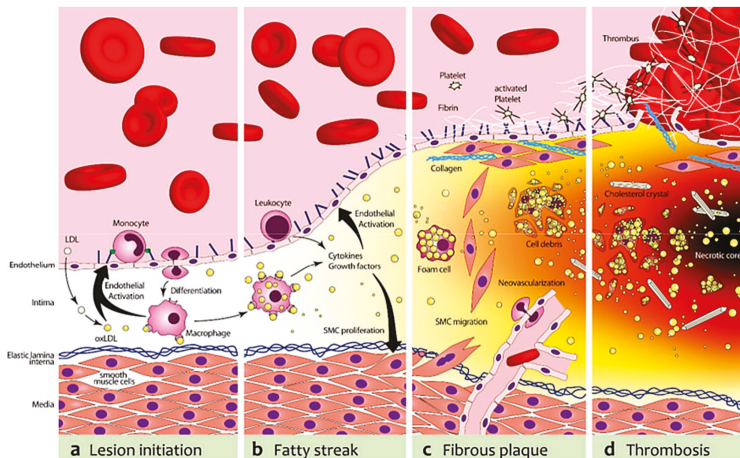


Figure 3. Schematic depiction of representative targets for molecular imaging of atherosclerosis and plaque vulnerability. (a) In the first stage, low-density lipoprotein cholesterol (LDL) is deposited in the endothelium and undergoes oxidative modification, resulting in oxidized LDL (oxLDL). OxLDL stimulates endothelial cells to express adhesion molecules (vascular cell adhesion molecule-1 (VCAM-1), P-Selectin and various chemokines, e.g., Monocyte Chemoattractant Protein-1 (MCP-1) and Interleukin 8 (IL-8)). This leads to a recruitment of monocytes, which transmigrate into the intima and differentiate to pro-atherogenic macrophages; (b) Macrophages harvest residual oxLDL via their scavenger receptors and add to the endothelial activation and, subsequently, leukocyte recruitment with the secretion of Tumor Necrosis Factor α (TNF- α) and IL-6; (c) The increasing plaque volume promotes neovascularization. Proliferating smooth muscle cells (SMCs) stabilize the nascent fibrous plaque. With deposition of fibrin and activated platelets on the dysfunctional endothelium that expresses tissue factor (TF) and von Willebrand factor (vWF), a pro-thrombotic milieu is formed; (d) Foam cells can undergo apoptosis and release cell-debris and lipids, which will result in the formation of a necrotic core. In addition, proteases secreted from foam cells can destabilize the plaque. This can lead to plaque rupture, in which the case of extracellular matrix molecules (e.g., collagens, elastin, TF, vWF) catalyze thrombotic events. (Reprinted from Reference [149]. Copyright with permission from © 2015, MDPI, Basel, Switzerland, Creative Commons Attribution License CC BY 4.0.)

Several works have mainly evaluated the major receptors expressed at the level of atherosclerotic plaques of ApoE $^{-/-}$ mice both ex vivo and in vivo. Therefore, we further summarize the current status of the knowledge of the main molecular factors identified in patients and in the murine models of atherosclerosis currently available, with a focus on the most promising imaging targets of key processes implicated in plaque destabilization.

2.2.1. Leukocyte Adhesion Receptors

Inflammation is recognized as a crucial factor for the development of atherosclerotic lesions and the progression of their vulnerability. In fact, macrophage-rich plaques appear to be more prone to rupture. Experimental evidence shows that in humans and animal models of atherosclerosis, one of the observed changes in the endothelium is an increased expression of leukocyte adhesion receptors, such

as P-selectin, E-selectin, VCAM-1, and ICAM-1 [150,151], which allow monocytes to roll and adhere to the artery wall and then enter the subendothelial space. Recently, the expression of several molecules of leukocyte adhesion in human atherosclerotic plaques, obtained from autopsies or from the hearts of patients undergoing heart transplantation, has been reviewed [152]. VCAM-1, which binds the very late antigen-4 (VLA 4) on the surface of leukocytes, was found to be expressed by activated endothelial cells, macrophages and SMCs even in the early stages of the atherogenic process, playing a major role in the recruitment of inflammatory cells. However, variable levels of VCAM-1 have been reported on the endothelium in human atherosclerotic lesions. Davies et al. [153] found that VCAM-1 appears focally on endothelial cells covering fibrous or lipid-rich plaques, on intraplaque neovessels, and on SMCs and macrophages. O'Brien et al. [154] identified significant expression of VCAM-1 on SMCs in atherosclerotic coronary plaques of humans, while its presence on the luminal endothelium was low in both lesions and control segments but was prevalent in association with the intimal neovasculature.

Despite the diversity of such data, George et al. [155] indicated that VCAM-1 is a very interesting diagnostic and therapeutic target because it is expressed only on activated endothelial cells that line the surface of atherosclerotic plaques, while it does not appear to be significantly expressed on the endothelium in non-affected areas. Furthermore, preclinical studies have shown that blocking or knocking out this receptor significantly inhibits macrophage recruitment and the formation of plaques. Mice with hyperglycemia exhibit increased VCAM-1 expression, and similar findings have been obtained in isolated human endothelial cells exposed to elevated glucose *in vitro* [156]. The over-expression of ICAM-1 has been demonstrated not only on the endothelium but also on SMCs and macrophages of human atherosclerotic plaques [153,157,158].

An increase in the levels of the adhesive molecules VCAM-1 and ICAM-1 at sites with atheromatous changes was also observed in ApoE^{-/-} mice. Nakashima et al. [159] characterized VCAM-1 on the endothelium of ApoE^{-/-} mice by immunohistochemistry, highlighting its early expression at the level of vascular sites susceptible to the development of plaques and at the periphery of the lesions in advanced stages. Few endothelial cells with a weakly positive VCAM-1 signal were instead shown in the control subjects. They also identified ICAM-1 on the endothelium at the same vascular sites, but without statistically significant differences compared to the controls [159]. In fact, the expression of ICAM-1 has been reported to be constitutively high in the endothelium of cardiac vessels of murine species [160]. In human atherosclerotic lesions, a marked expression of P-selectin has been demonstrated on the endothelium overlying active atherosclerotic plaques, but not on the normal arterial endothelium or covering fibrous plaques [161].

The role of P-selectin in the spontaneous development of advanced atherosclerosis was also evaluated in ApoE^{-/-} mice. P-selectin appears to be a key adhesion receptor mediating the recruitment of monocytes/macrophages into the lesions and promoting advanced atherosclerosis in ApoE^{-/-} mice, with earlier and more advanced lesions in mice lacking ApoE alone in comparison with double-knockout ApoE/P-selectin mice [162]. In accordance with this, Ramos et al. [163] demonstrated that anti-P-selectin antibodies inhibit monocytes rolling on the endothelium of carotid arteries isolated from ApoE^{-/-} mice. Furthermore, some studies have highlighted that advanced atherosclerotic lesions are actively promoted in ApoE^{-/-} mice not only by endothelial P-selectin but also by platelet P-selectin [164,165]. In humans, the expression of E-selectin is limited to endothelial cells on the surface of fibrous and lipid-rich plaques [153], whereas in the aortas of normal chow-fed ApoE^{-/-} mice, E-selectin was not expressed on endothelial cells in regions predisposed to atherosclerosis or in early and advanced plaques.

2.2.2. Indicators of Macrophage Infiltration

A large number of macrophages in atherosclerotic lesions is an indicator of a more unstable and rupture-prone phenotype [166,167]. In fact, these cells accumulate in plaques and phagocytize lipids, turning into foam cells, and release cytokines and growth factors, as well as metalloproteinases and reactive oxygen species that degrade the structures of plaques [168]. Therefore, the quantification of

macrophages is a potential target for the identification of vulnerable plaques. Xu et al. [169] demonstrated the expression of Toll-like receptor 4 (TLR-4) in the aortic atherosclerotic lesions of ApoE^{-/-} mice and in human coronary artery autopsy specimens by immunohistochemistry. Activated macrophages also express the receptor for folate (FR β). Ayala-Lopez et al. [170] demonstrated high FR β expression on macrophages in aortic atherosclerotic lesions of ApoE^{-/-} mice both in vivo using nuclear medicine imaging and ex vivo using immunohistochemistry, while Müller et al. [171] showed increased FR β expression in human specimens obtained from carotid endarterectomy, which co-localized with the macrophage activation marker “Cluster of Differentiation 68” (CD68).

2.2.3. Indicators of Angiogenesis

Histological examination of atherosclerotic plaques reveals a rich neovascularization. The microvessels most likely form in response to over-expressed angiogenic factors, including VEGF. Angiogenesis in plaques may favor their growth, a phenotype that is friable and prone to rupture and that leads to hemorrhages and thrombosis.

The expression of VEGF and its receptors (VEGFRs) by endothelial cells, macrophages and other cell types has been implicated in the development of atherosclerosis and vulnerable plaques, particularly in association with diabetes, both in humans [172–176] and in animal models [177,178]. An association between neovascularization and atherosclerosis has been confirmed by several studies, showing a correlation between the extent of atherosclerosis and plaque neovascularization in human pathological samples [179–182]. Enhanced VEGF/VEGFR signaling plays an important role in three critical processes leading to plaque vulnerability: stimulation of angiogenesis in plaques, recruitment of monocytes into plaques, and increasing permeability of plaque vasculature which leads to hemorrhage and inflammatory cell extravasation [174,175].

The strongest experimental evidence that angiogenesis plays a pathogenetic role in atherosclerosis was derived from studies in the ApoE^{-/-} mouse model. Moulton et al. [183,184] provided the first confirmation that the process of angiogenesis is involved in the progression of atherosclerosis, showing that neovascularization is seen in advanced atheromas of ApoE^{-/-} mice and that their development may be significantly reduced by specific endothelial inhibitors. However, the incidence of lesions with intimal vessels reported by Moulton et al. [183,184] in this mouse model was relatively low (13%); therefore, subsequent studies were performed in ApoE^{-/-} mice with streptozotocin-induced diabetes. Immunohistochemistry showed a significant increase of VEGFRs in aortic plaques, as well as the co-localization of VEGFR-1 primarily with the macrophage marker Mac3 and VEGFR-2 with the endothelial cell marker FVIII, highlighting their potential use in novel molecular imaging strategies [185]. Another potential marker for the targeting of angiogenesis in atherosclerotic lesions is $\alpha_v\beta_3$ integrin, a cell surface glycoprotein receptor that is highly expressed by macrophages, medial and some intimal SMCs, and endothelial cells [186–188]. Expression of $\alpha_v\beta_3$ integrin is found in the shoulder of advanced plaques and in the necrotic core of human atherosclerotic lesions [189]. Moreover, for in vivo imaging purposes, integrin $\alpha_v\beta_3$ is the most extensively examined marker of angiogenesis [190,191].

2.2.4. Other Potential Molecular Targets

Vulnerable plaques are characterized by the presence of apoptotic cell death and induction of atherothrombosis [5]. In advanced lesions, apoptosis of macrophages promotes thinning of the fibrous cap and the development of the necrotic core, a key factor in rendering plaques vulnerable to disruption and in the formation of luminal thrombi [192,193]. During apoptosis, phosphatidylserine (PS) is externalized on the cell membrane [194,195] and is recognized by the 35 kDa plasma protein Annexin V (A5) [196]. Therefore, A5 has been effectively used for various molecular imaging strategies in preclinical atherosclerosis models including ApoE^{-/-} mice [185,197,198], as well as in human cardiovascular disease [199,200]. The fibrous cap separates platelets and prothrombotic materials in the plaque. Rupture of this barrier leads to the exposure of a variety of intraplaque constituents to the

circulation, initiating atherothrombosis which may cause stroke or myocardial infarction. Therefore, thrombus formation is an important aspect in the instability of atherosclerotic lesions, and molecules present on activated platelets such as glycoprotein IIb/IIIa [201] or the specific collagen receptor glycoprotein VI (GPVI) [202], selective targets of fibrins [203,204], clotting factors or components of the exposed subendothelial matrix [205,206] can represent an interesting strategy for assessing their vulnerability, also using various molecular imaging techniques.

2.3. Emerging Applications for Molecular Imaging in Murine Models of Atherosclerosis

Atherosclerosis is a complex phenomenon that involves endothelial dysfunction, LDL accumulation and inflammation [82,150,151,170,183]. Moreover, it is a multigenic disease and patterns may vary in lesions from different persons and at different sites of the arterial tree, suggesting genetic differences in susceptibility as well as in response to therapy. Molecular imaging has greatly increased the possibility to visualize complex biochemical phenomena underlying atherosclerosis, using highly specialized instruments in combination with targeted imaging agents. Non-invasive imaging approaches for the detection of atherosclerotic plaques that are prone to rupture would have a significant clinical impact for diagnostic and therapeutic purposes. Animal models of plaque rupture are essential for testing new imaging modalities to enable the diagnosis of the patient at risk and the design of new preventive treatments. The advances of preclinical imaging and of nanotechnologies have provided new tools to study molecular structures, cellular behaviors, and metabolic pathways that underlie atherosclerosis. In particular, the development of a wide range of imaging contrast agents, functionalized with targeting ligands such as antibodies, peptides or aptamers, could be promising for probing the molecular biomarkers of the atherosclerotic processes, promoting the translational potential of novel technologies.

Molecular imaging relies on diverse imaging techniques, which include contrast-enhanced ultrasound (CEUS), magnetic resonance imaging (MRI), positron emission tomography (PET), single-photon emission computed tomography (SPECT), X-ray computed tomography (CT), fluorescent molecular tomography (FMT) and photoacoustic imaging (PAI). Each modality presents advantages and weaknesses; therefore, multimodality imaging approaches are desirable both in preclinical research and for human applications. Importantly, longitudinal imaging studies allow for the improvement of the accuracy of the experimental results and reduce the number of animals required for experimentation, according to the 3Rs principles (Replacement, Reduction and Refinement). Table 2 compares the main characteristics, advantages and limitations of different imaging modalities with respect to atherosclerosis mouse models. A growing range of potential imaging targets have been investigated in genetically engineered mouse models, mainly ApoE^{-/-} mice, while there are few imaging studies to date that use the ApoE^{-/-}C1039G^{+/+} model. In the following paragraphs of this review, the published literature on the molecular imaging of advanced atherosclerosis in murine models and its future directions will be summarized, emphasizing those strategies that provide new insight into the identification of vulnerable plaques and that have the greatest potential for clinical applications.

Table 3 describes the major targets for molecular imaging of atherosclerosis that have recently been evaluated in mouse models of vulnerable plaques, including the biological processes investigated, imaging modalities, and contrast agents used.

Table 2. Noninvasive molecular imaging in mouse models of vulnerable atherosclerotic plaques.

Imaging Modality	Spatial Resolution	Sensitivity (nmol/L)	Contrast Agent	Probe Concentration	Advantages	Limits
Ultrasound	50–500 μm	Not well characterized yet	Microbubbles	μM to nM	Real-time Low cost High temporal resolution (0.1–100 s) No ionizing radiation	Operator-dependent
Magnetic Resonance	10–100 μm	10^{-3} – 10^{-5}	Gadolinium-based contrast agents Iron oxide and other superparamagnetic nanoparticles (USPIO, SPIO)	μM to nM	High tissue contrast and functional parameters No ionizing radiation	High cost Operator-dependent
Nuclear imaging	PET 1–2 mm SPECT 0.5–2 mm	10^{-11} – 10^{-12} 10^{-10} – 10^{-11}	Position or gamma ray emitting radionuclides (^{18}F , ^{64}Cu , ^{99m}Tc tracers)	pM	Molecular and functional parameters High sensitivity	Ionizing radiation Limited spatial resolution (mm) High–medium cost
X-ray computed tomography	30–400 μm	10^{-2} – 10^{-3}	Iodinated particles Gold nanorods	μM to nM	Fast acquisition time Provides molecular and structural information	Ionizing radiation Low soft tissue contrast resolution Medium cost
Fluorescence tomographic imaging	1–2 mm	10^{-10} – 10^{-11}	NIR Fluorophores	nM to pM	High sensitivity No ionizing radiation Low cost	Limited depth of penetration (1–20 mm) Limited spatial resolution (mm)
Photoacoustic imaging	<100 μm	< 10^{-12}	NIR Fluorophores	nM to pM	High sensitivity No ionizing radiation High depth of penetration (>5 cm) Low cost	Data post-processing and acquisition procedures still being optimized

Table 3. Summary of the major targets for molecular imaging of atherosclerosis recently evaluated in mouse models with features of vulnerability.

Molecular Target	Biological Events	Imaging Techniques	Imaging Probes
VCAM1-R, ICAM1-R; P-selectin	Vascular inflammation	UBM, MRI, PET, SPECT, PAI	Targeted microbubbles, targeted USPIO, ¹⁸ F-, ^{99m} Tc-labeled VCAM1 antibodies, NIR Fluorophores
Phosphatidylserine	Apoptosis, vulnerable plaque, atherothrombosis	MRI, SPECT, FMT	Targeted USPIO, ^{99m} Tc-labeled annexin 5 or other tracers, NIR dyes conjugated with annexin 5
$\alpha_v\beta_3$	Neoangiogenesis	MRI, PET, FMT	Gadolinium-labeled RGD probes, ¹⁸ F-labeled RGD or other tracers, NIR dyes conjugated with RGD or other probes
GPVI-R	Platelet adhesion, atherothrombosis	UBM, PET	Targeted microbubbles, ⁶⁴ Cu-labeled GPVI fragment
GP IIb/IIIa-R	Platelet adhesion, atherothrombosis	UBM	Targeted microbubbles
Fibrin-fibronectin complex	Atherothrombosis	MRI, SPECT	Gadolinium-labeled CLT1 peptide or other agents, ^{99m} Tc-labeled antibodies
Von Willebrand factor	Atherothrombosis	MRI, SPECT	Targeted microbubbles,
LOX-1	Macrophagic lipid uptake	MRI, SPECT	Targeted USPIO, ^{99m} Tc-labeled antibodies
TSPO	Activated macrophages	SPECT	[¹²⁵ I]iodo-DPA-713
Cathepsins and metalloproteinases	Macrophagic proteinases activity	FMT	NIR dyes
Macrophages infiltration	Macrophage-rich, rupture-prone plaques	CT, MRI, PET, FMT, PAI	Liposomal-iodine formulations, PEGylated gold nanoparticles, gold-coated iron oxide nanoparticles targeted for CD163 receptor antibody, trimodality ⁶⁴ Cu-iron oxide-NIR dye nanoparticle targeted for CD68, ¹⁸ F-LyP-1 targeted for p32, NIR Fluorophores

2.3.1. Contrast-Enhanced Ultrasound Imaging

Contrast-enhanced ultrasound (CEUS) is an increasingly used molecular imaging modality for the phenotypic analysis of the cardiovascular system in mouse models. In particular, ultrasound characterization of atherosclerotic plaques may be improved using contrast agents producing intense acoustic reflection and enhancing the reflection signal-to-noise ratio for blood because of their size (equal in size or smaller than red blood cells). The ultrasound contrast agents are gas-filled microbubbles, typically ranging from 1 to 5 μm in diameter, encapsulated with protein, lipid or bio-compatible polymers. Microbubbles (MB) conjugated, directly or through an avidin/streptavidin biotinylation method, with targeting ligands such as antibodies, peptides or aptamers can be used to target specific biomarkers on the endothelium or activated platelets. They are strictly intravascular agents. They act as blood pool agents and can be targeted towards endothelial cell receptors, blood cell markers or blood proteins. When acoustic waves encounter microbubbles, they alternately exert their compression with positive pressure and expansion with negative pressure. When the transmitted acoustic pressure increases, the microbubbles are compressed in a different manner, and then they expand. As a result, an asymmetric oscillation of microbubbles occurs, called “non-linear oscillation.” In non-linear oscillation, the microbubbles, instead of producing sinusoidal echoes with a frequency spectrum similar to that of the incident ultrasounds, produce, differently from the tissues, asymmetric echoes. This asymmetry produces harmonics that are utilized to differentiate the ultrasound signal from the contrast agent from that coming from the tissue. The CEUS technique cancels the linear ultrasounds from tissues and utilizes the non-linear ones from the microbubbles to form images (as shown in Figure 4) [207,208].

Moreover, microbubbles can be destroyed by an ultrasonic pulse, confirming the specificity of binding and enabling localized drug delivery for therapeutic purposes [209,210].

Contrast-enhanced ultrasound offers significant advantages, such as high spatial resolution, high sensitivity and the lack of ionizing radiation; from a perspective of clinical translation, the portability and speed of the imaging acquisition ensure that this technique is well-suited to its potential application for screening large populations and making timely diagnoses. As a limitation, the current targeted microbubble agents can only be directed against intravascular endothelial or blood cell events, reducing the potential molecular targets. Moreover, microbubbles need a critical threshold amount of molecular expression to begin to see attachment [211].

Targeted contrast-enhanced ultrasonography has been shown to be a promising noninvasive imaging technique for evaluating the degree of atherosclerosis in mice [212–214] and may potentially be translated to clinical imaging in the future [215,216]. A number of specific targeted ultrasound probes has been tested *in vivo* for assessing biomarkers such as VCAM-1 [217–219], P-selectin [220] and von Willebrand factor [221,222] in genetically modified mouse models of atherosclerosis (as shown in Figure 5).

A thinning of the fibrous cap can ultimately induce plaque rupture and expose the core of the lesion to circulating coagulation factors. This critical event can trigger obstructive thrombosis that can cause clinical events. Molecular imaging that targets activated platelets or different steps of the coagulation cascade could be an interesting tool to detect the subocclusive thrombi and intraplaque hemorrhages that characterize vulnerable plaques. Microbubbles have been conjugated with the recombinant fusion soluble glycoprotein (GP) VI, which binds with high affinity to atherosclerotic lesions in ApoE^{-/-} mice. GPVI is a platelet-specific collagen receptor that favors platelet adhesion, activation and secretion, regulating mechanisms of ateroproliferation and atherothrombosis. The GPVI receptor has high affinity for collagen within atherosclerotic plaques. The soluble GPVI receptor competes for collagen binding sites with the surface-associated platelet GPVI receptor and thereby inhibits platelet adhesion onto collagen *in vitro* and *in vivo* [223,224]. Molecular imaging signals of GPVI-targeted microbubbles were substantially enhanced in the aortic arch and in the truncus brachiocephalicus in ApoE^{-/-} compared to wild-type mice. Moreover, high-frequency ultrasound (HFU)-guided disruption of GPVI-targeted microbubbles accumulated in the atherosclerotic lesions may interfere with ateroproliferation and may be an innovative therapeutic approach to prevent progression of atherosclerotic disease [202].

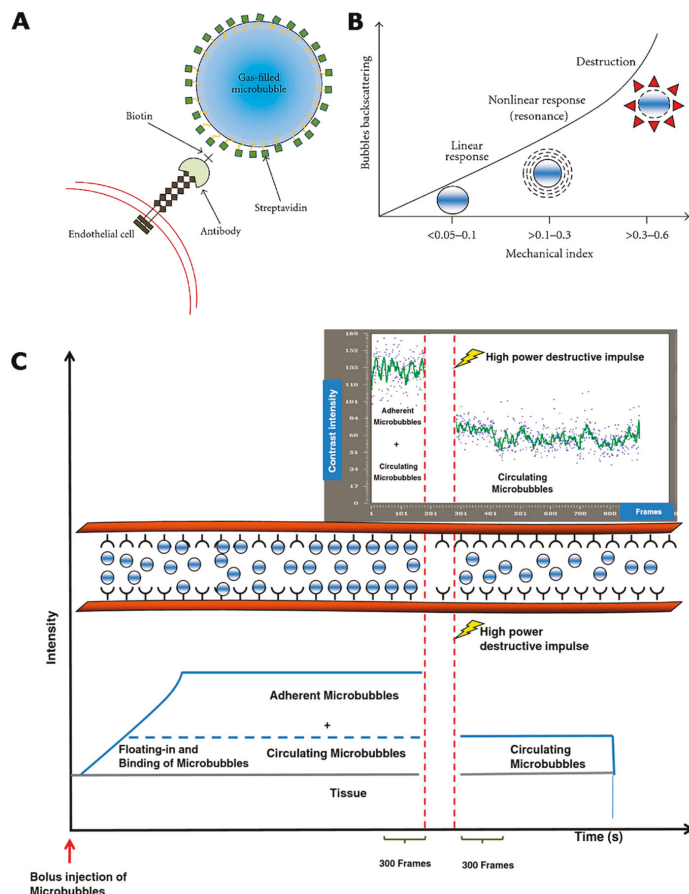


Figure 4. Molecularly targeted microbubbles. (A) Selective binding to sites of molecular expression on the endothelium: streptavidine is used for attachment of biotinylated ligands onto the shell of ultrasound contrast microbubbles; (B) At very low acoustic power, microbubbles oscillate in relatively symmetrical order, backscattering at the same frequency of incident ultrasound. At a slightly higher mechanical index, microbubbles oscillate in a nonlinear manner (nonlinear response), backscattering a variety of frequencies (harmonic). Higher acoustic pressures destroy the microbubbles with a high-intensity backscatter response; (C) Time course analysis of signal intensity before and after high-power destructive pulse and diagram representation of destructive methodology. After intravenous administration, targeted microbubbles can bind to specific antigens expressed on endothelial cells of tumor vessels (orange), whereas others remain in the vessel lumen, freely circulating. After a high-power destructive pulse (red dotted lines), both bound and circulating microbubbles are destroyed, following circulating microbubbles that arrive from outside of the scan plane, which remain freely circulating for several seconds. Contrast intensity is the sum of the intensity from the tissue, intensity from the circulating microbubbles and intensity from the microbubbles bound to receptors on endothelial cells. After digital subtraction of the video intensity calculated on 300 predestruction frames from video intensity calculated on 300 postdestruction frames, the resulting video intensity is due only to bound microbubbles. (Reprinted from Reference [207]. Copyright with permission from © 2012, Hindawi Publishing Corporation, Creative Commons Attribution License CC BY 3.0; and from Reference [208], Copyright with permission from © 2013, BioMed Central, Creative Commons Attribution License CC BY 4.0.)

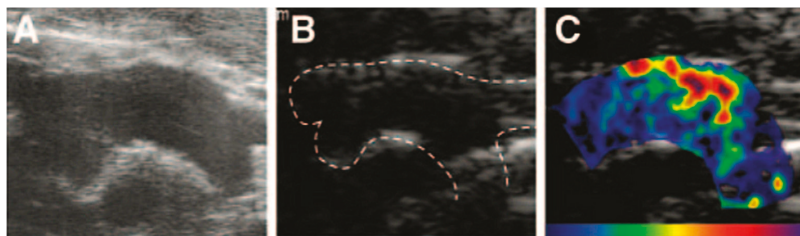


Figure 5. Illustration of spatial matching between morphology and targeted signal enhancement. (A) High-frequency ultrasound (40 MHz) image at the level of the aortic arch in a 10-week-old DKO animal; (B) Lower frequency multipulse contrast-specific imaging of the aorta at baseline, with the aorta defined by dashed lines, before contrast administration and (C) 10 min after administration of P-selectin-targeted microbubbles after background subtraction and color-coding (color scale at bottom). (Reprinted from Reference [220]. Copyright with permission from © 2010, Wolters Kluwer Health.)

The glycoprotein (GP) IIb/IIIa complex, also known as $\alpha\text{IIb}\beta_3$ integrin, is the major receptor expressed on the surface of activated platelets and is essential for their interactions with other activated platelets and adjacent cells in atherothrombosis [225–227]. Thus, the GP IIb/IIIa receptor is a potential marker for imaging aggregated platelets in atherosclerotic plaques. Peptides containing the Arg-Gly-Asp (RGD) sequence are highly adhesive for GP IIb/IIIa. Cyclic (c) RGD has 30-fold greater affinity for the GP IIb/IIIa complex than the linear form, which is particularly advantageous for binding under the conditions of rapid blood flow that occur in atherosclerotic arteries. A cRGD-modified MB (MB-cRGD) has recently been developed that is capable of binding to GP IIb/IIIa on activated platelets and thrombi in large arteries. It is used to examine whether GP IIb/IIIa receptors on activated platelets that are adhered and aggregated on the endothelium can serve as biomarkers of atherosclerotic plaque instability, and whether they can be identified and quantified by contrast-enhanced ultrasound using cRGD-targeted microbubbles [201].

2.3.2. Contrast-Enhanced Magnetic Resonance Imaging

Contrast-enhanced MRI is a noninvasive imaging modality for characterizing the composition of atherosclerotic plaques at the molecular level, with high spatial resolution, average sensitivity and non-ionizing radiation. Innovative MRI contrast agents seem promising for discriminating between stable and unstable lesions, due to their labeling with a molecular moiety that targets pathological over-expressed hallmarks. Targeted MRI imaging probes are mostly gadolinium compounds of small molecular weight, as well as iron oxide nanoparticles. In particular, ultrasmall superparamagnetic iron oxide nanoparticles (USPIO, <60 nm) are currently widely used as contrast agents for molecular and cellular imaging, and they consist of an iron-oxide core and a shell of dextran or polymers. Gadolinium chelate (Gd-DTPA) contrast agents strongly enhance the signal profile of the atherosclerotic wall in T1-weighted sequences. Targeted probes conjugated with USPIO generally result in a marked loss of signal intensity in the atherosclerotic plaques of mouse models with a T2-weighted, rapid-acquisition, relaxation-enhanced (RARE) imaging protocol, or in a positive contrast with the “susceptibility gradient mapping” post-processing method.

Several attractive biomarkers of vulnerable atherosclerotic plaques have been evaluated using molecular MRI in the ApoE^{-/-} model, including $\alpha\text{v}\beta_3$ integrin with an RGD peptide [228] and phosphatidylserine using a peptide mimicking the endogenous ligand annexin V specific for apoptosis that was grafted to Gd-DTPA [229], or VCAM-1 and apoptotic cells using targeted peptides conjugated with USPIO [230,231]. Intraplaque fibrin plays an important role in the progression of late-stage atherosclerotic plaques. Fibrin and fibronectin accumulation in atherosclerotic plaques is associated with plaque burden; therefore, molecular imaging of these biomarkers could have great potential

to prevent acute cardiovascular complications. Makowsky et al. [232] assessed intraplaque fibrin in ApoE^{-/-} mice fed a high-fat diet for one to three months using a gadolinium-conjugated agent. Molecular MRI revealed a significant increase in contrast agent uptake in brachiocephalic artery plaques, in agreement with immunohistochemical findings. Similarly, Wu et al. [233] tested the peptide CLT1, which is specific to fibrin-fibronectin complexes, conjugated with four DOTA-Gd chelates, for monitoring clots present in atherosclerotic plaques of ApoE^{-/-} mice over time. These authors found a stronger enhancement in the aortic lesions of the ApoE^{-/-} mice than in the controls at all time points and a good correlation of MRI signal progression with fibrin-fibronectin immunochemical analysis.

Distinguishing between stable and unstable rupture-prone lesions using noninvasive methods is one of the major diagnostic challenges, and the abundant presence of macrophages is a relevant imaging target for vulnerable plaque detection. Segers et al. [234] investigated the use of USPIO conjugated to a peptidic ligand of scavenger receptor AI that is highly expressed by lesional macrophages. These targeted USPIOS for inflammatory plaques have shown a significant accumulation in advanced atherosclerotic plaques of ApoE^{-/-} mice. Another recent study of Parolini et al. [235] evaluated the potential of a new blood-pool contrast agent referred to as B22956/1 to identify vulnerable plaques in the brachiocephalic arteries of ApoE^{-/-} mice. These authors highlighted a significant correlation between MRI signal enhancement and macrophage content in atherosclerotic lesions.

Tarin et al. [236] also tested a targeted probe based on gold-coated iron oxide nanoparticles vectorized with a specific antibody for the CD163 receptor, highly expressed on macrophages at inflammatory sites, in ApoE^{-/-} mice. A significant signal variation over time was observed in the aortic walls of ApoE^{-/-} mice with respect to the pre-injection signal or nontargeted nanoparticles; the MRI results were confirmed in autopic samples by specific immunostaining. Lectin-like Oxidized Low-Density Lipoprotein Receptor 1 (LOX-1) is a membrane receptor expressed on endothelium, inflammatory cells and SMCs present in atherosclerotic plaques which plays a crucial role in the destabilization and rupture of lesions. Wen et al. [237] reported a sensitive and specific LOX-1-targeted USPIO, producing a significant signal loss in MR images at the level of atherosclerotic lesions in carotid arteries of ApoE^{-/-} mice (as shown in Figure 6).

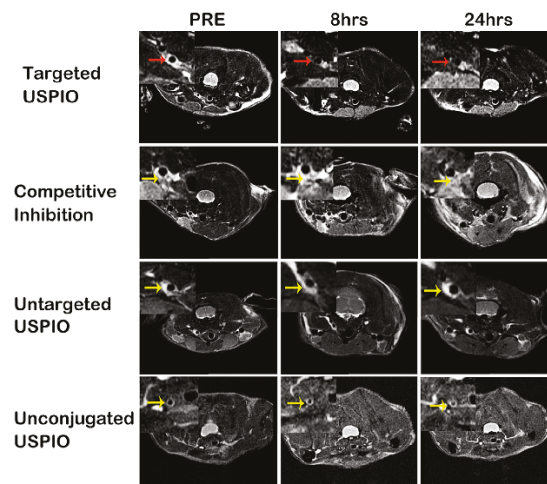


Figure 6. USPIOS MRI of ApoE^{-/-} mice in vivo. Representative in vivo carotid atherosclerotic lesion in ApoE^{-/-} mice pre-, 8 and 24 hrs after administration of various USPIOS. The red arrows indicate the location of signal loss within the plaque while the yellow arrows indicate the location of carotid atherosclerotic lesions with limited rSI changes. (Reprinted from Reference [237], Crown copyright with permission from © 2014, Elsevier Ltd.)

The MRI is characterized by high spatial resolution; nevertheless, it has relatively low sensitivity in comparison with other imaging techniques such as nuclear medicine or optical imaging. In particular, near-infrared fluorescence (NIRF) imaging can overcome this limitation, due to its high sensitivity, and also appears to be easy to perform and of relatively low cost. Therefore, several previously published studies have proposed interesting bimodality imaging strategies with *in vivo* and *ex vivo* NIRF: optical imaging was used to confirm nanoparticle uptake in the lesions, and MRI helps to accurately determine the location of *in vivo* fluorescence signals. Van Tiborg et al. [198] characterized a micellar nanoparticle conjugated to annexin A5, carrying both Gd-labeled lipids and a fluorescent dye. *In vivo* MR imaging highlighted cells, exposing phosphatidylserine in atherosclerotic lesions of ApoE^{-/-} mice, and *ex vivo* NIR fluorescence imaging of excised aortas was used to validate the quantification of nanoparticles in the plaques.

Very recently, Wang et al. [238] illustrated a novel multi-modality molecular imaging probe obtained by conjugating polyclonal profilin-1 antibody and NHS-Cy5.5 fluorescent dye to the surface of DMSA-Fe₃O₄ nanoparticles (PC-NPs) that can be used to perform noninvasive imaging of atherosclerotic plaques at the level of the carotid artery in ApoE^{-/-} mice. Profilin-1 is an actin-binding protein involved in the modulation of cytoskeleton architecture that is over-expressed in activated vascular SMCs present in atherosclerotic plaques, and therefore it is recognized as a promising potential target to comprehensively assess the vulnerability of plaques. To date, any other molecular probe targeted at activated SMCs in plaques is described. These authors revealed the accumulation of PC-NPs in atherosclerotic plaques of the analyzed model using *in vivo* MRI and NIRF imaging: fluorescence signals in the carotid arteries were significantly higher in ApoE^{-/-} mice compared to controls and significant T2-weighted MRI signal attenuation was observed, with a high correlation between the fluorescence imaging intensity and MRI signal changes. Moreover, this targeted probe has also been shown to be helpful in evaluating the therapeutic efficacy of atorvastatin through dynamic monitoring [238].

2.3.3. Nuclear Imaging Techniques and X-ray Computed Tomography

Nuclear techniques such as PET and SPECT potentially provide detection sensitivities in the nanomolar-picomolar range. Such functional imaging enables the investigation of biological events that lead to plaque rupture with high specificity and offers relevant potential results of clinical translatability from basic research to identify high-risk patients. Furthermore, the combination of the nuclear medicine images with the morphological information provided by CT in hybrid scanners, or with the high soft tissue contrast obtained through MRI, has the potential to map molecular signals with precise anatomic details. Also, more recently, the association with optical imaging was shown to be particularly helpful for testing innovative probes and for *in vivo* tracking of targeted cells.

Macrophage markers, such as CD68 glycoprotein, which binds to low-density lipoprotein, correlate well with atherosclerotic lesion vulnerability. Nahrendorf et al. [239] described a novel trimodal nanoparticle, which targets the CD68 macrophage marker, consisting of an iron oxide core for MRI and an optically detectable near infrared fluorochrome that is radiolabeled with the PET tracer ⁶⁴Cu. This agent was found to accumulate predominantly in macrophages present in plaques at the level of the carotid artery and aorta of ApoE^{-/-} mice, as confirmed by *ex vivo* autoradiography and fluorescence microscopy. More recently, Seo et al. [240] performed *in vivo* PET-CT studies in atherosclerotic ApoE^{-/-} mice using a fluorine-18-labeled dendritic form of a cyclic nine-amino-acid peptide, named LyP-1, which targets p32 proteins on macrophages and which was labeled with fluorine-18. PET-CT co-registered images have shown significant uptake of the radiotracer in the aortic root and descending aorta after two hours of biodistribution.

Macrophages can also be targeted with antibodies against LOX-1, which is upregulated in response to high levels of oxidized LDL and proinflammatory cytokines. For imaging purposes, Li et al. [241] conjugated a LOX-1 antibody with the SPECT radionuclide ^{99m}Technetium (^{99m}Tc), showing that this probe was able to reliably target macrophages *in vivo* in ApoE^{-/-} mice and LDLr^{-/-} (LOX1^{-/-}) mice. The peripheral benzodiazepine receptor (PBR), also known as translocator protein (TSPO),

is minimally expressed in non-inflamed tissue and is highly expressed on activated macrophages; therefore, it is exploited as a molecular imaging target.

Foss et al. [242] developed a SPECT imaging agent, [¹²⁵I]iodo-DPA-713, which targets macrophages, to selectively detect macrophage infiltrates along the descending aorta and within the myocardium of the ApoE^{-/-} mice. Radiotracers targeting VCAM-1 have been validated in murine experimental systems as attractive tools for imaging vulnerable plaques. Atherosclerotic lesions in the aortic arches of ApoE^{-/-} mice have been successfully identified by Nahrendorf et al. [243] using the peptide 4V, and very recently by Bala et al. [244] through the specific nanobody cAbVCAM-1-5, both radiolabeled with fluorine-18, showing a significant correlation between the uptake of the radiotracers and the level of expression of the VCAM-1 receptor in atherosclerotic lesions assessed by ex vivo analyses (as shown in Figure 7).

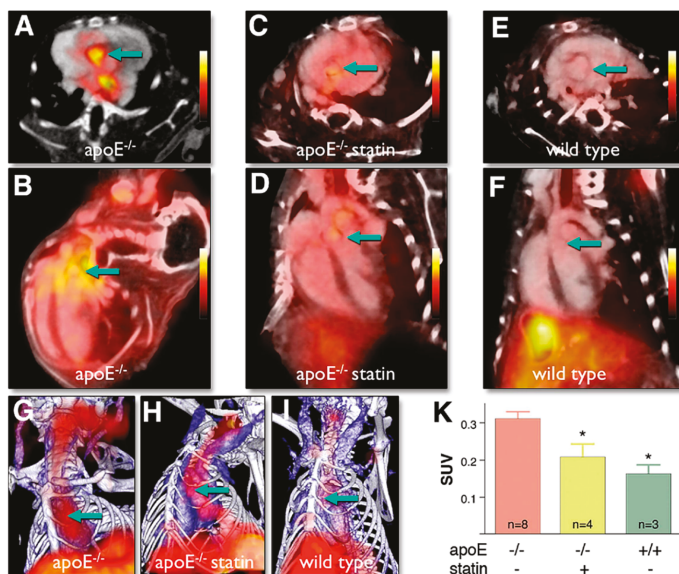


Figure 7. PET-CT in ApoE^{-/-} and statin-treated mice. PET-CT imaging shows uptake of ¹⁸F-4V in the aortic root (arrows) and arch of atherosclerotic mice. Uptake is lower in statin-treated and in wild-type mice. (A,C,E) Short-axis views; (B,D,F) Long-axis views; (G,H,I) Three-dimensional maximum intensity projection. Bone is shown in white, vasculature in blue, and ¹⁸F-4V PET signal in red. The PET signal occurs in the carotid arteries, and background signal in the liver, in addition to the strong uptake of ¹⁸F-4V PET observed in the root and arch (arrow). K = quantification of PET signal as the standard uptake value (SUV). Mean \pm SEM, * $p < 0.05$. Abbreviations as in Figures 1, 2 and 5. (Reprinted from Reference [243]. Copyright with permission from © 2009, American College of Cardiology Foundation, Elsevier Inc.)

Similarly, Broisat et al. [245] tested anti-VCAM-1 nanobodies labeled with ⁹⁹mTc both in vitro on murine and human endothelial cells and in vivo at the level of the aortic arch in ApoE^{-/-} mice. Dimastromatteo et al. [246] demonstrated in vivo the uptake of the peptide ⁹⁹mTc-B2702p1 at the level of the carotid arteries in the same model, confirming VCAM-1 expression using immunohistology.

Other relevant targets of plaque vulnerability, investigated through nuclear medicine imaging in the ApoE^{-/-} murine model, include other biomarkers of inflammation such as the following: P-selectin [247,248]; $\alpha_v\beta_3$ receptor with an RGD-galacto peptide [249] or the novel integrin ligand flotegatide [250], both labeled with fluorine-18; phosphatidylserine using ⁹⁹mTc-annexin V [197] or

⁹⁹mTc-AnxF568 and ¹²⁴I-Hypericin [251] for apoptosis imaging; and extracellular matrix proteins such as GPVI with a ⁶⁴Cu-labeled GPVI fragment crystallized [252] or fibronectin using a specific ⁹⁹mTc-antibody [253]. Finally, in an attempt to improve the detection of vulnerable lesions, contrast agents for CT imaging of macrophage-rich atherosclerotic plaques have been developed and tested in the major mouse models of atherosclerosis, for example liposomal-iodine [254] or PEGylated gold nanoparticles [255] in ApoE^{-/-} mice and, more recently, gold particles of 15 nm with a polyethylene glycol coating called Aurovist in the ApoE^{-/-} C1039G^{+/+} model [43].

2.3.4. Targeted Fluorescence Imaging

Currently, fluorescence imaging is emerging in preclinical research because it offers several advantages: high sensitivity, the possibility of simultaneous multi-spectral imaging, high-throughput capabilities, cost-effectiveness, and the absence of ionizing radiation. This technique can be applied both ex vivo for immunofluorescence microscopy and for in vivo applications such as intravital microscopy or tomographic imaging. In particular, FMT in the NIR window is gaining great relevance in cardiovascular research for longitudinal studies in mouse models of atherosclerosis. Atherosclerosis research using FMT is still sparse, but the previously mentioned peculiarities make it an attractive in vivo alternative to nuclear imaging. FMT is based on the collection of photons propagated in deep tissues from different points of view to obtain the tomographic distribution of fluorochromes.

A number of fluorescent targeted probes are available, with the possibility of obtaining in vivo quantitative three-dimensional data of fluorescence signal distribution. These probes are excitable with a laser at the appropriate wavelength, and, after excitation, they emit light at a higher wavelength, detectable with appropriate charge-coupled device cameras. FMT offers an improved penetration depth of light in the near-infrared spectrum and limited autofluorescence but has limited spatial resolution and is currently restricted to preclinical field or ex vivo human samples [256]. Moreover, multimodality imaging with the association of FMT-CT or -MRI holds promise for noninvasive imaging of murine models of atherosclerosis, adding anatomical details to molecular signals [257–259]. Macrophage content correlates with plaque vulnerability because the fibrotic cap can be destabilized by the secretion of matrix-degrading enzymes, contributing to acute thrombotic complications.

Cathepsins and metalloproteinases are highly expressed in rupture-prone plaques, and the activity of these macrophage-related molecules has been evaluated at the level of the ApoE^{-/-} mouse aortas both in vivo and ex vivo with fluorescent imaging [260]. Nahrendorf et al. [257] have also monitored the macrophage-protease function in vivo by FMT as a biomarker of destabilized atheromata and have coregistered FMT datasets with high-resolution CT angiography, localizing the highest fluorescence signal in the aortic root and arch of ApoE^{-/-} mice. Moreover, the same authors showed that FMT-CT may be useful for monitoring the efficacy of atorvastatin treatment in ApoE^{-/-} mice. In agreement, Lermann et al. [261] used FMT to test the plaque-stabilizing effects of high-dose atorvastatin treatment in ApoE^{-/-} mice through in vivo tracking of the recruitment of near-infrared fluorescent-labeled macrophages (as shown in Figure 8).

FMT-based quantification of macrophage recruitment in vulnerable plaques has demonstrated lesion stabilization after four days of atorvastatin therapy. Similarly, a recent study has successfully used FMT to visualize protease activity in ApoE^{-/-} mice and to assess the efficacy of an anti-inflammatory nanotherapeutic [262].

Apoptosis correlates with plaque vulnerability and, therefore, represents an important diagnostic target. Van Tiborg et al. [198] developed a fluorescent nanoparticle functionalized for annexin 5 that was applied both in vivo using MRI and ex vivo with near-infrared fluorescence imaging of excised aortas. Calcification in atherosclerotic plaques is associated with macrophage infiltration and is predictive of cardiovascular events. Plaque rupture occurs particularly at interface areas between high- and low-density tissues, and microcalcification in the fibrous cap induces microfractures. Aikawa et al. [139] used a bisphosphonate-derivatized near-infrared fluorescent agent to visualize osteogenic activity and iron oxide fluorescent nanoparticles for detection of macrophages in ApoE^{-/-} mouse aortas,

demonstrating with ex vivo fluorescence imaging an increased osteogenic activity in macrophage-rich atherosclerotic plaques of 20- to 30-week-old mice.

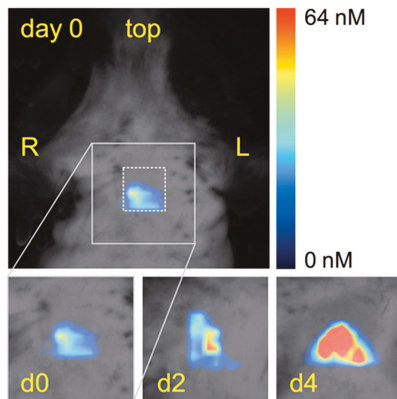


Figure 8. Fluorescence-mediated tomography (FMT) reliably quantifies 1,1'-dioctadecyl-3,3,3',3'-tetramethylindotricarbocyanineiodide (DiR)-enhanced green fluorescent protein (eGFP) macrophage recruitment over time in a region of interest covering aortic sinus, aortic arch, and brachiocephalic artery of ApoE^{-/-} mice. (Reprinted from Reference [261]. Copyright with permission from © 2013, Wolters Kluwer Health.)

More recently, Lin et al. [263] evaluated cathepsin activity and $\alpha_v\beta_3$ expression in ApoE^{-/-} mice using FMT, demonstrating that targeted NIRF agents can be successfully employed for molecular imaging of vulnerable plaques at the level of the aortic root and arch, and the descending aorta and carotid arteries. In preclinical testing, cathepsin agents can monitor the anti-inflammatory effects of ezetimibe. Also, in this case, the FMT signal was conveniently co-registered with CT angiographic images using anatomical details from CT to further identify the location of the molecular information. Similarly, Yao et al. [264] have shown that $\alpha_v\beta_3$ is highly expressed in atherosclerotic lesions of the ApoE^{-/-} model using a cyclic RGD peptide (cRGDyK) conjugated with the near-infrared dye Cy5.5 both in vivo and in excised carotid arteries. cRGDyK-Cy5.5 co-localization with MAC-3 expression was confirmed using fluorescence confocal microscopy.

2.3.5. Photoacoustic Imaging

Photoacoustic imaging (PAI), also called optoacoustic tomography (OAT), is a hybrid imaging modality that uses nonionizing optical radiation and ultrasonic detection. Recent advances in laser technology and detection strategies have led to significant improvements in the capabilities of optoacoustic systems. PAI is showing real promise as a convenient alternative to other imaging modalities. PAI combines the advantages of both optical and ultrasonic imaging methods, offers higher spatial resolution and allows imaging of deeper tissues compared to optical imaging techniques [265,266]. PAI is based on the photoacoustic effect: a short-pulsed laser irradiates biological tissues and induces ultrasonic waves due to transient thermoelastic expansion [265]. In comparison to optical imaging, PAI allows high-resolution visualization ($\leq 100 \mu\text{m}$) with a penetration depth within tissues of several centimeters, because it is less influenced by photon scattering.

Applications in the field of molecular imaging provide functional information regarding cellular events by using endogenous chromophores (hemoglobin, melanin, and lipids) and a great variety of exogenous contrast agents [267–269]. Furthermore, OAT contrast agents can be combined with CEUS for advantageous dual modality imaging approaches [270,271]. PAI has been used for various biological applications such as angiogenesis, oxygen saturation and drug response for oncologic

screening and studies on brain functions, including preclinical research using small animal models of atherosclerosis [272,273]. Despite its attractive features, PAI experienced a slow development and is still facing some issues for routine adoption, relying on the development and validation of molecular agents tailored to this imaging modality. Few studies have explored the feasibility and potential of this technique in atherosclerosis research. The main strategies explored through *in vitro* or *ex vivo* PA studies have included targeting of foamy macrophages and of inflammatory molecular biomarkers such as ICAM-1, VCAM-1 and E-selectin using gold nanoparticles (AuNPs) [274–276].

Very recently, some pilot preclinical studies have been conducted in ApoE^{-/-} mice to test the *in vivo* potential of molecular PA contrast agents to identify stable versus vulnerable plaques such as a VCAM-1-targeting gold nanoshell probe, which has highlighted a higher PA signal in the aortic arches of ApoE^{-/-} mice fed a WTD compared to controls [277] and indocyanine green (ICG) conjugated with a PEGylated polymer in a new ICG@PEG-Ag2S nanoprobe that was shown to selectively accumulate in the atherosclerotic plaques due to its lipophilicity and produced a six-fold enhancement of the PA signal intensity in the region of the aorta 3 h post-injection in ApoE^{-/-} mice compared to the signal produced after administration of free ICG [278] (as shown in Figure 9).

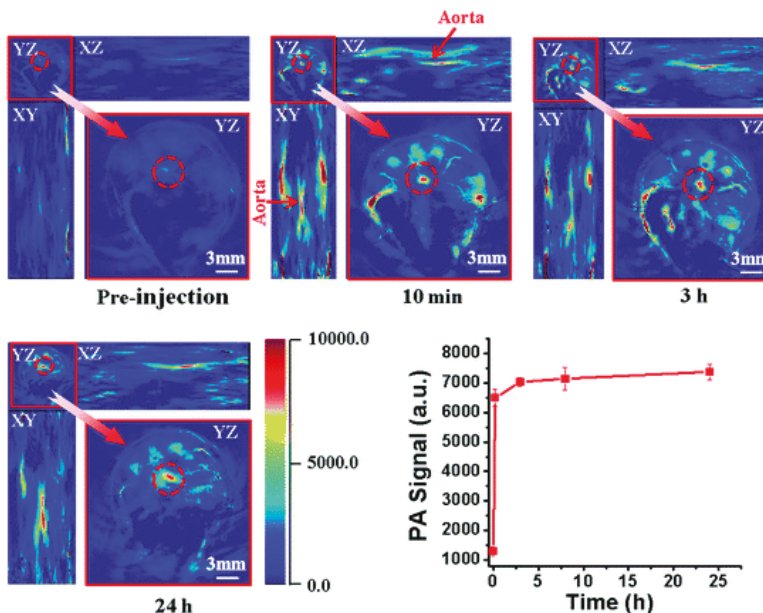


Figure 9. Representative PA imaging of abdominal aorta in an ApoE^{-/-} mouse after intravenous injection of ICG@PEG-Ag2S (longitudinal and transverse view): a low contrast in the whole body of the mouse is evident, while a remarkable enhancement of the PA intensity in the region of the aorta (as indicated by red arrows and red circles) was observed over time. Graph shows quantitative changes over time of PA signals in the aorta of the mouse corresponding to the red circle in images. (Reprinted from Reference [278]. Copyright with permission from © 2016, Royal Society of Chemistry.)

3. Conclusions and Future Directions

Atherosclerosis can start in the late years of childhood and can remain silent for many years. It becomes symptomatic when it interferes with the circulation and blood supply, causing heart attack, stroke, or ischemic symptoms. However, this mechanism is responsible for acute events in only 30%–40% of patients. A significant number of people with myocardial ischemia do not have plaques that significantly narrow the arteries. A total of 60%–70% of patients with acute coronary syndrome or

sudden cardiac death have thrombosis associated with rupture-prone plaques that have been shown in post-mortem evaluation to have specific characteristics such as increased macrophage activity and a peculiar molecular pattern. These features appear in an atherosclerotic plaque prior to rupture.

As outlined in the “response-to-injury” hypothesis by Ross et al. [150], the endothelial denudation injury or activation was considered the first step in the development of atherosclerosis. The monocyte-endothelial interactions giving rise to foam cells and growth factor-induced SMC proliferation trigger lesion formation. Presently, the knowledge of the atherogenic process has been considerably refined using murine models of atherosclerosis through recognition of other important factors such as the subendothelial accumulation of apolipoprotein B-containing lipoproteins; the roles of macrophages, neutrophils, T cells, and dendritic cells; and the identification of specific chemotactic signals that regulate the recruitment of inflammatory cells into the lesion, such as extracellular RNA (eRNA) acting as a cofactor of VEGFR-2-coupled or other intracellular signaling pathways [279,280]. The existence of a pathological interface between lipids and inflammation, the role of cytokines and the importance of highly specific molecular targets that can be used to develop diagnostic imaging systems and innovative therapeutic tools, such as RNA-degrading enzymes, RNA interference or silencing systems [279], are made quite clear by these studies. Thus, there is an urgent need for identifying vulnerable atherosclerotic plaques before acute cardiovascular events.

Many of the currently available clinical diagnostic methods still provide minimal information about the biological characteristics of plaques and/or are invasive. The imaging methods currently used provide only partial quantitative and morphological data on the atherosclerotic plaque. The cellular and molecular processes that characterize the atherosclerotic plaques require more advanced methods that can best represent the peculiarities of the pathological events with respect to size. The development of molecular imaging using probes for specific biological functions could be of great value to study the evolution and the chemical outcome of the atherosclerotic plaque and for the prediction of vulnerability. The study of atherosclerosis in animal models is of great relevance for the advancement of knowledge, but some precautions are required when relevant data are extrapolated from animals for new diagnostic and therapeutic tools. Proper design and generation of animal models are essential to make preclinical data more reproducible and translatable to the clinic. Atherosclerosis is a complex disease. The animal models are a simple representation of this complex system. Therefore, a single animal model may not be able to reproduce all aspects and all stages of the atherosclerotic process in humans in all of its complexities but rather may represent a specific aspect of the disease. In atherosclerosis research, mice are nowadays the most commonly used animals. Generally, the lipid metabolism in wild-type mice is significantly different from humans. The major fraction of plasmatic lipoproteins in wild-type mice is HDL, which is different from humans where LDL or VLDL lipoproteins are mainly represented, and therefore mice are well protected from atherosclerosis due to a beneficial cholesterol spectrum in the blood. Nevertheless, the C57BL6 strain of inbred mice is relatively susceptible to atherosclerosis, and by feeding them with an atherogenic diet, development of atherosclerosis can be augmented to such an extent that the resulting advanced lesions are useful to study disease mechanisms. Overcoming the limits of this latter model, the advent of the genetically modified mice has revolutionized the study of the pathogenetic mechanisms of atherosclerosis.

In particular, ApoE^{-/-} mice are currently the most well-characterized mouse model of atherosclerosis used by research groups worldwide. However, the ApoE^{-/-} mouse is a model of a rare disease in humans, named homozygous familial hypercholesterolemia, while the atherosclerosis induced by LDL accumulation is the most common pathological mechanism in humans. Additionally, several systemic factors could modify the course of the disease in the animal models, such as plasmatic levels of HDL, insulin resistance, and hemodynamic factors, which could make the process more or less different from that of humans. Moreover, considering that atherosclerosis development is largely dependent on local inflammation, it is important to consider that mechanisms of inflammation in atherosclerosis could differ between mice and humans [281]. Furthermore, the choice of the lesional area of the disease may affect the usefulness of information obtained from the animal

models and is essential to bridge the translational gap between preclinical and clinical research. Most preclinical studies refer to the aortic root, the whole descending aortic surface or the innominate artery. This endpoint is relevant for the early stages of the disease but is poorly predictive of the clinical features of the human condition.

Very recently, the ApoE^{-/-}/Fbn1C1039G^{+/+} mouse model has been developed. These mice exhibit vulnerable atherosclerotic plaque phenotypes, with a greater incidence of plaque rupture in comparison to the ApoE^{-/-} or LDL^{-/-} mice, which exhibit mainly stable plaques.

The new generation of imaging modalities comprises promising tools for the prediction of vulnerable atherosclerotic plaques. Although novel molecular imaging approaches for atherosclerosis have been tested in the previously mentioned experimental systems, accurate assessment of plaque characteristics and vulnerability is still in its infancy. Each imaging technique has its own strengths and drawbacks. At the moment, CEUS and molecular MRI appear to be the most suitable and promising because they have been applied to research the analysis of the compositional features of vulnerable plaques, they show high resolution and sensitivity, they use nonionizing radiation and they have potential clinical utility. The main concerns to overcome are: improvement of the sensitivity and specificity of the molecular probes; complex extrapolation of results from animal models; and scientific as well as financial challenges for translating new molecular imaging ligands from preclinical research to clinical practice. Further investigations of the mechanisms of plaque destabilization and rupture and technological advances of imaging equipment are required to reduce both mortality and morbidity worldwide. Successful translation of targets and ligands to clinical molecular imaging of the vulnerable plaque may also offer novel therapeutic perspectives for vulnerable plaques such as targeted drug delivery.

Author Contributions: Marcello Mancini proposed this subject, Sara Gargiulo and Matteo Gramanzini drafted the outline, collected previous works and wrote the paper under the guidance of Marcello Mancini. Marcello Mancini revised the paper.

Conflicts of Interest: The authors declare no conflict of interest.

Abbreviations

AHA	American Heart Association
ApoE ^{-/-}	apolipoprotein-E-knockout
WTD	western type diet
Fbn1	fibrillin-1
MRI	magnetic resonance imaging
CEUS	contrast-enhanced ultrasound
microCT	micro-computed tomography
HDL	high-density lipoprotein
LDL	low-density lipoprotein
VLDL	very low-density lipoprotein
SMCs	smooth muscle cells
LDL ^{-/-}	low-density lipoprotein-knockout
MMP	matrix metalloproteinase
LPS	lipopolysaccharide
Ang II	angiotensin II
MCP-1	monocyte chemoattractant protein-1
DIO	diet-induced obese
DD	diabetogenic diet
STZ	streptozotocin
T1D	type 1 diabetes
hAR	human aldose reductase
T2D	type 2 diabetic
PCSK9	proprotein convertase subtilisin/kexin type 9

VCAM-1	vascular cell adhesion molecule-1
ICAM-1	intercellular adhesion molecule-1
VLA 4	very late antigen-4
TLR-4	Toll-like receptor 4
FR β	folate receptor β
CD68	Cluster of Differentiation 68
VEGF	vascular endothelial growth factor
VEGFRs	vascular endothelial growth factor receptors
VEGFR-1	vascular endothelial growth factor receptor 1
VEGFR-2	vascular endothelial growth factor receptor 2
PS	phosphatidylserine
A5	annexin V
GPVI	glycoprotein VI
PET	positron emission tomography
SPECT	single-photon emission computed tomography
CT	X-ray computed tomography
FMT	fluorescent molecular tomography
PAI	photoacoustic imaging
HFU	high-frequency ultrasound
MB	microbubbles
GP IIb/IIIa	glycoprotein (GP) IIb/IIIa complex
RGD	Arg-Gly-Asp sequence
cRGD	cyclic RGD peptide
USPIO	ultrasmall superparamagnetic iron oxide nanoparticles
Gd-DTPA	gadolinium chelates
RARE	rapid-acquisition relaxation-enhanced
LOX-1	Lectin-like Oxidized Low-Density Lipoprotein Receptor 1
NIRF	near-infrared fluorescence
PC-NPs	DMSA-Fe ₃ O ₄ -nanoparticles
LyP-1	cyclic 9-amino acid peptide
^{99m} Tc	^{99m} Technetium
PBR	peripheral benzodiazepine receptor
TSPO	translocator protein
OAT	optoacoustic tomography
AuNPs	gold nanoparticles
ICG	indocyanine green
eRNA	extracellular RNA

References

1. Virmani, R.; Burke, A.P.; Kolodgie, F.D.; Farb, A. Vulnerable plaque: The pathology of unstable coronary lesions. *J. Interv. Cardiol.* **2002**, *15*, 439–446. [CrossRef] [PubMed]
2. Lusis, A.J. Atherosclerosis. *Nature* **2000**, *407*, 233–241. [CrossRef] [PubMed]
3. Naghavi, M.; Libby, P.; Falk, E.; Casscells, S.W.; Litovsky, S.; Rumberger, J.; Badimon, J.J.; Stefanadis, F.; Moreno, P.; Pasterkamp, G.; et al. From vulnerable plaque to vulnerable patient: A call for new definitions and risk assessment strategies: Part I. *Circulation* **2003**, *108*, 1664–1672. [CrossRef] [PubMed]
4. Stary, H.C. Natural history and histological classification of atherosclerotic lesions: An update. *Arterioscler. Thromb. Vasc. Biol.* **2000**, *20*, 1177–1178. [CrossRef] [PubMed]
5. Virmani, R.; Burke, A.P.; Farb, A.; Kolodgie, F.D. Pathology of the vulnerable plaque. *J. Am. Coll. Cardiol.* **2006**, *47*, 13–18. [CrossRef] [PubMed]
6. Schapira, K.; Heeneman, S.; Daemen, M.J. Animal models to study plaque vulnerability. *Curr. Pharm. Des.* **2007**, *13*, 1013–1020. [CrossRef] [PubMed]
7. Faggiotto, A.; Ross, R.; Harker, L. Studies of hypercholesterolemia in the nonhuman primate. I. Changes that lead to fatty streak formation. *Arteriosclerosis* **1984**, *4*, 323–340. [CrossRef] [PubMed]

8. Faggiotto, A.; Ross, R. Studies of hypercholesterolemia in the nonhuman primate. II. Fatty streak conversion to fibrous plaque. *Arteriosclerosis* **1984**, *4*, 341–356. [CrossRef] [PubMed]
9. Masuda, J.; Ross, R. Atherogenesis during low level hypercholesterolemia in the nonhuman primate. I. Fatty streak formation. *Arteriosclerosis* **1990**, *10*, 164–177. [CrossRef] [PubMed]
10. Masuda, J.; Ross, R. Atherogenesis during low level hypercholesterolemia in the nonhuman primate. II. Fatty streak conversion to fibrous plaque. *Arteriosclerosis* **1990**, *10*, 178–187. [CrossRef] [PubMed]
11. Schwartz, C.J.; Sprague, E.A.; Kelley, J.L.; Valente, A.J.; Suenram, C.A. Aortic intimal monocyte recruitment in the normo and hypercholesterolemic baboon (*Papio cynocephalus*). An ultrastructural study: Implications in atherogenesis. *Virchows Arch. A* **1985**, *405*, 175–191. [CrossRef]
12. Gerrity, R.G. The role of the monocyte in atherogenesis: I. Transition of blood-borne monocytes into foam cells in fatty lesions. *Am. J. Pathol.* **1981**, *103*, 181–190. [PubMed]
13. Gerrity, R.G. The role of the monocyte in atherogenesis: II. Migration of foam cells from atherosclerotic lesions. *Am. J. Pathol.* **1981**, *103*, 191–200. [PubMed]
14. Reitman, J.S.; Mahley, R.W.; Fry, D.L. Yucatan miniature swine as a model for diet-induced atherosclerosis. *Atherosclerosis* **1982**, *43*, 119–132. [CrossRef]
15. Davies, P.F. Hemodynamic shear stress and the endothelium in cardiovascular pathophysiology. *Nat. Clin. Pract. Cardiovasc. Med.* **2009**, *1*, 16–26. [CrossRef] [PubMed]
16. Koskinas, K.C.; Feldman, C.L.; Chatzizisis, Y.S.; Coskun, A.U.; Jonas, M.; Maynard, C.; Baker, A.B.; Papafaklis, M.I.; Edelman, E.R.; Stone, P.H. Natural history of experimental coronary atherosclerosis and vascular remodeling in relation to endothelial shear stress: A serial, in vivo intravascular ultrasound study. *Circulation* **2010**, *19*, 2092–2101. [CrossRef] [PubMed]
17. Prescott, M.F.; McBride, C.; Hasler-Rapacz, J.; von Linden, J.; Rapacz, J. Development of complex atherosclerotic lesions in pigs with inherited hyper-LDL cholesterolemia bearing mutant alleles for apolipoprotein B. *Am. J. Pathol.* **1991**, *139*, 139–147. [PubMed]
18. Brousseau, M.E.; Hoeg, J.M. Transgenic rabbits as models for atherosclerosis research. *J. Lipid Res.* **1999**, *3*, 365–375.
19. Huang, Y.; Schwender, S.W.; Rall, S.C., Jr.; Sanan, D.A.; Mahley, R.W. Apolipoprotein E2 transgenic rabbits. Modulation of the type III hyperlipoproteinemic phenotype by estrogen and occurrence of spontaneous atherosclerosis. *J. Biol. Chem.* **1997**, *272*, 22685–22694. [CrossRef] [PubMed]
20. Shiomi, M.; Ito, T.; Shiraishi, M.; Watanabe, Y. Inheritability of atherosclerosis and the role of lipoproteins as risk factors in the development of atherosclerosis in the WHHL rabbits: Risk factors related to coronary atherosclerosis are different from those related to aortic atherosclerosis. *Atherosclerosis* **1992**, *96*, 43–52. [CrossRef]
21. Niimi, M.; Yang, D.; Kitajima, S.; Ning, B.; Wang, C.; Li, S.; Liu, E.; Zhang, J.; Chen, Y.E.; Fan, J. ApoE knockout rabbits: A novel model for the study of human hyperlipidemia. *Atherosclerosis* **2015**, *245*, 187–193. [CrossRef] [PubMed]
22. Busnelli, M.; Froio, A.; Bacci, M.L.; Giunti, M.; Cerrito, M.G.; Giovannoni, R.; Forni, M.; Gentilini, F.; Scagliarini, A.; Deleo, G.; et al. Pathogenetic role of hypercholesterolemia in a novel preclinical model of vascular injury in pigs. *Atherosclerosis* **2009**, *207*, 384–390. [CrossRef] [PubMed]
23. Wang, F.; Tong, T.; Peng, Y.; Tian, J.; Gu, W.; Tang, G.; Geng, D.; Chen, Y. A modified rabbit model of carotid atherosclerotic plaque suitable for the stroke study and MRI evaluation. *Int. J. Neurosci.* **2011**, *121*, 662–669.
24. Tian, J.; Hu, S.; Sun, Y.; Ban, X.; Yu, H.; Dong, N.; Wu, J.; Yu, B. A novel model of atherosclerosis in rabbits using injury to arterial walls induced by ferric chloride as evaluated by optical coherence tomography as well as intravascular ultrasound and histology. *J. Biomed. Biotechnol.* **2012**, *2012*, 121867. [CrossRef] [PubMed]
25. Xiong, Q.; Feng, J.; Zhang, Y.; Sun, Y.; Lu, Y.; Jin, L.; Li, T.; Zhang, X.; Cao, R.; Wu, J. Promotion of atherosclerosis in high cholesterol diet-fed rabbits by immunization with the P277 peptide. *Immunol. Lett.* **2015**, *170*, 80–87. [CrossRef] [PubMed]
26. Bond, M.G.; Wilmoth, S.K.; Gardin, J.F.; Barnes, R.W.; Sawyer, J.K. Noninvasive assessment of atherosclerosis in nonhuman primates. *Adv. Exp. Med. Biol.* **1985**, *183*, 189–195. [PubMed]
27. Bloch, L.; Hansen, A.Y.; Pedersen, S.F.; Honge, J.L.; Kim, W.Y.; Hansen, E.S. Imaging of carotid artery vessel wall edema using T2-weighted cardiovascular magnetic resonance. *J. Cardiovasc. Magn. Reson.* **2014**, *16*, 22–28. [CrossRef] [PubMed]

28. Majdouline, Y.; Ohayon, J.; Keshavarz-Motamed, Z.; Roy Cardinal, M.H.; Garcia, D.; Allard, L.; Lerouge, S.; Arsenault, F.; Soulez, G.; Cloutier, G. Endovascular shear strain elastography for the detection and characterization of the severity of atherosclerotic plaques: In vitro validation and in vivo evaluation. *Ultrasound Med. Biol.* **2014**, *40*, 890–903. [CrossRef] [PubMed]
29. Teräs, M.; Kokki, T.; Durand-Schaefer, N.; Noponen, T.; Pietilä, M.; Kiss, J.; Hoppela, E.; Sipilä, H.T.; Knuuti, J. Dual-gated cardiac PET-clinical feasibility study. *Eur. J. Nucl. Med. Mol. Imaging* **2010**, *37*, 505–516. [CrossRef] [PubMed]
30. Pham, T.A.; Hua, N.; Phinikaridou, A.; Killiany, R.; Hamilton, J. Early in vivo discrimination of vulnerable atherosclerotic plaques that disrupt: A serial MRI study. *Atherosclerosis* **2016**, *244*, 101–107. [CrossRef] [PubMed]
31. Qi, C.; Deng, L.; Li, D.; Wu, W.; Gong, L.; Li, Y.; Zhang, Q.; Zhang, T.; Zhang, C.; Zhang, Y. Identifying vulnerable atherosclerotic plaque in rabbits using DMSA-USPIO enhanced magnetic resonance imaging to investigate the effect of atorvastatin. *PLoS ONE* **2015**, *10*, e0125677. [CrossRef] [PubMed]
32. Mouse Genome Sequencing Consortium. Initial sequencing and comparative analysis of the mouse genome. *Nature* **2002**, *420*, 520–561.
33. Stary, H.C.; Blankenhorn, D.H.; Chandler, A.B.; Dinsmore, R.E.; Fuster, V.; Glagov, S.; Insull, W.; Rosenfeld, M.E.; Schwartz, C.J.; Wagner, W.D.; et al. A definition of the intima of human arteries and of its atherosclerosis-prone regions. A report from the Committee on Vascular Lesions of the Council on Arteriosclerosis, American Heart Association. *Circulation* **1992**, *85*, 391–405. [CrossRef] [PubMed]
34. Stary, H.C.; Chandler, A.B.; Dinsmore, R.E.; Fuster, V.; Glagov, S.; Insull, W., Jr.; Rosenfeld, M.E.; Schwartz, C.J.; Wagner, W.D.; Wissler, R.W. A definition of advanced types of atherosclerotic lesions and a histological classification of atherosclerosis. A report from the Committee on Vascular Lesions of the Council on Arteriosclerosis, American Heart Association. *Circulation* **1995**, *92*, 1355–1374. [CrossRef] [PubMed]
35. Rosenfeld, M.E.; Polinsky, P.; Virmani, R.; Kauser, K.; Rubanyi, G.; Schwartz, S.M. Advanced atherosclerotic lesions in the innominate artery of the ApoE knockout mouse. *Arterioscler. Thromb. Vasc. Biol.* **2000**, *20*, 2587–2592. [CrossRef]
36. Von der Thüsen, J.H.; van Berkel, T.J.; Biessen, E.A. Induction of rapid atherogenesis by perivascular carotid collar placement in apolipoprotein E-deficient and low-density lipoprotein receptor-deficient mice. *Circulation* **2001**, *103*, 1164–1170. [CrossRef] [PubMed]
37. Cha, J.; Ivanov, V.; Ivanova, S.; Kalinovsky, T.; Rath, M.; Niedzwiecki, A. Evolution of angiotensin II-mediated atherosclerosis in ApoE^{-/-} mice. *Mol. Med. Rep.* **2010**, *3*, 565–570. [PubMed]
38. Chen, Y.C.; Bui, A.V.; Diesch, J.; Manasseh, R.; Hausding, C.; Rivera, J.; Haviv, I.; Agrotis, A.; Htun, N.M.; Jowett, J.; et al. A novel mouse model of atherosclerotic plaque instability for drug testing and mechanistic/therapeutic discoveries using gene and microRNA expression profiling. *Circ. Res.* **2013**, *113*, 252–265. [CrossRef] [PubMed]
39. Chiwata, T.; Aragane, K.; Fujinami, K.; Kojima, K.; Ishibashi, S.; Yamada, N.; Kusunoki, J. Direct effect of an acyl-CoA: Cholesterol acyltransferase inhibitor, F-1394, on atherosclerosis in apolipoprotein E and low density lipoprotein receptor double knockout mice. *Br. J. Pharmacol.* **2001**, *133*, 1005–1012. [CrossRef] [PubMed]
40. Reardon, C.A.; Blachowicz, L.; Lukens, J.; Nissenbaum, M.; Getz, G.S. Genetic background selectively influences innominate artery atherosclerosis: Immune deficiency as probe. *Arterioscler. Thromb. Vasc. Biol.* **2003**, *23*, 1449–1454. [CrossRef] [PubMed]
41. Lewis, P.; Stefanovic, N.; Pete, J.; Calkin, A.C.; Giunti, S.; Thallas-Bonke, V.; Jandeleit-Dahm, K.A.; Allen, T.J.; Kola, I.; Cooper, M.E.; et al. Lack of the antioxidant enzyme glutathione peroxidase-1 accelerates atherosclerosis in diabetic apolipoprotein E-deficient mice. *Circulation* **2007**, *115*, 2178–2187. [CrossRef] [PubMed]
42. Van der Donckt, C.; van Herck, J.L.; Schrijvers, D.M.; Vanhoutte, G.; Verhoye, M.; Blockx, I.; van der Linden, A.; Bauters, D.; Lijnen, H.R.; Sluimer, J.C.; et al. Elastin fragmentation in atherosclerotic mice leads to intraplaque neovascularization, plaque rupture, myocardial infarction, stroke and sudden death. *Eur. Heart J.* **2015**, *36*, 1049–1058. [CrossRef] [PubMed]
43. De Wilde, D.; Trachet, B.; van der Donckt, C.; Vandeghinste, B.; Descamps, B.; Vanhove, C.; de Meyer, G.R.; Segers, P. Vulnerable plaque detection and quantification with gold particle-enhanced computed tomography in atherosclerotic mouse models. *Mol. Imaging* **2015**, *14*, 9–19.

44. Paigen, B.; Plump, A.S.; Rubin, E.M. The mouse as a model for human cardiovascular disease and hyperlipidemia. *Curr. Opin. Lipidol.* **1994**, *5*, 258–264. [CrossRef] [PubMed]
45. Moghadasian, M.H. Experimental atherosclerosis: A historical overview. *Life Sci.* **2002**, *70*, 855–865. [CrossRef]
46. Jawien, J.; Nastalek, P.; Korbut, R. Mouse models of experimental atherosclerosis. *J. Physiol. Pharmacol.* **2004**, *55*, 503–517. [PubMed]
47. Getz, G.S.; Reardon, C.A. Animal Models of atherosclerosis. *Arterioscler. Thromb. Vasc. Biol.* **2012**, *32*, 1104–1115. [CrossRef] [PubMed]
48. Whitman, S.C. A practical approach to using mice in atherosclerosis research. *Clin. Biochem. Rev.* **2004**, *25*, 81–93. [PubMed]
49. Li, X.; Liu, Y.; Zhang, H.; Ren, L.; Li, Q.; Li, N. Animal models for the atherosclerosis research: A review. *Protein Cell* **2011**, *2*, 189–201.
50. Paigen, B.; Ishida, B.Y.; Verstuyft, J.; Winters, R.B.; Albee, D. Atherosclerosis susceptibility differences among progenitors of recombinant inbred strains of mice. *Arteriosclerosis* **1990**, *10*, 316–323. [CrossRef] [PubMed]
51. Liao, F.; Andalibi, A.; deBeer, F.C.; Fogelman, A.M.; Lusis, A.J. Genetic control of inflammatory gene induction and NF κB-like transcription factor activation in response to an atherogenic diet in mice. *J. Clin. Investig.* **1993**, *91*, 2572–2579. [CrossRef] [PubMed]
52. Moghadasian, M.H.; McManus, B.M.; Pritchard, P.H.; Frohlich, J.J. “Tall oil”-derived phytosterols reduce atherosclerosis in ApoE-deficient mice. *Arterioscler. Thromb. Vasc. Biol.* **1997**, *17*, 119–126. [CrossRef] [PubMed]
53. Föger, B.; Chase, M.; Amar, M.J.; Vaisman, B.L.; Shamburek, R.D.; Paigen, B.; Fruchart-Najib, J.; Paiz, J.A.; Koch, C.A.; Hoyt, R.F.; et al. Cholesteryl ester transfer protein corrects dysfunctional high density lipoproteins and reduces aortic atherosclerosis in lecithin cholesterol acyltransferase transgenic mice. *J. Biol. Chem.* **1999**, *274*, 36912–36920. [CrossRef] [PubMed]
54. Moghadasian, M.H.; McManus, B.M.; Godin, D.V.; Rodrigues, B.; Frohlich, J.J. Proatherogenic and antiatherogenic effects of probucol and phytosterols in apolipoprotein E-deficient mice: Possible mechanisms of action. *Circulation* **1999**, *99*, 1733–1739. [CrossRef] [PubMed]
55. Nakashima, Y.; Plump, A.S.; Raines, E.W.; Breslow, J.L.; Ross, R. ApoE-deficient mice develop lesions of all phases of atherosclerosis throughout the arterial tree. *Arterioscler. Thromb. Vasc. Biol.* **1994**, *14*, 133–140. [CrossRef]
56. Piedrahita, J.A.; Zhang, S.H.; Hagaman, J.R.; Oliver, P.M.; Maeda, N. Generation of mice carrying a mutant apolipoprotein E gene inactivated by gene targeting in embryonic stem cells. *Proc. Natl. Acad. Sci. USA* **1992**, *89*, 4471–4475. [CrossRef] [PubMed]
57. Plump, A.S.; Smith, J.D.; Hayek, T.; Aalto-Setala, K.; Walsh, A.; Verstuyft, J.G.; Rubin, E.M.; Breslow, J.L. Severe hypercholesterolemia and atherosclerosis in apolipoprotein E-deficient mice created by homologous recombination in ES cells. *Cell* **1992**, *71*, 343–353. [CrossRef]
58. Meir, K.S.; Leitersdorf, E. Atherosclerosis in the apolipoprotein E-deficient mouse. A decade of progress. *Arterioscler. Thromb. Vasc. Biol.* **2004**, *24*, 1006–1014. [CrossRef] [PubMed]
59. Hansson, G.K.; Libby, P.; Schonbeck, U.; Yan, Z.Q. Innate and adaptive immunity in the pathogenesis of atherosclerosis. *Circ. Res.* **2002**, *91*, 281–291. [CrossRef] [PubMed]
60. Pereira, T.M.C.; Nogueira, B.V.; Lima, L.C.F.; Porto, M.L.; Arruda, J.A.; Vasquez, E.C.; Meyrelles, S.S. Cardiac and vascular changes in elderly atherosclerotic mice: The influence of gender. *Lipids Health Dis.* **2010**, *9*, 87–96. [CrossRef] [PubMed]
61. Heistad, D.D. Unstable coronary artery plaques. *N. Engl. J. Med.* **2003**, *349*, 2285–2287. [CrossRef] [PubMed]
62. Stary, H.C. The sequence of cell and matrix changes in atherosclerotic lesions of coronary arteries in the first forty years of life. *Eur. Heart J.* **1990**, *11*, 3–19. [CrossRef] [PubMed]
63. Jonasson, L.; Holm, J.; Skalli, O.; Bondjers, G.; Hansson, G.K. Regional accumulations of T cells, macrophages, and smooth muscle cells in the human atherosclerotic plaque. *Arteriosclerosis* **1986**, *6*, 131–138. [CrossRef] [PubMed]
64. Ishibashi, S.; Goldstein, J.L.; Brown, M.S.; Herz, J.; Burns, D.K. Massive xanthomatosis and atherosclerosis in cholesterol-fed low density lipoprotein receptor-negative mice. *J. Clin. Investig.* **1994**, *93*, 1885–1893. [CrossRef] [PubMed]
65. Reddick, R.L.; Zhang, S.H.; Maeda, N. Atherosclerosis in mice lacking ApoE: Evaluation of lesional development and progression. *Arterioscler. Thromb. Vasc. Biol.* **1994**, *14*, 141–147. [CrossRef]

66. Ma, Y.; Wang, W.; Zhang, J.; Lu, Y.; Wu, W.; Yan, H.; Wang, Y. Hyperlipidemia and atherosclerotic lesion development in Ldlr-deficient mice on a long-term high-fat diet. *PLoS ONE* **2012**, *7*, e35835.
67. Williams, H.; Johnson, J.L.; Carson, K.G.; Jackson, C.L. Characteristics of intact and ruptured atherosclerotic plaques in brachiocephalic arteries of apolipoprotein E knockout mice. *Arterioscler. Thromb. Vasc. Biol.* **2002**, *22*, 788–792. [CrossRef] [PubMed]
68. Getz, G.S. Mouse model of unstable atherosclerotic plaque? *Arterioscler. Thromb. Vasc. Biol.* **2000**, *20*, 2503–2505. [CrossRef] [PubMed]
69. Burke, A.P.; Kolodgie, F.D.; Farb, A.; Weber, D.K.; Malcom, G.T.; Smialek, J.; Virmani, R. Healed plaque ruptures and sudden coronary death. *Circulation* **2001**, *103*, 934–940. [CrossRef] [PubMed]
70. Johnson, J.; Carson, K.; Williams, H.; Karanam, S.; Newby, A.; Angelini, G.; George, S.; Jackson, C. Plaque rupture after short periods of fat feeding in the apolipoprotein E-knockout mouse: Model characterization and effects of pravastatin treatment. *Circulation* **2005**, *111*, 1422–1430. [CrossRef] [PubMed]
71. Johnson, J.L.; Jackson, C.L. Atherosclerotic plaque rupture in the apolipoprotein E knockout mouse. *Atherosclerosis* **2001**, *154*, 399–406. [CrossRef]
72. Calara, F.; Silvestre, M.; Casanada, F.; Yuan, N.; Napoli, C.; Palinski, W. Spontaneous plaque rupture and secondary thrombosis in apolipoprotein E-deficient and LDL receptor-deficient mice. *J. Pathol.* **2001**, *195*, 257–263. [CrossRef] [PubMed]
73. Van Vlijmen, B.J.; van den Maagdenberg, A.M.; Gijbels, M.J.; van der Boom, H.; HogenEsch, H.; Frants, R.R.; Hofker, M.H.; Havekes, L.M. Diet-induced hyperlipoproteinemia and atherosclerosis in apolipoprotein E3-Leiden transgenic mice. *J. Clin. Investig.* **1994**, *93*, 1403–1410. [CrossRef] [PubMed]
74. Davies, M.J. Acute coronary thrombosis—The role of plaque disruption and its initiation and prevention. *Eur. Heart J.* **1995**, *16*, 3–7. [CrossRef] [PubMed]
75. Van der Wal, A.C.; Becker, A.E.; van der Loos, C.M.; Das, P.K. Site of intimal rupture or erosion of thrombosed coronary atherosclerotic plaques is characterized by an inflammatory process irrespective of the dominant plaque morphology. *Circulation* **1994**, *89*, 36–44. [CrossRef] [PubMed]
76. Reddick, R.L.; Zhang, S.H.; Maeda, N. Aortic atherosclerotic plaque injury in apolipoprotein E deficient mice. *Atherosclerosis* **1998**, *140*, 297–305. [CrossRef]
77. Bentzon, J.F.; Sondergaard, C.S.; Kassem, M.; Falk, E. Smooth muscle cells healing atherosclerotic plaque disruptions are of local, not blood, origin in apolipoprotein E knockout mice. *Circulation* **2007**, *116*, 2053–2061. [CrossRef] [PubMed]
78. Cheng, C.; Tempel, D.; van Haperen, R.; van der Baan, A.; Grosved, F.; Daemen, M.J.A.P.; Kramps, R.; de Crom, R. Atherosclerotic lesion size and vulnerability are determined by patterns of fluid shear stress. *Circulation* **2006**, *113*, 2744–2753. [CrossRef] [PubMed]
79. Sasaki, T.; Kuzuya, M.; Nakamura, K.; Cheng, X.W.; Shibata, T.; Sato, K.; Iguchi, A. A simple method of plaque rupture induction in apolipoprotein E-deficient mice. *Arterioscler. Thromb. Vasc. Biol.* **2006**, *26*, 1304–1309. [CrossRef] [PubMed]
80. Aono, J.; Suzuki, J.; Iwai, M.; Horiuchi, M.; Nagai, T.; Nishimura, K.; Inoue, K.; Ogimoto, A.; Okayama, H.; Higaki, J. Deletion of the Angiotensin II Type 1a Receptor Prevents Atherosclerotic Plaque Rupture in Apolipoprotein E^{-/-} Mice. *Arterioscler. Thromb. Vasc. Biol.* **2012**, *32*, 1453–1459. [CrossRef] [PubMed]
81. Jin, S.X.; Shen, L.H.; Nie, P.; Yuan, W.; Hu, L.H.; Li, D.D.; Chen, X.J.; Zhang, X.K.; He, B. Endogenous renovascular hypertension combined with low shear stress induces plaque rupture in apolipoprotein E-deficient mice. *Arterioscler. Thromb. Vasc. Biol.* **2012**, *32*, 2372–2379. [CrossRef] [PubMed]
82. Lima, L.C.F.; Porto, M.L.; Campagnaro, B.P.; Tonini, C.L.; Nogueira, B.V.; Pereira, T.M.C.; Vasquez, E.C.; Meyrelles, S.S. Mononuclear cell therapy reverts cuff-induced thrombosis in apolipoprotein E-deficient mice. *Lipids Health Dis.* **2012**, *11*, 96–105. [CrossRef] [PubMed]
83. Schwartz, S.M.; Galis, Z.S.; Rosenfeld, M.E.; Falk, E. Plaque rupture in humans and mice. *Arterioscler. Thromb. Vasc. Biol.* **2007**, *27*, 705–713. [CrossRef] [PubMed]
84. Falk, E.; Schwartz, S.M.; Galis, Z.S.; Rosenfeld, M.E. Neointimal cracks (plaque rupture?) and thrombosis in wrapped arteries without flow. *Arterioscler. Thromb. Vasc. Biol.* **2007**, *27*, 248–249. [CrossRef] [PubMed]
85. Von der Thusen, J.H.; van Vlijmen, B.J.M.; Hoeben, R.C.; Kockx, M.M.; Havekes, L.M.; van Berkel, T.J.C.; Biessen, E.A.L. Induction of atherosclerotic plaque rupture in apolipoprotein E^{-/-} mice after adenovirus-mediated transfer of p53. *Circulation* **2002**, *105*, 2064–2070. [CrossRef] [PubMed]

86. Mallat, Z.; Gojova, A.; Marchiol-Fournigault, C.; Esposito, B.; Kamate, C.; Merval, R.; Fradelizi, D.; Tedgui, A. Inhibition of transforming growth factor- signaling accelerates atherosclerosis and induces an unstable plaque phenotype in mice. *Circ. Res.* **2001**, *89*, 930–934. [CrossRef] [PubMed]
87. Lutgens, E.; Gijbels, M.; Smook, M.; Heeringa, P.; Gotwals, P.; Koteliansky, V.E.; Daemen, M.J. Transforming growth factor- β mediates balance between inflammation and fibrosis during plaque progression. *Arterioscler. Thromb. Vasc. Biol.* **2002**, *22*, 975–982. [CrossRef] [PubMed]
88. Lutgens, E.; de Frutos, P.G.; Apericio, C.; Moons, L.; Daemen, M.; Collen, D.; Carmeliet, P. Gas6 $^{-/-}$ /ApoE $^{-/-}$ mice develop a collagen-rich, disorganized plaque phenotype, prone to intraplaque hemorrhage. *Circulation* **2000**, *102*, 38.
89. Angelillo-Scherrer, A.; de Frutos, P.; Aparicio, C.; Melis, E.; Savi, P.; Lupu, F.; Arnout, J.; Dewerchin, M.; Hoylaerts, M.; Herbert, J.; et al. Deficiency or inhibition of Gas6 causes platelet dys-function and protects mice against thrombosis. *Nat. Med.* **2001**, *7*, 215–221. [CrossRef] [PubMed]
90. Braun, A.; Trigatti, B.L.; Post, M.J.; Sato, K.; Simons, M.; Edelberg, J.M.; Rosenberg, R.D.; Schrenzel, M.; Krieger, M. Loss of SR-BI expression leads to the early onset of occlusive atherosclerotic coronary artery disease, spontaneous myocardial infarctions, severe cardiac dysfunction, and premature death in apolipoprotein E-deficient mice. *Circ. Res.* **2002**, *90*, 270–276. [CrossRef] [PubMed]
91. Gough, P.J.; Gomez, I.G.; Wille, P.T.; Raines, E.W. Macrophage expression of active MMP-9 induces acute plaque disruption in ApoE-deficient mice. *J. Clin. Investig.* **2006**, *116*, 59–69. [CrossRef] [PubMed]
92. Ma, T.; Gao, Q.; Zhu, F.; Guo, C.; Wang, Q.; Gao, F.; Zhang, L. Th17 cells and IL-17 are involved in the disruption of vulnerable plaques triggered by short-term combination stimulation in apolipoprotein E-knockout mice. *Cell. Mol. Immunol.* **2013**, *10*, 338–348. [CrossRef] [PubMed]
93. Pellegrin, M.; Mazzolai, L. Angiotensin II as an inducer of atherosclerosis: Evidence from mouse studies. *J. Clin. Exp. Cardiol.* **2013**. [CrossRef]
94. Billet, S.; Aguilar, F.; Baudry, C.; Clauser, E. Role of angiotensin II AT1 receptor activation in cardiovascular diseases. *Kidney Int.* **2008**, *74*, 1379–1384. [CrossRef] [PubMed]
95. Lemarié, C.A.; Schiffrin, E.L. The angiotensin II type 2 receptor in cardiovascular disease. *J. Renin Angiotensin Aldosterone Syst.* **2010**, *11*, 19–31. [CrossRef] [PubMed]
96. Daugherty, A.; Manning, M.W.; Cassis, L.A. Angiotensin II promotes atherosclerotic lesions and aneurysms in apolipoprotein E-deficient mice. *J. Clin. Investig.* **2000**, *105*, 1605–1612. [CrossRef] [PubMed]
97. Weiss, D.; Kools, J.J.; Taylor, W.R. Angiotensin II-induced hypertension accelerates the development of atherosclerosis in ApoE-deficient mice. *Circulation* **2001**, *103*, 448–454. [CrossRef] [PubMed]
98. Mazzolai, L.; Duchosal, M.A.; Korber, M.; Bouzourene, K.; Aubert, J.F.; Hao, H.; Vallet, V.; Brunner, H.R.; Nussberger, J.; Gabbiani, G.; et al. Endogenous angiotensin II induces atherosclerotic plaque vulnerability and elicits a Th1 response in ApoE $^{-/-}$ mice. *Hypertension* **2004**, *44*, 277–282. [CrossRef] [PubMed]
99. Ni, W.; Kitamoto, S.; Ishibashi, M.; Usui, M.; Inoue, S.; Hiasa, K.; Zhao, Q.; Nishida, K.; Takeshita, A.; Egashira, K. Monocyte chemoattractant protein-1 is an essential inflammatory mediator in angiotensin II-induced progression of established atherosclerosis in hypercholesterolemic mice. *Arterioscler. Thromb. Vasc. Biol.* **2004**, *24*, 534–539. [CrossRef] [PubMed]
100. Griendling, K.K.; Minieri, C.A.; Ollerenshaw, J.D.; Alexander, R.W. Angiotensin II stimulates NADH and NADPH oxidase activity in cultured vascular smooth muscle cells. *Circ. Res.* **1994**, *74*, 1141–1148. [CrossRef] [PubMed]
101. Simon, G.; Abraham, G. Angiotensin II administration as an experimental model of hypertension. In *Hypertension: Pathophysiology, Diagnosis, and Management*, 2nd ed.; Laragh, J.H., Brenner, B.M., Eds.; Raven Press Ltd.: New York, NY, USA, 1995; pp. 1423–1435.
102. Candido, R.; Jandeleit-Dahm, K.A.; Cao, Z.; Nesteroff, S.P.; Burns, W.C.; Twigg, S.M.; Dilley, R.J.; Cooper, M.E.; Allen, T.J. Prevention of accelerated atherosclerosis by angiotensin-converting enzyme inhibition in diabetic apolipoprotein E-deficient mice. *Circulation* **2002**, *106*, 246–253. [CrossRef] [PubMed]
103. Howard, B.V.; Rodriguez, B.L.; Bennett, P.H.; Harris, M.I.; Hamman, R.; Kuller, L.H.; Pearson, T.A.; Wylie-Rosett, J. Prevention conference VI: Diabetes and cardiovascular disease: Writing Group I: Epidemiology. *Circulation* **2002**, *105*, e132–e137. [CrossRef] [PubMed]
104. Beckman, J.A.; Creager, M.A.; Libby, P. Diabetes and atherosclerosis: Epidemiology, pathophysiology, and management. *JAMA* **2002**, *287*, 2570–2581. [CrossRef] [PubMed]

105. Taguchi, S.; Oinuma, T.; Yamada, T. A comparative study of cultured smooth muscle cell proliferation and injury, utilizing glycated low density lipoproteins with slight oxidation, auto-oxidation, or extensive oxidation. *J. Atheroscler. Thromb.* **2000**, *7*, 132–137. [CrossRef]
106. Schreyer, S.A.; Wilson, D.L.; LeBoeuf, R.C. C57BL/6 mice fed high fat diets as models for diabetes-accelerated atherosclerosis. *Atherosclerosis* **1998**, *136*, 17–24. [CrossRef]
107. King, V.L.; Hatch, N.W.; Chan, H.W.; deBeer, M.C.; deBeer, F.C.; Tannock, L.R. A murine model of obesity with accelerated atherosclerosis. *Obesity* **2010**, *18*, 35–41. [CrossRef] [PubMed]
108. Cannizzo, B.; Luján, A.; Estrella, N.; Lembo, C.; Cruzado, M.; Castro, C. Insulin resistance promotes early atherosclerosis via increased proinflammatory proteins and oxidative stress in fructose-fed ApoE-KO mice. *Exp. Diabetes Res.* **2012**, *2012*, 941304. [CrossRef] [PubMed]
109. Merat, S.; Casanada, F.; Sutphin, M.; Palinski, W.; Reaven, P.D. Western-type diets induce insulin resistance and hyperinsulinemia in LDL receptor-deficient mice but do not increase aortic atherosclerosis compared with normoinsulinemic mice in which similar plasma cholesterol levels are achieved by a fructose-rich diet. *Arterioscler. Thromb. Vasc. Biol.* **1999**, *19*, 1223–1230. [CrossRef] [PubMed]
110. Schreyer, S.A.; Lystig, T.C.; Vick, C.M.; LeBoeuf, R.C. Mice deficient in apolipoprotein E but not LDL receptors are resistant to accelerated atherosclerosis associated with obesity. *Atherosclerosis* **2003**, *171*, 49–55. [CrossRef] [PubMed]
111. Kunjathoor, V.V.; Wilson, D.L.; LeBoeuf, R.C. Increased atherosclerosis in streptozotocin-induced diabetic mice. *J. Clin. Investig.* **1996**, *97*, 1767–1773. [CrossRef] [PubMed]
112. Park, L.; Raman, K.G.; Lee, K.J.; Lu, Y.; Ferran, L.J., Jr.; Chow, W.S.; Stern, D.; Schmidt, A.M. Suppression of accelerated diabetic atherosclerosis by the soluble receptor for advanced glycation endproducts. *Nat. Med.* **1998**, *4*, 1025–1031. [CrossRef] [PubMed]
113. Calkin, A.C.; Forbes, J.M.; Smith, C.M.; Lassila, M.; Cooper, M.E.; Jandeleit-Dahm, K.A.; Allen, T.J. Rosiglitazone attenuates atherosclerosis in a model of insulin insufficiency independent of its metabolic effects. *Arterioscler. Thromb. Vasc. Biol.* **2005**, *25*, 1903–9. [CrossRef] [PubMed]
114. Zuccollo, A.; Shi, C.; Mastroianni, R.; Maitland-Toolan, K.A.; Weisbrod, R.M.; Zang, M.; Xu, S.; Jiang, B.; Oliver-Krasinski, J.M.; Cayatte, A.J.; et al. The thromboxane A2 receptor antagonist S18886 prevents enhanced atherogenesis caused by diabetes mellitus. *Circulation* **2005**, *112*, 3001–3008. [CrossRef] [PubMed]
115. Veerman, K.J.; Venegas-Pino, D.E.; Shi, Y.; Khan, M.I.; Gerstein, H.C.; Werstuck, G.H. Hyperglycaemia is associated with impaired vasa vasorum neovascularization and accelerated atherosclerosis in apolipoprotein-E deficient mice. *Atherosclerosis* **2013**, *227*, 250–258. [CrossRef] [PubMed]
116. Vikramadithyan, R.K.; Hu, Y.; Noh, H.L.; Liang, C.P.; Hallam, K.; Tall, A.R.; Ramasamy, R.; Goldberg, I.J. Human aldose reductase expression accelerates diabetic atherosclerosis in transgenic mice. *J. Clin. Investig.* **2005**, *115*, 2434–2443. [CrossRef] [PubMed]
117. Jun, J.Y.; Ma, Z.; Segar, L. Spontaneously diabetic Ins²⁺/Akita:ApoE-deficient mice exhibit exaggerated hypercholesterolemia and atherosclerosis. *Am. J. Physiol. Endocrinol. Metabol.* **2011**, *301*, E145–E154. [CrossRef] [PubMed]
118. Zhou, C.; Pridgen, B.; King, N.; Xu, J.; Breslow, J.L. Hyperglycemic Ins²⁺/Akita/Ldlr^{-/-} mice show severely elevated lipid levels and increased atherosclerosis: A model of type 1 diabetic macrovascular disease. *J. Lipid Res.* **2011**, *52*, 1483–1493. [CrossRef] [PubMed]
119. Engelbertsen, D.; To, F.; Dunér, P.; Kotova, O.; Söderberg, I.; Alm, R.; Gomez, M.F.; Nilsson, J.; Bengtsson, E. Increased inflammation in atherosclerotic lesions of diabetic Akita-LDLr^{-/-} mice compared to nondiabetic LDLr^{-/-} mice. *Exp. Diabetes Res.* **2012**, *2012*, 1–12. [CrossRef] [PubMed]
120. Wang, Z.H.; Shang, Y.Y.; Zhang, S.; Zhong, M.; Wang, X.P.; Deng, J.T.; Pan, J.; Zhang, Y.; Zhang, W. Silence of TRIB3 suppresses atherosclerosis and stabilizes plaques in diabetic ApoE^{-/-}/LDL receptor^{-/-} mice. *Diabetes* **2012**, *61*, 463–473. [CrossRef] [PubMed]
121. Wu, K.K.; Wu, T.J.; Chin, J.; Mitnaul, L.J.; Hernandez, M.; Cai, T.Q.; Ren, N.; Waters, M.G.; Wright, S.D.; Cheng, K. Increased hypercholesterolemia and atherosclerosis in mice lacking both ApoE and leptin receptor. *Atherosclerosis* **2005**, *181*, 251–259. [CrossRef] [PubMed]
122. Wendt, T.; Harja, E.; Buccicarelli, L.; Qu, W.; Lu, Y.; Rong, L.L.; Jenkins, D.G.; Stein, G.; Schmidt, A.M.; Yan, S.F. RAGE modulates vascular inflammation and atherosclerosis in a murine model of type 2 diabetes. *Atherosclerosis* **2006**, *185*, 70–77. [CrossRef] [PubMed]

123. Vliegenthart, R.; Oudkerk, M.; Hofman, A.; Oei, H.H.; van Dijck, W.; van Rooij, F.J.; Witteman, J.C. Coronary calcification improves cardiovascular risk prediction in the elderly. *Circulation* **2005**, *112*, 572–577. [CrossRef] [PubMed]
124. Janssen, C.H.; Kuijpers, D.; Vliegenthart, R.; Overbosch, J.; van Dijkman, P.R.; Zijlstra, F.; Oudkerk, M. Coronary artery calcification score by multislice computed tomography predicts the outcome of dobutamine cardiovascular magnetic resonance imaging. *Eur. Radiol.* **2005**, *15*, 1128–1134. [CrossRef] [PubMed]
125. Otsuka, F.; Sakakura, K.; Yahagi, K.; Joner, M.; Virmani, R. Has our understanding of calcification in human coronary atherosclerosis progressed? *Arterioscler. Thromb. Vasc. Biol.* **2014**, *34*, 724–736. [CrossRef] [PubMed]
126. Lin, T.C.; Tintut, Y.; Lyman, A.; Mack, W.; Demer, L.L.; Hsiai, T.K. Mechanical response of a calcified plaque model to fluid shear force. *Ann. Biomed. Eng.* **2006**, *34*, 1535–1541. [CrossRef] [PubMed]
127. Maldonado, N.; Kelly-Arnold, A.; Vengrenyuk, Y.; Laudier, D.; Fallon, J.T.; Virmani, R.; Cardoso, L.; Weinbaum, S. A mechanistic analysis of the role of microcalcifications in atherosclerotic plaque stability: Potential implications for plaque rupture. *Am. J. Physiol. Heart Circ. Physiol.* **2012**, *303*, 619–628. [CrossRef] [PubMed]
128. Kelly-Arnold, A.; Maldonado, N.; Laudier, D.; Aikawa, E.; Cardoso, L.; Weinbaum, S. Revised microcalcification hypothesis for fibrous cap rupture in human coronary arteries. *Proc. Natl. Acad. Sci. USA* **2013**, *110*, 10741–10746. [CrossRef] [PubMed]
129. Qiao, J.H.; Xie, P.Z.; Fishbein, M.C.; Kreuzer, J.; Drake, T.A.; Demer, L.L.; Lusis, A.J. Pathology of atheromatous lesions in inbred and genetically engineered mice: Genetic determination of arterial calcification. *Arterioscler. Thromb.* **1994**, *14*, 1480–1497. [CrossRef] [PubMed]
130. Qiao, J.H.; Fishbein, M.C.; Demer, L.L.; Lusis, A.J. Genetic determination of cartilaginous metaplasia in mouse aorta. *Arterioscler. Thromb. Vasc. Biol.* **1995**, *15*, 2265–2272. [CrossRef] [PubMed]
131. Rattazzi, M.; Bennett, B.J.; Bea, F.; Kirk, E.A.; Ricks, J.L.; Speer, M.; Schwartz, S.M.; Giachelli, C.M.; Rosenfeld, M.E. Calcification of advanced atherosclerotic lesions in the innominate arteries of ApoE-deficient mice: Potential role of chondrocyte-like cells. *Arterioscler. Thromb. Vasc. Biol.* **2005**, *25*, 1420–1425. [CrossRef] [PubMed]
132. Matsui, Y.; Rittling, S.R.; Okamoto, H.; Inobe, M.; Jia, N.; Shimizu, T.; Akino, M.; Sugawara, T.; Morimoto, J.; Kimura, C.; et al. Osteopontin deficiency attenuates atherosclerosis in female apolipoprotein E-deficient mice. *Arterioscler. Thromb. Vasc. Biol.* **2003**, *23*, 1029–1034. [CrossRef] [PubMed]
133. Speer, M.Y.; Chien, Y.C.; Quan, M.; Yang, H.Y.; Vali, H.; McKee, M.D.; Giachelli, C.M. Smooth muscle cells deficient in osteopontin have enhanced susceptibility to calcification in vitro. *Cardiovasc. Res.* **2005**, *66*, 324–333. [CrossRef] [PubMed]
134. Debernardi, N.; Roijers, R.B.; Krams, R.; de Crom, R.; Mutsaers, P.H. A.; van der Vusse, G.J. Microcalcifications in atherosclerotic lesion of apolipoprotein E-deficient mouse. *Int. J. Exp. Pathol.* **2010**, *91*, 485–494. [CrossRef] [PubMed]
135. Towler, D.A.; Bidder, M.; Latifi, T.; Coleman, T.; Semenkovich, C.F. Diet-induced diabetes activates an osteogenic gene regulatory program in the aortas of low density lipoprotein receptor-deficient mice. *J. Biol. Chem.* **1998**, *273*, 30427–30434. [CrossRef] [PubMed]
136. Browner, W.S.; Seeley, D.G.; Vogt, T.M.; Cummings, S.R. Non-trauma mortality in elderly women with low bone mineral density. Study of Osteoporotic Fractures Research Group. *Lancet* **1991**, *338*, 355–358. [CrossRef]
137. Uyama, O.; Yoshimoto, Y.; Yamamoto, Y.; Kawai, A. Bone changes and carotid atherosclerosis in postmenopausal women. *Stroke* **1997**, *28*, 1730–1732. [CrossRef] [PubMed]
138. Demer, L.L. Vascular calcification and osteoporosis: Inflammatory responses to oxidized lipids. *Int. J. Epidemiol.* **2002**, *31*, 737–741. [CrossRef] [PubMed]
139. Aikawa, E.; Nahrendorf, M.; Figueiredo, J.L.; Swirski, F.K.; Shtatland, T.; Kohler, R.H.; Jaffer, F.A.; Aikawa, M.; Weissleder, R. Osteogenesis associates with inflammation in early-stage atherosclerosis evaluated by molecular imaging in vivo. *Circulation* **2007**, *116*, 2841–2850. [CrossRef] [PubMed]
140. Hjortnaes, J.; Butcher, J.; Figueiredo, J.L.; Riccio, M.; Kohler, R.H.; Kozloff, K.M.; Weissleder, R.; Aikawa, E. Arterial and aortic valve calcification inversely correlates with osteoporotic bone remodelling: A role for inflammation. *Eur. Heart J.* **2010**, *31*, 1975–1984. [CrossRef] [PubMed]
141. Li, J.; Yan, M. GW26-e5327 micro-calcification regression in ApoE^{-/-} mice spontaneous atherosclerotic plaque by simvastatin on inhibition of endoplasmic reticulum mediated apoptosis. *J. Am. Coll. Cardiol.* **2015**, *66*. [CrossRef]

142. Van Herck, J.L.; de Meyer, G.R.; Martinet, W.; van Hove, C.E.; Foubert, K.; Theunis, M.H.; Apers, S.; Bult, H.; Vrints, C.J.; Herman, A.G. Impaired fibrillin-1 function promotes features of plaque instability in apolipoprotein E-deficient mice. *Circulation* **2009**, *120*, 2478–2487. [CrossRef] [PubMed]
143. Daeichin, V.; Sluimer, J.C.; van der Heiden, K.; Skachkov, I.; Kooiman, K.; Janssen, A.; Janssen, B.; Bosch, J.G.; de Jong, N.; Daemen, M.J.A.P.; et al. Live observation of atherosclerotic plaque disruption in apolipoprotein E-Deficient mouse. *Ultrasound Int. Open* **2015**, *1*, E67–E71. [CrossRef]
144. Roth, L.; van Dam, D.; van der Donckt, C.; Schrijvers, D.M.; Lemmens, K.; van Brussel, I.; de Deyn, P.P.; Martinet, W.; de Meyer, G.R. Impaired gait pattern as a sensitive tool to assess hypoxic brain damage in a novel mouse model of atherosclerotic plaque rupture. *Physiol. Behav.* **2015**, *139*, 397–402. [CrossRef] [PubMed]
145. Roche-Molina, M.; Sanz-Rosa, D.; Cruz, F.M.; García-Prieto, J.; López, S.; Abia, R.; Muriana, F.J.G.; Fuster, V.; Ibáñez, B.; Bernalet, J.A. Induction of sustained hypercholesterolemia by single adeno-associated virus-mediated gene transfer of mutant hPCSK9. *Arterioscler. Thromb. Vasc. Biol.* **2015**, *35*, 50–59. [CrossRef] [PubMed]
146. Van der Heiden, K.; Hoogendoorn, A.; Daemen, M.J.; Gijssen, F.J.H. Animal models for plaque rupture: A biomechanical assessment. *Thromb. Haemost.* **2015**, *115*, 501–508. [CrossRef] [PubMed]
147. Liu, X.; Ni, M.; Ma, L.; Yang, J.; Wang, L.; Liu, F.; Dong, M.; Yang, X.; Zhang, M.; Lu, H.; et al. Targeting blood thrombogenicity precipitates atherothrombotic events in a mouse model of plaque destabilization. *Sci. Rep.* **2015**, *5*, 10225. [CrossRef] [PubMed]
148. Ni, M.; Wang, Y.; Zang, M.; Zang, P.F.; Ding, S.F.; Liu, C.X. Atherosclerotic plaque disruption induced by stress and lipopolysaccharide in apolipoprotein E knockout mice. *Am. J. Physiol. Heart Circ. Physiol.* **2009**, *296*, H1598–H1606. [CrossRef] [PubMed]
149. Steinl, D.C.; Kaufmann, B.A. Ultrasound Imaging for Risk Assessment in Atherosclerosis. *Int. J. Mol. Sci.* **2015**, *16*, 9749–9769. [CrossRef] [PubMed]
150. Ross, R. Atherosclerosis: An inflammatory disease. *N. Engl. J. Med.* **1999**, *340*, 115–126. [CrossRef]
151. Dong, Z.M.; Wagner, D.D. Leukocyte-endothelium adhesion molecules in atherosclerosis. *J. Lab. Clin. Med.* **1998**, *132*, 369–375. [CrossRef]
152. Wick, G.; Grundtman, C. *Inflammation and Atherosclerosis*; SpringerWien: New York, NY, USA, 2012; pp. 121–122.
153. Davies, M.J.; Gordon, J.L.; Gearing, A.J.; Pigott, R.; Katz, D.; Kyriakopoulos, A. The expression of the adhesion molecules ICAM-1, VCAM-1, PECAM, and E-selectin in human atherosclerosis. *J. Pathol.* **1993**, *171*, 223–229. [CrossRef] [PubMed]
154. O'Brien, K.D.; Allen, M.D.; McDonald, T.O.; Chait, A.; Harlan, J.M.; Fishbein, D.; McCarty, J.; Ferguson, M.; Hudkins, K.; Benjamin, C.D.; et al. Vascular cell adhesion molecule-1 is expressed in human coronary atherosclerotic plaques. Implications for the mode of progression of advanced coronary atherosclerosis. *J. Clin. Investig.* **1993**, *92*, 945–951. [CrossRef] [PubMed]
155. George, S.J.; Johnson, J. *Atherosclerosis: Molecular and Cellular Mechanisms*; WILEY-VCH Verlag GmbH & Co. KGaA: Weinheim, Germany, 2010; pp. 47–50.
156. El-Osta, A.; Brasacchio, D.; Yao, D.; Pocai, A.; Jones, P.L.; Roeder, R.G.; Cooper, M.E.; Brownlee, M. Transient high glucose causes persistent epigenetic changes and altered gene expression during subsequent normoglycemia. *J. Exp. Med.* **2008**, *205*, 2409–2417. [CrossRef] [PubMed]
157. Poston, R.N.; Haskard, D.O.; Coucher, J.R.; Gall, N.P.; Johnson-Tidey, R.R. Expression of intercellular adhesion molecule-1 in atherosclerotic plaques. *Am. J. Pathol.* **1992**, *140*, 665–673. [PubMed]
158. Wood, K.M.; Cadogan, M.D.; Ramshaw, A.L.; Parus, D.V. The distribution of adhesion molecules in human atherosclerosis. *Histopathology* **1993**, *22*, 437–444. [CrossRef] [PubMed]
159. Nakashima, Y.; Raines, E.W.; Plump, A.S.; Breslow, J.L.; Ross, R. Upregulation of VCAM-1 and ICAM-1 at Atherosclerosis-Prone Sites on the Endothelium in the ApoE-Deficient Mouse. *Arterioscler. Thromb. Vasc. Biol.* **1998**, *18*, 842–851. [CrossRef] [PubMed]
160. Henninger, D.D.; Panes, J.; Eppihimer, M.; Russel, J.; Gerritsen, M.; Anderson, D.C.; Granger, D.N. Cytokine-induced VCAM-1, and ICAM-1 expression in different organs of the mouse. *J. Immunol.* **1997**, *158*, 1825–1832. [PubMed]
161. Johnson-Tidey, R.R.; McGregor, J.L.; Taylor, P.R.; Poston, R.N. Increase in the adhesion molecule P-selectin in endothelium overlying atherosclerotic plaques. Coexpression with intercellular adhesion molecule-1. *Am. J. Pathol.* **1994**, *144*, 952–961. [PubMed]

162. Dong, Z.M.; Brown, A.A.; Wagner, D.D. Prominent role of P-selectin in the development of advanced atherosclerosis in ApoE-deficient mice. *Circulation* **2000**, *101*, 2290–2295. [CrossRef] [PubMed]
163. Ramos, C.L.; Huo, Y.; Jung, U.; Ghosh, S.; Manka, D.R.; Sarembock, I.J.; Ley, K. Direct demonstration of P-selectin- and VCAM-1-dependent mono-nuclear cell rolling in early atherosclerotic lesions of apolipoprotein E-deficient mice. *Circ. Res.* **1999**, *84*, 1237–1244. [CrossRef] [PubMed]
164. Burger, P.C.; Wagner, D.D. Platelet P-selectin facilitates atherosclerotic lesion development. Platelet P-selectin facilitates atherosclerotic lesion development. *Blood* **2003**, *101*, 2661–2666. [CrossRef] [PubMed]
165. Manka, D.; Forlow, S.B.; Sanders, J.M.; Hurwitz, D.; Bennett, D.K.; Green, S.A.; Ley, K.; Sarembock, I.J. Critical role of platelet P-selectin in the response to arterial injury in apolipoprotein-E-deficient mice. *Arterioscler. Thromb. Vasc. Biol.* **2004**, *24*, 1124–1129. [CrossRef] [PubMed]
166. Narula, J.; Garg, P.; Achenbach, S.; Motoyama, S.; Virmani, R.; Strauss, H.W. Arithmetic of vulnerable plaques for noninvasive imaging. *Nat. Clin. Pract. Cardiovasc. Med.* **2008**, *5*, S2–S10. [CrossRef] [PubMed]
167. Jaffer, F.A.; Libby, P.; Weissleder, R. Molecular and cellular imaging of atherosclerosis: Emerging applications. *J. Am. Coll. Cardiol.* **2006**, *47*, 1328–1338. [CrossRef] [PubMed]
168. Libby, P. Inflammation in atherosclerosis. *Nature* **2002**, *420*, 868–874. [CrossRef] [PubMed]
169. Xu, X.H.; Shah, P.K.; Faure, E.; Equils, O.; Thomas, L.; Fishbein, M.C.; Luthringer, D.; Xu, X.P.; Rajavashisth, T.B.; Yano, J.; et al. Toll-like receptor-4 is expressed by macrophages in murine and human lipid-rich atherosclerotic plaques and upregulated by oxidized LDL. *Circulation* **2001**, *104*, 3103–3108. [CrossRef] [PubMed]
170. Ayala-López, W.; Xia, W.; Varghese, B.; Low, P.S. Imaging of atherosclerosis in apolipoprotein E knockout mice: Targeting of a folate-conjugated radiopharmaceutical to activated macrophages. *J. Nucl. Med.* **2010**, *51*, 768–774. [CrossRef] [PubMed]
171. Müller, A.; Beck, K.; Rancic, Z.; Müller, C.; Fischer, C.R.; Betzel, T.; Kaufmann, P.A.; Schibli, R.; Krämer, S.D.; Ametamey, S.M. Imaging atherosclerotic plaque inflammation via folate receptor targeting using a novel 18F-folate radiotracer. *Mol. Imaging* **2014**, *13*, 1–11. [PubMed]
172. Chen, Y.X.; Nakashima, Y.; Tanaka, K.; Shiraishi, S.; Nakagawa, K.; Sueishi, K. Immunohistochemical expression of vascular endothelial growth factor/vascular permeability factor in atherosclerotic intimas of human coronary arteries. *Arterioscler. Thromb. Vasc. Biol.* **1999**, *19*, 131–139. [CrossRef] [PubMed]
173. Celletti, F.L.; Hilfiker, P.R.; Ghafouri, P.; Dake, M.D. Effect of human recombinant vascular endothelial growth factor165 on progression of atherosclerotic plaque. *J. Am. Coll. Cardiol.* **2001**, *37*, 2126–2130. [CrossRef]
174. Virmani, R.; Kolodgie, F.D.; Burke, A.P.; Finn, A.V.; Gold, H.K.; Tulenko, T.N.; Wrenn, S.P.; Narula, J. Atherosclerotic plaque progression and vulnerability to rupture: Angiogenesis as a source of intraplaque hemorrhage. *Arterioscler. Thromb. Vasc. Biol.* **2005**, *25*, 2054–2061. [CrossRef] [PubMed]
175. Holm, P.W.; Slart, R.H.; Zeebregts, C.J.; Hillebrands, J.L.; Tio, R.A. Atherosclerotic plaque development and instability: A dual role for VEGF. *Ann. Med.* **2009**, *41*, 257–264. [CrossRef] [PubMed]
176. Olson, F.J.; Strömbert, S.; Hjelmgren, O.; Kjeldahl, J.; Fagerberg, B.; Bergström, G.M. Increased vascularization of shoulder regions of carotid atherosclerotic plaques from patients with diabetes. *J. Vasc. Surg.* **2011**, *54*, 1324–1331. [CrossRef] [PubMed]
177. Johansson, F.; Kramer, F.; Barnhart, S.; Kanter, J.E.; Vaisar, T.; Merrill, R.D.; Merrill, R.D.; Geng, L.; Oka, K.; Chan, L.; et al. Type 1 diabetes promotes disruption of advanced atherosclerotic lesions in LDL receptor-deficient mice. *Proc. Natl. Acad. Sci. USA* **2008**, *105*, 2082–2087. [CrossRef] [PubMed]
178. Parathath, S.; Mick, S.L.; Feig, J.E.; Joaquin, V.; Grauer, L.; Habil, D.M.; Gassmann, M.; Gardner, L.B.; Fisher, E.A. Hypoxia is present in murine atherosclerotic plaques and has multiple effects on macrophage lipid metabolism. *Circ. Res.* **2011**, *109*, 1141–1152. [PubMed]
179. Zamir, M.; Silver, M.D. Vasculature in the walls of human coronary arteries. *Arch. Pathol. Lab. Med.* **1985**, *109*, 659–662. [PubMed]
180. Kamat, B.R.; Galli, S.J.; Barger, A.C.; Lainey, L.L.; Silverman, K.J. Neovascularization and coronary atherosclerotic plaque: Cinematographic localization and quantitative histologic analysis. *Hum. Pathol.* **1987**, *18*, 1036–1042. [PubMed]
181. Zhang, Y.; Cliff, W.J.; Schoefl, G.I.; Higgins, G. Immunohistochemical study of intimal microvessels in coronary atherosclerosis. *Am. J. Pathol.* **1993**, *143*, 164–172. [PubMed]
182. Sueishi, K.; Yonemitsu, Y.; Nakagawa, K.; Kaneda, Y.; Kumamoto, M.; Nakashima, Y. Atherosclerosis and angiogenesis: Its pathophysiological significance in humans as well as in an animal model induced by the gene transfer of vascular endothelial growth factor. *Ann. N. Y. Acad. Sci.* **1997**, *811*, 311–324. [CrossRef] [PubMed]

183. Moulton, K.S.; Heller, E.; Konerding, M.A.; Flynn, E.; Palinski, W.; Folkman, J. Angiogenesis inhibitors endostatin or TNP-470 reduce intimal neovascularization and plaque growth in apolipoprotein E-deficient mice. *Circulation* **1999**, *99*, 1726–1732. [CrossRef] [PubMed]
184. Moulton, K.S.; Vakili, K.; Zurakowski, D.; Soliman, M.; Butterfield, C.; Sylvain, E.; Lo, K.M.; Gillies, S.; Javaherian, K.; Folkman, J. Inhibition of plaque neovascularization reduces macrophage accumulation and progression of advanced atherosclerosis. *Proc. Natl. Acad. Sci. USA* **2003**, *8*, 4736–4741. [CrossRef] [PubMed]
185. Tekabe, Y.; Li, Q.; Luma, J.; Weisenberger, D.; Sedlar, M.; Harja, E.; Narula, J.; Johnson, L.L. Noninvasive monitoring the biology of atherosclerotic plaque development with radiolabeled annexin V and matrix metalloproteinase inhibitor in spontaneous atherosclerotic mice. *J. Nucl. Cardiol.* **2010**, *17*, 1073–1081. [CrossRef] [PubMed]
186. Waldeck, J.; Häger, F.; Höltke, C.; Lanckohr, C.; von Wallbrunn, A.; Torsello, G.; Heindel, W.; Theilmeier, G.; Schäfers, M.; Bremer, C. Fluorescence reflectance imaging of macrophage-rich atherosclerotic plaques using an $\alpha_v\beta_3$ integrin-targeted fluorochrome. *J. Nucl. Med.* **2008**, *49*, 1845–1851. [CrossRef] [PubMed]
187. Winter, P.M.; Caruthers, S.D.; Allen, J.S.; Cai, K.; Williams, T.A.; Lanza, G.M.; Wickline, S.A. Molecular imaging of angiogenic therapy in peripheral vascular disease with $\alpha_v\beta_3$ -integrin-targeted nanoparticles. *Magn. Reson. Med.* **2010**, *64*, 369–376. [PubMed]
188. Hoshiga, M.; Alpers, C.E.; Smith, L.L.; Giachelli, C.M.; Schwartz, S.M. $\alpha_v\beta_3$ integrin expression in normal and atherosclerotic artery. *Circ. Res.* **1995**, *77*, 1129–1135. [CrossRef] [PubMed]
189. Antonov, A.S.; Kolodgie, F.D.; Munn, D.H.; Gerrity, R.G. Regulation of macrophage foam cell formation by $\alpha_v\beta_3$ integrin—Potential role in human atherosclerosis. *Am. J. Pathol.* **2004**, *165*, 247–258. [CrossRef]
190. Beer, A.J.; Schwaiger, M. Imaging of integrin $\alpha_v\beta_3$ expression. *Cancer Metastasis Rev.* **2008**, *27*, 631–644. [CrossRef] [PubMed]
191. Dufourcq, P.; Louis, H.; Moreau, C.; Daret, D.; Boisseau, M.R.; Lamaziere, J.M.D.; Bonnet, J. Vitronectin expression and interaction with receptors in smooth muscle cells from human atheromatous plaque. *Arterioscler. Thromb. Vasc. Biol.* **1998**, *18*, 168–176. [CrossRef] [PubMed]
192. Tabas, I. Macrophage apoptosis in atherosclerosis: Consequences on plaque progression and the role of endoplasmic reticulum stress. *Antioxid. Redox Signal.* **2009**, *11*, 2333–2339. [CrossRef] [PubMed]
193. Seimon, T.; Tabas, I. Mechanisms and consequences of macrophage apoptosis in atherosclerosis. *J. Lipid Res.* **2009**, *50*, S382–S387. [CrossRef] [PubMed]
194. Van Engeland, M.; Nieland, L.J.; Ramaekers, F.C.; Schutte, B.; Reutelingsperger, C.P. Annexin V-affinity assay: A review on an apoptosis detection system based on phosphatidylserine exposure. *Cytometry* **1998**, *31*, 1–9. [CrossRef]
195. Koopman, G.; Reutelingsperger, C.P.; Kuijten, G.A.; Keehnen, R.M.; Pals, S.T.; van Oers, M.H. Annexin V for flow cytometric detection of phosphatidylserine expression on B cells undergoing apoptosis. *Blood* **1994**, *84*, 1415–1420. [PubMed]
196. Laufer, E.M.; Reutelingsperger, C.P.; Narula, J.; Hofstra, L. Annexin A5: An imaging biomarker of cardiovascular risk. *Basic Res. Cardiol.* **2008**, *103*, 95–104. [CrossRef] [PubMed]
197. Isobe, S.; Tsimikas, S.; Zhou, J.; Fujimoto, S.; Sarai, M.; Branks, M.J.; Fujimoto, A.; Hofstra, L.; Reutelingsperger, C.P.; Murohara, T.; et al. Noninvasive imaging of atherosclerotic lesions in apolipoprotein E-deficient and low-density-lipoprotein receptor-deficient mice with annexin A5. *J. Nucl. Med.* **2006**, *47*, 1497–1505. [PubMed]
198. Van Tilborg, G.A.; Vucic, E.; Strijkers, G.J.; Cormode, D.P.; Mani, V.; Skajaa, T.; Reutelingsperger, C.P.; Fayad, Z.A.; Mulder, W.J.; Nicolay, K. Annexin A5-functionalized bimodal nanoparticles for MRI and fluorescence imaging of atherosclerotic plaques. *Bioconjug. Chem.* **2010**, *21*, 1794–1803. [CrossRef] [PubMed]
199. Laufer, E.M.; Winkens, H.M.; Corsten, M.F.; Reutelingsperger, C.P.; Narula, J.; Hofstra, L. PET and SPECT imaging of apoptosis in vulnerable atherosclerotic plaques with radiolabeled Annexin A5. *Q. J. Nucl. Med. Mol. Imaging* **2009**, *53*, 26–34. [PubMed]
200. Kietselaer, B.L.; Reutelingsperger, C.P.; Heidendal, G.A.; Daemen, M.J.; Mess, W.H.; Hofstra, L.; Narula, J. Noninvasive detection of plaque instability with use of radiolabeled annexin A5 in patients with carotid-artery atherosclerosis. *N. Engl. J. Med.* **2004**, *350*, 1472–1473. [CrossRef] [PubMed]
201. Guo, S.; Shen, S.; Wang, J.; Wang, H.; Li, M.; Liu, Y.; Hou, F.; Liao, Y.; Bin, J. Detection of high-risk atherosclerotic plaques with ultrasound molecular imaging of glycoprotein IIb/IIIa receptor on activated platelets. *Theranostics* **2015**, *5*, 418–430. [CrossRef] [PubMed]

202. Metzger, K.; Vogel, S.; Chatterjee, M.; Borst, O.; Seizer, P.; Schönberger, T.; Geisler, T.; Lang, F.; Langer, H.; Rheinlaender, J.; et al. High-frequency ultrasound-guided disruption of glycoprotein VI-targeted microbubbles targets atheropressison in mice. *Biomaterials* **2015**, *36*, 80–89. [CrossRef] [PubMed]
203. Katoh, M.; Haage, P.; Wiethoff, A.J.; Gunther, R.W.; Bucker, A.; Tacke, J.; Spuentrup, E. Molecular magnetic resonance imaging of deep vein thrombosis using a fibrin-targeted contrast agent: A feasibility study. *Investig. Radiol.* **2009**, *44*, 146–150. [CrossRef] [PubMed]
204. Vymazal, J.; Spuentrup, E.; Cardenas-Molina, G.; Wiethoff, A.J.; Hartmann, M.G.; Caravan, P.; Parsons, E.C., Jr. Thrombus imaging with fibrin-specific gadolinium-based MR contrast agent EP-2104R: Results of a phase II clinical study of feasibility. *Investig. Radiol.* **2009**, *44*, 697–704. [CrossRef] [PubMed]
205. Jaffer, F.A.; Tung, C.H.; Wykrzykowska, J.J.; Ho, N.H.; Houng, A.K.; Reed, G.L.; Weissleder, R. Molecular imaging of factor XIIIa activity in thrombosis using a novel, near-infrared fluorescent contrast agent that covalently links to thrombi. *Circulation* **2004**, *110*, 170–176. [CrossRef] [PubMed]
206. Miserus, R.J.; Herias, M.V.; Prinzen, L.; Lobbes, M.B.; van Suylen, R.J.; Dirksen, A.; Hackeng, T.M.; Heemskerk, J.W.; van Engelshoven, J.M.; Daemen, M.J.; et al. Molecular MRI of early thrombus formation using a bimodal α 2-antiplasmin-based contrast agent. *JACC Cardiovasc. Imaging* **2009**, *2*, 987–996. [CrossRef] [PubMed]
207. Greco, A.; Mancini, M.; Gargiulo, S.; Gramanzini, M.; Claudio, P.P.; Brunetti, A.; Salvatore, M. Ultrasound biomicroscopy in small animal research: Applications in molecular and preclinical imaging. *J. Biomed. Biotechnol.* **2012**, *2012*, 519238. [CrossRef] [PubMed]
208. Mancini, M.; Greco, A.; Salvatore, G.; Liuzzi, R.; di Maro, G.; Vergara, E.; Chiappetta, G.; Pasquinelli, R.; Brunetti, A.; Salvatore, M. Imaging of thyroid tumor angiogenesis with microbubbles targeted to vascular endothelial growth factor receptor type 2 in mice. *BMC Med. Imaging* **2013**, *13*, 31–40. [CrossRef] [PubMed]
209. Bekererdjian, R.; Chen, S.; Frenkel, P.A.; Grayburn, P.A.; Shohet, R.V. Ultrasound-targeted microbubble destruction can repeatedly direct highly specific plasmid expression to the heart. *Circulation* **2003**, *108*, 1022–1026. [CrossRef] [PubMed]
210. Bekererdjian, R.; Chen, S.; Grayburn, P.A.; Shohet, R.V. Augmentation of cardiac protein delivery using ultrasound targeted microbubble destruction. *Ultrasound Med. Biol.* **2005**, *31*, 687–691. [CrossRef] [PubMed]
211. Inaba, Y.; Linder, J.R. Molecular Imaging of disease with targeted contrast ultrasound imaging. *Transl. Res.* **2012**, *159*, 140–148. [CrossRef] [PubMed]
212. Khanicheh, E.; Mitterhuber, M.; Xu, L.; Haeuselmann, S.P.; Kuster, G.M.; Kaufmann, B.A. Noninvasive ultrasound molecular imaging of the effect of statins on endothelial inflammatory phenotype in early atherosclerosis. *PLoS ONE* **2013**, *8*, e58761. [CrossRef] [PubMed]
213. Liu, Y.; Davidson, B.P.; Yue, Q.; Belcik, T.; Xie, A.; Inaba, Y.; McCarty, O.J.; Tormoen, G.W.; Zhao, Y.; Ruggeri, Z.M.; et al. Molecular imaging of inflammation and platelet adhesion in advanced atherosclerosis effects of antioxidant therapy with NADPH oxidase inhibition. *Circ. Cardiovasc. Imaging* **2013**, *6*, 74–82. [CrossRef] [PubMed]
214. Wang, X.; Hagemeyer, C.E.; Hohmann, J.D.; Leitner, E.; Armstrong, P.C.; Jia, F.; Olschewski, M.; Needles, A.; Peter, K.; Ahrens, I. Novel single-chain antibody-targeted microbubbles for molecular ultrasound imaging of thrombosis: Validation of a unique noninvasive method for rapid and sensitive detection of thrombi and monitoring of success or failure of thrombolysis in mice. *Circulation* **2012**, *125*, 3117–3126. [CrossRef] [PubMed]
215. Kiessling, F.; Fokong, S.; Koczera, P.; Lederle, W.; Lammers, T. Ultrasound microbubbles for molecular diagnosis, therapy, and theranostics. *J. Nucl. Med.* **2012**, *53*, 345–348. [CrossRef] [PubMed]
216. Schinkel, A.F.L.; Kaspar, M.; Staub, D. Contrast-enhanced ultrasound: Clinical applications in patients with atherosclerosis. *Int. J. Cardiovasc. Imaging* **2016**, *32*, 35–48. [CrossRef] [PubMed]
217. Kaufmann, B.A.; Sanders, J.M.; Davis, C.; Xie, A.; Aldred, P.; Sarembock, I.J.; Linder, J.R. Molecular imaging of inflammation in atherosclerosis with targeted ultrasound detection of vascular cell adhesion molecule-1. *Circulation* **2007**, *116*, 276–284. [CrossRef] [PubMed]
218. Wu, J.; Leong-Poi, H.; Bin, L.; Yang, L.; Liao, Y.; Liu, Y.; Cai, J.; Xie, J.; Liu, Y. Efficacy of contrast-enhanced US and magnetic microbubbles targeted to vascular cell adhesion molecule-1 for molecular imaging of atherosclerosis. *Radiology* **2011**, *2*, 463–471. [CrossRef] [PubMed]

219. Khanicheh, E.; Qi, Y.; Xie, A.; Mitterhuber, M.; Xu, L.; Mochizuki, M.; Daali, Y.; Jaquet, V.; Krause, K.H.; Ruggeri, Z.M.; et al. Molecular imaging reveals rapid reduction of endothelial activation in early atherosclerosis with apocynin independent of antioxidative properties. *Arterioscler. Thromb. Vasc. Biol.* **2013**, *33*, 2187–2192. [CrossRef] [PubMed]
220. Kaufmann, B.A.; Carr, C.L.; Belcik, J.T.; Xie, A.; Yue, Q.; Chadderton, S.; Caplan, E.S.; Khangura, J.; Bullens, S.; Bunting, S.; et al. Molecular imaging of the initial inflammatory response in atherosclerosis. Implications for early detection of disease. *Arterioscler. Thromb. Vasc. Biol.* **2010**, *30*, 54–59. [CrossRef] [PubMed]
221. McCarty, O.J.T.; Conley, R.B.; Shentu, W.; Tormoen, J.W.; Zha, D.; Xie, A.; Qi, Y.; Zhao, Y.; Carr, C.; Belchic, T.; et al. Molecular imaging of activated von willebrand factor to detect high-risk atherosclerotic phenotype. *ACC Cardiovasc. Imaging* **2010**, *3*, 947–955. [CrossRef] [PubMed]
222. Shim, C.Y.; Liu, Y.N.; Atkinson, T.; Xie, A.; Foster, T.; Davidson, B.P.; Treible, M.; Qi, Y.; López, J.A.; Munday, A.; et al. molecular imaging of platelet–endothelial interactions and endothelial von willebrand factor in early and mid-stage atherosclerosis. *Circ. Cardiovasc. Imaging* **2015**, *8*, e002765. [CrossRef] [PubMed]
223. Massberg, S.; Gawaz, M.; Gruner, S.; Schulte, V.; Konrad, I.; Zohlnhofer, D.; Heinemann, U.; Nieswandt, B. A crucial role of glycoprotein VI for platelet recruitment to the injured arterial wall in vivo. *J. Exp. Med.* **2003**, *197*, 41–49. [CrossRef] [PubMed]
224. Massberg, S.; Konrad, I.; Bultmann, A.; Schulz, C.; Munch, G.; Peluso, M.; Lorenz, M.; Schneider, S.; Besta, F.; Müller, I.; et al. Soluble glycoprotein VI dimer inhibits platelet adhesion and aggregation to the injured vessel wall in vivo. *FASEB J.* **2004**, *18*, 397–399. [CrossRef] [PubMed]
225. Jackson, S.P. Arterial thrombosis—insidious, unpredictable and deadly. *Nat. Med.* **2011**, *17*, 1423–1436. [CrossRef] [PubMed]
226. Wagner, C.L.; Mascelli, M.A.; Neblock, D.S.; Weisman, H.F.; Coller, B.S.; Jordan, R.E. Analysis of GPIIb/IIIa receptor number by quantification of 7E3 binding to human platelets. *Blood* **1996**, *88*, 907–914. [PubMed]
227. Aukrust, P.; Halvorsen, B.; Ueland, T.; Michelsen, A.E.; Skjelland, M.; Gullestad, L.; Yndestad, A.; Otterdal, K. Activated platelets and atherosclerosis. *Expert Rev. Cardiovasc. Ther.* **2010**, *8*, 1297–1307. [CrossRef] [PubMed]
228. Burtea, C.; Laurent, S.; Murariu, O.; Rattat, D.; Toubeau, G.; Verbruggen, A.; Vanherethem, D.; Vander Elst, L.; Muller, R.N. Molecular imaging of $\alpha_v\beta_3$ integrin expression in atherosclerotic plaques with a mimetic of RGD peptide grafted to Gd-DTPA. *Cardiovasc. Res.* **2008**, *78*, 148–157. [CrossRef] [PubMed]
229. Burtea, C.; Laurent, S.; Lancelot, E.; Ballet, S.; Murariu, O.; Rousseaux, O.; Port, M.; Vander Elst, L.; Corot, C.; Muller, R.N. Peptidic targeting of phosphatidylserine for the MRI detection of apoptosis in atherosclerotic plaques. *Mol. Pharmacol.* **2009**, *6*, 1903–1919. [CrossRef] [PubMed]
230. Burtea, C.; Ballet, S.; Laurent, S.; Rousseaux, O.; Dencausse, A.; Gonzalez, W.; Port, M.; Corot, C.; Vander Elst, L.; Muller, R.N. Development of a magnetic resonance imaging protocol for the characterization of atherosclerotic plaque by using vascular cell adhesion molecule-1 and apoptosis-targeted ultrasmall superparamagnetic iron oxide derivatives. *Arterioscler. Thromb. Vasc. Biol.* **2012**, *32*, e36–e48. [CrossRef] [PubMed]
231. Michalska, M.; Machtoub, L.; Manthey, H.D.; Bauer, E.; Herold, V.; Krohne, G.; Lykowsky, G.; Hildenbrand, M.; Kampf, T.; Jakob, P.; et al. Visualization of vascular inflammation in the atherosclerotic mouse by ultrasmall superparamagnetic iron oxide vascular cell adhesion molecule-1-specific nanoparticles. *Arterioscler. Thromb. Vasc. Biol.* **2012**, *32*, 2350–2357. [CrossRef] [PubMed]
232. Makowski, M.R.; Forbes, S.C.; Blume, U.; Warley, A.; Jansen, C.H.; Schuster, A.; Wiethoff, A.J.; Botnar, R.M. In vivo assessment of intraplaque and endothelial fibrin in ApoE^{-/-} mice by molecular MRI. *Atherosclerosis* **2012**, *222*, 43–49. [CrossRef] [PubMed]
233. Wu, X.; Balu, N.; Li, W.; Chen, Y.; Shi, X.; Kummitta, C.M.; Yu, X.; Yuan, C.; Lu, Z.R. Molecular MRI of atherosclerotic plaque progression in an ApoE^{-/-} mouse model with a CLT1 peptide targeted macrocyclic Gd(III) chelate. *Am. J. Nucl. Med. Mol. Imaging* **2013**, *3*, 446–455. [PubMed]
234. Segers, F.M.; den Adel, B.; Bot, I.; van der Graaf, L.M.; van der Veer, E.P.; Gonzalez, W.; Raynal, I.; de Winther, M.; Wodzig, W.K.; Poelmann, R.E.; et al. Scavenger receptor-AI-targeted iron oxide nanoparticles for in vivo MRI detection of atherosclerotic lesions. *Arterioscler. Thromb. Vasc. Biol.* **2013**, *33*, 1812–1819. [CrossRef] [PubMed]

235. Parolini, C.; Busnelli, M.; Ganzetti, G.S.; Deller, F.; Manzini, S.; Scanziani, E.; Johnson, J.L.; Sirtori, C.R.; Chiesa, G. Magnetic resonance imaging visualization of vulnerable atherosclerotic plaques at the brachiocephalic artery of apolipoprotein E knockout mice by the blood pool contrast agent B22956/1. *Mol. Imaging* **2014**, *13*. [CrossRef]
236. Tarin, C.; Carril, M.; Martin-Ventura, J.L.; Markuerkiaga, I.; Padro, D.; Llamas-Granda, P.; Moreno, J.A.; García, I.; Genicio, N.; Plaza-Garcia, S.; et al. Targeted gold-coated iron oxide nanoparticles for CD163 detection in atherosclerosis by MRI. *Sci. Rep.* **2015**, *5*, 17135. [CrossRef] [PubMed]
237. Wen, S.; Liu, D.F.; Cui, Y.; Harris, S.S.; Chen, Y.C.; Li, K.C.; Ju, S.H.; Teng, G.J. In vivo MRI detection of carotid atherosclerotic lesions and kidney inflammation in ApoE-deficient mice by using LOX-1 targeted iron nanoparticles. *Nanomedicine* **2014**, *10*, 639–649. [CrossRef] [PubMed]
238. Wang, Y.; Chen, J.; Yang, B.; Qiao, H.; Gao, L.; Su, T.; Ma, S.; Zhang, X.; Li, X.; Liu, G.; et al. In vivo MR and fluorescence dual-modality imaging of atherosclerosis characteristics in mice using profilin-1 targeted magnetic nanoparticles. *Theranostics* **2016**, *6*, 272–286. [CrossRef] [PubMed]
239. Nahrendorf, M.; Zhang, H.; Hembrador, S.; Panizzi, P.; Sosnovik, D.E.; Aikawa, E.; Libby, P.; Swirski, F.K.; Weissleder, R. Nanoparticle PET-CT imaging of macrophages in inflammatory atherosclerosis. *Circulation* **2008**, *117*, 379–387. [CrossRef] [PubMed]
240. Seo, J.W.; Baek, H.; Mahackian, L.M.; Kusunose, J.; Hamzah, J.; Ruoslahti, E.; Ferrara, K.W. ^{64}Cu -labeled LyP-1-dendrimer for PET-CT imaging of atherosclerotic plaque. *Bioconjug. Chem.* **2014**, *25*, 231–239. [CrossRef] [PubMed]
241. Li, D.; Patel, A.R.; Klibanov, A.L.; Kramer, C.M.; Ruiz, M.; Kang, B.Y.; Metha, J.L.; Beller, J.L.; Glover, D.K.; Meyer, C.H. Molecular imaging of atherosclerotic plaques targeted to oxidized LDL receptor LOX-1 by SPECT/CT and magnetic resonance. *Circ. Cardiovasc. Imaging* **2010**, *3*, 464–472. [CrossRef] [PubMed]
242. Foss, C.A.; Bedja, D.; Mease, R.C.; Wang, H.; Kass, D.A.; Chatterjee, S.; Pomper, M.G. Molecular imaging of inflammation in the ApoE $^{-/-}$ mouse model of atherosclerosis with IodoDPA. *Biochem. Biophys. Res. Commun.* **2015**, *461*, 70–75. [CrossRef] [PubMed]
243. Nahrendorf, M.; Keliher, E.; Panizzi, P.; Zhang, H.; Hembrador, S.; Figueiredo, J.L.; Aikawa, E.; Kelly, K.; Libby, P.; Weissleder, R. ^{18}F -4V for PET-CT imaging of VCAM-1 expression in atherosclerosis. *J. Am. Coll. Cardiol. Cardiovasc. Imag.* **2009**, *2*, 1213–1222. [CrossRef] [PubMed]
244. Bala, G.; Blykers, A.; Xavier, C.; Descamps, B.; Broisat, A.; Ghezzi, C.; Fagret, D.; van Camp, G.; Caveliers, V.; Vanhove, C.; et al. Targeting of vascular cell adhesion molecule-1 by ^{18}F -labelled nanobodies for PET/CT imaging of inflamed atherosclerotic plaques. *Eur. Heart J. Cardiovasc. Imaging* **2016**, *17*, 1001–1008. [CrossRef] [PubMed]
245. Broisat, A.; Hernot, S.; Toczek, J.; de Vos, J.; Riou, L.M.; Martin, S.; Ahmadi, M.; Thielens, N.; Wernery, U.; Caveliers, V.; et al. Nanobodies targeting mouse/human VCAM1 for the nuclear imaging of atherosclerotic lesions. *Circ. Res.* **2012**, *110*, 927–937. [CrossRef] [PubMed]
246. Dimastromatteo, J.; Broisat, A.; Perret, P.; Ahmadi, M.; Boturyn, D.; Dumy, P.; Fagret, D.; Riou, L.M.; Ghezzi, C. In vivo molecular imaging of atherosclerotic lesions in ApoE $^{-/-}$ mice using VCAM-1-specific, $^{99\text{m}}\text{Tc}$ -labeled peptidic sequences. *J. Nucl. Med.* **2013**, *54*, 1442–1449. [CrossRef] [PubMed]
247. Li, X.; Bauer, W.; Israel, I.; Kreissl, M.C.; Weirather, J.; Richter, D.; Bauer, E.; Herold, V.; Jakob, P.; Buck, A.; et al. Targeting P-selectin by gallium-68-labeled fucoidan positron emission tomography for noninvasive characterization of vulnerable plaques: Correlation with in vivo 17.6T MRI. *Arterioscler. Thromb. Vasc. Biol.* **2014**, *34*, 1661–1667. [CrossRef] [PubMed]
248. Nakamura, I.; Hasegawa, K.; Wada, Y.; Hirase, T.; Node, K.; Watanabe, Y. Detection of early stage atherosclerotic plaques using PET and CT fusion imaging targeting P-selectin in low density lipoprotein receptor-deficient mice. *Biochem. Biophys. Res. Commun.* **2013**, *433*, 47–51. [CrossRef] [PubMed]
249. Laitinen, I.; Saraste, A.; Weidl, E.; Poethko, T.; Weber, A.W.; Nekolla, S.G.; Leppänen, P.; Ylä-Herttuala, S.; Hözlwimmer, G.; Walch, A.; et al. Evaluation of $\alpha_v\beta_3$ integrin-targeted positron emission tomography tracer ^{18}F -galacto-RGD for imaging of vascular inflammation in atherosclerotic mice. *Circ. Cardiovasc. Imaging* **2009**, *2*, 331–338. [CrossRef] [PubMed]
250. Su, H.; Gorodny, N.; Gomez, L.F.; Gangadharan, U.B.; Mu, F.; Chen, G.; Walsh, J.C.; Szardenings, K.; Berman, D.S.; Kolb, H.C.; et al. Atherosclerotic plaque uptake of a novel integrin tracer ^{18}F -Flotegatide in a mouse model of atherosclerosis. *J. Nucl. Cardiol.* **2014**, *21*, 553–562. [CrossRef] [PubMed]

251. De Saint-Hubert, M.; Bauwens, M.; Deckers, N.; Drummen, M.; Douma, K.; Granton, P.; Hendrikx, G.; Kusters, D.; Bucerius, J.; Reutelingsperger, C.P.; et al. In vivo molecular imaging of apoptosis and necrosis in atherosclerotic plaques using microSPECT-CT and microPET-CT imaging. *Mol. Imaging Biol.* **2014**, *16*, 246–254. [CrossRef] [PubMed]
252. Bigalke, B.; Phinikaridou, A.; Andia, M.E.; Cooper, M.S.; Schuster, A.; Schönberger, T.; Griessinger, C.M.; Wurster, T.; Onthank, D.; Ungerer, M.; et al. Positron emission tomography/computed tomographic and magnetic resonance imaging in a murine model of progressive atherosclerosis using ^{64}Cu -labeled glycoprotein VI-Fc. *Circ. Cardiovasc. Imaging* **2013**, *6*, 957–964. [CrossRef] [PubMed]
253. Dietrich, T.; Berndorff, D.; Heinrich, T.; Hucko, T.; Stepina, E.; Hauff, P.; Dinkelborg, L.M.; Atrott, K.; Giovannoni, L.; Neri, D.; et al. Targeted ED-B fibronectin SPECT in vivo imaging in experimental atherosclerosis. *Q. J. Nucl. Med. Mol. Imaging* **2015**, *59*, 228–237. [PubMed]
254. Bhavane, R.; Badea, C.; Ghaghada, K.B.; Clark, D.; Vela, D.; Moturu, A.; Annapragada, A.; Johnson, G.A.; Willerson, J.T.; Annapragada, A. Dual-energy computed tomography imaging of atherosclerotic plaques in a mouse model using a liposomal-iodine nanoparticle contrast agent. *Circ. Cardiovasc. Imaging* **2013**, *6*, 285–294. [CrossRef] [PubMed]
255. Qin, J.; Peng, C.; Zhao, B.; Ye, K.; Yuan, F.; Peng, Z.; Yang, X.; Huang, L.; Jiang, M.; Zhao, Q.; et al. Noninvasive detection of macrophages in atherosclerotic lesions by computed tomography enhanced with PEGylated gold nanoparticles. *Int. J. Nanomed.* **2014**, *9*, 5575–5590.
256. Ntziachristos, V.; Tung, C.H.; Bremer, C.; Weissleder, R. Fluorescence molecular tomography resolves protease activity in vivo. *Nat. Med.* **2002**, *8*, 757–760. [CrossRef] [PubMed]
257. Nahrendorf, M.; Waterman, P.; Thurber, G.; Groves, K.; Rajopadhye, M.; Panizzi, P.; Marinelli, B.; Aikawa, E.; Pittet, M.J.; Swirski, F.K.; et al. Hybrid in vivo FMT-CT imaging of protease activity in atherosclerosis with customized nanosensors. *Arterioscler. Thromb. Vasc. Biol.* **2009**, *29*, 1444–1451. [CrossRef] [PubMed]
258. Ale, A.; Ermolayev, V.; Herzog, E.; Cohrs, C.; de Angelis, M.H.; Ntziachristos, V. FMT-XCT: In vivo animal studies with hybrid fluorescence molecular tomography-X-ray computed tomography. *Nat. Methods* **2012**, *9*, 615–620. [CrossRef] [PubMed]
259. Li, B.; Maafi, F.; Berti, R.; Pouliot, P.; Rhéaume, E.; Tardif, J.C.; Lesage, F. Hybrid FMT-MRI applied to in vivo atherosclerosis imaging. *Biomed. Opt. Express* **2014**, *5*, 1664–1676. [CrossRef] [PubMed]
260. Deguchi, J.; Aikawa, M.; Tung, C.H.; Aikawa, E.; Kim, D.E.; Ntziachristos, V.; Weissleder, R.; Libby, P. Inflammation in atherosclerosis visualizing matrix metalloproteinase action in macrophages in vivo. *Circulation* **2006**, *114*, 55–62. [CrossRef] [PubMed]
261. Lermann, J.; Frenzel, T.; Schmitz, M.; Hahnkamp, A.; Demmer, P.; Immenschuh, S.; Tietge, U.J.; Bremer, C.; Theilmeier, G. In vivo fluorescence-mediated tomography imaging demonstrates atorvastatin-mediated reduction of lesion macrophages in ApoE $^{-/-}$ mice. *Anesthesiology* **2013**, *119*, 129–141. [CrossRef] [PubMed]
262. Duivenvoorden, R.; Tang, J.; Cormode, D.P.; Mieszawska, A.J.; Izquierdo-Garcia, D.; Ozcan, C.; Otten, M.J.; Zaidi, N.; Lobatto, M.E.; van Rijs, S.M.; et al. A statin-loaded reconstituted high-density lipoprotein nanoparticle inhibits atherosclerotic plaque inflammation. *Nat. Commun.* **2014**, *5*, 3065–3090. [PubMed]
263. Lin, S.A.; Patel, M.; Suresch, D.; Connolly, B.; Bao, B.; Groves, K.; Rajopadhye, M.; Peterson, J.D.; Klimas, M.; Sur, C.; Bednar, B. Quantitative longitudinal imaging of vascular inflammation and treatment by ezetimibe in ApoE mice by FMT using new optical imaging biomarkers of cathepsin activity and $\alpha_v\beta_3$ Integrin. *Int. J. Mol. Imaging* **2012**, *2012*, 189254. [CrossRef] [PubMed]
264. Yao, Y.; Jiang, I.; Sheng, Z.; Zhang, Y.; An, Y.; Yan, F.; Ma, G.; Liu, N.; Teng, G.; Cheng, Z. Analysis of in situ and ex vivo $\alpha_v\beta_3$ integrin expression during experimental carotid atherogenesis. *Int. J. Nanomed.* **2012**, *7*, 641–649.
265. Oraevsky, A.A.; Karabutov, A.A. Optoacoustic tomography. In *Biomedical Photonics Handbook*; Vo-Dinh, T., Ed.; CRC Press/Francis and Taylor Group: Boca Raton, FL, USA, 2003; pp. 1–34.
266. Xu, M.H.; Wang, L.H.V. Photoacoustic imaging in biomedicine. *Rev. Sci. Instrum.* **2006**, *77*, 041101. [CrossRef]
267. Kim, C.; Favazza, C.; Wang, L.V. In vivo photoacoustic tomography of chemicals: High-resolution functional and molecular optical imaging at new depths. *Chem. Rev.* **2010**, *110*, 2756–2782. [CrossRef] [PubMed]
268. Razansky, D.; Deliolanis, N.C.; Vinegoni, C.; Ntziachristos, V. Deep tissue optical and optoacoustic molecular imaging technologies for pre-clinical research and drug discovery. *Curr. Pharm. Biotechnol.* **2012**, *13*, 504–522. [CrossRef] [PubMed]

269. Luke, G.P.; Yeager, D.; Emelianov, S.Y. Biomedical applications of photoacoustic imaging with exogenous contrast agents. *Ann. Biomed. Eng.* **2012**, *40*, 422–437. [CrossRef] [PubMed]
270. Bouchard, R.; Sahin, O.; Emelianov, S. Ultrasound-guided photoacoustic imaging: Current state and future development. *IEEE Trans. Ultrason. Ferroelectr. Freq. Control* **2014**, *61*, 450–466. [CrossRef] [PubMed]
271. Jeon, M.; Song, W.; Huynh, E.; Kim, J.; Kim, J.; Helfield, B.L.; Leung, B.Y.; Goertz, D.E.; Zheng, G.; Oh, J.; et al. Methylene blue microbubbles as a model dual-modality contrast agent for ultrasound and activatable photoacoustic imaging. *J. Biomed. Opt.* **2014**, *19*, 16005. [CrossRef] [PubMed]
272. Li, W.; Chen, X. Gold nanoparticles for photoacoustic imaging. *Nanomedicine* **2015**, *10*, 299–320. [CrossRef] [PubMed]
273. Taruttis, A.; Ntziachristos, V. Advances in real-time multispectral optoacoustic imaging and its applications. *Nat. Photonics* **2015**, *9*, 219–227. [CrossRef]
274. Kim, K.; Huang, S.W.; Ashkenazi, S.; O'Donnell, M.; Agarwal, A.; Kotov, N.A.; Denny, M.F.; Kaplan, M.J. Photoacoustic imaging of early inflammatory response using gold nanorods. *Appl. Phys. Lett.* **2007**, *90*, 223901. [CrossRef]
275. Wang, B.; Yantsen, E.; Larson, T.; Karpiouk, A.B.; Sethuraman, S.; Su, J.L.; Sokolov, K.; Emelianov, S.Y. Plasmonic intravascular photoacoustic imaging for detection of macrophages in atherosclerotic plaques. *Nano Lett.* **2008**, *9*, 2212–2217. [CrossRef] [PubMed]
276. Ha, S.; Carson, A.; Agarwal, A.; Kotov, N.A.; Kim, K. Detection and monitoring of the multiple inflammatory responses by photoacoustic molecular imaging using selectively targeted gold nanorods. *Biomed. Opt. Express* **2011**, *2*, 645–657. [CrossRef] [PubMed]
277. Rouleau, L.; Berti, R.; Ng, V.W.K.; Matteau-Pelletier, C.; Lam, T.; Saboural, P.; Kakkar, A.K.; Lesage, F.; Rhéaume, E.; Tardif, J.C. VCAM-1-targeting gold nanoshell probe for photoacoustic imaging of atherosclerotic plaque in mice. *Contrast Media Mol. Imaging* **2013**, *8*, 27–39. [CrossRef] [PubMed]
278. Wu, C.; Zhang, Y.; Li, Z.; Li, C.; Wang, Q. A novel photoacoustic nanoprobe of ICG@PEG-Ag2S for atherosclerosis targeting and imaging in vivo. *Nanoscale* **2016**, *8*, 12531–12539. [CrossRef] [PubMed]
279. Simsekylilmaz, S.; Cabrera-Fuentes, H.A.; Meiler, S.; Kostin, S.; Baumer, Y.; Liehn, E.A.; Weber, C.; Boisvert, W.A.; Preissner, K.T.; Zernecke, A. Role of extracellular RNA in atherosclerotic plaque formation in mice. *Circulation* **2014**, *129*, 598–606. [CrossRef] [PubMed]
280. Simsekylilmaz, S.; Cabrera-Fuentes, H.A.; Meiler, S.; Kostin, S.; Baumer, Y.; Liehn, E.A.; Weber, C.; Boisvert, W.A.; Preissner, K.T.; Zernecke, A. Response to letter regarding article “Role of extracellular RNA in atherosclerotic plaque formation in mice”. *Circulation* **2014**, *130*, e144–e145. [CrossRef] [PubMed]
281. Mestas, J.; Hughes, C.C.W. Of mice and not men: Differences between mouse and human immunology. *J. Immunol.* **2004**, *172*, 2731–2738. [CrossRef] [PubMed]



© 2016 by the authors. Licensee MDPI, Basel, Switzerland. This article is an open access article distributed under the terms and conditions of the Creative Commons Attribution (CC BY) license (<http://creativecommons.org/licenses/by/4.0/>).

Article

Preoperative 3D FSE T1-Weighted MR Plaque Imaging for Severely Stenotic Cervical ICA: Accuracy of Predicting Emboli during Carotid Endarterectomy

Yasushi Ogasawara ¹, Yuiko Sato ¹, Shinsuke Narumi ², Makoto Sasaki ³, Shunrou Fujiwara ¹, Masakazu Kobayashi ¹, Kenji Yoshida ¹, Yasuo Terayama ² and Kuniaki Ogasawara ^{1,*}

- ¹ Department of Neurosurgery, School of Medicine, Iwate Medical University, 19-1 Uchimaru, Morioka 020-8505, Japan; oneandonlytoearth@yahoo.co.jp (Y.O.); okiuyotas@yahoo.co.jp (Y.S.); shunfuji@iwate-med.ac.jp (S.F.); kobamasa@iwate-med.ac.jp (M.K.); kenyoshi@iwate-med.ac.jp (K.Y.)
² Department of Neurology and Gerontology, School of Medicine, Iwate Medical University, 19-1 Uchimaru, Morioka 020-8505, Japan; snarumi@iwate-med.ac.jp (S.N.); teray@iwate-med.ac.jp (Y.T.)
³ Division of Ultra-High Field MRI and Department of Radiology, School of Medicine, Iwate Medical University, 19-1 Uchimaru, Morioka 020-8505, Japan; masasaki@iwate-med.ac.jp

* Correspondence: kuogasa@iwate-med.ac.jp; Tel.: +81-19-651-5111; Fax: +81-19-652-7284

Academic Editor: Michael Henein

Received: 27 July 2016; Accepted: 17 October 2016; Published: 27 October 2016

Abstract: The aim of the present study was to determine whether preoperative three-dimensional (3D) fast spin-echo (FSE) T1-weighted magnetic resonance (MR) plaque imaging for severely stenotic cervical carotid arteries could accurately predict the development of artery-to-artery emboli during exposure of the carotid arteries in carotid endarterectomy (CEA). Seventy-five patients underwent preoperative MR plaque imaging and CEA under transcranial Doppler ultrasonography of the ipsilateral middle cerebral artery. On reformatted axial MR image slices showing the maximum plaque occupation rate (POR) and maximum plaque intensity for each patient, the contrast ratio (CR) was calculated by dividing the internal carotid artery plaque signal intensity by the sternocleidomastoid muscle signal intensity. For all patients, the area under the receiver operating characteristic curve (AUC)—used to discriminate between the presence and absence of microembolic signals—was significantly greater for the CR on the axial image with maximum plaque intensity (CR_{max} intensity) (0.941) than for that with the maximum POR (0.885) ($p < 0.05$). For 32 patients in whom both the maximum POR and the maximum plaque density were identified, the AUCs for the CR were 1.000. Preoperative 3D FSE T1-weighted MR plaque imaging accurately predicts the development of artery-to-artery emboli during exposure of the carotid arteries in CEA.

Keywords: carotid endarterectomy; artery-to-artery embolism; plaque imaging; three-dimensional; fast spin echo magnetic resonance

1. Introduction

Magnetic resonance (MR) plaque imaging is used to assess plaque characteristics in patients with cervical carotid stenosis. Of various two-dimensional (2D) T1-weighted sequences for MR plaque imaging, the spin echo (SE) T1-weighted imaging (WI) technique, with appropriate scanning parameters, is the most accurate for quantifying intraplaque components [1–4]. However, a three-dimensional (3D) fast spin-echo (FSE) T1-WI technique capable of minimizing partial volume effects and motion artifacts, enhancing black-blood effects, and maintaining T1-WI contrast has recently been adopted [5]. A comparison of diagnostic accuracy between 2D SE T1-WI and 3D FSE T1-WI for carotid plaque characterization using pathologic specimens excised from carotid endarterectomy (CEA) was performed. It was shown that, because it provides improved contrast of lipid-rich plaques,

3D FSE T1-WI could characterize carotid plaque composition more accurately than 2D SE T1-WI [5]. In addition, 3D FSE T1-WI could differentiate vulnerable from stable plaques with excellent sensitivity and specificity [5].

Although CEA has been shown to be an effective method for preventing stroke in select patients [6–8], more than 70% of intraoperative procedure-related strokes are due to cerebral embolism from the surgical site [9]. Intraoperative transcranial Doppler (TCD) monitoring of the middle cerebral artery (MCA) detects emboli from the surgical site as microembolic signals (MES) [9–15]. A significant correlation has been reported between detection of MES during exposure of the carotid arteries and the development of new ischemic lesions or neurological deficits after CEA [10–15]. When solid masses such as thrombi are present on the internal carotid artery (ICA) plaque surface, they can be dislodged by manipulating the carotid arteries for exposure during CEA, resulting in the development of cerebral ischemic lesions [16]. This suggests that MES during exposure of the carotid arteries may be associated with vulnerable carotid plaques [17]; therefore, identifying plaque vulnerability preoperatively may improve risk stratification in patients eligible for CEA.

A recent study demonstrated that, of various 2D T1-WI plaque imaging techniques, non-gated SE predicted the development of MES during carotid exposure in CEA more accurately than other MR plaque imaging techniques [18]. However, whereas the sensitivity and negative-predictive value for the 2D SE T1-WI in predicting the development of MES during carotid exposure were high, its specificity and positive-predictive value were less than 50%. In that study, the signal intensity of the carotid plaque was measured in only one axial section set at the location where the stenosis was most severe. This measurement may result in low specificity and positive-predictive value because MES do not always originate from the location with the most severe stenosis during exposure of the carotid arteries [18]. Therefore, analysis of plaque using 3D MR imaging may provide a more accurate prediction of the development of MES during carotid exposure.

The aims of the present study were (1) to determine whether preoperative 3D FSE T1-weighted plaque imaging for cervical carotid artery stenosis could accurately predict the development of MES on TCD during exposure of the carotid arteries in CEA; and (2) to compare the predictive accuracy of 3D FSE T1-weighted plaque imaging and 2D SE T1-weighted plaque imaging in historical controls [18].

2. Results

2.1. Clinical Characteristics

From December 2013 to August 2015, 88 patients satisfying the inclusion criteria consecutively underwent 3D FSE T1-WI and subsequent CEA, except for one who underwent urgent CEA because of crescendo transient ischemic attacks and thus did not undergo 3D FSE T1-WI. Although TCD was attempted in all participants, reliable TCD monitoring was not achieved throughout the entire operation in 12 patients because an adequate bone window could not be obtained. Therefore, after excluding these 13 patients from analysis, a total of 75 patients were enrolled into the present study. Table 1 shows the basic characteristics of these 75 patients and comparisons with 80 patients as historical controls who were consecutively measured using 2D SE T1-WI from July 2010 to January 2012 [18]. No significant differences were found in background characteristics between the two groups.

2.2. Intraoperative and Postoperative Events

When the ICA was manipulated to allow exposure from the carotid sheath, MES were detected in 19 (25%) of the 75 patients. Among these 19 patients, two developed neurological deficits after recovery from general anesthesia; all deficits included hemiparesis contralateral to the CEA and completely resolved within 12 h. None of the remaining 56 patients (without MES during exposure of the carotid arteries) experienced postoperative neurological deficits.

Table 1. Comparison of basic characteristics between patients undergoing 3D fast spin-echo (FSE) T1-weighted imaging (WI) plaque imaging and historical controls undergoing 2D T1-WI SE plaque imaging. ICA, internal carotid artery; SD, standard deviation.

Patient Characteristics	3D FSE T1-WI Plaque Imaging (n = 75)	Historical Controls (n = 80) [18]	p
Age (years) (mean \pm SD)	69.8 \pm 7.0	69.4 \pm 6.8	0.6231
Male sex	68 (91%)	77 (96%)	0.2762
Hypertension	68 (91%)	64 (80%)	0.0728
Diabetes mellitus	26 (35%)	26 (33%)	0.8651
Dyslipidemia	24 (32%)	21 (26%)	0.4810
Symptomatic lesions	47 (62%)	50 (63%)	0.9998
Degree of ICA stenosis (%) (mean \pm SD)	87.6 \pm 8.8	88.2 \pm 8.4	0.8056
Length of stenotic lesion (mm) (mean \pm SD)	54.3 \pm 10.8	53.7 \pm 11.7	0.6482
Height of distal end of stenotic lesion relative to cervical vertebra (mean \pm SD) (mmHg) (mean \pm SD)	2.7 \pm 0.9	2.8 \pm 0.8	0.8421
Tortuosity of stenotic lesion ($^{\circ}$) (mean \pm SD)	111.4 \pm 25.8	109.9 \pm 23.8	0.7838
Ulceration of stenotic lesion	23 (31%)	27 (34%)	0.7327

2.3. Relationship between the Image with the Maximum Plaque Occupation Rate and the Image with the Maximum Plaque Intensity

On 3D FSE T1-WI, it was determined that both the image with the maximum plaque occupation rate (POR_{max} occupation) and the image with the maximum plaque intensity were identified in 32 patients (43%). In the remaining 43 patients (57%), the distance between the two images ranged from 3 to 17 mm (6 \pm 4 mm).

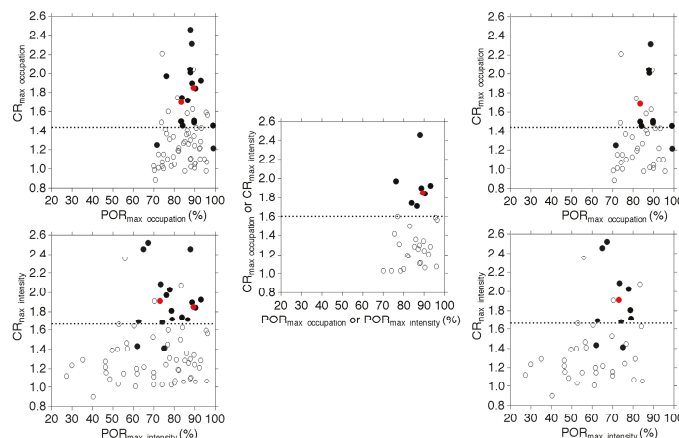


Figure 1. Relationship between the plaque occupation rate (POR) in the image with the maximum POR (POR_{max} occupation) or that in the image with the maximum plaque intensity (POR_{max} intensity), contrast ratio (CR) in the image with POR_{max} occupation (CR_{max} occupation), or that in the image with the maximum plaque intensity (CR_{max} intensity) and development of microembolic signals (MES) during exposure of the carotid arteries (left, for all patients; middle, for patients with identification of the image with the POR_{max} occupation and the image with the maximum plaque intensity; right, for patients without this identification). In the middle panel, each POR_{max} occupation or CR_{max} occupation is identical to POR_{max} intensity or CR_{max} intensity, respectively. Closed and open circles indicate patients with and without MES, respectively. Red and black circles indicate patients with and without postoperative new neurological deficits, respectively. Dashed horizontal lines denote the cutoff points closest to the left upper corners of the receiver operating characteristic (ROC) curves in predicting the development of MES.

2.4. Relationship between Development of Microembolic Signals (MES) during Exposure of the Carotid Arteries and the Plaque Occupation Rate or the Plaque Intensity

Figure 1 shows the relationship between POR_{max} occupation, POR in the image with the maximum plaque intensity (POR_{max} intensity), contrast ratio (CR) on the image with the POR_{max} occupation (CR_{max} occupation), or CR on the image with the maximum plaque intensity (CR_{max} intensity) and development of MES during exposure of the carotid arteries.

Table 2 shows the areas under the receiver operating characteristic curves (AUCs) and the sensitivity, specificity, and positive- and negative-predictive values for CR_{max} occupation and CR_{max} intensity at the cutoff point closest to the left upper corner of the receiving operator characteristic (ROC) curve for predicting the development of MES during exposure of the carotid arteries.

Figure 2 shows the ROC curves for CR_{max} occupation and CR_{max} intensity in predicting the development of MES during exposure of the carotid arteries.

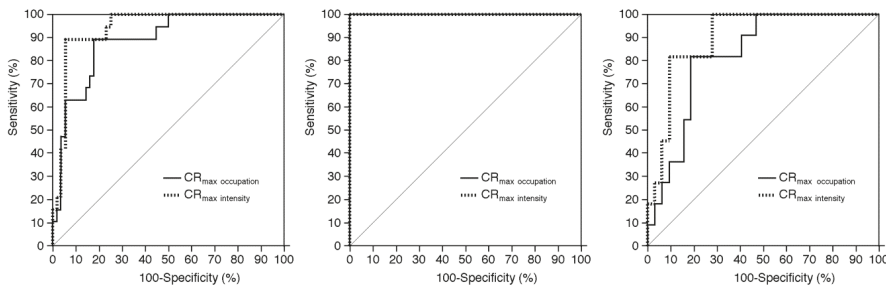


Figure 2. Receiving operator characteristic (ROC) curves used to compare predictive accuracy between CR_{max} occupation and CR_{max} intensity for the development of MES during exposure of the carotid arteries (left, for all patients; middle, for patients with identification of the image with the POR_{max} occupation and that with the maximum plaque intensity; right, for patients without this identification). In the middle panel, each area under the ROC curve for CR_{max} occupation or CR_{max} intensity (each CR_{max} occupation is identical to CR_{max} intensity, respectively) is 1.000.

Table 2. Area under the ROC curve (AUC), sensitivity, specificity, and positive- and negative-predictive values for contrast ratio (CR) in the development of microembolic signals (MES) during exposure of the carotid arteries. NS, not significant.

Items	All Patients (<i>n</i> = 75)			Patients with identification of the Two Images * (<i>n</i> = 32)			Patients without identification of the Two Images * (<i>n</i> = 43)			F CR in Historical Controls (<i>n</i> = 80) [18]			p		
	A CR _{max} occupation	B CR _{max} intensity	C CR _{max} occupation or CR _{max} intensity	D CR _{max} occupation	E CR _{max} intensity	F CR _{max} intensity	A vs. B	D vs. E	C vs. D	C vs. E	A vs. F	B vs. F			
AUC 95% CI	0.885 0.791–0.947	0.941 0.861–0.982	1.000 0.925–1.000	0.824 0.673–0.923	0.901 0.770–0.971	0.821 0.723–0.901	<0.05 **	<0.05 **	<0.01 ***	<0.05 **	NS	NS	NS	NS	NS
Sensitivity 95% CI	90% 67%–99%	90% 67%–99%	100% 82%–100%	82% 45%–98%	82% 48%–98%	100% 85%–100%	—	—	—	—	NS	NS	NS	NS	NS
Specificity 95% CI	82% 67%–91%	95% 85%–99%	100% 88%–100%	8% 67%–93%	91% 75%–98%	49% 36%–63%	—	—	—	—	<0.05	<0.05	<0.05	<0.05	<0.05
Positive predictive value 95% CI	63% 42%–81%	85% 62%–97%	100% 82%–100%	60% 32%–80%	75% 43%–95%	44% 31%–59%	—	—	—	—	NS	NS	NS	<0.05	<0.05
Negative predictive value 95% CI	96% 88%–100%	96% 88%–100%	100% 88%–100%	93% 77%–99%	94% 79%–99%	100% 88%–100%	—	—	—	—	NS	NS	NS	NS	NS
Cutoff point	1.44	1.66	1.60	1.44	1.66	1.16	—	—	—	—	—	—	—	—	—

* The image with the maximum plaque occupation rate and the image with the maximum plaque intensity; ** difference between AUCs of 0.056, pairwise comparison; *** difference between AUCs of 0.077, pairwise comparison.

For all patients, the AUC for CR_{\max} intensity was significantly greater than that for CR_{\max} occupation. For patients with identification of the image with both the POR_{\max} occupation and the maximum plaque intensity, the AUCs for CR_{\max} occupation and CR_{\max} intensity were 1.000. For patients without this identification, the AUC was significantly greater for CR_{\max} intensity than for CR_{\max} occupation. Furthermore, while the AUCs for CR_{\max} intensity did not differ between patients with and without the identification, the AUCs for CR_{\max} occupation were significantly greater for the former than the latter.

Of two patients with postoperative neurological deficits, one patient had identification of the image with both the POR_{\max} occupation and the maximum plaque intensity; CR_{\max} occupation ($=\text{CR}_{\max}$ intensity) was 1.85 (Figure 1). Another patient with the deficit had no identification of the two images; CR_{\max} occupation and CR_{\max} intensity were 1.69 and 1.91, respectively (Figure 1). These values were greater than each cutoff point closest to the left upper corner of the ROC curve for predicting the development of MES during exposure of the carotid arteries.

Sixteen patients with CR_{\max} occupation ≥ 1.60 were classified into two subgroups: eight patients with higher CR_{\max} occupation (≥ 1.90) and eight patients with lower CR_{\max} occupation (between 1.60 and 1.90). The incidence of MES during exposure of the carotid arteries did not differ between these two subgroups (6/8 (75%) for higher CR_{\max} occupation; 6/8 (75%) for lower CR_{\max} occupation) ($p > 0.9999$). Twenty-three patients with CR_{\max} intensity ≥ 1.60 were classified into two subgroups: 11 patients with higher CR_{\max} intensity (≥ 1.90) and 12 patients with lower CR_{\max} intensity (between 1.60 and 1.90). The incidence of MES during exposure of the carotid arteries did not differ between these two subgroups (8/11 (73%) for higher CR_{\max} intensity; 9/12 (75%) for lower CR_{\max} intensity) ($p > 0.9999$).

The results of univariate analysis of factors related to the development of MES during exposure of the carotid arteries (except CR_{\max} occupation, CR_{\max} intensity, POR_{\max} occupation, and POR_{\max} intensity) are summarized in Table 3.

Table 3. Risk factors related to the development of MES during exposure of the carotid arteries.

Factors	Development of MES		<i>p</i>
	Yes (n = 19)	No (n = 56)	
Age (years) (mean \pm SD)	69.6 \pm 7.8	69.9 \pm 6.8	0.8119
Male sex	18 (95%)	50 (89%)	0.6709
Hypertension	18 (95%)	50 (89%)	0.6709
Diabetes mellitus	9 (47%)	17 (30%)	0.2641
Dyslipidemia	5 (26%)	19 (34%)	0.7765
Symptomatic lesion	16 (84%)	31 (55%)	0.0296
Degree of ICA stenosis (%) (mean \pm SD)	85.9 \pm 9.6	87.9 \pm 8.7	0.5011
Length of stenotic lesion (mm) (mean \pm SD)	53.6 \pm 11.8	55.6 \pm 10.1	0.5143
Height of distal end of stenotic lesion relative to cervical vertebra (mean \pm SD)	2.8 \pm 1.1	2.7 \pm 0.8	0.7432
Tortuosity of stenotic lesion ($^{\circ}$) (mean \pm SD)	109.3 \pm 27.2	112.0 \pm 24.9	0.4328
Ulceration of stenotic lesion	10 (53%)	13 (23%)	0.0226
Identification of an image with POR_{\max} occupation and that with maximal plaque intensity	8 (42%)	24 (43%)	>0.9999

Patients with MES had a significantly higher prevalence of symptomatic lesions and ulceration of stenotic lesion than those without. No other significant associations with the development of MES during exposure of the carotid arteries were observed. In multivariate analysis of factors related to the development of MES during exposure of the carotid arteries, symptomatic lesions and ulceration of stenotic lesion, as items showing $p < 0.2$ in univariate analyses, were used as confounders in the logistic regression model. The AUC in predicting the development of MES during exposure of the carotid arteries was greater for CR_{\max} intensity than for CR_{\max} occupation, and POR_{\max} occupation was also added as a confounder. As a result, only CR_{\max} intensity was significantly associated with the development of MES during exposure of the carotid arteries (95% confidence interval (CI): 17.5–351.5; $p < 0.0001$).

Figure 3 shows the relationship among ulceration of stenotic lesions, CR_{max} intensity and development of MES during exposure of the carotid arteries.

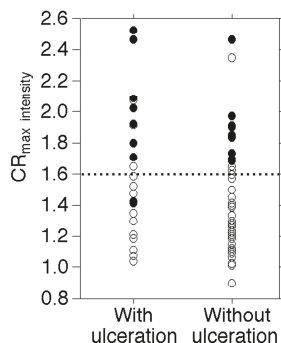


Figure 3. Relationship among ulceration of stenotic lesions, CR_{max} intensity, and development of MES during exposure of the carotid arteries. Closed and open circles indicate patients with and without MES, respectively. Dashed horizontal line denotes CR_{max} intensity of 1.60.

In a subgroup of patients with CR_{max} intensity < 1.60, the incidence of the MES was greater in patients with ulceration (2/12 (17%) than in those without (0/40 (0%)) ($p = 0.0498$); in another subgroup of patients with CR_{max} intensity ≥ 1.60 , the incidence did not differ between patients with (8/11 (73%)) and without (9/12 (75%)) the ulceration ($p > 0.9999$).

2.5. Comparisons of Area under Curve (AUC), Sensitivity, Specificity, and Positive- and Negative-Predictive Values for CR_{max} occupation or CR_{max} intensity and Those for CR in Historical Controls Measured Using 2D SE T1-WI

No differences were observed between the AUC of CR_{max} occupation or CR_{max} intensity or that of CR in the historical controls (Table 2). While sensitivity and positive- and negative-predictive values did not differ between CR_{max} occupation and CR in the historical controls, specificity was significantly greater for the former than for the latter (Table 2). While the sensitivity and negative-predictive value did not differ between CR_{max} intensity and CR in the historical controls, the specificity and positive-predictive value were significantly greater for the former than for the latter (Table 2).

3. Discussion

3.1. Findings

The results of the present study demonstrated that preoperative 3D FSE T1-weighted MR plaque imaging for cervical carotid artery stenosis could accurately predict the development of MES on TCD during exposure of the carotid arteries in CEA. 3D FSE T1-WI plaque imaging may therefore provide greater predictive accuracy than 2D SE T1-weighted plaque imaging.

3.2. Data Interpretation

3D MR plaque imaging minimizes partial volume effects and motion artifacts, enhances black-blood effects, and maintains T1-WI contrast [1–4]. Furthermore, 2D images can be obtained in arbitrary sections from 3D imaging data. In the present study, 2D axial images perpendicular to the long axis of the common carotid artery and the ICA were generated from 3D imaging data. These methods may be suitable for the assessment of carotid plaques because the carotid artery is tortuous and the plaques are typically elongated in a superoinferior direction [5]. While several investigators have measured plaque intensity on the axial image slice with the greatest degree of

carotid stenosis [1,3,4,18,19], others have measured plaque intensity on the image slice with the highest plaque intensity [20–22]. However, it remains unclear which of these two methods is more suitable for predicting the development of new postoperative ischemic events in patients undergoing carotid artery stenting or CEA or the development of future ischemic events in patients treated with medication alone. Therefore, we evaluated plaque intensity on two axial images obtained from 3D images as follows: the image slice with the maximum POR—possibly corresponding to the image slice with the greatest degree of carotid stenosis on angiography—and the image slice with the maximum plaque intensity. As a result, plaque intensity on the latter image more accurately predicted the development of MES during exposure of the carotid arteries than that on the former image. Furthermore, these two images failed to be identified in more than half of our patients, and plaque intensity more accurately predicted the development of MES for patients with identification than for those without. In addition, while the sensitivity and negative-predictive value in predicting the development of MES during carotid exposure did not differ between 3D FSE T1-WI and 2D SE T1-WI, the specificity and positive-predictive value were significantly greater in the former than in the latter. These findings suggest that 3D plaque-imaging is effective for predicting the development of MES in patients undergoing CEA for carotid stenosis; the findings also support the hypothesis that MES do not always originate from the site with the most severe stenosis during exposure of the carotid arteries.

According to a study that used the same methods for performing MR plaque imaging and measuring plaque intensity as those used in the present study [5], CR in 3D FSE T1-WI identified intraplaque components with a sensitivity and specificity of >90%: CRs in calcified lesion or fibrotic plaque without a lipid core ranged from 0.94 to 1.29; CRs in lipid-rich or necrotic core ranged from 1.33 to 1.54; and CRs in plaque with hemorrhage or thrombus were greater than 1.53. In particular, plaque with a CR \geq 1.60 always indicated hemorrhage or thrombus. Our data showed that the optimal cutoff point for the CR on the image with the maximum plaque intensity was 1.66 or 1.60. These data correspond to previous findings that the development of MES during exposure of the carotid arteries in CEA is strongly associated with carotid plaque that histopathologically consists of hemorrhage [17]. Intraplaque hemorrhage depicted on MR plaque imaging is reportedly related to a histologically disrupted plaque surface (fissured fibrous cap), implying that thrombi are exposed to blood flow in patients with severe carotid artery stenosis (>70%) [23]. Surgical manipulation of the carotid arteries with such plaques likely leads to the development of emboli from this vulnerable plaque.

Several investigators have histopathologically classified intraplaque hemorrhage in the cervical carotid arteries into three stages: fresh (<1 week after hemorrhage, intact red blood cells with intracellular methemoglobin), recent (1–6 weeks after hemorrhage, lytic red blood cells with extracellular methemoglobin), and old (>6 weeks after hemorrhage, amorphous material) [24,25]. They also correlated these histological categories with findings on MR plaque imaging [24,25]. Fresh and recent intraplaque hemorrhages exhibited hyperintensity on T1-WI MR, and the former signal intensity was stronger than the latter [24,25]. Thus, while a plaque with a CR \geq 1.60 consists of hemorrhage or thrombus, a plaque containing fresh hemorrhage may more greatly exhibit higher CR on MR plaque imaging. We also developed a hypothesis that when the carotid arteries are surgically manipulated, embolism from the surgical site is more likely to develop in the carotid arteries with fresh intraplaque hemorrhage than in those with recent intraplaque hemorrhage. To validate this hypothesis, we compared the incidence of MES during exposure of the carotid arteries between patients with higher CRs and lower CRs, but only in patients with a CR \geq 1.60. We found that CR was not associated with a tendency to develop MES during exposure of the carotid arteries among patients with CR \geq 1.60.

In the present study, although patients with MES during exposure of the carotid arteries had a significantly higher prevalence of ulceration of a stenotic lesion than those without, only CR_{max} intensity was significantly associated with the development of MES using the logistic regression model. In further analyses, development of MES was related to the presence of ulceration of a stenotic lesion in patients with CR_{max} intensity $<$ 1.60, which indicates plaque composed of components other than hemorrhage or thrombus. However, this relationship does not exist in patients with CR_{max} intensity \geq 1.60,

which indicates plaque composed of hemorrhage or thrombus. This may be a reason why ulceration of a stenotic lesion was a weaker predictor of development of MES than CR_{max} intensity.

3.3. Clinical Applications

Caplan and Hennerici [26] have reported that hemodynamic and embolic mechanisms are strictly linked and may interact to determine the ultimate degree of cerebral ischemia. According to their concept, low blood flow velocity in the cerebral artery may impair clearance of emboli generated from a proximal lesion, subsequently facilitating the onset of ischemia caused by emboli in poorly perfused areas of the brain. Indeed, low blood-flow velocity in the MCA reportedly correlated with the development of diffusion-weighted imaging (DWI)-characterized postoperative cerebral ischemic lesions related to the generation of microemboli during exposure of the carotid arteries in CEA [27]. The concept presented by Caplan and Hennerici also suggests that increased blood-flow velocity may prevent the development of cerebral ischemic lesions due to emboli. Actually, another study showed that the incidence of DWI-characterized postoperative cerebral ischemic lesions was significantly lower in patients with MCA blood-flow velocity increased by intentional hypertension during exposure of the carotid arteries than in patients without such a procedure [28]. Thus, we attempted to keep the increase in systolic blood pressure at least 10% above the preoperative value during exposure of the carotid arteries.

On the basis of these findings and our data, we propose the following practical clinical algorithm to prevent development of MES-related ischemic events in CEA. Patients undergo preoperative MR imaging of plaque using 3D FSE T1-WI; when the CR_{max} intensity is >1.60 for patients with identification of the image with both the POR_{max} occupation, and the maximum plaque intensity or the CR_{max} intensity is >1.66 for patients without such identification, intentional hypertension is performed during exposure of the carotid arteries; and for other combinations, intentional hypertension is unnecessary.

3.4. Study Limitations

The present study did have several limitations. First, we did not directly compare the predictive accuracy of 3D FSE T1-WI with that of 2D SE T1-WI in identical subjects. Second, to standardize the surgical procedures as much as possible, all surgeries were performed by the same senior neurosurgeon, who was blinded to the intraoperative TCD findings and therefore continued with the surgeries regardless of what was found. However, the degree of stress on the carotid arteries due to manipulation during exposure might not have been equivalent among all patients, and this may have affected the development of MES. Finally, the small sample size and patient selection bias (14% of patients were excluded because of failure to obtain TCD data) were also limitations.

4. Materials and Methods

4.1. Subjects

The present study was designed as a prospective observational study, and the case cohort was compared with historical controls [18] composed of patients who underwent preoperative 2D SE T1-weighted plaque imaging and CEA. This study was approved by the Regional Ethical Board of Iwate Medical University (H22-31) and conducted in compliance with the Helsinki Declaration. Written, informed consent was obtained from all patients or their next of kin prior to participation.

The present study included patients with ipsilateral ICA stenosis $\geq 70\%$ as per the North American Symptomatic Carotid Endarterectomy Trial [8]. Patients underwent the previously described angiography study [18] with arterial catheterization, had useful residual function (modified Rankin disability scale, 0–2), and underwent CEA of the carotid bifurcation in our institution. Patients who did not undergo preoperative 3D FSE T1-WI were excluded, as were patients in whom reliable TCD monitoring could not be obtained throughout the surgery due to a failure to obtain an adequate bone window.

4.2. Preoperative, Intraoperative, and Postoperative Management

Before surgery, on angiography with arterial catheterization, the length of the ICA stenotic lesion was measured, and the height of the distal end of the lesion relative to the cervical vertebra was determined in the lateral view; lesion tortuosity was defined using a previously described method [18]; and according to the method presented by Randoux et al. [18,29], a stenotic lesion was classified as having ulceration when it fulfilled the radiographic criteria for an ulcer niche, seen in profile as a crater penetrating a stenotic lesion in any projection.

Antiplatelet therapy was administered to all patients until the morning of the day on which CEA was performed. Furthermore, all patients underwent surgery under general anesthesia with an operative microscope. All skin incisions were made by the same senior neurosurgeon who was blinded to the MR plaque imaging findings. Dissection of the carotid sheath and exposure of the carotid arteries were routinely performed as follows [18,30]. First, the upper plane of the carotid sheath surrounding the common carotid artery was cut with scissors; next, the other planes of the carotid sheath were bluntly separated from the common and external carotid arteries and the ICA with Pean forceps. Scissors were used when the carotid sheath was adhered to the carotid arteries. The surgeon was blinded to the intraoperative TCD findings and proceeded with surgical procedures regardless of these findings.

During exposure of the carotid arteries, attempts were made to keep the increase in systolic blood pressure at least 10% above the preoperative value [28]. If needed, a vasodilator (nitroglycerin or nicardipine) or a vasoconstrictor (theoadrenalin) was administered intravenously. No intraluminal shunt or patch graft was used in these procedures [18,28]. Prior to ICA clamping, a bolus of heparin (5000 IU) was administered.

All patients were neurologically tested immediately before the induction of and after recovery from general anesthesia by a neurologist who was blinded to the patients' clinical information, and the presence or absence of new postoperative neurological deficits was recorded [18].

4.3. Magnetic Resonance (MR) Plaque Imaging and Data Processing

Preoperative sagittal 3D FSE T1-WI of the affected carotid bifurcation was performed within 1 week prior to CEA using a 1.5-T MR imaging scanner (Signa HDxt; GE Healthcare, Milwaukee, WI, USA) and an eight-channel neurovascular coil under a previously described imaging protocol [5]. The voxel size was $0.5\text{ m} \times 0.5\text{ m} \times 0.5\text{ m}$.

An investigator (blinded to other data) processed the 3D FSE T1-WI data using a free software package (OsiriX; Pixmeo, Geneva, Switzerland) as follows (Figure 4). The curved planar reformation image was generated parallel to the long axis of the common carotid artery and the ICA by manually setting and automatically connecting reference points in the center of the vessel lumen on each axial source image. On the curved planar reformation image with the center line, axial images with 1.0 mm thickness were newly reformatted as sections perpendicular to the center line. Thus, the final voxel size was $0.5\text{ m} \times 0.5\text{ m} \times 1.0\text{ m}$.

In each reformatted axial image, the investigator manually traced a plaque and vessel lumen of the common carotid artery or the ICA (Figure 4). The resulting area was obtained in each image. First, POR was defined as follows: (an area of a plaque divided by an area of a vessel lumen) $\times 100\text{ (\%)}$. In each patient, the image with the maximum value of the POR (defined as $\text{POR}_{\max \text{ occupation}}$) was determined. Next, a signal intensity of the traced plaque was obtained on each image (total of 51 images) between 25 mm above and below the image with the $\text{POR}_{\max \text{ occupation}}$ in each patient. Of these 51 images, the image with the highest value of the signal intensity was determined and defined as the image with the maximum plaque intensity. In the image with the maximum plaque intensity, the POR was also determined (defined as $\text{POR}_{\max \text{ intensity}}$). In each patient, when the distance between the image with the $\text{POR}_{\max \text{ occupation}}$ and the image with the maximum plaque intensity ranged from 0–2 mm, the patient was defined as having identification of the two images (Figure 4).

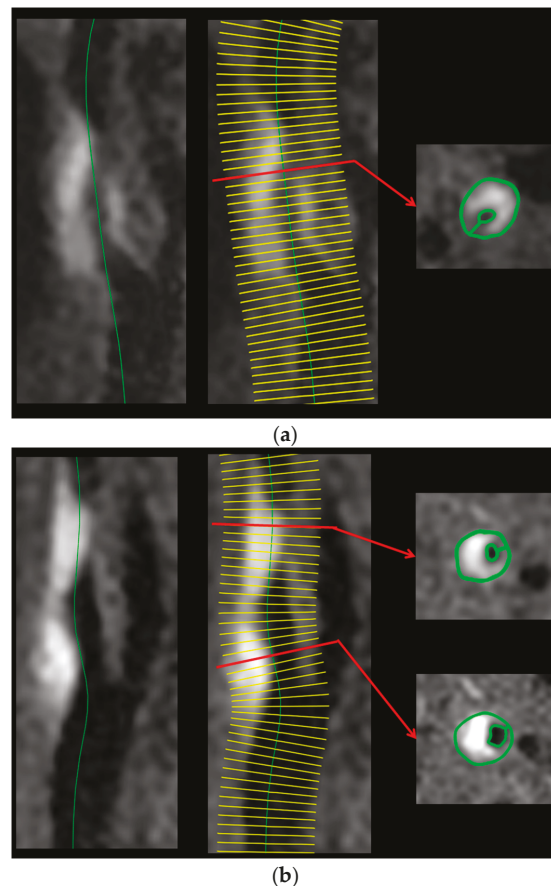


Figure 4. Preoperative three-dimensional fast spin echo T1-weighted magnetic resonance (3D FSE T1-weighted MR) plaque images of two patients with MES during exposure of the carotid arteries in endarterectomy. (a) The curved planar reformation is performed parallel to the long axis of the common and internal carotid arteries (**left**). The green line indicates the center line of the vessel lumen. On the image of the curved planar reformation, axial images with 1.0 mm thickness are reformatted as sections perpendicular to the center line (**middle**). Yellow lines indicate the position of each reformatted axial image. A reformatted axial image with the maximum POR and maximum plaque intensity (red arrows) are determined by tracing a plaque and vessel lumen of the common or internal carotid artery (**right**, green lines). A 65-year-old man with asymptomatic right internal carotid artery stenosis exhibits identification of the image with the maximum POR and the image with the maximum plaque intensity; (b) Preoperative 3D FSE T1-weighted MR plaque images of two patients with MES during exposure of the carotid arteries in endarterectomy. The curved planar reformation is performed parallel to the long axis of the common and internal carotid arteries (**left**). The green line indicates the center line of the vessel lumen. On the image of the curved planar reformation, axial images with 1.0 mm thickness are reformatted as sections perpendicular to the center line (**middle**). Yellow lines indicate the position of each reformatted axial image. A reformatted axial image with the maximum POR and maximum plaque intensity (red arrows) are determined by tracing a plaque and vessel lumen of the common or internal carotid artery (**right**, green lines). A 77-year-old man with symptomatic right internal carotid artery stenosis exhibits no identification of the image with the maximum POR (**upper**) and the image with the maximum plaque intensity (**lower**).

Of the 51 images in each patient, the image on which the sternocleidomastoid muscle adjacent to the carotid arteries was displayed as larger was determined, after which the investigator manually traced the muscle and measured the signal intensity. The CR on the image with the POR_{max} occupation (defined as CR_{max} occupation) and that on the image with the maximum plaque intensity (defined as CR_{max} intensity) were calculated by dividing the signal intensity of the plaque by that of the muscle.

4.4. Transcranial Doppler (TCD) Monitoring

TCD was performed using a PIONEER TC2020 system (EME, Überlingen, Germany; software version 2.50, 2-MHz probe; diameter, 1.5 cm; insonation depth, 40–66 mm; scale, –100 and +150 cm/s; sample volume, 2 mm; 64-point fast Fourier transform; fast Fourier transform length, 2 mm, fast Fourier transform overlap, 60%; high-pass filter, 100 Hz; detection threshold, 9 dB; minimum increase time, 10 ms) for insonation of the MCA ipsilateral to the carotid artery undergoing CEA [18]. TCD data were stored on a hard disk using a coding system and were later manually analyzed by a clinical neurophysiologist who was blinded to patient information [18]. MES were identified during exposure of the carotid arteries (from skin incision until ICA clamping) according to the recommended guidelines [31].

4.5. Statistical Analysis

Data are expressed as the mean \pm standard deviation (SD). Differences of variables between two groups were evaluated using the Mann–Whitney U test or the χ^2 test. The accuracy of the CR to predict development of MES during exposure of the carotid arteries was determined using an ROC curve, and the ability to discriminate between the presence or absence of MES during exposure of the carotid arteries was estimated using the AUC. Pairwise comparison of the AUCs using the method proposed by Pepe and Longton [32] was performed between CR_{max} occupation and CR_{max} intensity. Differences in the AUCs for the CR between patients with and without identification of the image with the POR_{max} occupation and that with the maximum plaque intensity were analyzed using 95% CIs. Differences in the AUC, sensitivity, specificity, and positive- and negative-predictive values between the CR_{max} occupation or CR_{max} intensity and CR in historical controls [18] that were measured using 2D SE T1-WI at the location at which the stenosis was most severe were also analyzed using 95% CIs. The relationship between development of MES during exposure of the carotid arteries and each variable (except CR and POR) was evaluated with univariate analysis using the Mann–Whitney U test or the χ^2 test. Multivariate statistical analysis of factors related to the development of MES during exposure of the carotid arteries was performed using logistic regression modeling. Variables showing values of $p < 0.2$ in univariate analyses were entered into the final model. For all statistical analyses, significance was set at the $p < 0.05$ level.

5. Conclusions

The results of the present study demonstrated that preoperative 3D FSE T1-weighted plaque imaging for cervical carotid artery stenosis accurately predicts the development of MES on TCD during exposure of the carotid arteries in CEA. These findings also suggest that 3D FSE T1-weighted plaque imaging may provide greater predictive accuracy than 2D SE T1-weighted plaque imaging.

Acknowledgments: The author (Kuniaki Ogasawara) discloses receipt of the following financial support for the research, authorship, and/or publication of this article: Strategic Medical Science Research from the Ministry of Education, Culture, Sports, Science and Technology of Japan, Grant Number S1491001; Scientific Research from Japan Society for the Promotion of Science, Grant Number JP15K10313.

Author Contributions: Yasushi Ogasawara and Kuniaki Ogasawara conceived and designed the study; Yasushi Ogasawara, Yuiko Sato, Shinsuke Narumi and Makoto Sasaki performed measurements and analyses of MR plaque imaging; Masakazu Kobayashi performed measurements and analyses of MES on TCD; Shunrou Fujiwara analyzed the data; Kenji Yoshida and Yasuo Terayama critically revised the manuscript and helped with interpretation of the results; and Yasushi Ogasawara and Kuniaki Ogasawara wrote the paper.

Conflicts of Interest: The founding sponsors had no role in the design of the study; in the collection, analyses, or interpretation of data; in the writing of the manuscript, and in the decision to publish the results.

Abbreviations

MR	magnetic resonance
MCA	middle cerebral artery
3D FSE T1-WI	three-dimensional fast spin echo T1-weighted imaging
2D SE T1-WI	two-dimensional spin echo T1-weighted imaging
SD	standard deviation
ICA	internal carotid artery
CEA	carotid endarterectomy
TCD	transcranial Doppler
MES	microembolic signals
POR _{max occupation}	maximum plaque occupation rate
AUC	area under receiver operating characteristic curve
CR	contrast ratio
CI	confidence interval
vs.	versus

References

1. Narumi, S.; Sasaki, M.; Ohba, H.; Ogasawara, K.; Kobayashi, M.; Hitomi, J.; Mori, K.; Ohura, K.; Yamaguchi, M.; Kudo, K.; et al. Prediction of carotid plaque characteristics using non-gated MR imaging: correlation with endarterectomy specimens. *Am. J. Neuroradiol.* **2013**, *34*, 191–197. [CrossRef] [PubMed]
2. Watanabe, Y.; Nagayama, M.; Suga, T.; Yoshida, K.; Yamagata, S.; Okumura, A.; Amoh, Y.; Nakashita, S.; van Cauteren, M.; Dodo, Y. Characterization of atherosclerotic plaque of carotid arteries with histopathological correlation: Vascular wall MR imaging vs. color Doppler ultrasonography (US). *J. Magn. Reson. Imaging* **2008**, *28*, 478–485. [CrossRef] [PubMed]
3. Saito, A.; Sasaki, M.; Ogasawara, K.; Kobayashi, M.; Hitomi, J.; Narumi, S.; Ohba, H.; Yamaguchi, M.; Kudo, K.; Terayama, Y. Carotid plaque signal differences among four kinds of T1-weighted magnetic resonance imaging techniques: A histopathological correlation study. *Neuroradiology* **2012**, *54*, 1187–1194. [CrossRef] [PubMed]
4. Narumi, S.; Sasaki, M.; Ohba, H.; Ogasawara, K.; Hitomi, J.; Mori, K.; Ohura, K.; Ono, A.; Terayama, Y. Altered carotid plaque signal among different repetition times on T1-weighted magnetic resonance plaque imaging with self-navigated radial-scan technique. *Neuroradiology* **2010**, *52*, 285–290. [CrossRef] [PubMed]
5. Narumi, S.; Sasaki, M.; Natori, T.; Yamaguchi-Oura, M.; Ogasawara, K.; Kobayashi, M.; Sato, Y.; Ogasawara, Y.; Hitomi, J.; Terayama, Y. Carotid plaque characterization using 3D T1-weighted MR imaging with histopathologic validation: A comparison with 2D technique. *Am. J. Neuroradiol.* **2015**, *36*, 751–756. [CrossRef] [PubMed]
6. Rothwell, P.M.; Eliasziw, M.; Gutnikov, S.A.; Fox, A.J.; Taylor, D.W.; Mayberg, M.R.; Warlow, C.P.; Barnett, H.J. Analysis of pooled data from the randomised controlled trials of endarterectomy for symptomatic carotid stenosis. *Lancet* **2003**, *361*, 107–116. [CrossRef]
7. Executive Committee for the Asymptomatic Carotid Atherosclerosis Study. Endarterectomy for asymptomatic carotid artery stenosis. *JAMA* **1995**, *273*, 1421–1428.
8. North American Symptomatic Carotid Endarterectomy Trial Collaborators. Beneficial effect of carotid endarterectomy in symptomatic patients with high-grade carotid stenosis. *N. Engl. J. Med.* **1991**, *325*, 445–453.
9. Spencer, M.P. Transcranial Doppler monitoring and causes of stroke from carotid endarterectomy. *Stroke* **1997**, *28*, 685–691. [CrossRef] [PubMed]
10. Ackerstaff, R.G.; Moons, K.G.; van de Vlasakker, C.J.; Moll, F.L.; Vermeulen, F.E.; Algra, A.; Spencer, M.P. Association of intraoperative transcranial Doppler monitoring variables with stroke from carotid endarterectomy. *Stroke* **2000**, *31*, 1817–1823. [CrossRef] [PubMed]

11. Wolf, O.; Heider, P.; Heinz, M.; PopPERT, H.; Sander, D.; Greil, O.; Weiss, W.; Hanke, M.; Eckstein, H.H. Microembolic signals detected by transcranial Doppler sonography during carotid endarterectomy and correlation with serial diffusion-weighted imaging. *Stroke* **2004**, *35*, e373–e375. [CrossRef] [PubMed]
12. Gavrilescu, T.; Babikian, V.L.; Cantelmo, N.L.; Rosales, R.; Pochay, V.; Winter, M. Cerebral microembolism during carotid endarterectomy. *Am. J. Surg.* **1995**, *170*, 159–164. [CrossRef]
13. Verhoeven, B.A.; de Vries, J.P.; Pasterkamp, G.; Ackerstaff, R.G.; Schoneveld, A.H.; Velema, E.; de Kleijn, D.P.; Moll, F.L. Carotid atherosclerotic plaque characteristics are associated with microembolization during carotid endarterectomy and procedural outcome. *Stroke* **2005**, *36*, 1735–1740. [CrossRef] [PubMed]
14. Gaunt, M.E.; Martin, P.J.; Smith, J.L.; Rimmer, T.; Cherryman, G.; Ratliff, D.A.; Bell, P.R.; Naylor, A.R. Clinical relevance of intraoperative embolization detected by transcranial Doppler ultrasonography during carotid endarterectomy: A prospective study of 100 patients. *Br. J. Surg.* **1994**, *81*, 1435–1439. [CrossRef] [PubMed]
15. Jansen, C.; Ramos, L.M.; van Heesewijk, J.P.; Moll, F.L.; van Gijn, J.; Ackerstaff, R.G. Impact of microembolism and hemodynamic changes in the brain during carotid endarterectomy. *Stroke* **1994**, *25*, 992–997. [CrossRef] [PubMed]
16. Rosario, J.A.; Hachinski, V.C.; Lee, D.H.; Fox, A.J. Adverse reactions to duplex scanning. *Lancet* **1987**, *330*, 1023. [CrossRef]
17. Sitzer, M.; Müller, W.; Siebler, M.; Hort, W.; Kniemeyer, H.W.; Jäncke, L.; Steinmetz, H. Plaque ulceration and lumen thrombus are the main sources of cerebral microemboli in high-grade internal carotid artery stenosis. *Stroke* **1995**, *26*, 1231–1233. [CrossRef] [PubMed]
18. Sato, Y.; Ogasawara, K.; Narumi, S.; Sasaki, M.; Saito, A.; Tsushima, E.; Namba, T.; Kobayashi, M.; Yoshida, K.; Terayama, Y.; et al. Optimal magnetic resonance plaque imaging for cervical carotid artery stenosis in predicting development of microembolic signals during exposure of carotid arteries in endarterectomy: Comparison of four T1-weighted imaging techniques. *Am. J. Neuroradiol.* **2016**, *37*, 1146–1154. [CrossRef] [PubMed]
19. Liu, X.S.; Zhao, H.L.; Cao, Y.; Lu, Q.; Xu, J.R. Comparison of carotid atherosclerotic plaque characteristics by high-resolution black-blood MR imaging between patients with first-time and recurrent acute ischemic stroke. *Am. J. Neuroradiol.* **2012**, *33*, 1257–1261. [CrossRef] [PubMed]
20. Altaf, N.; Beech, A.; Goode, S.D.; Gladman, J.R.; Moody, A.R.; Auer, D.P.; MacSweeney, S.T. Carotid intraplaque hemorrhage detected by magnetic resonance imaging predicts embolization during carotid endarterectomy. *J. Vasc. Surg.* **2007**, *46*, 31–36. [CrossRef] [PubMed]
21. Yamada, N.; Higashi, M.; Otsubo, R.; Sakuma, T.; Oyama, N.; Tanaka, R.; Iihara, K.; Naritomi, H.; Minematsu, K.; Naito, H. Association between signal hyperintensity on T1-weighted MR imaging of carotid plaques and ipsilateral ischemic events. *Am. J. Neuroradiol.* **2007**, *28*, 287–292. [PubMed]
22. Hosseini, A.A.; Kandiyil, N.; MacSweeney, S.T.S.; Altaf, N.; Auer, D.P. Carotid plaque hemorrhage on magnetic resonance imaging strongly predicts recurrent ischemia and stroke. *Ann. Neurol.* **2013**, *73*, 774–784. [CrossRef] [PubMed]
23. Van Dijk, A.C.; Truijman, M.T.; Hussain, B.; Zadi, T.; Saiedie, G.; de Rotte, A.A.; Liem, M.I.; van der Steen, A.F.; Daemen, M.J.; Koudstaal, P.J.; et al. Intraplaque hemorrhage and the plaque surface in carotid atherosclerosis: The plaque at risk study (PARISK). *Am. J. Neuroradiol.* **2015**, *36*, 2127–2133. [CrossRef] [PubMed]
24. Chu, B.; Kampschulte, A.; Ferguson, M.S.; Kerwin, W.S.; Yarnykh, V.L.; O'Brien, K.D.; Polissar, N.L.; Hatsukami, T.S.; Yuan, C. Hemorrhage in the atherosclerotic carotid plaque: A high-resolution MRI Study. *Stroke* **2004**, *35*, 1079–1084. [CrossRef] [PubMed]
25. Qiao, Y.; Hallock, K.J.; Hamilton, J.A. Magnetization transfer magnetic resonance of human atherosclerotic plaques ex vivo detects areas of high protein density. *J. Cardiovasc. Magn. Reson.* **2011**, *13*, 73. [CrossRef] [PubMed]
26. Caplan, L.R.; Hennerici, M. Impaired clearance of emboli (washout) is an important link between hypoperfusion, embolism, and ischemic stroke. *Arch. Neurol.* **1998**, *55*, 1475–1482. [CrossRef] [PubMed]
27. Ogasawara, K.; Suga, Y.; Sasaki, M.; Chida, K.; Kobayashi, M.; Yoshida, K.; Otawara, Y.; Ogawa, A. Intraoperative microemboli and low middle cerebral artery blood flow velocity are additive in predicting development of cerebral ischemic events after carotid endarterectomy. *Stroke* **2008**, *39*, 3088–3091. [CrossRef] [PubMed]

28. Kobayashi, M.; Ogasawara, K.; Yoshida, K.; Sasaki, M.; Kuroda, H.; Suzuki, T.; Kubo, Y.; Fujiwara, S.; Ogawa, A. Intentional hypertension during dissection of carotid arteries in endarterectomy prevents postoperative development of new cerebral ischemic lesions caused by intraoperative microemboli. *Neurosurgery* **2011**, *69*, 301–307. [CrossRef] [PubMed]
29. Randoux, B.; Marro, B.; Koskas, F.; Duyme, M.; Sahel, M.; Zouaoui, A.; Marsault, C. Carotid artery stenosis: Prospective comparison of CT, three-dimensional gadolinium-enhanced MR, and conventional angiography. *Radiology* **2001**, *220*, 179–185. [CrossRef] [PubMed]
30. Yoshida, K.; Ogasawara, K.; Kobayashi, M.; Tsuboi, J.; Okabayashi, H.; Ogawa, A. Scar formation of the carotid sheath identified during carotid endarterectomy in patients with previous cardiac surgery: Significance of history of intraoperative Swan-Ganz catheter insertion. *J. Neurosurg.* **2010**, *113*, 885–889. [CrossRef] [PubMed]
31. Consensus Committee of the Ninth International Cerebral Hemodynamic Symposium. Basic identification criteria of Doppler microembolic signals. *Stroke* **1995**, *26*, 1123. [CrossRef]
32. Pepe, M.S.; Longton, G. Standardizing diagnostic markers to evaluate and compare their performance. *Epidemiology* **2005**, *16*, 598–603. [CrossRef] [PubMed]



© 2016 by the authors. Licensee MDPI, Basel, Switzerland. This article is an open access article distributed under the terms and conditions of the Creative Commons Attribution (CC BY) license (<http://creativecommons.org/licenses/by/4.0/>).



Article

Age-Related Renal Microvascular Changes: Evaluation by Three-Dimensional Digital Imaging of the Human Renal Microcirculation Using Virtual Microscopy

Noriko Uesugi ^{1,*}, Yoshihito Shimazu ², Kazunori Kikuchi ³ and Michio Nagata ¹

¹ Department of Kidney and Vascular Pathology, Faculty of Medicine, University of Tsukuba, Tsukuba 305-8571, Japan; nagatam@md.tsukuba.ac.jp

² Laboratory of Food and Physiological Sciences, Azabu University, Sagamihara 252-5201, Japan; shimazu@azabu-u.ac.jp

³ Division of Pathology, Tsukuba Medical Center, Tsukuba 305-0005, Japan; k-kikuchi@tmch.or.jp

* Correspondence: nouesugi@md.tsukuba.ac.jp; Tel./Fax: +81-29-853-3938

Academic Editors: Michael Henein and William Chi-shing Cho

Received: 31 August 2016; Accepted: 27 October 2016; Published: 2 November 2016

Abstract: The renal microvasculature is targeted during aging, sometimes producing chronic kidney disease (CKD). Overdiagnosis of CKD in older persons is concerning. To prevent it, a new concept of “healthy aging” is arising from a healthy renal donor study. We investigated the renal microcirculatory changes of three older persons and compared them with that of one patient with nephrosclerosis using a three-dimensional (3D) reconstruction technique that we previously developed. This method uses a virtual slide system and paraffin-embedded serial sections of surgical material that was double-immunostained by anti-CD34 and anti- α smooth muscle actin (SMA) antibodies for detecting endothelial cells and medial smooth muscle cells, respectively. In all cases, the 3D images proved that arteriosclerotic changes in large proximal interlobular arteries did not directly induce distal arterial change or glomerulosclerosis. The nephrosclerotic patient showed severe hyalinosis with luminal narrowing of small arteries directly inducing glomerulosclerosis. We also visualized an atubular glomerulus and intraglomerular dilatation of an afferent arteriole during healthy aging on the 3D image and showed that microcirculatory changes were responsible for them. Thus, we successfully visualized healthy aged kidneys on 3D images and confirmed the underlying pathology. This method has the ability to investigate renal microcirculatory damage during healthy aging.

Keywords: human renal microcirculation; healthy aging; paraffin-embedded sections; three-dimensional imaging; virtual microscopy

1. Introduction

The microcirculation of the kidney is essential for controlling glomerular filtration and tubular reabsorption and for regulating the medullary concentration gradient [1]. Dysfunction of the renal microcirculation directly induces glomerular, tubular, and interstitial damage. Benign nephrosclerosis, or arterio-/arteriolonephrosclerosis, a disease of renal microcirculation, develops in response to hemodynamic changes associated with chronic hypertension, aging, obesity, diabetes, and chronic kidney disease (CKD) [1]. Characteristic changes are hyaline degeneration of arterioles, intimal fibrous thickening with medial atrophy of the small arteries, segmental and global sclerosis of glomeruli, and interstitial fibrosis [2]. These changes are also typical morphological changes associated with aging [3]. In other words, aging is one of the most popular causes of nephrosclerosis.

Aging is an inevitable biological process that results in structural and functional changes. The kidney is one of the most susceptible organs to aging. One-half of adults over the age of 70 years have a low estimated glomerular filtration rate and are diagnosed as having CKD [4]. A biopsy study of transplant donors' kidneys [5] proved that nephrosclerosis is observed in >50% of kidneys of persons >60 years old.

In this study, however, many older donors were systematically evaluated as "healthy" or at least "healthy for age" before biopsy. It is concerning that too many older patients could be unnecessarily labeled as "diseased" and treated without any proven clinical benefit [6]. Elderly persons with early-stage CKD might better be evaluated as undergoing "normal aging" or "healthy aging". To prevent over-diagnosis, it is necessary to distinguish "healthy aging-related morphological changes" or "less harmful changes" from "harmful changes that cause advanced renal dysfunction". To confirm that this is a good idea, we must first evaluate the direct relation between the renal microvasculature and its relevant tissue damage. Our "renal microvascular three-dimensional (3D) imaging" technique [7] might be a good tool for determining the difference.

In a previous article [7], we proposed 3D reconstruction of the human renal microvasculature using paraffin-embedded surgically removed tissue and a vertical slide system. The advantage of this method is that it enables us to examine the direct connection between arteries and peripheral tissue and then identify the underlying pathology [7–11]. The purpose of this study was to investigate whether our 3D imaging could distinguish less harmful renal vascular changes from the dangerous changes that induce renal dysfunction using 2D and 3D images of human tissue.

2. Results

2.1. Clinical and Pathological Characteristics of Four Cases

The clinical features and pathological characteristics of four patients (all older Japanese men) are shown in Table 1. In three of them, we did not detect renal disease, proteinuria, hypertension, diabetes, or hyperlipidemia. Patient 4 (case 4) was diagnosed as having hypertensive nephrosclerosis with mild renal dysfunction and hyperlipidemia. Among the four patients, he had the highest percentages of glomerulosclerosis and interstitial fibrosis. Patient 3 (case 3) had larger glomeruli than patient 1 (case 1). All patients except patient 4 (case 4) had clear cell carcinoma. Patient 4 had chromophobe carcinoma. All tumors were in stage I with no metastasis and no multifocal lesions.

Table 1. Clinical characteristics of four cases.

Parameter	Case 1	Case 2	Case 3	Case 4
Age (years)	78	78	86	71
Height (cm)	171	164	160	168
Weight (kg)	63	53	54	68
BMI (kg/m^2)	21	20	21	24
BUN (mg/dL)	17	15	18	18
Creatinine (mg/dL)	0.91	0.96	0.80	1.27
eGFR ($\text{mL}/\text{min}/1.73 \text{ m}^2$)	61	59	69	43
CKD stage	2	3a	3a	3b
%Glomerular sclerosis	9	17	11	32
Creatinine at 6 month after surgery (mg/dL)	1.3	1.5	1.2	2.1
%Interstitial fibrosis	5	7	11	14
Mean Gl diameter (μm)	158 ± 18	161 ± 10	$187 \pm 22^*$	162 ± 28
Gl density ($/\text{mm}^2 \text{ cortex}$)	4.4	3.7	2.5	2.7
Tumor pathology	Clear cell ca. $3.0 \times 3.0 \text{ cm}$	Clear cell ca. $4.7 \times 4.7 \text{ cm}$	Clear cell ca. $3.8 \times 3.9 \text{ cm}$	Chromophobe ca. $2.6 \times 2.4 \text{ cm}$
Stage of tumor (UICC)	Stage I	Stage I	Stage I	Stage I

* $p < 0.05$ vs. Case 1, 2, 4. Abbreviation: BUN: blood urea nitrogen; eGFR: estimated Glomerular Filtration Rate; CKD: chronic kidney disease; Gl: glomerular; Ca: Carcinoma; UICC: Union for International Cancer Control.

2.2. Original 2D Images

In the original 2D images, glomeruli were seen as tufts of capillaries positive for CD34 (brown) (Figure 1A,B). Arteries were identified as lumens with endothelial cells positive for CD34 (brown) surrounded by strongly expressed α -smooth muscle actin (SMA) (blue) in the media (Figure 1A,B).

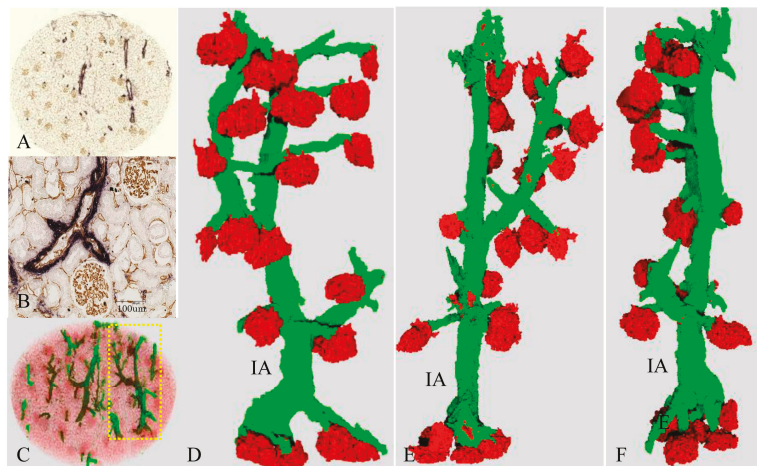


Figure 1. Vascular tree with glomeruli and the corresponding two-dimensional (2D) views in the patient with minimal Vascular Damage (Case 1). (A,B) original slice of a circular 3×3 mm core specimen with double immunostaining using anti-CD34 (brown) and then anti-SMA (blue); (A) and its magnified image (B); (C) three-dimensional (3D) reconstruction of the vascular tree; (D–F) an extracted vascular tree of yellow dotted circle of (C). IA is an interlobular artery; (E,F) rotated images of (D); and (D–F) original brown and blue correspond to red and green in the red-green-blue 3D images. Glomeruli can be identified as red figures. Arteries and arterioles are extracted as tubular formations of green SMA-positive smooth muscle cells. Interlobular arteries bifurcate and give rise to afferent arterioles, some of which branch off directly from large interlobular arteries (D–F).

2.3. Three-Dimensional Reconstruction of the Vascular Tree in the Presence of Minimal Vascular Damage (Case 1)

Figure 1C is a reconstructed 3D image of the vascular tree, which is a continuous arterial structure composed of interlobular arteries and afferent arterioles in case 1. Figure 1D–F are 3D images of the isolated single vascular tree with accompanying glomeruli (corresponding yellow dot circle in Figure 1C). In the 3D image, red corresponds to the original brown of the CD34-positive endothelial cells, and green corresponds to the original blue of SMA-positive smooth muscle cells. Arteries are identified as green tubes. Glomeruli are expressed as red ovals. The vascular tree can be freely rotated, thereby enabling assessment of the running pattern, the length and branching angles of arteries, and the shape and size of glomeruli.

In case 1, the interlobular arteries showed no distortion and a regular distribution of green smooth muscle cells as seen by inspection (Figure 1C–F). The corresponding 2D images showed minimal intimal thickening (intima/media ratio: range, average; 0.03–0.3, 0.2 ± 0.12), preserved inner lumens (diameter: range, average; 9–41 μm , $20 \pm 8 \mu\text{m}$), and no atrophy of the media (Figure 1A,B). The 3D rotated images proved that most arterioles ran straight and branched off from their interlobular arteries at nearly a right angle. In addition, their diameters were almost the same as seen by inspection. The diameter of the interlobular artery was rather preserved until its last branching. Most of the glomeruli revealed similar shapes and sizes.

2.4. Three-Dimensional Reconstruction of the Vascular Tree in the Presence of Mildly Damaged Arteries (Case 2)

Compared with case 1, the interlobular artery of case 2 showed irregular distribution of the smooth muscle cells and was mildly distorted in the 3D image as seen by inspection (Figure 2A–E).

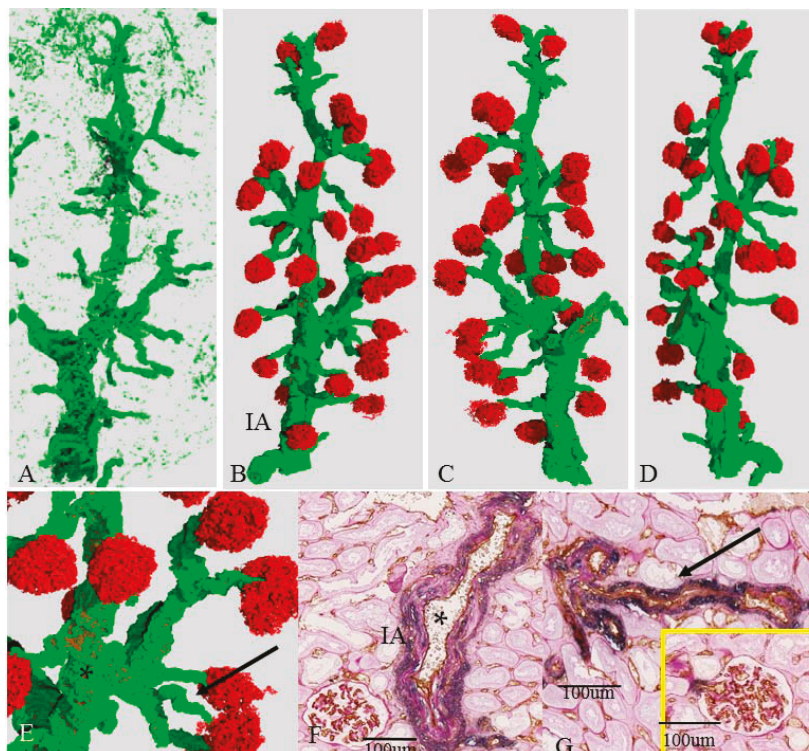


Figure 2. Vascular tree with mild change (Case 2). (A–E) single vascular tree with (B–E) or without (A) associated glomeruli; (C,D) rotated images of (B); (E) magnified view of (B). Red and green color correspond to CD34 and SMA in the 2D image, respectively. IA is an interlobular artery (F,G) corresponding 2D image that is double-immunostained with anti-CD34 (brown) and anti-SMA (blue) and then periodic acid-Schiff (PAS) stain. The asterisk (*) (F) and arrow (G) correspond to the same symbols in (E); (A–E) the interlobular arteries show irregular distribution of SMA and are mildly distorted; (F) corresponding 2D view shows that the media (blue) is atrophic, and SMA is irregularly distributed; the afferent arterioles are mildly distorted in the 3D view (A–E); whereas the corresponding 2D view (G) reveals regular media and segmental hyalinosis. The yellow circle represents a glomerulus supplied by this afferent arteriole.

The diameter of the proximal interlobular artery ($102 \mu\text{m}$) was larger than that of case 1 ($92 \mu\text{m}$), and the distal interlobular artery was much smaller than the proximal one. In the corresponding 2D image (Figure 2G), the interlobular arteries had fibrous intimal thickening (intima/media ratio: $0.4\text{--}1.5$, 0.96 ± 0.082) and irregular medial atrophy, but a preserved lumen. Many afferent arterioles in case 2 were mildly distorted in the 3D image as seen by inspection. (Figure 2A–E). The corresponding 2D image (Figure 2H) showed hyalinosis and mild luminal narrowing (Figure 2G). Many glomeruli had preserved morphology and were of similar size. There were eight atrophic or sclerotic glomeruli in this vascular tree. Six of them were located at the distal end of the vascular tree near the cortical surface.

2.5. Three-Dimensional Reconstruction of the Vascular Tree in an Older Patient (Case 3)

In case 3, the proximal interlobular artery showed marked intimal thickening (intima/media ratio 2.1) and medial atrophy but with preserved lumens in the 2D image (arrow, Figure 3A,G). The distal interlobular artery and the afferent arteriole, however, revealed minimal intimal thickening (intima/media ratio 0.04–0.57, 0.34 ± 0.35) and no hyalinosis (Figure 3D–G). The luminal spaces were sufficiently large (14–41 μm). The accompanying glomeruli showed no definitive changes. Among the four cases, case 3 had the lowest glomerular density, and the average diameter was larger than those of cases 1, 2, and 3 ($p < 0.05$) (Table 1). The corresponding 3D image of the vascular tree (Figure 3B–F) showed that arteries and arterioles ran straight, and almost all glomeruli had similar shape and size (diameter 171–233 μm), but one (marked with *) was small (140 μm) and had an irregular shape compared with the others. The distal end of the interlobular artery had a rather small lumen. The branching angles of some arterioles from the interlobular artery were sharp compared with those in cases 1 and 2 (Figure 3G).

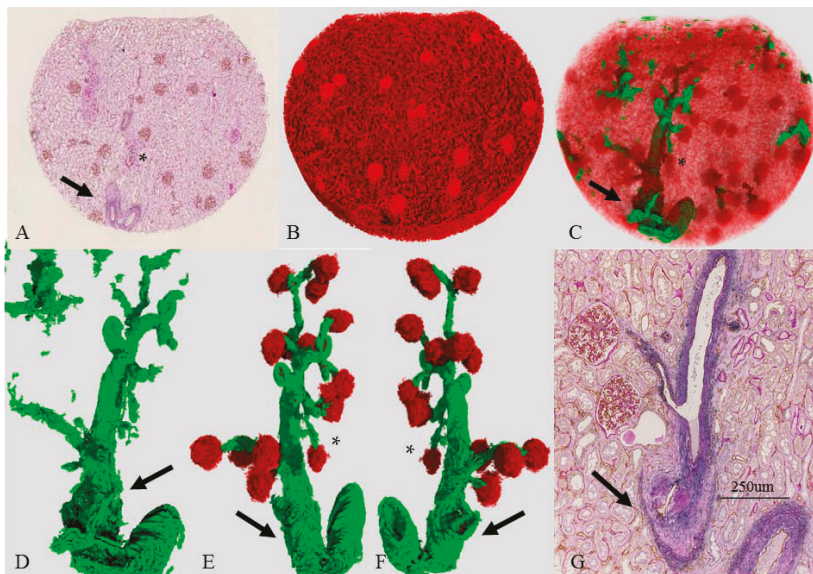


Figure 3. Vascular tree with decreased glomeruli (case 3). (A) Original 2D image of the section double-immunostained with anti-CD34 (brown) and anti-SMA (blue) and then PAS stain; (B) 3D reconstructed image of CD34. Glomeruli are round. Capillaries resemble a mesh network (red). Density of glomeruli is low; (C) 3D image of the vascular tree; (D–F) A single vascular tree with (E,F) or without (D) associated glomeruli; Red and green represent CD34 and SMA, respectively. All of the arteries show a regular SMA distribution and smooth surface. Arteries run straight. The branching angles of the afferent arterioles are sharp; (G) corresponding 2D image double-stained for CD34 and SMA with PAS stain. The diameter of the proximal interlobular artery is wide; and (A,G) corresponding 2D view reveals marked intimal fibrosis and medial atrophy; luminal area is preserved (A); and the arrow in (G) points to a bifurcation site and shows irregular intimal hyperplasia. Although the lumen seems narrow, the consecutive specimen reveals a large lumen, as seen in (A). The arrow and asterisk (*) correspond to the same symbols (A,C–G) and represent the interlobular artery and the atubular glomerulus in Figure 5, respectively.

2.6. Three-Dimensional Reconstruction of the Vascular Tree in the Presence of Nephrosclerosis (Case 4)

Figure 4 shows the 2D and the 3D images of the renal microcirculation in the case of hypertensive nephrosclerosis with mild renal dysfunction. The 2D image (Figure 4A) highlights the prominent interstitial fibrosis and the presence of many sclerotic glomeruli near the capsule. In the corresponding 3D image (Figure 4B,C), SMA-positive areas were widely distributed in the cortex, especially near the renal surface and around each interlobular artery. Complete reconstruction of the vascular tree was difficult because the arterial media was not clearly distinguished from the surrounding interstitial fibrosis. In the 3D image, many interlobular arteries ran straight but were small and narrow (Figure 4D,E). The corresponding 2D view proved that the proximal interlobular artery (Figure 4F) showed no marked change in the media but mild hyalinosis in the intima. The distal interlobular arteries (arrows, Figure 4F,G) showed prominent hyalinosis and a decreased luminal area. The glomerular shape was irregular, and some glomeruli were enlarged. Glomerular density was decreased compared with those in cases 1 and 2 (Table 1).

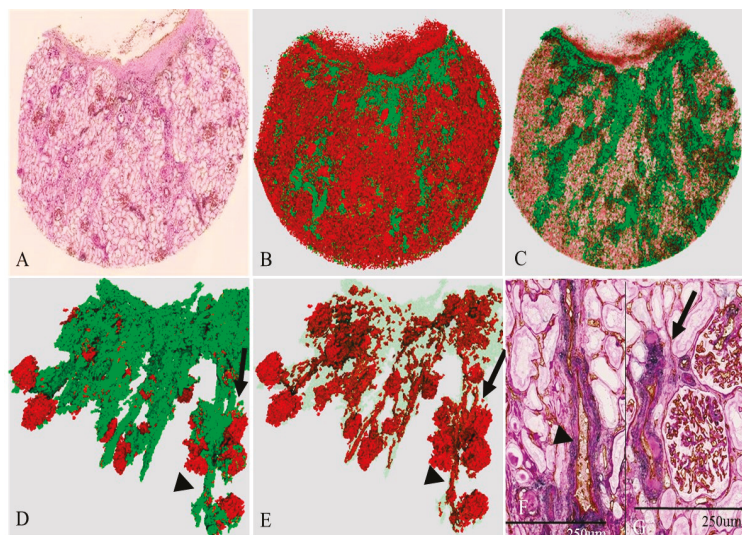


Figure 4. Vascular tree in Nephrosclerosis (Case 4). (A) Original 2D image of a section double-immunostained with anti-CD34 (brown) and the anti-SMA (blue) and then PAS stain; (B,C) 3D image of the renal microvasculature; (D,E) extracted view of the vascular tree; (F,G) 2D image. In the 2D image (A), differentiating the vessels from surrounding fibrotic interstitium is difficult. Thus, complete reconstruction of the vascular tree was not obtained, although some vessels can be identified; and the proximal interlobular artery (arrowhead, D–F) is smaller than that in case 2 (Figure 2) and case 3 (Figure 3). The smaller interlobular artery (arrow) (G) shows high hyalinosis and a reduced lumen.

2.7. Three-Dimensional Image of an Atubular Glomerulus (Case 3D)

Figure 5 shows the 3D and 2D images of a single “atubular glomerulus” in case 3, which corresponds to the asterisks (*) in Figure 3E,F. Because of its long atrophic proximal tubule, the glomerulus was diagnosed as an “atubular glomerulus”. The 2D image (Figure 5C,F,G) proved that the glomerulus was small and exhibited shrinkage of the tuft and fibrous thickening of the Bowman capsule. The 3D and its corresponding 2D image confirmed the morphology of its supplying vessels. The interlobular artery had a large lumen with no definitive morphological changes in the 2D image (Figure 5C). In contrast, the afferent artery had a small diameter, and there was a great distance from the branching off of the interlobular artery (Figure 5A–C). The glomerulus had a small exit (*) near

the afferent arteriole (Figure 5D,F), but we also found an extra exit apart from the afferent arteriole (arrows, Figure 5D–G). This extra exit is divided into several tiny capillaries soon after leaving the glomerulus and ran near the glomerulus (arrow, Figure 5A,B). Some were so tiny they could not be pursued (perhaps disappearing into the interstitium).

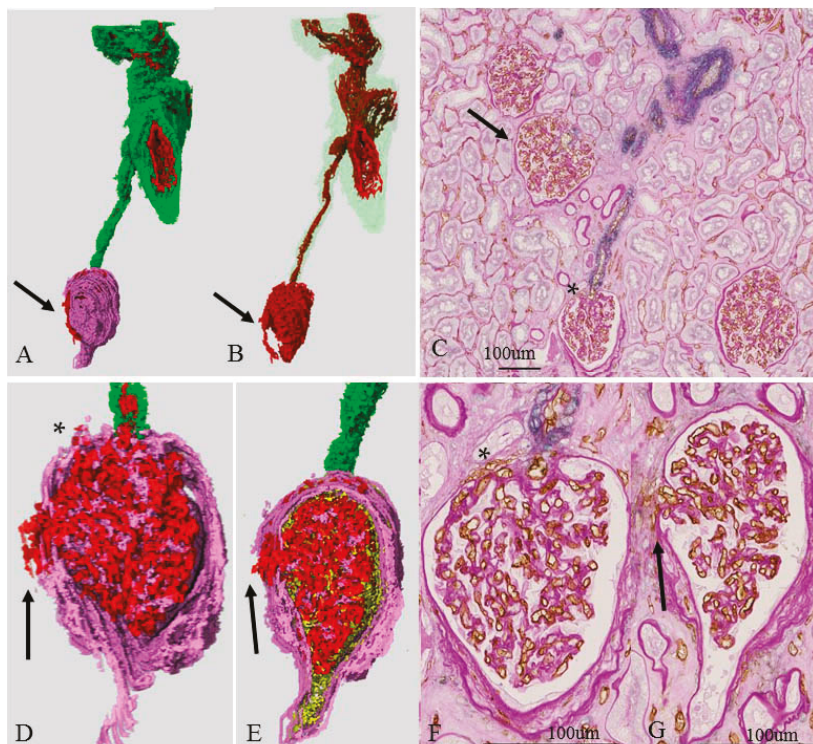


Figure 5. Three-and two-dimensional image of atubular glomerulus (Case 3). (A,B,D,E) 3D image of an atubular glomerulus with the interlobular artery and the afferent artery. Red, green, pink, and yellow represent CD34-positive endothelial cells, SMA-positive smooth muscle cells, PAS-positive basement membranes of the Bowman capsule and glomerulus, and epithelial cells of the glomerulus, Bowman's capsule, and proximal tubule, respectively. These structures correspond to * in Figure 3A,C–F. (C,F,G) 2D image double-immunostained with anti-CD34 (brown) and SMA (blue) and then PAS stain. The interlobular artery has a large lumen (C). The afferent arteriole is long and has small lumen (B,C). The glomerulus (*) (C) corresponds to (A,B,D–G). The glomerulus (*) is smaller than the other glomerulus (arrow) (C) and shows shrinkage of the tuft (F,G); and the glomerulus has two exits (* and arrow) (D–G).

2.8. Three-Dimensional Image of a Single Glomerulus and Cystic Dilation of an Afferent Arteriole (Case 3) near the Atubular Glomerulus

Figure 6 shows the 2D and 3D images of a single glomerulus in case 3, which corresponds to the * in Figure 5G. The afferent arteriole was distorted and has an irregular lumen (Figure 6B) compared with case 1 (Figure 5C). Within the glomerulus, the afferent arteriole had surrounding abundant SMA-positive cells and was dilated. The exit of the efferent arteriole was apart from the entrance of the afferent arteriole in the 3D image (Figure 6A–E), whereas the 3D image in case 1 (Figure 6C) showed

that the exits and entrances of the arterioles were closely located. The interlobular artery of case 3 had a small lumen compared with that in case 1 (Figure 6C).

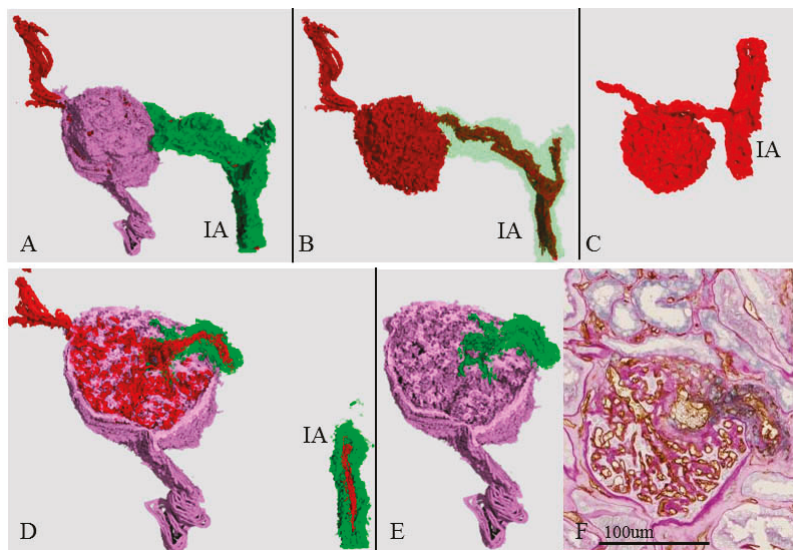


Figure 6. Three-dimensional image of abnormal efferent arteriole (Case 3). 3D images of a single glomerulus with abnormal efferent arterioles (A,B,D–F) in case 1; (A–E) Red, green, and pink are the CD34-positive endothelial cells, SMA-positive smooth muscle cells, and PAS-positive basement membranes of a Bowman capsule and glomerular basement membrane, respectively. IA is the interlobular artery. These structures correspond to the arrow in Figure 5C. The afferent arteriole is mildly distorted. Within the glomerulus, smooth muscle cells are still observed around the dilated afferent arteriole in the 3D view (D,E) and the 2D view (F); and the afferent arteriole is located apart from the efferent arteriole, whereas the arterioles were closely associated in case 1 (C).

3. Discussion

We examined 3D images of the renal microvasculature, especially glomeruli and their connecting vessels, in older persons with preserved renal function or mild renal dysfunction. We used the images to investigate the morphological changes seen during healthy aging.

The renal morphological changes in kidneys due to aging have been investigated using both 2D [12–16] and 3D [3] imaging. Age-related changes have been identified as mesangial matrix expansion, irregular foot process fusion, glomerulosclerosis [12–15], decreased number of glomeruli [12–14], glomerular hypertrophy [15], interstitial fibrosis [16], and arterial changes [3,17]. Arteries show hyalinosis and intimal thickening with medial atrophy [17]. Macroscopically, decreased kidney volume and size, reduced size of the cortex [18], formation of cysts, and cortical scars are also common findings in the aging kidney.

The abovementioned changes were found in each of our four cases in different degrees and morphology. Three had normal or nearly normal renal function for their age and had no complications. Compared with case 1, cases 2 and 3 showed more prominent sclerotic changes in the proximal interlobular arteries and increased sclerotic glomeruli and interstitial damage. Three-dimensional imaging, however, proved that the glomeruli and distal arteries and arterioles supplied by the damaged proximal interlobular artery had no severe morphological changes, although the increased number of sclerotic glomeruli had increased in the distal ends. Case 4, with severe intimal changes in the distal interlobular artery and many sclerotic glomeruli, exhibited only mildly impaired renal function.

In the 3D images, the distal arteries and arterioles and glomeruli showed marked pathological changes. Our results revealed that the morphological changes in the large proximal interlobular artery or arcuate arteries did not directly induce severe renal damage, whereas small arterial changes were more critical to the development of glomerulosclerosis and interstitial damage. Nimomiya et al. [13] presented similar results based on Japanese autopsy cases with excellent statistical analyses. They showed that atherosclerotic changes in large arteries had no correlation with glomerular sclerosis and concluded that the arteries most susceptible to hypertension were the small ones (diameter < 150 μm). We successfully visualized this concept with 2D and 3D images.

We also visualized glomerular modifications in a case of healthy aging, in which an atubular glomerulus and cystic dilatation of the afferent arteriole were apparent. The glomerulus showed long, atrophic, proximal tubules—part of the definition of an atubular glomerulus [19]. Proximal tubules, known for their high rates of oxygen consumption and relative paucity of endogenous antioxidant defenses, are susceptible to many types of injury, including obstructive, ischemic, hypoxic, oxidative, and metabolic changes [19,20]. These injuries are believed to induce the formation of atubular glomeruli [19]. Our atubular glomerulus was considered to have an ischemic etiology because it showed tuft shrinkage and it was supplied by long, small afferent arterioles. Our 3D images also clearly identified an extra exit of this glomerulus. Inadequate glomerular circulation might have induced the formation of the extra exit and atrophic tubules. Our 3D image clarified the modifications of the glomerulus. The intraglomerular afferent arteriole was dilated and surrounded by abundant SMA-positive cells, and it was located apart from the efferent arteriole. These changes might also be induced by inadequate hyperfiltration because case 3 showed glomerular hypertrophy probably due to nephron loss. Modification of afferent and efferent arterioles has been proven in cases of aging. Such modifications include anastomoses and a direct channel between the afferent and efferent arterioles. We suspected that the glomerular modification might be a compensatory change in response to alteration of the glomerular circulation and possibly a morphological change due to aging.

Recent technical advances have enabled us to reconstruct high-resolution 3D images of the renal microvasculature, which have proved useful for investigating renal damage caused by an altered microvasculature [21–25]. Micro-computed tomography with contrast media can successfully quantify vessel density and vascular volume and has confirmed the rarefaction of renal capillaries in eNOS^{-/-} rat kidney [21]. Confocal microscopy with fluorescence micro-angiography proved the reduction of glomerular and peritubular capillary density [1] and the increase in capillary branching of glomeruli [22,23] in a diseased rat kidney. Recently, Torres et al. created 3D images of the whole kidney in cisplatin-treated mice and successfully reconstructed a complete nephron using multi-photon microscopy [24].

All 3D imaging of the renal microvasculature requires special tools. In addition, the techniques are rarely applied to humans and do not provide the underlying histology. Our technique is superior to those methods because it uses conventional paraffin-embedded sections and enables detection of the underlying histology. The disadvantages of our method are that it requires an expensive virtual slide system and human labor for reconstruction. In addition, the reconstructions are of limited size. Clearer figures of 3D reconstructions of the renal microcirculation may be obtained by X-ray micro-computed tomography [21], or scanning electron microscopy [25]. Our method, however, has great ability to reconstruct the boundaries between arterioles, glomeruli, and surrounding interstitium. It also enables comparisons between 3D and 2D histology, which is not achieved by any other 3D technique.

4. Materials and Methods

4.1. Tissue Preparation

Conventional surgical, formalin-fixed, paraffin-embedded tissue blocks from non-neoplastic renal parenchyma of four Japanese patients diagnosed with renal cell carcinoma were used in this study

(Table 1). The tumor was diagnosed Kazumori Kikuchi, a pathologist who is one of our authors, and was classified according to Union for International Cancer Control (UICC) criteria. The institutional review board of Tsukuba Medical Center approved this data analysis (23 December 2011).

Conventional stains—e.g., hematoxylin-eosin, periodic acid Schiff (PAS), Masson trichrome, elastic-van Gieson—were used for morphological analysis and determination of suitable areas for tissue preparation. Details of tissue preparation are described elsewhere [7–11].

4.2. Immunohistochemistry and Microscopic Image Digitization

Double immunohistochemical staining with mouse anti-CD34 (Dako, Glostrup, Denmark) and anti-SMA (Dako) was performed to identify endothelial cells and smooth muscle cells of the arterial media (Figure 1A). The PAS stain was then applied to the sections to identify the tubular basement membranes, Bowman's capsules, sclerotic glomeruli, and interstitial fibrosis (Figure 2F,G, Figure 3A,G, Figure 4F,G, Figure 5C,F,G and Figure 6G). Details of the tissue preparation are described elsewhere [7–10]. Each stained specimen was digitized using virtual slide microscopy (NanoZoomer RSTM; Hamamatsu Photonics, Hamamatsu, Japan), using a 40 \times optical lens.

4.3. Image Registration, Segmentation of Tissue Components, Geometric Reconstruction

Image registration, segmentation of tissue components, and geometric reconstruction were performed using two software packages, Image-J (version 1.48, NIH, Bethesda, MA, USA) and TRI/3D-SRF (version 64, Ratoc System Engineering Co., Tokyo, Japan) as described previously [8–10]. Histological digitized images have a resolution of 0.92 μ m per pixel, 5120 \times 4096 pixels, 60 MB, and a 32-bit RGB TIFF format.

4.4. Conventional Histological Analysis of Surgical Specimens

Percentages of sclerotic glomeruli and tubular cortical interstitial fibrosis were assessed using image-processing software (WinRoof®; Mitani Corp., Tokyo, Japan) (Table 1). Using serial sections used for 3D reconstructions, the glomerular diameter was measured in 25–35 glomeruli. Diameter is defined as the largest one in the serial sections. Glomerular density was calculated as the glomerular number/mm² cortex in a large surgical specimen. Intima/media ratio and luminal diameter were majorly in the serial 2D sections.

4.5. Statistical Analysis

Results are expressed as means \pm standard error of the mean (SEM). Comparisons between two and among cases were performed using paired Student's *t*-tests and one-way ANOVA, respectively. A value of *p* < 0.05 was considered to indicate statistical significance.

5. Conclusions

In conclusion, our 3D imaging of the renal microvasculature has the ability to prove a direct relation not only between the arteries and glomeruli but also between arteries and arterioles and between glomeruli and tubular structures. We successfully visualized 3D images of healthy aging microvascular changes. Our 3D imaging was of great help for clarifying the mechanism of microvascular renal injury in older persons and others with chronic renal disease.

Acknowledgments: This study was supported by two Japanese Grants-in-Aid for Scientific Research from the Japan Society for the Promotion of Science (C23591179, C26461211).

Author Contributions: Noriko Uesugi designed the study and wrote the initial draft of the manuscript. Yoshihito Shimazu reconstructed 3D images using software. Kazunori Kikuchi collected human kidney samples and their clinical information. Michio Nagata contributed to analysis and interpretation of data, and assisted in the preparation of the manuscript. All other authors have contributed to data collection and interpretation, and critically reviewed the manuscript. The final version of the manuscript was approved by all authors.

Conflicts of Interest: The authors declare no conflict of interest.

Abbreviations

CKD	Chronic Kidney Disease
3D	Three-Dimensional
2D	Two-Dimensional
SMA	α -Smooth Muscle Actin

References

1. Navar, L.G.; Arendshorst, W.J.; Pallone, T.L.; Inscho, E.W.; Imig, J.D.; Bell, P.D. The renal microcirculation. In *Comprehensive Physiology*; Pollock, D.M., Ed.; Wiley: Hoboken, NJ, USA, 2011; pp. 550–683.
2. Alpers, C.E.; Fogo, A.B. Kidney and its collecting system. In *Robbins Basic Pathology*, 9th ed.; Kumar, V., Abbas, A.K., Aster, J.C., Eds.; Elsevier: Philadelphia, PA, USA, 2013; pp. 539–540.
3. Ljungqvist, A.; Lagergren, C. Normal intrarenal arterial pattern in adult and ageing human kidney: A microangiographical and histological study. *J. Anat. Lond.* **1962**, *96*, 285–300.
4. Schaeffner, E.S.; Ebert, N.; Delanaye, P.; Frei, U.; Gaedeke, J.; Jakob, O.; Kuhlmann, M.K.; Schuchardt, M.; Tölle, M.; Ziebig, R.; et al. Two novel equations to estimate kidney function in persons aged 70 years or older. *Ann. Intern. Med.* **2012**, *157*, 471–481. [CrossRef] [PubMed]
5. Rule, A.D.; Amer, H.; Cornell, L.D.; Taler, S.J.; Cosio, F.G.; Kremers, W.K.; Textor, S.C.; Stegall, M.D. The association between age and nephrosclerosis on renal biopsy among healthy adults. *Ann. Intern. Med.* **2010**, *152*, 561–567. [CrossRef] [PubMed]
6. Moynihan, R.; Glasscock, R.; Doust, J. Chronic kidney disease controversy: How expanding definitions are unnecessarily labelling many people as diseased. *BMJ* **2013**, *347*, 19–22. [CrossRef] [PubMed]
7. Uesugi, N.; Shimazu, Y.; Aoba, T.; Kikuchi, K.; Nagata, M. High-resolution three-dimensional digital imaging of human renal microcirculation: An aid to evaluate microvascular alterations in chronic kidney disease. *Pathol. Int.* **2015**, *65*, 575–584. [CrossRef] [PubMed]
8. Kudo, T.; Shimazu, Y.; Yagishita, H.; Izumo, T.; Soeno, Y.; Sato, K.; Taya, Y.; Aoba, T. Three-dimensional reconstruction of oral tongue squamous cell carcinoma at invasion front. *Int. J. Dent.* **2013**, *13*, 424–440. [CrossRef] [PubMed]
9. Kurata, M.; Nose, M.; Shimazu, Y.; Aoba, T.; Kohada, Y.; Yorioka, S.; Suehiro, S.; Fukuoka, E.; Matsumoto, S.; Watanabe, H.; et al. Microvasculature of carotid atheromatous plaques: Hemorrhagic plaques have dense microvessels with fenestrations to the arterial lumen. *J. Stroke Cerebrovasc. Dis.* **2014**, *23*, 1440–1446. [CrossRef] [PubMed]
10. Maruyama, S.; Shimazu, Y.; Kudo, T.; Sato, K.; Yamazaki, M.; Abé, T.; Babkair, H.; Cheng, J.; Aoba, T.; Saku, T. Three-dimensional visualization of perlecan-rich neoplastic stroma induced concurrently with the invasion of oral squamous cell carcinoma. *J. Oral Pathol. Med.* **2014**, *43*, 627–636. [CrossRef] [PubMed]
11. Shimazu, Y.; Kudo, T.; Yagishita, H.; Aoba, T. Three-dimensional visualization and quantification for the growth and invasion of oral squamous cell carcinoma. *Jpn. Dent. Sci. Rev.* **2010**, *46*, 17–25. [CrossRef]
12. Kubo, M.; Kiyohara, Y.; Kato, I.; Tanizaki, Y.; Katafuchi, R.; Hirakata, H.; Okuda, S.; Tsuneyoshi, M.; Sueishi, K.; Fujishima, M.; et al. Risk factors for renal glomerular and vascular changes in an autopsy-based population survey: The Hisayama study. *Kidney Int.* **2003**, *63*, 1508–1515. [CrossRef] [PubMed]
13. Ninomiya, T.; Kubo, M.; Doi, Y.; Yonemoto, K.; Tanizaki, Y.; Tsuruya, K.; Sueishi, K.; Tsuneyoshi, M.; Iida, M.; Kiyohara, Y. Prehypertension increases the risk for renal arteriosclerosis in autopsies: The Hisayama Study. *J. Am. Soc. Nephrol.* **2007**, *18*, 2135–2142. [CrossRef] [PubMed]
14. Tan, J.C.; Busque, S.; Workeneh, B.; Ho, B.; Derby, G.; Blouch, K.L.; Sommer, F.G.; Edwards, B.; Myers, B.D. Effects of aging on glomerular function and number in living kidney donors. *Kidney Int.* **2010**, *78*, 686–692. [CrossRef] [PubMed]
15. Elsherbiny, H.E.; Alexander, M.P.; Kremers, W.K.; Park, W.D.; Poggio, E.D.; Prieto, M.; Lieske, J.C.; Rule, A.D. Nephron hypertrophy and glomerulosclerosis and their association with kidney function and risk factors among living kidney donors. *Clin. J. Am. Soc. Nephrol.* **2014**, *9*, 1892–1902. [CrossRef] [PubMed]
16. Kappel, B.; Olsen, S. Cortical interstitial tissue and sclerosed glomeruli in the normal human kidney, related to age and sex. A quantitative study. *Virchows Arch. A Pathol. Anat. Histol.* **1980**, *387*, 271–277. [CrossRef] [PubMed]

17. Haas, M.; Segev, D.L.; Racusen, L.C.; Bagnasco, S.M.; Melancon, J.K.; Tan, M.; Kraus, E.S.; Rabb, H.; Ugarte, R.M.; Burdick, J.F.; et al. Arteriosclerosis in kidneys from healthy live donors: Comparison of wedge and needle core perioperative biopsies. *Arch. Pathol. Lab. Med.* **2008**, *132*, 37–42. [PubMed]
18. Samuel, T.; Hoy, W.E.; Douglas-Denton, R.; Hughson, M.D.; Bertram, J.F. Determinants of glomerular volume in different cortical zones of the human kidney. *J. Am. Soc. Nephrol.* **2005**, *16*, 3102–3109. [CrossRef] [PubMed]
19. Chevalier, R.L.; Forbes, M.S. Generation and evolution of atubular glomeruli in the progression of renal disorders. *J. Am. Soc. Nephrol.* **2008**, *19*, 197–206. [CrossRef] [PubMed]
20. Chevalier, R.L. The proximal tubule is the primary target of injury and progression of kidney disease: Role of the glomerulotubular junction. *Am. J. Physiol. Ren. Physiol.* **2016**, *311*, F145–F161. [CrossRef] [PubMed]
21. Ramot, Y.; Brauner, R.; Kang, K.; Heymach, J.V.; Furtado, S.; Nyska, A. Quantitative evaluation of drug-induced microvascular constriction in mice kidney using a novel tool for 3D geometrical analysis of ex vivo organ vasculature. *Toxicol. Pathol.* **2014**, *42*, 774–783. [CrossRef] [PubMed]
22. Advani, A.; Connelly, K.A.; Yuen, D.A.; Zhang, Y.; Advani, S.L.; Trogadis, J.; Kabir, M.G.; Shachar, E.; Kuliszewski, M.A.; Leong-Poi, H.; et al. Fluorescent microangiography is a novel and widely applicable technique for delineating the renal microvasculature. *PLoS ONE* **2011**, *7*, e24695. [CrossRef] [PubMed]
23. Scruggs, B.S.; Zuo, Y.; Donnert, E.; Ma, L.; Bertram, J.F.; Fogo, A.B. Increased capillary branching contributes to angiotensin type 1 receptor blocker (ARB)-induced regression of sclerosis. *Am. J. Pathol.* **2011**, *178*, 1891–1898. [CrossRef] [PubMed]
24. Torres, R.; Velazquez, H.; Chang, J.J.; Levine, M.J.; Moeckel, G.; Desir, G.V.; Safirstein, R. Three-Dimensional Morphology by Multiphoton Microscopy with Clearing in a Model of Cisplatin-Induced CKD. *J. Am. Soc. Nephrol.* **2016**, *27*, 1102–1112. [CrossRef] [PubMed]
25. Giuvărășteanu, I. Scanning electron microscopy of vascular corrosion casts—standard method for studying microvessels. *Rom. J. Morphol. Embryol.* **2007**, *48*, 257–261. [PubMed]



© 2016 by the authors. Licensee MDPI, Basel, Switzerland. This article is an open access article distributed under the terms and conditions of the Creative Commons Attribution (CC BY) license (<http://creativecommons.org/licenses/by/4.0/>).



Article

Intracranial Thrombus Morphology and Composition Undergoes Time-Dependent Changes in Acute Ischemic Stroke: A CT Densitometry Study

Slaven Pikija ¹, Jozef Magdic ², Vladimir Trkulja ³, Peter Unterreuter ⁴,
Johannes Sebastian Mutzenbach ¹, Helmut F. Novak ¹, Friedrich Weymayr ⁵, Larissa Hauer ^{6,†}
and Johann Sellner ^{1,7,8,*,†}

¹ Department of Neurology, Christian Doppler Medical Center, Paracelsus Medical University, 5020 Salzburg, Austria; s.pikija@salk.at (S.P.); j.mutzenbach@salk.at (J.S.M.); h.novak@salk.at (H.F.N.)

² Department of Neurology, Univerzitetni Klinični Center, 2000 Maribor, Slovenia; jozef_magdic@yahoo.com

³ Department for Pharmacology, School of Medicine, University of Zagreb, 10000 Zagreb, Croatia; vtrkulja@mef.hr

⁴ Department of Neurology, Bezirkskrankenhaus Lienz, 9900 Lienz, Austria; p.unterreuter@kh-lienz.at

⁵ Division of Neuroradiology, Christian Doppler Medical Center, Paracelsus Medical University, 5020 Salzburg, Austria; f.weymayr@salk.at

⁶ Department of Psychiatry, Christian Doppler Medical Center, Paracelsus Medical University, 5020 Salzburg, Austria; l.hauer@salk.at

⁷ Department of Neurology, Klinikum rechts der Isar, Technische Universität, 81675 München, Germany

⁸ Institute of Linguistics, University of Salzburg, 5020 Salzburg, Austria

* Correspondence: j.sellner@salk.at; Tel.: +43-5-7255-34762

† These authors contributed equally to this work.

Academic Editor: Michael Henein

Received: 4 September 2016; Accepted: 18 November 2016; Published: 23 November 2016

Abstract: The aim of our study was to assess whether cerebral artery clots undergo time-dependent morphological and compositional changes in acute ischemic stroke. We performed a retrospective chart review of patients admitted within 5 h from symptom onset to three European stroke centers and evaluated non-contrast-enhanced CT (NECT) for hyperdense artery signs (HAS) in 2565 scans. The occlusion site, density of HAS expressed in Hounsfield units (HU), area of HAS, and relative density (rHU) (HU clot/HU non-affected artery) were studied and related to time from symptom onset, clinical severity, stroke etiology, and laboratory parameters. A HAS was present in the middle cerebral artery (MCA) in 185 (7.2%) and further explored. The mean time from symptom onset to CT was 100 min (range 17–300). We found a time-dependent loss of density in the occluded M1 segment within the first 5 h ($N = 118$, 95% CI [$-15, -2$], $p = 0.01$). Further, the thrombus area in the M2 segment decreased with time (cubic trend $N = 67$, 95% CI [$-63, -8$], $p = 0.02$). Overall, and especially in the M2 segment, a lower clot area was associated with higher fibrinogen (-21.7% , 95% CI [$-34.8, -5.8$], $p = 0.009$). In conclusion, our results disclosed time-dependent changes of intracranial thrombi with regard to occlusion site, density and area.

Keywords: acute ischemic stroke; intracranial clot; vascular disease; atherosclerosis; neuroimaging; hyperdense artery sign; biomarker

1. Introduction

Acute occlusion of intracranial vessels is responsible for up to 80% of ischemic strokes [1,2]. The susceptibility of clot material to reperfusion therapy is being actively researched; however, more data is needed to fill the knowledge gap [3–6]. The composition of clots is thought to be dependent

on the embolic source. Hence, fibrin-rich “white” thrombi are presumed to originate from high-flow larger arteries and thrombi with a predominant red blood cell (RBC) composition are more likely to stem from low-flow cardiac sources [3]. The clots composed predominantly of RBC are considered to be fresh, less compact and more hyperdense than fibrin-rich clots. After local plaque rupture in coronary vessels, the development of proximal and distal of fibrin-/thrombocyte-rich nidus have been reported [7]. A similar mechanism could take place for embolized clots in acute ischemic stroke (AIS). Indeed, interspersed formations of fibrin-platelet-rich deposits with linear collections of nucleated cells and erythrocytes have also been reported in AIS [4]. Several later studies, however, disclosed that the thrombi from these two locations do not differ in composition, being heterogeneous with both fibrin- and RBC-rich layers interspersed, probably reflecting time-dependent changes [4,8]. A recent CT densitometry study hypothesized that the clot loses its density by acquiring fibrin, since more hypodense clots were found in patients with lower fibrinogen values [9]. The RBC count, on the other hand, showed no correlation with clot density. In addition, the fibrinogen serum levels were lower in patients with larger intracranial clots.

In AIS, the hyperdense artery sign (HAS) on non-contrast-enhanced computed tomography (NECT) is thought to represent the intraluminal thrombus and subsequent arterial obstruction. A recent meta-analysis found a sensitivity and specificity of HAS for arterial obstruction on angiography of 52% and 95%, respectively [10]. Of note, thrombus characteristics can be evaluated reliably on non-contrast-enhanced CT by further characterizing the HAS [11,12]. In this regard, thrombi with lower Hounsfield units (HU) on NECT appear to be more resistant to pharmacological lysis and mechanical thrombectomy [11,13–15]. Given the varied choice of catheters and techniques currently available, pre-therapeutic thrombus characterization may help in the selection of the most effective method [16]. Here, we present the results of the retrospective three-center study on the time-dependent thrombus dynamics seen as HAS on NECT in patients with AIS.

2. Results

2.1. Patient Eligibility and Characteristics

Of the 2562 patients with NECT scans, a HAS was present in 270 cases. Of those, 250 patients had the time between symptom onset and NECT scan exactly recorded: in 41 patients the elapsed time was >300 min (up to 960) (Figure 1). To avoid a potential bias arising from a lower number of patients beyond 300 min, only the patients with NECT performance within 300 min were selected for detailed analysis. Among the remaining 209, an occlusion of the middle cerebral artery (MCA) was by far prevailing (Figure 1).

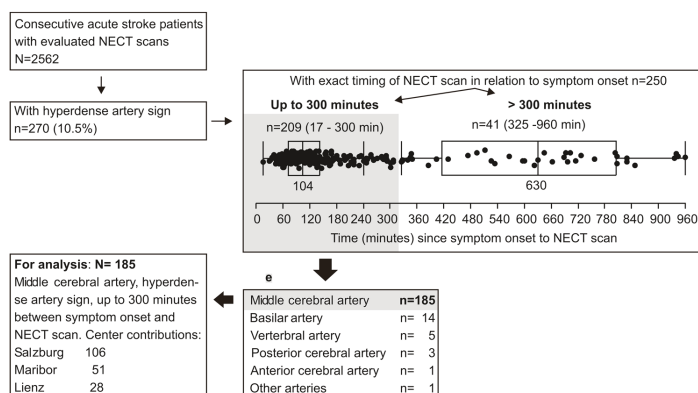


Figure 1. Flow of the patient selection process.

To avoid a further bias due to low patient numbers for other occluded vessels, the present analysis was restricted to 185 patients with MCA involvement (Figure 1). Clinical details are depicted in Table 1 and give insight to characteristics of the entire cohort and in subgroups stratified for the affected MCA segment (proximal or distal). Patient subsets by MCA segment were fairly comparable in all aspects, except that thrombectomy was, by far, more frequently performed when proximal MCA was affected (Table 1).

Table 1. Patient characteristics, overall and by the affected medial cerebral artery (MCA) segment. Data are median (range) or count (percent), unless otherwise stated.

Variables	All Patients		Proximal MCA		Distal MCA	
	N	Values	N	Values	N	Values
Age (years)	185	75 (19–98)	118	75 (41–97)	67	75 (19–98)
Men	185	82 (44.3)	118	52 (44.1)	67	30 (44.8)
		100 (17–300)		104 (31–286)		94 (17–300)
Symptom onset to NECT (min)	185	(Q1–Q3 = 71–136)	118	(Q1–Q3 = 71–133)	67	(Q1–Q3 = 70–147)
Side affected (left/right)	185	92 (49.7)/93	118	62 (52.5)/56	67	30 (44.8)/37
Average clot density (HU)	185	46.3 (36.1–56.1)	118	46.5 (36.9–56.1)	67	45.9 (36.1–55.3)
Non-affected side density (HU)	185	35.8 (18.6–45.7)	118	35.7 (24.4–45.7)	67	33.9 (18.6–45.7)
Ratio clot/non-affected rHU	185	1.30 (0.86–2.75)	118	1.30 (1.02–2.18)	67	1.32 (0.86–2.75)
Hyperdense area (mm^2)	176	30.2 (2.5–211.4)	115	31.7 (2.9–211.4)	61	28.2 (2.5–119.0)
Admission NIHSS	185	16 (0–32)	118	17 (0–32)	67	13 (0–32)
TOAST class	185		118		67	
Cardioembolic		93 (50.3)		59 (50.0)		34 (50.8)
Large artery atherosclerosis		23 (12.4)		20 (16.9)		3 (4.5)
Other (all arterial dissections)		6 (3.2)		4 (3.4)		2 (3.0)
Undetermined		9 (4.9)		3 (2.5)		6 (8.9)
Unknown		54 (29.1)		32 (27.1)		22 (32.8)
Angiography performed *	185	118 (63.8)	118	89 (75.4)	67	29 (43.3)
Thrombolysis	185	139 (75.1)	118	90 (76.3)	67	49 (73.1)
Thrombectomy	185	52 (28.1)	118	48 (40.7)	67	4 (6.0)
Thrombolysis + thrombectomy	185	44 (23.8)	118	40 (33.9)	67	4 (6.0)
Usage of antiplatelets	185	55 (29.7)	118	33 (28.0)	67	22 (32.8)
Usage of anticoagulants	185	19 (10.3)	118	12 (10.2)	67	7 (10.5)
History of stroke or TIA	185	25 (13.5)	118	14 (11.9)	67	11 (16.4)
Peripheral arterial disease	185	14 (7.6)	118	9 (7.6)	67	5 (7.5)
Atrial fibrillation	185	91 (49.5)	118	56 (47.5)	67	35 (53.0)
Diabetes mellitus	185	31 (16.8)	118	19 (16.1)	67	12 (17.9)
Arterial hypertension	185	127 (68.6)	118	84 (71.2)	67	43 (64.2)
Carotid stenosis >50%	185	24 (13.0)	118	16 (13.6)	67	8 (11.9)
Chronic heart failure	185	30 (16.2)	118	21 (17.8)	67	9 (13.4)
Blood glucose (mg/dL)	184	119 (76–351)	118	119 (76–254)	66	120 (77–351)
Total cholesterol (mg/dL)	160	181 (78–300)	102	185 (78–300)	58	175 (99–275)
Serum fibrinogen (mg/dL)	170	346 (55–785)	111	350 (166–785)	59	335 (55–685)

* Computed tomography or/and magnetic resonance or/and digital subtraction angiography. HU—Hounsfield units; NECT—non-contrast enhanced computed tomography; NIHSS—National Institutes of Health Stroke Scale score; TIA—transitory ischemic attack; TOAST—trial of Org 10172 in acute stroke treatment criteria.

2.2. Univariate Association between Timing of NECT (Non-Contrast-Enhanced CT) Relative to Symptom Onset and Ratio of Density (rHU) or Hyperdense Area

Initial exploration of the relationship between the timing of NECT relative to symptom onset (time-lag) and the ratio of the density (rHU) or hyperdense area indicated that these relationships were apparently different at the proximal and distal MCA (Figure 2). In detail, rHU tended to decrease with a longer time-lag at the proximal MCA but not at the distal MCA, and the difference between the slopes of the two regression lines of $\ln(\text{rHU})$ vs. time was significant ($p = 0.019$). In contrast, the hyperdense area tended to decrease with a longer time-lag at the distal MCA, but not at the proximal MCA. The difference between the slopes of the two regression lines of $\ln(\text{hyperdense area})$ vs. time was significant ($p = 0.018$).

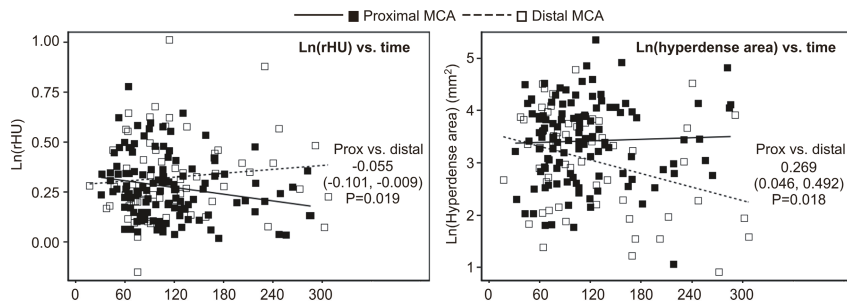


Figure 2. Exploration of the relationship between timing of NECT relative to symptom onset and ratio of density (rHU) (left) or hyperdense area (right). A separate linear mixed model (center as a cluster) was fitted to ln-transformed rHU and hyperdense area (to achieve normality of residuals) with time, MCA segment and time × MCA segment interaction term as independent variables. In the analysis of ln(rHU), there was no overall effect of time ($F = 0.05, p = 0.824$) and no overall difference between the MCA segments ($F = 1.21, p = 0.274$), but the interaction term was significant ($F = 5.61, p = 0.019$). Difference in slopes of ln(rHU) vs. time (per 60 min) at the two MCA segments is depicted numerically. Similarly, in the analysis of ln(hyperdense area), there was no overall effect of time ($F = 1.27, p = 0.261$) and no overall difference between the two MCA segments ($F = 0.00, p = 0.964$), but the interaction term was significant ($F = 5.68, p = 0.018$). Difference in slopes of ln(hyperdense area) vs. time (per 60 min) at the two MCA segments is depicted numerically.

Since the sample was limited, and particularly for the MCA subset groups with inadequate power for an analysis based on an interaction term (MCA segment × time), we assessed the relationships of interest separately at the proximal MCA and the distal MCA. Moreover, we treated time as a categorical variable (by quartiles, see Table 1 for limit values) since cases for the later time-lag were relatively sparse and variable. The relationship between the rHU and hyperdense area vs. quartiles of time-lag is shown in Figure 3. The key findings were:

- (a) rHU decreased linearly across quartiles of time (linear trend $p = 0.025$) at the proximal MCA and values at Q4 were 9% lower than at Q1 ($p = 0.010$) (Figure 1A); at the distal MCA, an apparent cubic trend ($p = 0.016$) was observed since rHU values declined from Q1 to Q2 and then increased at Q3 and Q4, and hence values at Q4 were actually no different than the values at Q1 (Figure 3A);
- (b) At the proximal MCA, there was no apparent difference regarding the hyperdense area across quartiles of time (Figure 3B), whereas at distal MCA there was a significant cubic trend ($p = 0.017$)—the values slightly increased from Q1 to Q3, and then declined at Q4, so that the values at Q4 were 42% lower than at Q1 ($p = 0.020$) (Figure 3B).

2.3. Multivariate (Independent) Association between Timing of NECT Relative to Symptom Onset and Ratio of Density (rHU) or Hyperdense Area

With adjustment for age, we analyzed the clinical severity of disease at presentation (represented by the NIHSS score) and stroke etiology (TOAST criteria) categorized as “cardioembolic”, “large artery atherosclerosis” (two readily identifiable categories with specific, distinct pathophysiology) and “other” (unknown or undetermined) with different readouts of clot characteristics. The relationship between the timing of NECT relative to the symptom onset and rHU and hyperdense area remained practically unchanged (Table 2). Further findings were:

- (a) At the proximal MCA, the rHU linearly decreased across quartiles of the time-lag (linear trend $p = 0.019$) and values at the fourth quartile were 10% lower than at the first quartile ($p = 0.008$); at the distal MCA, the cubic trend remained significant and there was no difference in rHU at the fourth vs. first quartile of the time-lag; and

- (b) At the proximal MCA there was no apparent change in the hyperdense area across quartiles of the time-lag, whereas at the distal MCA the cubic trend remained significant and values at the fourth quartile were 39% lower than at the first quartile (Table 2).

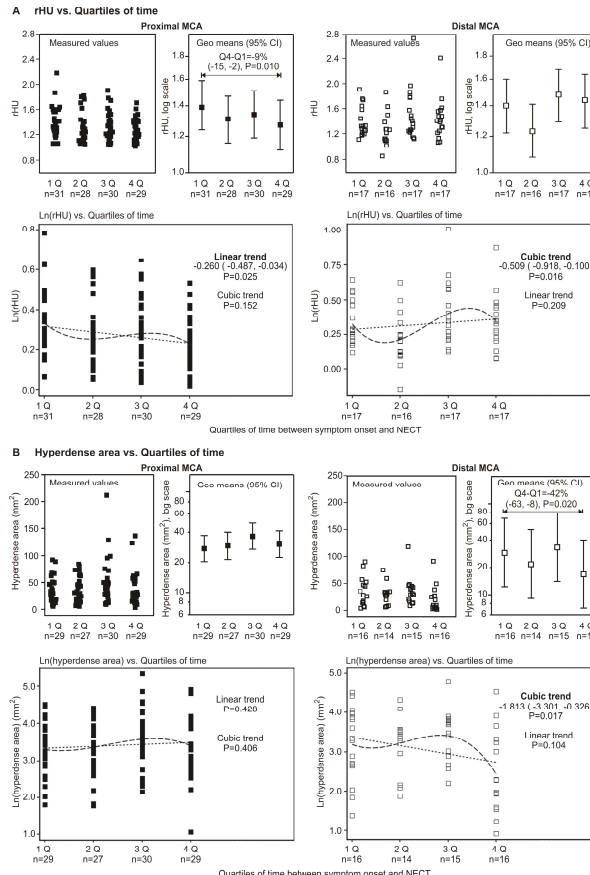


Figure 3. Univariate relationship between timing of NECT relative to symptom onset (as quartiles of time-lag) and ratio of density (rHU) (A) or hyperdense area (B) by segment of medial cerebral artery (MCA). (A) A mixed model (center as a cluster) was fitted to ln-transformed rHU (to achieve normality of residuals) with time-lag as the only independent variable. The relationship was tested for a linear, quadratic and cubic trend. At the proximal MCA, a significant linear decreasing trend was observed (depicted numerically) across quartiles of time-lag and values at the fourth quartile of elapsed time were by 9% lower than at the first quartile. At the distal MCA, values at the second quartile were lower than at the first quartile of the time-lag, and then increased to the third and fourth quartile, yielding a significant cubic trend (depicted numerically); however values at the fourth quartile of the time-lag were closely similar to the values at the first quartile; (B) The same analysis was repeated for the ln-transformed hyperdense area. At the proximal MCA, no apparent trend across quartiles of time was observed and values at the fourth quartile were closely similar to the values at the first quartile. At the distal MCA, values slightly increased towards the third quartile and then decreased to the fourth quartile of the time-lag, yielding a significant cubic trend (depicted numerically), and values at the fourth quartile were 42% lower than at the first quartile. Percentage difference between the fourth and the first quartile of time-lag = $(1 - e^{\text{coeff}}) \times 100$.

Table 2. Independent association between timing of NECT relative to the symptoms onset and ratio of density (rHU) or hyperdense area: summary of adjusted effects.

Associations	At Proximal MCA		At Distal MCA	
	Estimate (95% CI)	p	Estimate (95% CI)	p
<i>Dependent: rHU</i>				
Linear trend across time-lag quartiles	−0.280 (−0.513, −0.046)	0.019	0.230 (−0.224, 0.684)	0.315
Cubic trend across time-lag quartiles	−0.169 (−0.404, 0.066)	0.158	−0.480 (−0.914, −0.046)	0.031
Difference in fourth to first quartile (%)	−10 (−16, −3)	0.008	2 (−11, 17)	0.761
<i>Dependent: hyperdense area</i>				
Linear trend across time-lag quartiles	0.652 (−0.543, 1.848)	0.282	−0.976 (−2.586, 0.671)	0.243
Cubic trend across time-lag quartiles	−0.906 (−2.104, 0.292)	0.137	−2.092 (−3.672, −0.512)	0.011
Difference in fourth to first quartile (%)	11 (−24, 62)	0.581	−39 (−63, −1)	0.046

A separate mixed model (center as a cluster) was fitted to the ln-transformed rHU and hyperdense area (to achieve normality of residuals) with quartiles of time-lag, age, NIHSS score at admission and stroke etiology by TOAST criteria (categorized as “cardioembolic”, “large artery atherosclerosis” or “other”) as independents, and the linear, quadratic and cubic relationships between time and dependent variables were tested. Depicted are adjusted effects. Percentage difference between the fourth and the first quartile of time-lag = $(1 - e^{\text{coeff}}) \times 100$.

2.4. Exploration of the Relationship between Serum Fibrinogen Levels and rHU or Hyperdense Area

On-admission serum fibrinogen levels were available for 170/185 patients (91.9%). Among these patients there were 111/118 (94.1%) with proximal MCA and 59/67 (88.1%) with distal MCA pathology. A separate mixed model (center as a cluster) was fitted to ln(rHU) and ln(hyperdense area) with the MCA segment, serum fibrinogen, stroke type (by TOAST criteria) and MCA segment \times fibrinogen interaction term. Figure 4 depicts adjusted regressions of either dependent variable on the serum fibrinogen and adjusted estimates are shown in Table 3. In detail, we found:

- (a) there was an overall trend of association between higher serum fibrinogen and higher rHU (2.3% higher with 100 mg/dL increase in fibrinogen). However, there was no association between fibrinogen and rHU in patients with an affected proximal MCA, whereas the association was stronger and statistically significant in patients with an affected distal MCA (4.2% higher rHU by 100 mg/dL increase in fibrinogen);
- (b) for the entire cohort, higher fibrinogen was associated with a smaller hyperdense area (15% by 100 mg/dL increase in fibrinogen) ($p = 0.005$). However, this association was much weaker and not statistically significant in patients with an affected proximal MCA, whereas it was stronger and significant in patients with an affected distal MCA (Table 3). Due to incompleteness, data should be viewed with caution, but suggest that at proximal MCA, rHU apparently declines over the first 300 min after the stroke onset, though the hyperdense area does not appear to change. Further, neither of these two radiological outcomes seems to be associated with serum fibrinogen levels. Moreover, at the distal MCA, rHU does not appear to change while the hyperdense area tends to diminish over the first 300 min after the stroke onset. At the same time, a higher rHU and lower hyperdense area appear to be associated with higher serum fibrinogen.

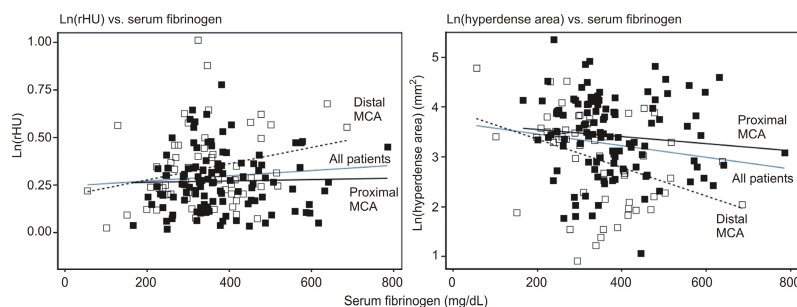


Figure 4. Adjusted regression lines of \ln -transformed rHU (left) and hyperdense area (right) vs. serum fibrinogen, overall and by the segment of medial cerebral artery (MCA). Regressions are from the model depicted in Table 3.

Table 3. Association between serum fibrinogen and ratio of density (rHU) or hyperdense area: summary of adjusted effects expressed as % change in dependent variable by 100 mg/dL increase in serum fibrinogen.

Affected Artery	rHU		Hyperdense Area (mm^2)	
	Estimate (95% CI)	<i>p</i>	Estimate (95% CI)	<i>p</i>
Proximal and distal MCA	2.27% (-0.10, 4.67)	0.059	-15.2% (-24.3, -5.0)	0.005
Proximal MCA	0.41% (-2.23, 3.17)	0.769	-8.2% (-29.3, 4.5)	0.191
Distal MCA	4.16% (0.39, 8.08)	0.031	-21.7% (-34.8, -5.8)	0.009

A separate mixed model (center as a cluster) was fitted to the \ln -transformed rHU and hyperdense area (to achieve normality of residuals) with quartiles of time-lag, stroke etiology by TOAST criteria (categorized as “cardioembolic”, “large artery atherosclerosis” or “other”), serum fibrinogen levels, MCA segment and fibrinogen \times MCA segment interaction as independent variables. Percentage change in rHU or hyperdense area = $(1 - e^{\text{coeff}}) \times 100$.

3. Discussion

The efficacy of recanalization efforts in AIS is variable and biomarkers for stratifying patients with a lower probability of success are eagerly awaited. The anatomical site, composition and spread of clot in various arteries are potential parameters which could assist decision-making processes in order to individually optimize treatment [17,18]. NECT is a fast, widely available and readily used method in acute stroke and it enables non-invasive thrombus characterization. Importantly, thrombus characterization by NECT could provide additional useful information regarding clot susceptibility to thrombolysis and mechanical recanalization. Clot characteristics, however, could undergo dynamic changes over time as a multitude of biochemical pathways are activated when a vessel is occluded and the clot is exposed to hemodynamic and humoral changes of the local milieu [19–21]. These include a combination of proximal and distal apposition of new thrombotic material as well as proteolytic processes, which dissolve less compact thrombus material and leave a place for further fibrin meshwork propagation.

Here, we found indirect evidence of changes in clot composition and morphology within the first 5 h of AIS. Our study disclosed that MCA M1 clots, but not MCA M2 loses its density within the first 5 h. Moreover, we report a decline of the clot plane over time for the M2 segment. The area reduction was also associated with higher fibrinogen blood levels, which corroborates our previous observation [9]. The clots situated in the M1 segment did not change with regard to area and time, and thrombus characteristics did not correlate with fibrinogen levels.

Why is there a difference between the proximal and distal MCA occlusion with regard to time-dependent changes? This observation could, on one hand, be related to differences of embolic material, and indeed, large artery atherosclerosis was a more frequent etiology in M1 segment occlusion

(16.9% vs. 4.5%). The other factor playing a possible role could be the availability of collateral perfusion regarding the occluded segment. This issue was not assessed in our study. Although there are conflicting reports, Kim et al. found higher proportions of RBCs and a lower proportion of fibrin in clots arising from cardioembolic (CE) than in those with large artery arteriosclerosis (LAA) etiology. The predominant histology of distal clots is not reported in published studies. Accordingly, we could speculate that distal thrombi, having originally more fibrin content that is more resistant to endogenous lysis, shield the RBC-rich part from degradation and accordingly these clots do not change in density with time. However, the later the patient arrives, the area of the distal thrombi seems to be somewhat smaller, possibly reflecting the degradation of RBC content later in time since the change is not obvious until the last quartile of time.

A time-dependent drop in clot density (absolute HU) was previously reported by Topcuoglu et al. [22]. In contrast to our findings, one study with 106 patients showed no changes in the relative HU density of the hyperdense artery within the first 4.5 h [23]. The reason for this discrepancy remains unclear. The density of the clot as seen on NECT is augmented by RBC content. Loss of density after embolism in MCA M1 occlusion is probably due to the preferential degradation of the erythrocyte-rich part of the clot [7]. Reports from a murine ischemic model provide evidence that the urokinase plasminogen activator is activated in the first 1 to 2 h following acute MCA occlusion, with gradual weakening of activity thereafter, which could explain our observation [19].

The second largest group concerning stroke pathogenesis consisted of patients with unknown etiology, accounting for 29%. Although we have not specifically reassessed details of the diagnostic stroke workup, the usual standard of care in stroke units includes blood analysis, 24 h electrocardiography (ECG), heart ultrasound and vessel imaging in every patient. Accordingly, it is unlikely that a lack of workup is responsible for this unexpectedly high number of cryptogenic strokes. With the presence of the intracranial clot, many of these patients could be classified as embolic stroke of undetermined source (ESUS) as the underlying etiology [24]. The prevalence of cryptogenic or ESUS strokes in cohorts with evaluation of the HAS is rarely reported. A pilot study identified nine patients with HAS of the MCA, which accounted for 20% of all stroke cases. Cryptogenic and ESUS stroke made up 26% of stroke cases in a larger study [25]. One study revealed that patients without detectable stroke etiology may have better clinical outcomes [26]. Further studies are required to prove whether hints for stroke etiology could be determined by analysis of clot morphology on NECT in cases where the causality remains unclear from ancillary investigations.

Limitations of our study are the usage of different scanning parameters and non-uniform slice thickness. This influences the detection rate of HA which is known to be dependent on slice thickness, and studies confirmed that thinner NECT slices have a greater sensitivity [12]. In addition, the rather low detection rate of HA in nearly 10% of all consecutive strokes could be interpreted as low sensitivity of our study. However, the prevalence of the HA sign among non-selected stroke patients and larger cohorts has not been reported so far. Selected populations, i.e., patients chosen for thrombolysis or with specific stroke syndromes such as posterior cerebral artery stroke, have higher detection rates, but this varies widely (5%–75%) [27]. In our study, some form of angiography (CT, magnetic resonance imaging (MRI) or digital subtraction angiography (DSA)) was performed in 63.8% patients with a correlation of vessel occlusion. For other patients, the clinical stroke syndrome was taken for the verification of vessel obstruction and this always corresponded to the side of the artery occlusion. Of note, we acknowledge the difficulty of discerning the hyperdense artery on plain CT without additional angiography but we presume that the combination of hematocrit correction and correlation with the clinical syndrome suffices for the identification of the occluded artery. Naturally, the presumption that time-dependent changes can be approximated from various patients is subjected to biases. Ideally, each patient should be re-examined with NECT at fixed time points. Such an approach, however, is not feasible due to ethical constraints and patient safety. Nevertheless, in our population, on follow up CT scans in 45 patients, HA was still visible (29%); of them 32 (71%) showed no change or had a drop in rHU values, thus further confirming our findings. Eventually, our observation needs to be confirmed in a

larger cohort. Moreover, the characterization of thrombus dynamics beyond 5 h from symptom onset should follow as well.

4. Materials and Methods

We performed a retrospective study of consecutive patients with AIS who presented to the emergency department in three stroke centers. These were Christian-Doppler-Klinik Salzburg, Austria (CDK), University Clinical Center Maribor, Slovenia (MB) and Bezirkskrankenhaus Lienz, Austria (LZ). The study periods for CDK and MB were 2013–2015, and for LZ 2011–2014.

The inclusion criteria were age ≥ 18 years, presentation within 16 h from stroke onset and available head NECT. We excluded those cases where brain hemorrhage, brain tumor or non-stroke pathology was seen. In addition to usual laboratory examinations we recorded HbA1c and acute fibrinogen values. Stroke subtypes were classified according to the modified Trial of Org 10172 in Acute Treatment (TOAST) criteria [28]. NECT was performed before treatment with rt-PA in all patients.

CT scans were acquired in LZ and CDK with the multidetector CT scanner Sensation 64 (Siemens, Erlangen, Germany) and in MB with the multidetector CT scanner (Aquilion 64, Toshiba Medical Systems, Tochigi, Japan). The CT scans were reconstructed into 4, 2.4 and 3 mm (for CDK, LZ and MB, respectively) thick adjacent slices through the whole brain with the specifications of 120 kV (all centers) and 250, 440 and 150–350 mAs (for CDK, LZ and MB respectively) (mean value, using automatic exposure control) and matrix size of 512×512 . The mean equivalent dose was 1.2 mSv for CDK and LZ and 1.9 mSv for MB.

The evaluation of CT-scans were performed by two experienced stroke physicians who were blinded to the clinical data. When in doubt of presence of hyperdense vessel sign, consensus was reached. HAS was recognized as the area of hyperattenuating artery on NECT. The hyperdense area was manually delineated in IMPAX software (Impax Laboratories Inc., Hayward, CA, USA), the vessel location and the side (when applicable) were recorded. Areas with calcifications ($HU > 90$) were not delineated. Measurements of hyperdense artery were made as previously described [11]. In short, the region of interest (ROI) was manually placed on the margins of the clot. Average HU was then obtained from all voxels within the ROI, summed across all slices (if present on more than one) producing HU sum. The final HU value was calculated by dividing the HU sum with number of slices. We recorded area in mm^2 of manually circumscribed hyperdensity. The area was summed across slices (when present in more than one). Analyses depending on variables including time, disease severity and location of the HAS were performed with respective cohorts.

In order to correct for the impact of hematocrit values we measured the density of the vessel contralateral to affected one, in the case of basilar artery hyperdensity the measurement was in posterior cerebral artery. From measured final HU value, relative HU ratio (rHU) (final HU value divided by average HU of contralateral/appropriate non-affected artery) was derived. After hyperdense artery detection, the medical records were checked to ensure correspondence with clinical symptoms.

Data Analysis

In line with the study objective, data analysis was conceived to explore the relationship, univariate and independent (adjusted), between time (defined as time elapsed between symptom onset and NECT scan, i.e., time-lag) and the two radiological outcomes—rHU and size of the hyperdense area. For all analyses, center was treated as a random effect to account for potential correlation of data coming from one site. In randomized trials, this approach was shown to improve power and maintain nominal coverage rates [29]. Univariate models contained “time” as the only fixed effect. Selection of covariates (additional fixed effects) in multivariate models was based on rationale that adjustments should account for biologically plausible potential confounders and/or moderators. We did not intend to detect “all possible effects” or to define the best set of explanatory variables of variability of rHU or hyperdense area. Finally, in an attempt to explore a potential biological background for the observed time effects on rHU and hyperdense area, we investigated the relationship between these outcomes

and serum fibrinogen levels at admission. All mixed models were fitted using SAS for Windows 9.4 software (SAS Inc., Cary, NC, USA).

5. Conclusions

There are time-dependent changes in MCA thrombus morphology and composition within the first 5 h from symptom onset in patients with AIS. Moreover, we found that proximal and distal MCA clots differ with regard to these dynamics. Further studies, ideally with the evaluation of mechanically retrieved intracranial clots, are required to understand the complex pathophysiological processes determining the intrinsic and extrinsic post-processing of an intracranial thrombus.

Acknowledgments: The preparation of the manuscript was supported by Teva-Ratiopharm, open access publishing was covered by the University of Salzburg.

Author Contributions: Slaven Pikija, Larissa Hauer and Johann Sellner conceived and designed the experiments; Slaven Pikija, Jozef Magdic and Peter Unterkreuter performed the experiments; Slaven Pikija, Vladimir Trkulja, Johannes Sebastian Mutzenbach, Helmut F. Novak, Friedrich Weymayr, Larissa Hauer and Johann Sellner analyzed the data; Slaven Pikija, Larissa Hauer and Johann Sellner wrote the paper; all authors contributed to the revision.

Conflicts of Interest: The authors declare no conflict of interest.

Abbreviations

AIS	Acute ischemic stroke
LAA	Large artery atherosclerosis
HAS	Hyperdense artery sign
NECT	Non-enhanced CT
TOAST	Trial of Org 10172 in Acute Treatment criteria
HU	Hounsfield units
rHU	Average HU of hyperdense artery/average HU of non-affected artery
DSA	Digital subtraction angiography
MRI	Magnetic resonance imaging
CT	Computertomography
ESUS	Embolic stroke of unknown source
CE	Cardioembolic

References

1. Williams, G.R.; Jiang, J.G.; Matchar, D.B.; Samsa, G.P. Incidence and occurrence of total (first-ever and recurrent) stroke. *Stroke* **1999**, *30*, 2523–2528. [CrossRef] [PubMed]
2. Pikija, S.; Trkulja, V.; Malojcic, B.; Mutzenbach, J.S.; Sellner, J. A High Burden of Ischemic Stroke in Regions of Eastern/Central Europe is Largely Due to Modifiable Risk Factors. *Curr. Neurovasc. Res.* **2015**, *12*, 341–352. [CrossRef] [PubMed]
3. Goldmakher, G.V.; Camargo, E.C.; Furie, K.L.; Singhal, A.B.; Roccagliata, L.; Halpern, E.F.; Chou, M.J.; Biagini, T.; Smith, W.S.; Harris, G.J.; et al. Hyperdense basilar artery sign on unenhanced CT predicts thrombus and outcome in acute posterior circulation stroke. *Stroke* **2009**, *40*, 134–139. [CrossRef] [PubMed]
4. Marder, V.J.; Chute, D.J.; Starkman, S.; Abolian, A.M.; Kidwell, C.; Liebeskind, D.; Ovbiagele, B.; Vinuela, F.; Duckwiler, G.; Jahan, R.; et al. Analysis of thrombi retrieved from cerebral arteries of patients with acute ischemic stroke. *Stroke* **2006**, *37*, 2086–2093. [CrossRef] [PubMed]
5. Mattle, H.P.; Arnold, M.; Georgiadis, D.; Baumann, C.; Nedeltchev, K.; Benninger, D.; Remonda, L.; von Budingen, C.; Diana, A.; Pangalu, A.; et al. Comparison of intraarterial and intravenous thrombolysis for ischemic stroke with hyperdense middle cerebral artery sign. *Stroke* **2008**, *39*, 379–383. [CrossRef] [PubMed]
6. Niesten, J.M.; van der Schaaf, I.C.; Biessels, G.J.; van Otterloo, A.E.; van Seeters, T.; Horsch, A.D.; Luitse, M.J.; van der Graaf, Y.; Kappelle, L.J.; Mali, W.P.; et al. Relationship between thrombus attenuation and different stroke subtypes. *Neuroradiology* **2013**, *55*, 1071–1079. [CrossRef] [PubMed]

7. Jang, I.K.; Gold, H.K.; Ziskind, A.A.; Fallon, J.T.; Holt, R.E.; Leinbach, R.C.; May, J.W.; Collen, D. Differential sensitivity of erythrocyte-rich and platelet-rich arterial thrombi to lysis with recombinant tissue-type plasminogen activator. A possible explanation for resistance to coronary thrombolysis. *Circulation* **1989**, *79*, 920–928. [CrossRef] [PubMed]
8. Liebeskind, D.S.; Sanossian, N.; Yong, W.H.; Starkman, S.; Tsang, M.P.; Moya, A.L.; Zheng, D.D.; Abolian, A.M.; Kim, D.; Ali, L.K.; et al. CT and MRI early vessel signs reflect clot composition in acute stroke. *Stroke* **2011**, *42*, 1237–1243. [CrossRef] [PubMed]
9. Pikić, S.; Trkulja, V.; Mutzenbach, J.S.; McCoy, M.R.; Ganger, P.; Sellner, J. Fibrinogen consumption is related to intracranial clot burden in acute ischemic stroke: A retrospective hyperdense artery study. *J. Transl. Med.* **2016**, *14*, 250. [CrossRef] [PubMed]
10. Mair, G.; Boyd, E.V.; Chappell, F.M.; von Kummer, R.; Lindley, R.I.; Sandercock, P.; Wardlaw, J.M.; Group, I.S.T.C. Sensitivity and specificity of the hyperdense artery sign for arterial obstruction in acute ischemic stroke. *Stroke* **2015**, *46*, 102–107. [CrossRef] [PubMed]
11. Puig, J.; Pedraza, S.; Demchuk, A.; Daunis, I.E.J.; Termes, H.; Blasco, G.; Soria, G.; Boada, I.; Remollo, S.; Banos, J.; et al. Quantification of thrombus hounsfield units on noncontrast CT predicts stroke subtype and early recanalization after intravenous recombinant tissue plasminogen activator. *Am. J. Neuroradiol.* **2012**, *33*, 90–96. [CrossRef] [PubMed]
12. Riedel, C.H.; Jensen, U.; Rohr, A.; Tietke, M.; Alfke, K.; Ulmer, S.; Jansen, O. Assessment of thrombus in acute middle cerebral artery occlusion using thin-slice nonenhanced Computed Tomography reconstructions. *Stroke* **2010**, *41*, 1659–1664. [CrossRef] [PubMed]
13. Moftakhar, P.; English, J.D.; Cooke, D.L.; Kim, W.T.; Stout, C.; Smith, W.S.; Dowd, C.F.; Higashida, R.T.; Halbach, V.V.; Hetts, S.W. Density of thrombus on admission CT predicts revascularization efficacy in large vessel occlusion acute ischemic stroke. *Stroke* **2013**, *44*, 243–245. [CrossRef] [PubMed]
14. Niesten, J.M.; van der Schaaf, I.C.; van der Graaf, Y.; Kappelle, L.J.; Biesseels, G.J.; Horsch, A.D.; Dankbaar, J.W.; Luitse, M.J.; van Seeters, T.; Smit, E.J.; et al. Predictive value of thrombus attenuation on thin-slice non-contrast CT for persistent occlusion after intravenous thrombolysis. *Cerebrovasc. Dis.* **2014**, *37*, 116–122. [CrossRef] [PubMed]
15. Mokin, M.; Morr, S.; Natarajan, S.K.; Lin, N.; Snyder, K.V.; Hopkins, L.N.; Siddiqui, A.H.; Levy, E.I. Thrombus density predicts successful recanalization with Solitaire stent retriever thrombectomy in acute ischemic stroke. *J. Neurointerv. Surg.* **2015**, *7*, 104–107. [CrossRef] [PubMed]
16. Bouchez, L.; Lovblad, K.O.; Kulcsar, Z. Pretherapeutic characterization of the clot in acute stroke. *J. Neuroradiol.* **2016**, *43*, 163–166. [CrossRef] [PubMed]
17. Riedel, C.H.; Zimmermann, P.; Jensen-Kondering, U.; Stingle, R.; Deuschl, G.; Jansen, O. The importance of size: Successful recanalization by intravenous thrombolysis in acute anterior stroke depends on thrombus length. *Stroke* **2011**, *42*, 1775–1777. [CrossRef] [PubMed]
18. Molina, C.A. Imaging the clot: Does clot appearance predict the efficacy of thrombolysis? *Stroke* **2005**, *36*, 2333–2334. [CrossRef] [PubMed]
19. Hosomi, N.; Lucero, J.; Heo, J.H.; Koziol, J.A.; Copeland, B.R.; del Zoppo, G.J. Rapid differential endogenous plasminogen activator expression after acute middle cerebral artery occlusion. *Stroke* **2001**, *32*, 1341–1348. [CrossRef] [PubMed]
20. Alvarez-Perez, F.J.; Castelo-Branco, M.; Alvarez-Sabin, J. Usefulness of measurement of fibrinogen, D-dimer, D-dimer/fibrinogen ratio, C reactive protein and erythrocyte sedimentation rate to assess the pathophysiology and mechanism of ischaemic stroke. *J. Neurol. Neurosurg. Psychiatry* **2011**, *82*, 986–992. [CrossRef] [PubMed]
21. De Meyer, S.F.; Denorme, F.; Langhauser, F.; Geuss, E.; Fluri, F.; Kleinschnitz, C. Thromboinflammation in Stroke Brain Damage. *Stroke* **2016**, *47*, 1165–1172. [CrossRef] [PubMed]
22. Topcuoglu, M.A.; Arsava, E.M.; Akpinar, E. Clot Characteristics on Computed Tomography and Response to Thrombolysis in Acute Middle Cerebral Artery Stroke. *J. Stroke Cerebrovasc. Dis.* **2015**, *24*, 1363–1372. [CrossRef] [PubMed]
23. Haridy, J.; Churilov, L.; Mitchell, P.; Dowling, R.; Yan, B. Is there association between hyperdense middle cerebral artery sign on CT scan and time from stroke onset within the first 24-hours? *BMC Neurol.* **2015**, *15*, 101. [CrossRef] [PubMed]

24. Hart, R.G.; Diener, H.C.; Connolly, S.J. Embolic strokes of undetermined source: Support for a new clinical construct—Authors' reply. *Lancet Neurol.* **2014**, *13*, 967. [CrossRef]
25. Fonseca, A.C.; Ferro, J.M. Cryptogenic stroke. *Eur. J. Neurol.* **2015**, *22*, 618–623. [CrossRef] [PubMed]
26. Scullen, T.A.; Monlezun, D.J.; Siegler, J.E.; George, A.J.; Schwickerath, M.; El Khoury, R.; Cho, M.C.; Martin-Schild, S. Cryptogenic stroke: Clinical consideration of a heterogeneous ischemic subtype. *J. Stroke Cerebrovasc. Dis.* **2015**, *24*, 993–999. [CrossRef] [PubMed]
27. Krings, T.; Noelchen, D.; Mull, M.; Willmes, K.; Meister, I.G.; Reinacher, P.; Toepper, R.; Thron, A.K. The hyperdense posterior cerebral artery sign: A computed tomography marker of acute ischemia in the posterior cerebral artery territory. *Stroke* **2006**, *37*, 399–403. [CrossRef] [PubMed]
28. Kolominsky-Rabas, P.L.; Weber, M.; Gefeller, O.; Neundoerfer, B.; Heuschmann, P.U. Epidemiology of ischemic stroke subtypes according to TOAST criteria: Incidence, recurrence, and long-term survival in ischemic stroke subtypes: A population-based study. *Stroke* **2001**, *32*, 2735–2740. [CrossRef] [PubMed]
29. Kahan, B.C.; Morris, T.P. Adjusting for multiple prognostic factors in the analysis of randomised trials. *BMC Med. Res. Methodol.* **2013**, *13*, 99. [CrossRef] [PubMed]



© 2016 by the authors. Licensee MDPI, Basel, Switzerland. This article is an open access article distributed under the terms and conditions of the Creative Commons Attribution (CC BY) license (<http://creativecommons.org/licenses/by/4.0/>).



Article

Validating Intravascular Imaging with Serial Optical Coherence Tomography and Confocal Fluorescence Microscopy

Pier-Luc Tardif ^{1,2,*}, Marie-Jeanne Bertrand ^{2,3}, Maxime Abran ^{1,2}, Alexandre Castonguay ¹, Joël Lefebvre ¹, Barbara E. Stähli ², Nolwenn Merlet ², Teodora Mihalache-Avram ², Pascale Geoffroy ², Mélanie Mecteau ², David Busseuil ², Feng Ni ⁴, Abedelnasser Abulrob ⁴, Éric Rhéaume ^{2,3}, Philippe L'Allier ^{2,3}, Jean-Claude Tardif ^{2,3} and Frédéric Lesage ^{1,2,*}

¹ Département de Génie Électrique et Institut de Génie Biomédical, École Polytechnique de Montréal, Montreal, QC H3T 1J4, Canada; maxime.abran@gmail.com (M.A.); alexandre.castonguay87@gmail.com (A.C.); joel.lefebvre@gmail.com (J.L.)

² Montreal Heart Institute, Montreal, QC H1T 1C8, Canada; mariejeanne.bertrand@gmail.com (M.-J.B.); barbarastaeeli@hotmail.com (B.E.S.); nolwenn.merlet@gmail.com (N.M.); Teodora.Mihalache-Avram@icm-mhi.org (T.M.-A.); Pascale.Geoffroy@icm-mhi.org (P.G.); melanie.mecteau@icm-mhi.org (M.M.); david.busseuil@icm-biobanque.org (D.B.); Eric.Rheaume@icm-mhi.org (É.R.); philippe.l_lallier@icloud.com (P.L.); jean-claude.tardif@icm-mhi.org (J.-C.T.)

³ Département de Médecine, Université de Montréal, Montreal, QC H3C 3J7, Canada

⁴ National Research Council Canada (NRCC), Montreal, QC H3A 1A3, Canada; Feng.Ni@cnrc-nrc.gc.ca (F.N.); abedelnasser.abulrob@nrc-cnrc.gc.ca (A.A.)

* Correspondence: pierluctardif@gmail.com (P.-L.T.); frederic.lesage@polymtl.ca (F.L.);
Tel.: +1-514-340-4711 (ext. 7542) (F.L.)

Academic Editors: Michael Henein and Joseph V. Moxon

Received: 31 August 2016; Accepted: 9 December 2016; Published: 15 December 2016

Abstract: Atherosclerotic cardiovascular diseases are characterized by the formation of a plaque in the arterial wall. Intravascular ultrasound (IVUS) provides high-resolution images allowing delineation of atherosclerotic plaques. When combined with near infrared fluorescence (NIRF), the plaque can also be studied at a molecular level with a large variety of biomarkers. In this work, we present a system enabling automated volumetric histology imaging of excised aortas that can spatially correlate results with combined IVUS/NIRF imaging of lipid-rich atheroma in cholesterol-fed rabbits. Pullbacks in the rabbit aortas were performed with a dual modality IVUS/NIRF catheter developed by our group. Ex vivo three-dimensional (3D) histology was performed combining optical coherence tomography (OCT) and confocal fluorescence microscopy, providing high-resolution anatomical and molecular information, respectively, to validate in vivo findings. The microscope was combined with a serial slicer allowing for the imaging of the whole vessel automatically. Colocalization of in vivo and ex vivo results is demonstrated. Slices can then be recovered to be tested in conventional histology.

Keywords: intravascular ultrasound (IVUS); near-infrared fluorescence (NIRF); atherosclerosis; ex vivo three-dimensional (3D) histology; optical coherence tomography (OCT); confocal fluorescence microscopy

1. Introduction

Atherosclerosis is a chronic immune-mediated inflammatory disease that arises from a series of complex events triggered by endothelial dysfunction, lipid accumulation in the arterial wall, and infiltration of monocyte-derived macrophages [1,2]. Acute coronary syndromes (ACS) occur mostly

from the rupture of modestly stenotic lipid-rich “vulnerable” plaques, which leads to endoluminal thrombus formation, myocardial ischemia, and sudden cardiac death [3,4]. Although coronary angiography remains the gold standard for epicardial coronary stenoses assessment and treatment, it frequently underestimates true plaque burden and provides no information regarding plaque composition [5]. Intravascular ultrasound (IVUS) imaging has been established as an adjunct imaging technology to coronary angiography, widely used in both clinical and research applications [6]. By generating *in vivo* cross-sectional images of the vessel wall and lumen, IVUS enables the characterization of atherosclerotic vessel segments by providing accurate lumen and vessel dimensions, as well as non-protruding plaques, positive vascular remodeling, and plaque burden assessment [7,8]. Conventional grayscale IVUS is, however, limited with regards to the analysis of plaque composition [9], whereas emerging molecular imaging technologies, such as fluorescence imaging, have been developed to overcome these limitations. Multimodality imaging systems, such as the dual-modality IVUS/near-infrared fluorescence (NIRF) imaging catheter previously engineered by our group and others [10–13], were designed for integrated microstructural and molecular plaque imaging, thus enabling a more detailed plaque characterization. The use of molecular probes in conjunction with fluorescence imaging has been shown to provide complementary information with regards to plaque activity and inflammation [14–19]. Translation of molecular imaging results to clinical applications, however, requires validation; and despite impressive advances in intravascular imaging over the past decade, histology remains the gold standard for determining plaque composition and geometry. Although providing high-resolution cross-sectional images of the arterial wall, histology remains limited to the number of tissue sections analyzed and by the lack of anatomical context; thus resulting in missed valuable data. When comparing *in vivo* intravascular imaging applications with histology, colocalization is often challenged by geometric distortions and tissue shrinkage, as well as the lack of anatomical landmarks and the limited resolution of IVUS imaging.

OCT-based block-face three-dimensional (3D) histology combined with serial cutting of tissues has been proven in the past to be an efficient technique to reconstruct and visualize whole intact organs or tissues [20,21]. Previous work has demonstrated the use of serial OCT imaging primarily for brain imaging. However, this method has so far never been used for cardiovascular imaging. From the spatial resolution of optical coherence tomography (OCT), largely superior to IVUS [6], and the capacity of confocal fluorescence microscopy to efficiently identify the same molecular biomarkers as NIRF imaging [22], we developed a novel *ex vivo* automated 3D histology platform comprising a dual-modality imaging system based on OCT-coupled fluorescence sensitive confocal microscopy [21]. In this work we detail the process of image reconstruction using this system and, for the first time, describe its use for the purpose of atherosclerosis detection and localization in iliac arteries and aortas of an atherosclerotic rabbit model. Fluorescent signal colocalization obtained from *in vivo* and *ex vivo* imaging was performed to validate the potential of these methods to be co-registered and for OCT-combined fluorescence sensitive confocal microscopy to serve as a future histology add-on validation tool in the development of novel molecular probes.

2. Results

2.1. *In Vitro* Affinity of Anti-ICAM-1 Antibody

A fluorescently labelled anti-intercellular adhesion molecule-1 (ICAM-1) antibody was used as a marker of inflammation below. Four ICAM-1 probes were initially tested *in vitro*, but only one showed positive affinity with inflammation (Figure 1). Fluorescence confocal microscopy images were taken to evaluate the affinity of the anti-ICAM-1 antibody with mammalian cells. Human Umbilical Vein Cells (HUVEC) were imaged before and after being activated by Tumor Necrosis Factor Alpha (TNF-alpha), which induces inflammation. Placing the fluorophore bound to the ICAM-1 antibody in the cell growth medium followed by flushing, it was observed that the signal was far more present for the TNF-alpha activated cells, suggesting that the ICAM-1 antibody does in fact have affinity with

inflammation (Figure 1). Deconvolution was also performed to form a transverse image of the cell to show that the signal was localized on the cellular membrane and not in the growth medium or the cytoplasm (Figure 1C).

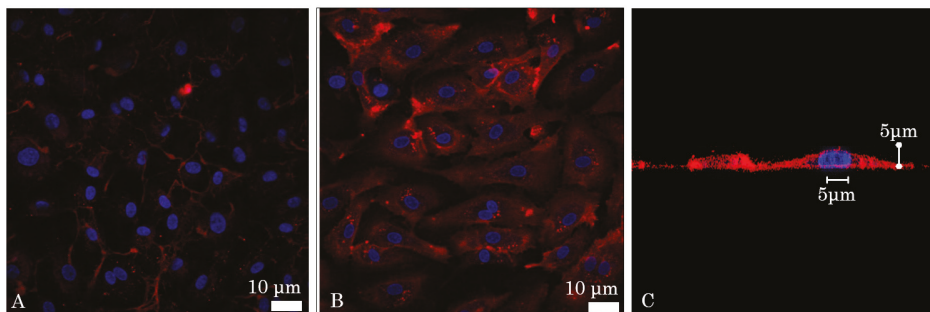


Figure 1. Fluorescent confocal images of in vitro affinity of the intercellular adhesion molecule-1 (ICAM-1) antibody: (A) Inactivated and (B) Tumor Necrosis Factor Alpha (TNF- α) activated Human Umbilical Vein Cells (HUVEC). The nuclei (blue) were stained with DAPI (4',6-Diamidino-2-Phenylindole, Dilactate) (C) deconvolved image of a cell. The fluorescence signal (red) is not present in the cytoplasm or the nucleus, but is, rather, located on the cell membrane.

2.2. *In Vivo Catheter Imaging*

Five atherosclerotic rabbits were imaged following either an *in vivo* targeted molecular probes injection (model 1) or an intravenous indocyanine green (ICG) (model 2) injection with a dual IVUS/NIRF imaging catheter designed by our group (Figure 2). The IVUS had a frequency of 45 MHz and the excitation wavelength of the NIRF was 780 nm. As shown in Figure 2B,C, a strong *in vivo* signal was obtained following injection of an ICAM-1 nanobody probe at 30.05 mm of pullback in model 1, with partial correlation with the echolucent region on IVUS imaging. Other ICAM-1 nanobodies that did not show affinity *in vitro* were also injected with the purpose of evaluating their targeting ability. For these, weak signals were detected by *in vivo* NIRF/IVUS imaging, despite the presence of plaque on IVUS. In model 2, a strong but localized signal was seen at 8.4 mm of catheter pullback correlated with IVUS imaging, with the plaque pointed by the red arrow (Figure 2E). The pulse generated by the ultrasound (US), created an artifact and a mask was applied to hide the catheter on the images up to the artifact radial position, which extended 50 μ m past the wall of the catheter. Thus, part of the mask intersected the vessel wall (Figure 2E) in smaller vessels, but not in bigger ones (Figure 2C). A ring artifact that can be seen of Figure 2C was caused by a reflection on the sheath surrounding the catheter.

2.3. *Serial Imaging System, Ex Vivo OCT Reconstructions and Fluorescence Alignment*

A serial microscopy imaging system was designed combining OCT and confocal fluorescence imaging (Figure 3A). Micrometer-precise motors and a razor blade attached to a custom vibratome allowed automatic serial mosaic imaging of agarose-embedded artery sections to be performed. OCT and fluorescence data were measured simultaneously which enabled co-registration of OCT imaging with fluorescence. OCT provided 3D volumes for each slice (200 μ m thickness) while a single confocal image was taken (2D) with focus centered in the slice. For confocal fluorescence, a trade-off was required in the system to enable the combination of OCT (which requires a long focal depth for accurate 3D images) and confocal microscopy requiring filling the objective for optimal resolution. In this design, the confocal beam under-filled the objective, leading to a fluorescent point-spread-function that extended in depth.

The model 1 rabbits were imaged with a 3 \times objective whereas the model 2 rabbit was imaged with a 10 \times water immersion objective. The former being designed to work in air, a chamber was

built between the end of the objective and water by gluing a glass window to the aluminum lens tube. Typical results are presented in Figure 3B–D for raw, processed, and 3D reconstruction data, respectively. Fluorescence signal was higher at the surface or near the arterial wall, which suggests that the ICAM-1 nanobodies bind to lipid plaques and that these molecular probes are sources of specific signals. The processed slices can then be recovered after slicing and imaged in standard histology (Figure 3E,F), here, with Masson Trichrome (Figure 2E) and Von Kossa (Figure 3F) to detect calcification.

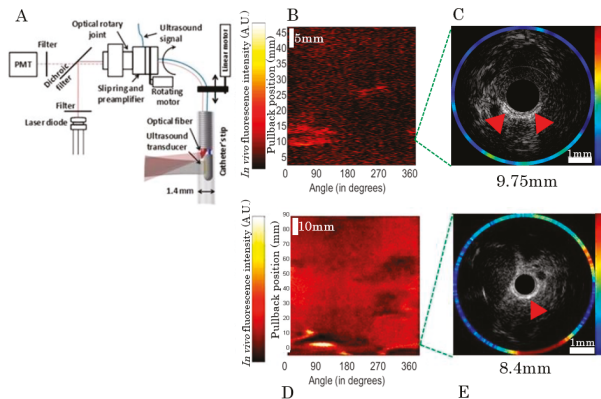


Figure 2. In vivo imaging system and typical images. (A) Overview of the bimodal catheter system with a detailed view of the catheter's tip. PMT stands for photomultiplier tube; (B) Paired in vivo near-infrared fluorescence signal detected over 360 degrees with 50 mm pullback length; and (C) integrated NIRF-IVUS cross-sectional imaging with partial fluorescence signal and echolucent plaque colocalization (shown by red arrows) in model 1. Atherosclerotic plaque, shown by echolucent signal on IVUS (D,E), was partly correlated with indocyanine green (ICG)-fluorescence signal at 8.4 mm of pullback (red arrow) in model 2.

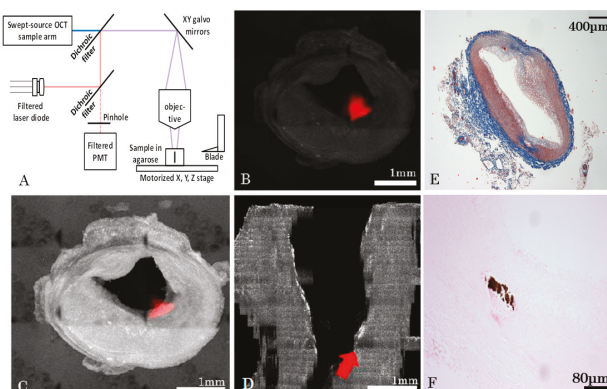


Figure 3. Ex vivo optical coherence tomography (OCT) and confocal reconstruction for a model 1-type rabbit. (A) Overview of the serial histology imaging system; (B) Example of an averaged slice (raw data) with the fluorescence image superimposed on it (i.e., red signal); (C) Example of the same slice after Beer-Lambert corrections, contrast adjustment, and deconvolution (Log-scale), with superimposed fluorescence image (red); (D) Localization of the tissue slice (c) on a 3D reconstruction (shown by red arrow); (E) Histology slice colored with Masson Trichrome and a 4× objective (F) Same slice imaged with VonKossa and a 20× objective.

Data Reconstruction

Due to tissue attenuation of the OCT signal and serial mosaic acquisitions, specific algorithms were developed to reconstruct full 3D volumes. A custom Python stitching and signal correction algorithm was developed, allowing complete artery reconstructions and atherosclerosis localization based on both modalities. The following steps were implemented:

- For each tissue slice, the volume position in the mosaic reference frame was estimated using microscope acquisition data;
- Volumes were then stitched for each tissue slice;
- Post processing was performed that included cropping of the field of view, identification of lumen mask and Beer-Lambert intensity correction;
- After post processing steps, slices were assembled together in order to form a longitudinal 3D volume.

Figure 4A,B show typical images after the post processing steps (masks, Beer-Lambert correction, intensity artifacts correction, and cropping) applied to an averaged OCT slice and fluorescence image, respectively. Figure 4C shows the attenuation map used for Beer-Lambert correction for a particular slice.

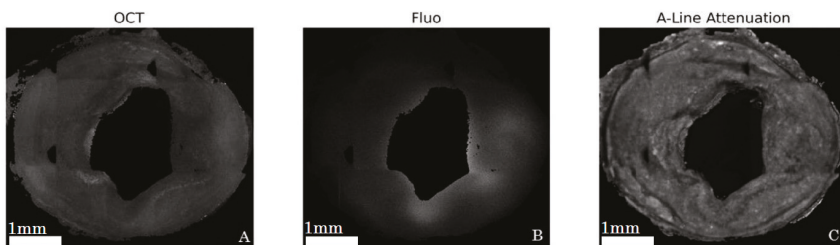


Figure 4. Corrected images for model 1 rabbit for OCT (A); and fluorescence (B); A-line attenuation map used for OCT intensity correction outlines detailed tissue structures (C).

As previously mentioned, with an under-filled objective used in fluorescence imaging, deeper tissue slices could contaminate the signal of the imaged slice in fluorescence due to the extended point-spread function (PSF), thus, requiring a deconvolution algorithm to generate precise fluorescence images. A synthetic PSF was generated using the PSF generator plugin in the ImageJ software (National Institutes of Health, New York, NY, USA) using the Born and Wolf 3D optical model. It had a FWHM of $4.4\text{ }\mu\text{m}$ in the $x\text{-}y$ direction and of $146\text{ }\mu\text{m}$ in the z direction and was used to correct fluorescence images.

When comparing to brain imaging obtained from a similar technology, the automatic ex vivo imaging technique required careful preparation of arterial tissues, as conjunctive tissues could cause cutting artifacts (Figure 5A), thus making it challenging to obtain uniform cuts. An algorithm was applied during image acquisitions to ensure fine control of the focal depth and to avoid placing tissues in areas where OCT had instrumental artifacts (spurious reflections) or outside the focal zone of the objective (Figure 5B,C).

2.4. Alignment and Tissue Deformation

Due to ex vivo tissue fixation and a lack of intra-arterial pressure, which led to tissue dehydration and shrinkage, the comparison of in vivo and corresponding ex vivo vessel segments was challenging. Despite the average tissue shrinkage ratio of 61% that was calculated in our experiments, imaging colocalization was possible using landmarks. Longitudinal views of both IVUS and OCT anatomical imaging of an arterial segment are presented in Figure 6. The abdominal aorta and iliac arteries were visualized with both modalities, which served as reference points for colocalization. While longitudinal

co-registration was possible, precise pixel-wise deformation models could not be applied since the arterial wall was highly distorted in ex vivo OCT images given the lack of blood flow in fixed tissues. Nevertheless, longitudinal segments could be identified accurately, which enabled comparisons of pullback in vivo results to ex vivo data.

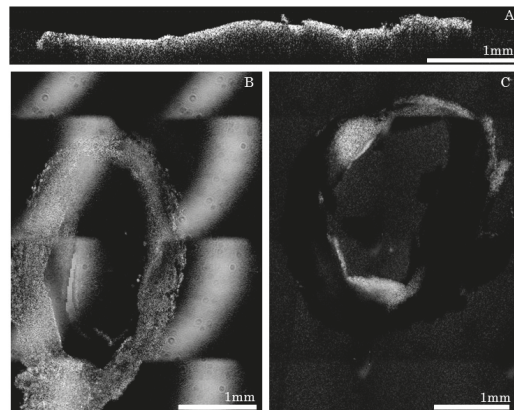


Figure 5. Sources of imaging artifacts and their effects during acquisitions: (A) Unevenly cut slice; (B) Artifact caused by the glass when the reference arm was not properly placed; (C) Slice that was imaged while not placed at the focal point of the lens.

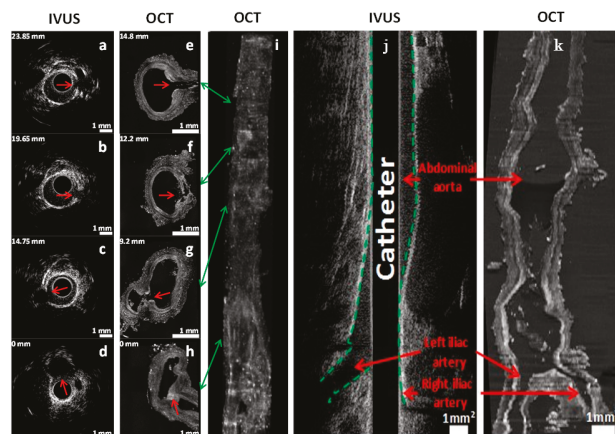


Figure 6. Intravascular ultrasound (IVUS) and OCT colocalization of anatomical landmarks in model 2. (a–d) In vivo IVUS cross-sectional images; (e–h) Ex vivo OCT cross-sectional images; (i) 3D reconstruction in OCT using a maximum intensity projection algorithm. Indicated numbers in mm (upper left of each image) represent the distances between the cross-section and the iliac bifurcation. The catheter was introduced in the right iliac artery, located at the bottom-right in the OCT image in (h,i). Green arrows indicate the location of the cross-section slices on 3D reconstruction. Red arrows denote side branches (anatomical landmarks) used for colocalization. Longitudinal view of the abdominal aorta and iliac arteries in IVUS and OCT imaging in model 2; (j) In vivo IVUS image of a 50 mm artery segment (green dashed lines delineates the arterial wall); (k) Ex vivo OCT image of the same segment, which shrunk to a length of 30 mm after ex vivo tissue fixation. Scale bars represent a region of 1 mm by 1 mm².

2.5. Validation of Intravascular Molecular Imaging

Using the methodological steps outlined above, in vivo ICG accumulation identified with NIRF imaging was confirmed using high-resolution fluorescence confocal imaging, as shown in Figure 7. Intimal thickening was also observed on ex vivo OCT, an indication of the presence of plaque. Figure 7b shows that the intimal thickness varied from 100 μm to 200 μm (red arrows), a difference not perceptible in IVUS, which has a resolution of about 100 μm .

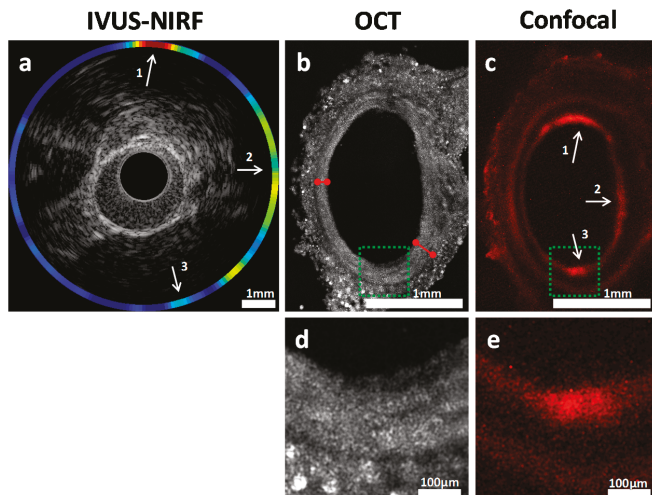


Figure 7. Cross-sectional view of the abdominal aorta in model 2. (a) IVUS-NIRF imaging in vivo; (b) OCT imaging ex vivo; (c) Confocal fluorescence microscopy imaging ex vivo; (d,e) Enlarged sections of the green region of (b,c). Red arrows identify the intimal thickness at two locations in the OCT image. White arrows indicate colocalization between in vivo and ex vivo fluorescence. Arrow 3 shows a weaker colocalization due to the limitation of our blood attenuation compensation algorithm [19], further supporting the need for co-registered ex vivo validation.

3. Discussion

Combining IVUS and fluorescence imaging (NIRF) within a single catheter may yield a reliable method that could be used to detect and locate atherosclerotic plaques in the arterial wall. This imaging method overcomes the shortcomings of coronary angiography, whereas fluorescence provides information regarding plaque composition and biology. Translation of such imaging technology to clinical applications requires robust preclinical validation, and co-registration of in vivo data to ex vivo assessments is essential for better plaque assessment. In the present work, we demonstrated that multimodal custom serial imaging of tissue sections can be used to corroborate in vivo findings using OCT and confocal imaging to provide high spatial resolution. Our system is also compatible with conventional histology, as the slices from the vibratome can be recovered in the correct order using a small container placed in front of the agarose block and stained using standard procedures.

The main shortcoming of conventional histology is that although it offers information on molecular tissue composition, it does not provide accurate anatomical localization of said tissues. There is, at the moment, no existing method that can reliably corroborate the in vivo plaque localization and composition measurements done with an intravascular catheter during pullbacks. The method described here can, however, combine the molecular composition determination aspect of conventional histology, while the 3D reconstructions allow colocalization to be performed. Furthermore, in conventional histology, images are formed after the tissue is sliced, which leads to additional

deformations and difficulties in reconstructing the 3D view. With the block-face OCT technique, images are taken before slicing, facilitating 3D assembly. Our method, while not a substitute for standard histology, is projected to be a complementary method that can help to bridge in vivo and histological data. The ability to co-localize tissues between the in vivo and ex vivo tissues offers a novel approach that could be used to validate future intravascular molecular imaging studies. Having a reliable way to confirm the data gathered in in vivo scans will smooth the transition between the fundamental research and clinical domains, leading to more effective, invasive imagery techniques and eventually better treatments for patients.

3.1. Slicing Optimization

One of the most challenging aspect of the ex vivo imaging process was to obtain uniform flat slices with the vibratome, as the connective tissue surrounding the artery rendered slicing more difficult. Residual connective tissue remaining above the sample after slicing appeared to block the light and/or cause inaccurate surface detection, thus, leading to some slices being imaged while being out of focus. Furthermore, slice stitching in the z-direction was very sensitive to the flatness of the slices. Keeping the slicer blade completely flat and straight at all times was difficult and resulted in different slice thicknesses. Crooked or uneven slices were problematic during reconstructions, since stitching was based on surface detection. To overcome these difficulties, a fixed overlap between slices was imposed. However, this could create gaps, which sometimes led to the presence of dark bands between slices in the longitudinal reconstruction of the aorta. It should be noted that those overlaps may also induce a small bias when approximating tissue shrinkage as the z-stitching was highly dependent on these. Finally, evaluating the shrinking factor was also made more difficult by the fact that our method relied on finding landmarks, which were sometimes sparse. Optimizing tissue embedding and a careful removal of connective tissue is, thus, key to gathering quality data.

3.2. Optical Optimization

In the case of the $3\times$ objective, the glass used to protect it from water where the sample was imaged was a source of artifacts, since a reflection and its harmonics could be seen with the OCT scanner. While adjusting the reference arm's length could minimize the effect of the glass by imaging in the opportune zones, it was never possible to fully remove its effects since the automatic imaging process, which takes a few days to perform, always yielded a few images that were not situated in the ideal zone. Since the glass has very high reflectivity, the artifact often saturated the detector and information was lost when it could be observed within the imaged tissue. It was, thus, very important for the experimenter to place the glass at a position that did not create an artifact near the focal point of the objective.

3.3. Big-Data Processing

The size of the datasets acquired was a factor that rendered data analysis quite cumbersome. A raw dataset of 500 GB for a single artery section required significant computing power to process and disk space for storage. Even lowering the resolution by going from a $10\times$ to a $3\times$ objective, the image sizes only decreased by half. Improvement in processing in terms of efficiency and storage will be required to enable large-scale studies.

4. Materials and Methods

4.1. Animal Model for Atherosclerosis

Six adult, male, New Zealand White rabbits (3–4 kg, 3 months old; Charles River Laboratories, Saint-Constant, QC, Canada) were fed a 0.5% cholesterol diet (Harlan Techlab Diets, Madison, WI, USA) to induce atherosclerosis. Two rabbit models were used: model 1 ($n = 5$), balloon injury performed at week 0, followed by 14-weeks cholesterol-enriched diet; model 2 ($n = 1$), 14-weeks of high-cholesterol

diet. One rabbit did not complete the study due to neurologic complications after completion of balloon denudation. The experimental protocols were approved by the animal ethics committee of the Montreal Heart Institute Research Center (Projet ID code: 2015-1827, 2015-32-02, accepted on 24 March 2015) according to the guidelines of the Canadian Council on Animal Care.

4.2. Balloon Dilatation Procedures

Under general anesthesia (ketamine (35 mg/kg) and buprenorphine (10 mg/kg) administered intramuscularly, inhaled isoflurane (3% *v/v*, Baxter, Deerfield, IL, USA) and supplemental oxygen), balloon injury of the abdominal arterial wall was performed using a 5 French (F) radial introducer catheter (Cordis Corporation, Fremont, CA, USA) introduced through the right carotid artery. Under fluoroscopic guidance (Siemens, Berlin, Germany), a 4.0 mm PTCA balloon catheter (Boston Scientific, Marlborough, MA, USA) was advanced at the iliac bifurcation over a 0.014 inch guidewire (Abbott Vascular, Santa Clara, CA, USA), inflated with 8 atm and retracted three times in the distal 40 mm of the abdominal aorta. The right carotid artery was ligated at the end of the procedure.

4.3. Bimodal Near-Infrared Fluorescence (NIRF)/Intravascular Ultrasound (IVUS) Imaging Catheter System

The *in vivo* imaging system (Figure 3A) used in this study, designed as an ultrasound-optical imaging catheter linked to an optical assembly and custom-made electronics, was previously described in [10]. The catheter combines an optical fiber for fluorescence imaging and an ultrasound transducer for acoustic imaging. An electronic circuit synchronizes the acquisition with two motors driving the rotating/translating catheter assembly, and raw data is transferred directly to a laptop via a universal serial bus (USB) connection at rates of up to 250 Mbps. A custom Matlab (The MathWorks, Inc., Natick, MA, USA) user interface filters the signals and reconstructs and displays the images in real time during acquisition. Fluorescence excitation was performed using a 780 nm laser diode and emission was detected by a photomultiplier tube (Hamamatsu Photonics, Hamamatsu City, Japan), combined with a bandpass optical filter (832 ± 19 nm). A compensation algorithm was used to adjust the fluorescence signal amplitude for blood attenuation [10].

4.4. In Vivo NIRF Imaging Procedure

In vivo NIRF imaging was performed under anesthesia, as previously described, using a 5 F introducer (Cordis Corporation, Fremont, CA, USA) placed in the left carotid artery (model 1; $n = 4$). Four novel tentative imaging probes (nanobodies) targeting ICAM-1 receptors (National Research Council Canada, Ottawa, CA, USA), labeled with infrared dye 800CW, were injected under fluoroscopic guidance (Siemens, Germany) in the denuded segment of the abdominal aorta of model 1, followed by intravascular IVUS/NIRF imaging. Intravenous indocyanine green (ICG, 10 mg/kg) was injected in model 2 ($n = 1$) and intravascular imaging was performing through a right carotid artery access 40 min after dye injection. Automated imaging pullbacks were performed in the abdominal aorta of both animal models and in the right iliac artery of model 2 at a pullback speed of 0.5 mm/s and a frame rate of 10 images/s over a total length of 50 and 100 mm, respectively. After *in vivo* imaging procedures, the animals were sacrificed by exsanguination under anesthesia and then underwent abdominal aorta and iliac arteries resection. The samples were fixed in 4% formaldehyde and kept at 4 °C.

4.5. Ex Vivo Imaging System and Methods

Prior to *ex vivo* imaging, the distal 40 mm of the abdominal aorta and iliac arteries were mounted in a 4% cylindrical agarose block with 0.5% ethylenediaminetetraacetic acid (EDTA). *Ex vivo* imaging was performed using a custom made automated serialized dual-modality setup for OCT and confocal fluorescence microscopy, incorporating a swept-source laser with a central wavelength of 1310 nm and a tuning bandwidth of 100 nm for OCT. The confocal laser passed through a filter cube before being reflected at a 90° angle by a long pass dichroic mirror at 875 nm which allowed for it to be combined with the OCT laser beam (Figure 3), allowing simultaneous acquisition of OCT and confocal data.

To overcome limited light penetration in the tissue and scattering from microscopic imaging, a vibratome allowed sequential sectioning of the tissue block face in order to reveal new tissue regions to image. Following a previously described design, a dual flexure part isolated vibration of the blade from a direct current (DC) motor on a one-axis yielding precise cutting of the tissue. X and Y stages allowed moving the sample relative to the objective and imaging every sub-region (1 by 1 mm). Tissue samples embedded in agarose blocks were placed underneath a 10 \times water immersion objective for model 2. After an entire section was imaged, a 200- μm slice of tissue was removed and the process was repeated automatically. For each slice, the Z position of the sample was adjusted in order to have the focus approximately 50 μm under the tissue surface, thus avoiding imaging of deformed tissue due to its slicing. The images from both in vivo and ex vivo systems were analyzed using Matlab. Anatomical landmarks allowed for a precise sub-millimeter colocalization of in vivo and ex vivo images, along with the calculation of the shrinkage ratio of the excised tissue. To obtain three-dimensional (3D) reconstructions, imaging data was downsampled to a voxel size of 4 μm by 4 μm by 200 μm , converted in DICOM and loaded with Osirix (Pixmeo, Geneva, Switzerland). A maximum intensity projection algorithm was applied to generate a three-dimensional view of the vessels. The ex vivo imaging system generated cross-sectional OCT image slices with a pixel size of 2 μm by 2 μm and a depth of 6.5 μm . The resulting dataset had a size of over 500 GB. In fluorescence confocal microscopy, one cross-sectional image was obtained for each 200- μm depth. Colocalization between the IVUS and OCT images was performed. Figure 6 compares the OCT reconstruction with the IVUS scan for rabbit 1. Colocalization between images relied on finding biological landmarks, primarily bifurcations. Pullbacks began at the bifurcation between the left and right iliac artery and could be seen on both types of scans, providing a good starting point.

For model 1, aortas were imaged using the aforementioned OCT/confocal microscope, but with a 3 \times air objective and a 5 μm \times 5 μm pixel size. Axial resolution was unchanged. A glass was added between the objective and the water to create an air chamber. The field of view (FOV) in the lateral directions was set to 2.5 mm \times 2.5 mm. The ICAM-1 fluorophore was sensitive to a 776 nm wavelength. The 3 \times objective did not allow for a high enough signal-to-noise ratio (SNR) with a small pinhole (100 μm), and an iris was used instead. This, however, came at the cost of lateral resolution (4.4 μm). The vibratome blade was inclined at an approximately 20-degree angle with the plane of the agarose gel. Connective tissue was removed before embedding the aorta in agarose with a razor blade. Three-dimensional reconstructions of the aortas were done using custom Python algorithms developed for this purpose. Since an iris was used instead of a pinhole, deconvolution was performed on the fluorescence images in order to locate more accurately the sources of signal.

For OCT images, the first reconstruction step was to find the volumes position within the mosaic reference frame. A displacement model of the sample-motorized stage was used to estimate each XY tile position within the mosaic. The model parameters were estimated from the data by computing the phase-correlation based pairwise registration [23] of all neighboring tiles within the mosaic and by inverting the model, solving for each parameter. The next step was to stitch together the volumes for each slice. Adjacent volumes were blended together by finding the medial axis of their 2D overlap region and by applying a small Gaussian feathering to ensure a smooth transition between tiles. Each tissue slice was stitched separately.

A few post processing steps were then applied on each slice to remove intensity artifacts, to limit the field of view to the tissue, to compute the lumen mask, and, finally, to estimate and compensate the light attenuation with depth in the OCT volumes. This last step was done by fitting a Beer-Lambert law on each A-Line and by estimating the attenuation coefficient from this fit [24]. The Beer-Lambert law was then used again with the average tissue attenuation coefficient to normalize the OCT volume and thus reduce its contrast variation with depth.

The last reconstruction step was to stitch the slices together in the z direction to get a complete 3D volume. This was done by computing the shift between adjacent slices using the cross-correlation of their 2D image gradient magnitude. Then, the slices were stitched together by solving the Laplace

equation with Dirichlet boundary conditions over their masked overlap region. The tissue mask was used to remove the gaps introduced by the slice cutting artifacts.

Colocalization between the IVUS and OCT images was performed. Colocalization between images relied on finding biological landmarks, primarily vessel bifurcations. Pullbacks began at the bifurcation between the left and right iliac artery and could be seen on both types of scans for model 2, providing a good starting point. The distance between the same landmarks was measured by knowing the pixel size (6.5 μm) for OCT, and by comparing it to the distance found on the IVUS data, which was recorded during acquisition.

5. Conclusions

In conclusion, a method for atherosclerotic plaque detection and molecular characterization has been investigated both *in vivo* and *ex vivo* in a rabbit model. The *in vivo* method relied on an intravascular catheter that combined IVUS and fluorescence imaging, while the *ex vivo* method combined an OCT and a fluorescence confocal microscope with a custom serial slicer and stitching algorithm to reconstruct whole 3D segments of aortas and locate the presence of plaque with great accuracy. Colocalization between the *in vivo* and *ex vivo* data was performed by finding landmarks between the IVUS and OCT volumes. This massive histology method is a promising approach to validating future intravascular catheters; it could potentially become a new gold standard to validate intravascular molecular imaging, and it is a great addition to the currently used histology methods.

Acknowledgments: This study was supported by CIHR operating grant 273578 to Frédéric Lesage.

Author Contributions: Pier-Luc Tardif, Maxime Abran, Alexandre Castonguay, and Joël Lefebvre acquired the 3D histology data and performed image reconstruction; Philippe L'Allier, Marie-Jeanne Bertrand, Maxime Abran, Nolwenn Merlet, Teodora Mihalache-Avram, Pascale Geoffroy, Mélanie Mecteau, and David Busseuil performed the catheter experiments; Feng Ni and Abedelnasser Abulrob synthesized the molecular probes; Éric Rhéaume and Teodora Mihalache-Avram performed histological validations; Philippe L'Allier, Marie-Jeanne Bertrand, Barbara E. Stähli and Frédéric Lesage wrote the article; Philippe L'Allier, Jean-Claude Tardif, and Frédéric Lesage designed and supervised the study.

Conflicts of Interest: The authors declare no conflict of interest.

References

1. Libby, P.; Okamoto, Y.; Rocha, V.Z.; Folco, E. Inflammation in atherosclerosis transition from theory to practice. *Circ. J.* **2010**, *74*, 213–220. [CrossRef] [PubMed]
2. Libby, P.; Ridker, P.M.; Hansson, G.K. Progress and challenges in translating the biology of atherosclerosis. *Nature* **2011**, *473*, 317–325. [CrossRef] [PubMed]
3. Bentzon, J.F.; Otsuka, F.; Virmani, R.; Falk, E. Mechanisms of plaque formation and rupture. *Circ. Res.* **2014**, *114*, 1852–1866. [CrossRef] [PubMed]
4. Muller, J.E.; Tofler, G.H.; Stone, P.H. Circadian variation and triggers of onset of acute cardiovascular disease. *Circulation* **1989**, *79*, 733–743. [CrossRef] [PubMed]
5. Mintz, G.S.; Painter, J.A.; Picard, A.D.; Kent, K.M.; Satler, L.F.; Popma, J.J.; Chuang, Y.C.; Bucher, T.A.; Sokolowicz, L.E.; Leon, M.B. Atherosclerosis in angiographically “normal” coronary artery reference segments: An intravascular ultrasound study with clinical correlations. *J. Am. Coll. Cardiol.* **1995**, *25*, 1479–1485. [CrossRef]
6. Tardif, J.C.; Lesage, F.; Harel, F.; Romeo, P.; Pressacco, J. Imaging biomarkers in atherosclerosis trials. *Circ. Cardiovasc. Imaging* **2011**, *4*, 319–333. [CrossRef] [PubMed]
7. Berry, C.L.; L'Allier, P.; Grégoire, J.; Lespérance, J.; Lévesque, S.; Ibrahim, R.; Tardif, J.C. Comparison of intravascular ultrasound and quantitative coronary angiography for the assessment of coronary artery disease progression. *Circulation* **2007**, *115*, 1851–1857. [CrossRef] [PubMed]
8. Mintz, G.S.; Garcia-Garcia, H.M.; Nicholls, S.J.; Weissman, N.J.; Bruining, N.; Crowe, T.; Tardif, J.C.; Serruys, P.W. Clinical experts consensus document on standards of acquisition, measurement and reporting of intravascular ultrasound regression/progression studies. *EuroIntervention* **2011**, *6*, 1123–1130. [CrossRef] [PubMed]

9. Sanchez, O.D.; Sakakura, K.; Otsuka, F.; Yahagi, K.; Virmani, R.; Joner, M. Expectations and limitations in contemporary intravascular imaging: Lessons learned from pathology. *Expert Rev Cardiovasc. Ther.* **2014**, *12*, 601–611. [CrossRef] [PubMed]
10. Abran, M.; Cloutier, G.; Cardinal, M.H.R.; Chayer, B.; Tardif, J.C.; Lesage, F. Development of a photoacoustic ultrasound and fluorescence imaging catheter for the study of atherosclerotic plaque. *IEEE Trans. Biomed. Circuits Syst.* **2014**, *8*, 696–703. [CrossRef] [PubMed]
11. Dixon, A.J.; Hossack, J. Intravascular near-infrared fluorescence catheter with ultrasound guidance and blood attenuation correction. *J. Biomed. Opt.* **2013**, *18*. [CrossRef] [PubMed]
12. Mallas, G.; Brooks, D.H.; Rosenthal, A.; Nudelman, R.N.; Mauskapf, A.; Jaffer, F.A.; Ntziachristos, V. Improving quantification of intravascular fluorescence imaging using structural information. *Phys. Med. Biol.* **2012**, *57*, 6395–6406. [CrossRef] [PubMed]
13. Bec, J.; Xie, H.; Yankelevich, D.R.; Zhou, F.; Sun, Y.; Ghata, N.; Aldredge, R.; Marcu, L. Design construction and validation of a rotary multifunctional intravascular diagnostic catheter combining multispectral fluorescence lifetime imaging and intravascular ultrasound. *J. Biomed. Opt.* **2011**, *4*, 319–333. [CrossRef] [PubMed]
14. Jaffer, F.A.; Calfon, M.A.; Rosenthal, A.; Mallas, G.; Razansky, R.N.; Mauskapf, A.; Weissleder, R.; Libby, P.; Ntziachristos, V. Two-dimensional intravascular near-infrared fluorescence molecular imaging of inflammation in atherosclerosis and stent-induced vascular injury. *J. Am. Coll. Cardiol.* **2011**, *57*, 2516–2526. [CrossRef] [PubMed]
15. Jaffer, F.A.; Vinegoni, C.; John, M.C.; Aikawa, E.; Gold, H.K.; Finn, A.V.; Ntziachristos, V.; Libby, P.; Weissleder, R. Real-time catheter molecular sensing of inflammation in proteolytically active atherosclerosis. *Circulation* **2008**, *118*, 1802–1809. [CrossRef] [PubMed]
16. Nahrendorf, M.; Jaffer, F.A.; Kelly, K.A.; Sosnovik, D.E.; Aikawa, E.; Libby, P.; Weissleder, R. Noninvasive vascular cell adhesion molecule-1 imaging identifies inflammatory activation of cells in atherosclerosis. *Circulation* **2006**, *114*, 1504–1511. [CrossRef] [PubMed]
17. Rouleau, L.; Berti, R.; Ng, V.W.K.; Matteau-Pelletier, C.; Lam, T.; Saboural, P.; Kakkar, A.K.; Lesage, F.; Rhéaume, E.; Tardif, J.C. VCAM-1-targeting gold nanoshell probe for photoacoustic imaging of atherosclerotic plaque in mice. *Contrast Med. Mol. Imaging* **2013**, *8*, 27–39. [CrossRef] [PubMed]
18. De Vries, B.M.W.; Hillebrands, J.; van Dam, G.M.; Tio, R.A.; de Jong, J.S.; Slart, R.H.J.A.; Zeebregts, C.J. Images in cardiovascular medicine. Multispectral near-infrared fluorescence molecular imaging of matrix metalloproteinases in a human carotid plaque using a matrix-degrading metalloproteinase-sensitive activatable fluorescent probe. *Circulation* **2009**, *119*, e534–e536. [CrossRef] [PubMed]
19. Abran, M.; Stähli, B.E.; Merlet, N.; Mihalache-Avram, T.; Mecteau, M.; Rhéaume, E.; Busseuil, D.; Tardif, J.C.; Lesage, F. Validating a bimodal intravascular ultrasound (IVUS) and near-infrared fluorescence (NIRF) catheter for atherosclerotic plaque detection in rabbits. *Biomed. Opt. Express* **2015**, *6*, 3989–3999. [CrossRef] [PubMed]
20. Wang, H.; Zhu, J.; Akkin, T. Serial optical coherence scanner for large-scale brain imaging at microscopic resolution. *NeuroImage* **2014**, *84*, 1007–1017. [CrossRef] [PubMed]
21. Castonguay, A.; Avti, P.K.; Moeini, M.; Pouliot, P.; Tabatabaei, M.S.; Bélanger, S.; Lesage, F. Investigating the correlation between white matter and microvasculature in aging using large scale optical coherence tomography and confocal fluorescence imaging combined with tissue sectioning. *Proc. SPIE* **2015**, *9328*. [CrossRef]
22. Pande, A.N.; Kohler, R.H.; Aikawa, E.; Weissleder, R.; Jaffer, F.A. Detection of macrophage activity in atherosclerosis in vivo using multichannel, high-resolution laser scanning fluorescence microscopy. *J. Biomed. Opt.* **2006**, *11*. [CrossRef] [PubMed]
23. Preibisch, S.; Saalfeld, S. Fast stitching of large 3d biological datasets. In Proceedings of the 2nd ImageJ User and Developer Conference, Luxembourg, 7–8 November 2008.
24. Faber, D.; van der Meer, F.; Aalders, M.; van Leeuwen, T. Quantitative measurement of attenuation coefficients of weakly scattering media using optical coherence tomography. *Opt. Express* **2004**, *12*, 4353–4365. [CrossRef] [PubMed]



© 2016 by the authors. Licensee MDPI, Basel, Switzerland. This article is an open access article distributed under the terms and conditions of the Creative Commons Attribution (CC BY) license (<http://creativecommons.org/licenses/by/4.0/>).



Review

Brain Vascular Imaging Techniques

Bàrbara Laviña

Department of Immunology, Genetics and Pathology, Rudbeck Laboratory, Uppsala University, 75185 Uppsala, Sweden; barbara.lavina-siemsen@igp.uu.se; Tel.: +46-018-471-4504

Academic Editor: Michael Henein

Received: 24 October 2016; Accepted: 26 December 2016; Published: 30 December 2016

Abstract: Recent major improvements in a number of imaging techniques now allow for the study of the brain in ways that could not be considered previously. Researchers today have well-developed tools to specifically examine the dynamic nature of the blood vessels in the brain during development and adulthood; as well as to observe the vascular responses in disease situations *in vivo*. This review offers a concise summary and brief historical reference of different imaging techniques and how these tools can be applied to study the brain vasculature and the blood-brain barrier integrity in both healthy and disease states. Moreover, it offers an overview on available transgenic animal models to study vascular biology and a description of useful online brain atlases.

Keywords: brain vascular disorders; imaging; vascular biology; brain atlas; animal models; molecular imaging; computed tomography (CT); positron emission tomography (PET); magnetic resonance angiography (MRI); photoacoustic imaging (PAI); magnetic resonance angiography (MRA)

1. Introduction

The brain is one of the most sophisticated and complex organs generated by evolution and its impressive anatomical composition and its entangled functionality has been admired for thousands of years. Although early civilizations lacked adequate means to obtain knowledge about the nervous system, the ancient Egyptians in the 17th century Before Common Era (BCE) wrote the earliest recorded reference to the brain in the Edwin Smith papyrus [1]. It was not until the 5th century BCE that the concept of the nervous system appeared [2]. In the 1600s, William Harvey proved the theory of blood circulation in *De Motu Cordis* [3], although the first descriptions of the pulmonary circulation by Ibn al-Nafis date back to the 16th century BCE [4]. The interest in dynamics stimulated the study of angiography and neuroanatomy and, in 1664, Thomas Willis published *Cerebri anatome*, a text on the brain that was a groundbreaking work for neuroscience and remained very influential for the next two centuries [5,6].

In 1882, Angelo Mosso invented the first neuroimaging technique, called “human circulated balance” that could non-invasively measure the redistribution of blood during emotional and intellectual activity [7]. Nevertheless, the origin of structural imaging was the X-ray, discovered by Roentgen in 1895 [8]. Shortly after, Haschek and Lindenthal produced radiographs of blood vessels by injecting opaque solution into cadavers; however, it was not until 1927 that Egas Moniz performed the first cerebral angiography in humans [9]. Since then, key events and major technological innovations in physics, mathematics, computing and clinical imaging have promoted the development of at least the following techniques: (1) computed tomography (CT), for which Hounsfield and Cormack were awarded the Nobel Prize in 1979; (2) positron emission tomography (PET) [10]; and (3) magnetic resonance imaging (MRI), for which Lauterbur and Mansfield were awarded the Nobel Prize in 2003 and magnetic resonance angiography (MRA). The abovementioned techniques together with other imaging modalities, including digital subtraction angiography (DSA), photoacoustic imaging (PAI) and

trans-cranial doppler (TCD), have contributed to the knowledge of the brain vasculature, promoting and improving our understanding of the complexity of the central nervous system (CNS).

The strategies that scientists have adopted for studying the brain have varied over the years as new techniques and methods have been developed. Elucidating the composition and functions of the brain is one of the most challenging areas of research. Characterizing the structure of the brain at high resolution is crucial for understanding its functions and dysfunction. Neuroimaging, the process of producing images of the structure or activity of the brain, is becoming an increasingly important tool in both research and clinical care, tremendously helping our understanding of brain morphology and physiology in healthy and disease states.

The aim of this review is to give a short overview of the most important recent scientific advances achieved using imaging techniques, with particular focus on their relevance to the field of brain vascular imaging and including a section on molecular imaging of the blood-brain barrier (BBB). A special focus on animal models is also included, as their use is motivated by a desire to better understand human diseases. Moreover, a summary of available online brain atlases for both human and animal models and the way these approaches contribute to a better understanding of the brain on multiple levels are also highlighted.

2. Computed Tomography (CT)

On October 1, 1971, in London, England, CT imaging performed by Godfrey Hounsfield and James Ambrose produced the first scan of a patient with a cerebral cyst. The image proved it was possible to produce non-superimposed images of an object slice [11].

Since that time, CT has been improved by a number of important technological advancements, leading to the current ability to acquire thousands of thin-slice images with voxel isotropy in a few seconds with a reduced radiation dose [12,13]. CT angiography (CTA) has gained the most benefit from such evolution in terms of improved diagnostic performance and broadened clinical indications [14,15]. Color-coded CT angiography, a new method of displaying dynamic cerebral CT angiography, provides important additional information on cerebral hemodynamics, including specifically differentiation between antegrade and retrograde flow [16].

Micro-scale computed tomography (microCT) [17,18] and nano-computed tomography (nanoCT) [19] are high-resolution cross-sectional imaging techniques and are essential tools for phenotyping and for elucidating diseases and their therapies. Compared to other imaging methods, the strengths of microCT and nanoCT lay with their high-resolution scanning efficiency, velocity and relatively low cost. Additionally, it is a structural imaging modality that provides a high-resolution volumetric representation of vascular structures in brains of rodents [20–24] as well as measurements of cerebral blood volume (CBV) [25].

Recent applications of microCT to the mouse brain vasculature include the *in situ* analysis of adult brains using iodine-based contrast [26], the evaluation of animal models of cerebral cavernous malformations (CCM) [27] and the imaging of brain tumors in live mice [28].

Perfusion CT is a relatively new imaging technique that allows rapid qualitative and quantitative evaluation of cerebral vascular physiology and hemodynamics including measurement of cerebral blood flow (CBF) and CBV. It involves the sequential acquisition of cerebral CT images performed during the intravenous administration of contrast material [29]. It is an alternative imaging modality with several clinical indications including stroke [30], head trauma [31] and brain tumors [32]. Published data have suggested that perfusion CT might be comparable to MRI [33,34]. Moreover, perfusion CT has been used to evaluate possible clinical benefits of pharmacology therapy in early stroke onset [35], as well as to predict survival in in high-grade gliomas [36].

3. Positron Emission Tomography (PET) and Single Photon Emission Computed Tomography (SPECT)

The development of CT soon led to other imaging techniques, including PET [37,38], which involves injecting rapidly decaying radioactive substances into the bloodstream. The first simple PET scanner able to detect brain tumors was made in the early 1950s by Bromwell and Sweet and by 1975, more sophisticated types of PET, which could measure blood flow, were developed [39–41].

The first PET image of a rat brain using a clinical PET scanner was performed in 1991 [42] and the initial dedicated small PET scanner was introduced several years later in 1995 [43]. The recent development of a high-resolution small animal PET scanner suitable for imaging the mouse brain will quickly improve the imaging quality of brain analysis [44].

PET functional imaging is most useful in combination with anatomical imaging and hybrid imaging systems such as PET/MRI [45,46] and PET/CT [47,48]. Multimodality imaging PET/CT and PET/MRI provide advantages in the imaging evaluation of patients with a variety of diseases [49]. A PET/CT scanner has the ability to improve image quality and image accuracy of PET images, enhancing lesion identification and localization, which affects clinical decision making and thereby improves patient management [50–52]. PET/MRI combination offers functional structural and metabolic data, which can potentially contribute to more accurate diagnoses and ultimately affect patient survival. The advantages and drawbacks of PET/CT are discussed in [53,54].

Multimodality imaging is nowadays available in the clinical practice and for small animals [55]. Rodent SPECT/CT has been used to assess *in vivo* CBF and blood-brain barrier (BBB) disruption after focal cerebral ischemia [56] and the recently developed trimodal PET/SPECT/CT scanner for small animals [57] has allowed for new insights into brain function and the visualization of cerebral ischemia in living rats [58].

PET and single photon emission computed tomography (SPECT) [59,60] are molecular imaging modalities which by the use of specific radioactive tracers, allow visualization and measurement of physiological processes in intact living brains [61].

Recently PET has been used to study hypoxia and inflammation in ischemic stroke [62–65], to explore the possible relationship between an acute ischemic stroke and A β deposition in patients [66], and to noninvasively image VEGFR expression kinetics to analyze post stroke angiogenesis in rats [67]. Moreover, ^{11}C -methionine is the most popular tracer used in PET imaging of brain tumors [68], and can predict prognosis in gliomas [69]. Other recent examples of brain vascular disorders imaged utilizing PET or SPECT include thrombosis [70], Alzheimer's [71] and Moyamoya disease [72].

4. Magnetic Resonance Imaging (MRI) and Other Similar Techniques

The basic idea behind the MR phenomenon first appeared in 1946 from discoveries by Bloch and Purcell. It took another 25 years before MRI was applied to medical diagnosis, when the first discoveries concerning the development of the technique to visualize different structures were published [73–75]. A great advantage with MRI is that it uses magnetic forces rather than potentially harmful ionizing radiation. Moreover, image quality has advanced to a remarkable extent with scan times decreasing by factors of 10 to 100 since the early 1980s [76,77].

The main concepts required to understand MRI include the classification of the image contrast following its sensitivity to three different parameters: proton density (ρ), the spin-lattice or longitudinal relaxation times T_1 , and the spin-spin or transverse relaxation times T_2 or T_2^* . A proton-density-weighted image is a sequence that is mainly sensitive to ρ and T_1 - or T_2 -weighted images are, respectively, sensitive to T_1 or T_2 relaxation times [78]. Additionally, different contrast agents, which enrich MRI, can be used in the so-called Contrast-Enhanced MRI [79]. Several reviews have recently focused on cerebrovascular MRI, compared to other imaging techniques and described the key developments in the last years [12,80–83].

These new advances in neuroimaging methods could also be applied as biomarkers [84]. Biomarkers can be used as a diagnostic tool, a prognostic tool, a predictive tool (for predicting

response to an intervention), or a substitute for a clinical outcome to measure the response to an intervention (surrogate end point). Some examples of biomarkers based on MR imaging used in acute ischemic stroke are summarized in [85]. Biomarkers based on brain imaging may relate to prognosis in high-grade gliomas [86] and recently, vessel caliber analysis has been proposed as a possible biomarker of tumor response in clinical trials, revised in [87].

The study of hemodynamic alterations in patients with cerebrovascular disease is important to understand the disease, potentially improving diagnostic capabilities and therapeutic planning. There is a demand for noninvasive imaging of cerebrovascular territories; therefore, new emerging techniques for evaluation cerebrovascular hemodynamics and CBF [88], including four-dimensional (4D) flow MRI [89–92]; 2D phase contrast MRI (PC-MRI) [93–95] and magnetic resonance black-blood thrombus imaging technique (MRBTI) [96] are being developed.

4.1. Diffusion and Perfusion Weighted MRI.

Diffusion (DWI) and perfusion (PWI) weighted MRI have an increasingly important clinical role (see [97] for a detailed description of the basic principles). The combination of both techniques is especially promising for the early detection and assessment of stroke [98,99]; and for brain tumor characterization [100], as they provide complementary information.

DWI is based on the random movement of water molecules caused by their kinetic energy dissipation, known as Brownian motion, in the presence of magnetic pulses. The apparent diffusion coefficient is a measure that displays the magnitude of diffusion of the water molecules within tissue [101,102]. In the field of brain imaging, DWI has been applied to diagnose and monitor stroke [103,104] and characterize brain tumors [105].

PWI refers to methods that make use of the effect of endogenous or exogenous tracers on the MR images for deriving various hemodynamic parameters offering the potential for measuring brain perfusion in several pathological conditions including stroke [106] and brain tumors [107,108]. Perfusion MRI techniques can be used for quantitative assessment of specific pathophysiologic parameters, more accurate grading of intracranial tumors and may predict survival and patient outcome [109,110].

4.2. Susceptibility-Weighted Imaging (SWI)

SWI is an MRI technique that enhances image contrast by using the susceptibility differences between tissues and has become a part of routine brain MRI protocols [111]. The clinical success of SWI arises from its superior sensitivity for detecting small quantities of blood product, its ability to differentiate between arterial and venous vessels, and its ability to differentiate between calcification and blood product. Thus, SWI is nowadays utilized to obtain images of diverse brain vascular disorders including: hemorrhages, traumatic brain injury, stroke, tumors and multiple sclerosis [112–114]. The fact that this technique does not provide quantitative measurements, which is an important limitation, is currently overcome by the advancement of new technology such as quantitative susceptibility mapping (QSM) [115] and susceptibility tensor imaging (STI) [116].

4.3. Quantitative Susceptibility Mapping (QSM)

QSM [117] is expected to play an increasing role in the clinic as it permits to unambiguously differentiate between calcified and hemorrhagic lesions which permits a differential diagnosis and simultaneously reveals brain anatomy. This technique allows investigating and obtaining valuable information not only on compositional changes in aging brain, but also in numerous neurodegenerative disorders, providing valuable guidance to clinicians during diagnosis.

QSM has recently been applied to monitor CCM disease progression and iron deposition [118,119], intracranial hemorrhages [120], hematoma volume [121] and to differentiate hemorrhages from calcifications [122]. The usefulness of QSM in visualizing the microstructure of the mouse brain at a 10 μm resolution, has been shown by the revealing of detailed structures [123].

4.4. Intracranial Vessel Wall Imaging (IVW)

Recently available IVW methods provide the possibility of directly assessing the vessel wall [124–127], providing a useful diagnostic tool, which may improve patient outcomes by helping treatment choice, in comparison to other invasive and non-invasive methods currently available. IVM is especially challenging due to the small caliber and tortuosity of the intracranial vessels and is an upcoming field of interest to assess intracranial atherosclerotic lesions [128–130], intracranial vasculopathies [131,132], cerebrovascular inflammation [133], CNS vasculitis [134], brain arteriovenous malformations [135], Moyamoya disease [136,137], Cerebral aneurysms [138–140] and intracranial arterial dissection [141].

4.5. MR Angiography (MRA)

MRA is a group of techniques based on MRI to image blood vessels [142,143]. MRA techniques can be divided into two categories: contrast-enhanced and non-contrast enhanced MRA. Since its introduction in 1994 by Prince [144], first-pass contrast-enhanced MRA has seen widespread acceptance and details about techniques and contrast agents are reported in [145–149]. A detailed description of non-contrast MRA techniques and the physical mechanisms underlying each method including their clinical applications can be found in [150] and [151]. In the brain, MRA is used to visualize cerebrovascular territories [152,153], and to evaluate stenosis and occlusions [154], aneurysms [155] and other cerebral malformations [156]. A complete description of MRA in brain vascular disorders is reviewed in [157].

5. Digital Subtraction Angiography (DSA)

DSA is an imaging method that permits a distinct visualization of the vasculature in a skeletal or dense soft tissue environment. The introduction of the technique in 1980 provided a method for real-time 2D subtraction imaging, spawning a steady progression of related methods, including 3D [158] and 4D DSA [159] (an outline of some historical milestones and future directions are nicely reviewed in [160,161]).

An overview of the technical principles of DSA can be found in [162,163]. Briefly, the target tissue is initially exposed to X-ray or MRI, to obtain the first set of images; then a contrast agent is administered into the vasculature and additional X-ray or MRI are obtained. The mask, which is the first set of images, is then subtracted from the latter or contrast enhanced images, allowing the visualization of the vascular structure free of the surrounding tissue.

DSA can be utilized to visualize intracranial vascular structures [164], vascular abnormalities such as arteriovenous malformations [165], aneurysms [166], carotid stenosis [167], as well as grading Moyamoya disease [168] and collateral flow in acute middle cerebral artery occlusion [169].

6. Trans-Cranial Doppler (TCD)

TCD ultrasound is a specialized technique introduced in 1982 by Rune Aaslid for detecting blood flow in the basal intracerebral arteries [170]. It is a noninvasive technique that involves the use of a low-frequency (≤ 2 MHz) transducer probe to insonate specific areas of the cranium that are relatively thin. TCD enables users to acquire images of some of the major intracranial vessels through the intact skull and monitor cerebral blood flow (CBF) velocity and vessel pulsatility over extended time periods with a high temporal resolution. [171]. Advanced applications of TCD in neurovascular diseases have been extensively revised in [172–175].

7. Photoacoustic Imaging (PAI)

Photoacoustic imaging (PAI) is also called optoacoustic imaging and is an emerging imaging modality that shows great potential for preclinical research and clinical practice [176]. The method is based on the photoacoustic effect; briefly, the tissue of interest is excited by a pulsed laser and part

of the locally absorbed light produces thermal excitation, leading to an expansion of the tissue and subsequent generation of ultrasonic waves. Ultrasonic transducers detect the emitted ultrasonic waves, which are finally converted into images.

The applications in biomedicine of the photoacoustic effect, first reported by Alexander Graham Bell in 1880, began in the 1970s [177] but progressed slowly until the last decade of the 20th century, when many pioneering works demonstrated the photoacoustic effect in optically scattering media and biological tissue, extensively reviewed in [178–180].

As a hybrid technique, PAI is based on the acoustic detection of optical absorption from either endogenous chromophores or exogenous contrast agents [181], such as chemical dyes [182], nanoparticles [183,184] and reporter genes [185,186]. PAI is especially useful in visualizing blood vessels *in vivo* due to the fact that blood hemoglobin and deoxyhemoglobin, have a substantially higher absorption than surrounding tissues and therefore create sufficient endogenous contrast. Over the past decade, the photoacoustic technique has been evolving rapidly, leading to a variety of exciting discoveries and applications such as photoacoustic tomography (PAT) that is cross-sectional or three-dimensional (3D) PAI [187–189].

PAT allows visualizing and studying a diverse range of structures: from organelles to whole organs [190] and based on the spatial resolution of the method, PAT is classified into optical-resolution photoacoustic microscopy (OR-PAM) [191], acoustic-resolution photoacoustic microscopy (AR-PAM) [192], photoacoustic computed tomography (PACT) [193,194], and photoacoustic endoscopy (PAE) [195].

PAI has been successfully used in the past few years in small animal models to image the brain [196,197] and determine CBF through the intact skull [198]. Recently, a wearable system has been developed that is capable of providing images of cerebral blood vessels noninvasively [199]. Moreover, PAI is a new strategy to visualize and study several brain disorders [200] including stroke [201–203], brain tumors [204–206]; cerebral edema [207], epilepsy [208]; traumatic brain injury [209] and inflammation [210].

PAT imaging in patients with brain pathologies is currently not used in clinical practice and is still under development. The main challenge and limitation in humans is the thickness of the skull, but promising recent advances suggest that this technology could be implemented as a clinical device for noninvasive functional brain imaging [184,211–213].

8. Molecular Imaging of the Blood-Brain Barrier (BBB)

Multiple cell types, which coordinately form the neurovascular unit (NVU), include neurons; vascular cells (endothelial cells (EC), smooth muscle cells and pericytes); and glia (astrocytes, microglia and oligodendroglia), which are key factors to maintaining CNS functions. Within the NVU, the EC form the BBB that limits entry of substances into the brain and maintains the ideal environment for the brain to properly function [214,215].

A detailed molecular atlas of the BBB transport systems and cellular functions, based on available data on protein and RNA expression, as well as physiological measurements from different published investigations, is meticulously provided in this recent review [216].

Dysfunction of the BBB has been shown to be a common denominator in many CNS disease pathogeneses observed in stroke, cerebral edema, Parkinson's disease, Alzheimer's disease, seizures, microcephaly and CCMs, among others [214,217,218].

Work in key molecular components of the ECs composing the BBB—including macromolecule transporters such as the glucose transporter GLUT1 [219]; the major facilitator superfamily domain-containing protein 2a (MFSD2a) [220,221]; and tight junction complexes [222], such as Occludin [223]; and the junctional adhesion molecule C (JAM-C) [224]—and their implication in several brain diseases with BBB dysfunction and altered cerebrovascular integrity have raised the interest in molecular imaging of the BBB.

Dynamic contrast-enhanced MRI (DCE-MRI) is the most widely used imaging method for assessing BBB integrity [225–228]. It has been used to assess abnormal BBB permeability in several

pathological conditions including: traumatic brain injury [229], vascular cognitive impairment [230], multiple sclerosis [231], Alzheimer's disease [232], brain tumors [233] and stroke [234].

The development of novel state-of-the art neuroimaging and molecular biomarker approaches are key aspects of future investigations addressing whether molecular and imaging biomarkers of BBB dysfunction can serve as reliable prognostic and/or diagnostic tools to predict the development of several CNS disorders [235].

9. Transgenic Animal Models for Vascular Biology

Recent advances in imaging techniques [236,237] together with the development of tissue-clearing methods, facilitating volumetric imaging without sectioning [238–240], do now provide the possibility, with adequate resolution, to obtain live imaging data from the vasculature in organs and even whole experimental animals during development and disease conditions.

The development of transgenic animal models with fluorescent markers for specific proteins or specific vascular cell types are necessary to fully benefit from the newly available microscope techniques.

So far, zebrafish has been the most suitable animal model to perform *in vivo* live imaging experiments of the vascular system. Therefore, several transgenic lines, which express different kinds of fluorescent probes in vascular cell types, are currently available and have extensively contributed to improving our knowledge of key vascular processes such as lumen formation, angiogenic sprouting, remodeling, cell proliferation and circulation of blood cells, reviewed in [241,242].

Although the establishment of fluorescent vascular reporters in mice models to study vascular biology has been slower, it is in fact becoming more relevant. Some transgenic mouse lines are already available and label different cell types including: EC [243–252]; lymphatic endothelial cells (LEC) [253–257], reviewed in [258] and pericytes [259–261]. While the above referenced transgenic lines are useful reporters for the major vascular cell types, other transgenic lines have been developed to visualize various organelles or subcellular structures [262–265].

The effort to develop new tools such as fluorescent reporter mice is not only performed by single scientific groups but also by joined projects. One example is the Gene Expression Nervous System Atlas (GENSAT) project, which is mapping the expression pattern of genes in the CNS and has created several mouse reporters, expressing enhanced green fluorescent protein (EGFP) and td-Tomato, to investigate the distinct gene expression patterns [266] (www.gensat.com). Moreover, other interesting fluorescent reporter mice are also available in the Jackson Laboratory (www.jax.org).

10. Brain Atlases

Another useful tool generated using some of the imaging methods mentioned in this review are brain atlases [267]. Brain atlases are applicable in all areas of neuroscience including research, education and clinical applications. An enormous amount of data is produced every day in laboratories worldwide regarding brain mapping, and there are many initiatives to make these data available through public databases. At present, brain atlases are printed, electronic, web-based and some are even available on mobile platforms [268].

The recent technical advances in areas such as sample preparation, optical techniques, quantitative 2D and 3D imaging analysis and high-performance computing, have relevantly contributed to the development of new brain mapping approaches (reviewed in [269]). The latest news about the worldwide brain research initiatives can be found in [270].

Following the publication of the mouse [271], adult [272] and prenatal [273] human brain gene expression atlases in recent years, a high-resolution transcriptional atlas of pre- and post-natal brain development for the rhesus monkey has now become available [274].

Table 1 gives examples of some of the most relevant web-based brain atlases in human, rodents and other species [271,272,274–293].

Table 1. Examples of available online brain atlases.

Species	Atlas Name	Comments	Link	Selected References
Human	The Human Brain Atlas at Michigan State University	MRI from one specimen + myelin and cell bodies staining	https://msu.edu/~brains/human/index.html	Tool developed by Sudheimer, K.D.; Winn, B.M.; Kendt, G.M.; Shoops, J.M.; Davis, K.K.; Fobbs Jr, A.J.; Johnson, J.L. [272,275,276]
	Allen Brain Atlas	MRI, <i>in situ</i> hybridization, microarray	http://human.brain-map.org/	[277]
	Scalable Brain Atlas	Brain atlas templates for different species	https://scalablebrainatlas.incf.org/main/index.php	[277]
	Atlas of the Human Brain	Macroscopic and microscopic levels	http://www.thehumanbrain.info/	[293]
	Human Connectome Project	MRI-based imaging modalities to measure brain architecture, function and connectivity	http://www.humanconnectomeproject.org/	[278–281]
	BigBrain	Cell bodies' staining	https://bigbrain.loris.ca/main.php	[282]
	Jubrain	Probabilistic maps based on post mortem brains	https://www.jubrain.fz-juelich.de/apps/cytoviewer/cytoviewer-main.php	[283]
	The Whole Brain Atlas	Contains atlas from different cerebrovascular diseases	http://www.med.harvard.edu/aanlib/home.html	[284]
	Human Brainnetome Atlas	Structural and connectivity features	http://atlas.brainnetome.org/	[285]
	Brain Development Atlases (Imperial College London)	Different atlas datasets are available (adult, pediatric and neonatal)	http://brain-development.org/brain-atlases/	[286–288]
Rodents	FSL Atlas	Library of analysis tools for fMRI, MRI and DTI brain imaging data	http://fsl.fmrib.ox.ac.uk/fsl/fslwiki/	[289]
	Allen Brain Atlas	Includes developing brain, spinal cord and connectivity brain atlas	http://mousebrain-map.org/	[271,276]
	Mouse Atlas Project	Contains also a neonatal brain atlas	http://map.loni.usc.edu/	[290]
Others	The Mouse Brain Library	Includes developing mouse brain atlas	http://www.mbl.org/	Tool developed by Williams, R.W. and colleagues [291]
	Zebrafish Brain Atlas	Includes information about the neuroanatomy of the developing zebrafish brain	http://zebrafishbrain.org/	[274]
	Blueprint Atlas (Rhesus macaque)	Gene expression data, neuroanatomical data	http://www.blueprintinpatlas.org/	[292]
	Virtual Fly Brain (<i>Drosophila melanogaster</i>)	Neural anatomy and imaging data	http://www.virtualflybrain.org/	[292]

11. Conclusions

Imaging is becoming an increasingly important tool in research and clinical care. A range of imaging techniques now provides unprecedented capacity to visualize the structure of the brain, including the vasculature, from the level of individual molecules and encompassing the whole brain. Most imaging methods are noninvasive and allow monitoring dynamic processes over time. Imaging enables researchers to identify brain vascular abnormalities, understand disease pathways, evaluate blood-brain barrier (BBB) integrity, recognize and diagnose pathologies and determine efficacy of different therapies and treatments. Each technique has strengths and weaknesses relating to cost, availability, temporal and spatial resolution and risk factors, thus improving our knowledge and ensuring the innovation of such tools will be beneficial in the near future.

The imaging techniques described in this review, alone and in combination, contribute to transforming and improving our understanding of how the brain functions in health and disease.

Acknowledgments: I acknowledge Christer Betsholtz for scientific support and Jennifer Hofmann for textual suggestions and corrections. Bárbara Laviña was supported by the Spanish Ministry of Education through a Fundación Española para la ciencia y la tecnología (FECYT) grant, via the postdoctoral mobility contract EDU/2934/2009.

Conflicts of Interest: The author declares no conflict of interest.

Abbreviations

BCE	Before Common Era
CNS	central nervous system
CT	computed tomography
MRI	magnetic resonance imaging
PET	positron emission tomography
SPECT	single photon emission computed tomography
CTA	computed tomography angiography
MicroCT	micro-computed tomography
NanoCT	nano-computed tomography
CCM	cerebral cavernous malformations
QSM	quantitative susceptibility mapping
STI	susceptibility tensor imaging
SWI	susceptibility-weighted imaging
4D	four-dimensional
IVW	intracranial vessel wall imaging
PAI	photoacoustic imaging
PAT	photoacoustic tomography
3D	three-dimensional
2D	two-dimensional
EC	endothelial cells
LEC	lymphatic endothelial cells
MRBTI	magnetic resonance black-blood thrombus imaging technique
NVU	neurovascular unit
DCE-MRI	dynamic contrast-enhanced MRI
BBB	blood-brain barrier
CBV	cerebral blood volume
TCD	transcranial doppler
PC-MRI	phase contrast MRI
MRA	magnetic resonance angiography
DSA	digital subtraction angiography
DWI	diffusion weighted MRI
PWI	perfusion weighted MRI
EGFP	Enhanced green fluorescent protein

References

1. Breasted, J.H. (Ed.) *The Edwin Smith Surgical Papyrus. Published in Faesimile and Hieroglyphie Transliteration, with Translation and Commentary*; The Univesity of Chicago Press: Chicago, IL, USA, 1930.
2. Wickens, A.P. *A History of the Brain: From Stone Age surgery to Modern Neuroscience*; Psychology Press: London, UK; New York, NY, USA, 2015; p. 27.
3. Aird, W.C. Discovery of the cardiovascular system: From Galen to William Harvey. *J. Thromb. Haemost.* **2011**, *9*, 118–129. [CrossRef] [PubMed]
4. Numan, M.T. Ibn Al Nafis: His seminal contributions to cardiology. *Pediatr. Cardiol.* **2014**, *35*, 1088–1090. [CrossRef] [PubMed]
5. O'Connor, J.P.B. Thomas Willis and the background to Cerebri Anatome. *J. R. Soc. Med.* **2003**, *96*, 139–143. [CrossRef] [PubMed]
6. Eadie, M.J. A pathology of the animal spirits—The clinical neurology of Thomas Willis (1621–1675) part I—Background, and disorders of intrinsically normal animal spirits. *J. Clin. Neurosci.* **2003**, *10*, 14–29. [CrossRef]
7. Sandrone, S.; Bacigaluppi, M.; Galloni, M.R.; Cappa, S.F.; Moro, A.; Catani, M.; Filippi, M.; Monti, M.M.; Perani, D.; Martino, G. Weighing brain activity with the balance: Angelo Mosso's original manuscripts come to light. *Brain* **2014**, *137*. [CrossRef] [PubMed]
8. Weber, A.L. History of head and neck radiology: Past, present, and future. *Radiology* **2001**, *218*, 15–24. [CrossRef] [PubMed]
9. Antunes, J.L. Egas Moniz and cerebral angiography. *J. Neurosurg.* **1974**, *40*, 427–432. [CrossRef] [PubMed]
10. Zimmer, L.; Luxen, A. PET radiotracers for molecular imaging in the brain: Past, present and future. *Neuroimage* **2012**, *61*, 363–370. [CrossRef] [PubMed]
11. Petrik, V.; Apok, V.; Britton, J.A.; Bell, B.A.; Papadopoulos, M.C. Godfrey Hounsfield and the dawn of computed tomography. *Neurosurgery* **2006**, *58*, 780–787. [CrossRef] [PubMed]
12. Runge, V.M.; Aoki, S.; Bradley, W.G.; Chang, K.-H.; Essig, M.; Ma, L.; Ross, J.S.; Valavanis, A. Magnetic Resonance Imaging and Computed Tomography of the Brain—50 Years of Innovation, With a Focus on the Future. *Investig. Radiol.* **2015**, *50*, 551–556. [CrossRef] [PubMed]
13. Lell, M.M.; Wildberger, J.E.; Alkadhi, H.; Damilakis, J.; Kachelriess, M. Evolution in Computed Tomography: The Battle for Speed and Dose. *Investig. Radiol.* **2015**, *50*, 629–644. [CrossRef] [PubMed]
14. Kamalian, S.; Lev, M.H.; Gupta, R. Computed tomography imaging and angiography—Principles. *Handb. Clin. Neurol.* **2016**, *135*, 3–20. [PubMed]
15. Fleischmann, D.; Chin, A.S.; Molvin, L.; Wang, J.; Hallett, R. Computed Tomography Angiography: A Review and Technical Update. *Radiol. Clin. N. Am.* **2016**, *54*, 1–12. [CrossRef] [PubMed]
16. Thierfelder, K.M.; Havla, L.; Beyer, S.E.; Ertl-Wagner, B.; Meinel, F.G.; von Baumgarten, L.; Janssen, H.; Ditt, H.; Reiser, M.F.; Sommer, W.H. Color-coded cerebral computed tomographic angiography: Implementation of a convolution-based algorithm and first clinical evaluation in patients with acute ischemic stroke. *Investig. Radiol.* **2015**, *50*, 361–365. [CrossRef] [PubMed]
17. Schambach, S.J.; Bag, S.; Schilling, L.; Groden, C.; Brockmann, M.A. Application of micro-CT in small animal imaging. *Methods* **2010**, *50*, 2–13. [CrossRef] [PubMed]
18. Clark, D.P.; Badea, C.T. Micro-CT of rodents: State-of-the-art and future perspectives. *Phys. Med.* **2014**, *30*, 619–634. [CrossRef] [PubMed]
19. Kampschulte, M.; Langheinrich, A.C.; Sender, J.; Litzbauer, H.D.; Althöhn, U.; Schwab, J.D.; Alejandre-Lafont, E.; Martels, G.; Krombach, G.A. Nano-Computed Tomography: Technique and Applications. In *RöFo-Fortschritte auf dem Gebiet der Röntgenstrahlen und der bildgebenden Verfahren*; Georg Thieme Verlag KG: Stuttgart, Germany, 2016; Volume 188, pp. 146–154.
20. Dorr, A.; Sled, J.G.; Kabani, N. Three-dimensional cerebral vasculature of the CBA mouse brain: A magnetic resonance imaging and micro computed tomography study. *Neuroimage* **2007**, *35*, 1409–1423. [CrossRef] [PubMed]
21. Schambach, S.J.; Bag, S.; Groden, C.; Schilling, L.; Brockmann, M.A. Vascular imaging in small rodents using micro-CT. *Methods* **2010**, *50*, 26–35. [CrossRef] [PubMed]

22. Starosolski, Z.; Villamizar, C.A.; Rendon, D.; Paldino, M.J.; Milewicz, D.M.; Ghaghada, K.B.; Annapragada, A.V. Ultra High-Resolution In vivo Computed Tomography Imaging of Mouse Cerebrovasculature Using a Long Circulating Blood Pool Contrast Agent. *Sci. Rep.* **2015**, *5*, 10178. [CrossRef] [PubMed]
23. Ghanavati, S.; Yu, L.X.; Lerch, J.P.; Sled, J.G. A perfusion procedure for imaging of the mouse cerebral vasculature by X-ray micro-CT. *J. Neurosci. Methods* **2014**, *221*, 70–77. [CrossRef] [PubMed]
24. Mancini, M.; Greco, A.; Tedeschi, E.; Palma, G.; Ragucci, M.; Bruzzone, M.G.; Coda, A.R.D.; Torino, E.; Scotti, A.; Zucca, I.; et al. Head and Neck Veins of the Mouse. A Magnetic Resonance, Micro Computed Tomography and High Frequency Color Doppler Ultrasound Study. *PLoS ONE* **2015**, *10*, e0129912.
25. Chugh, B.P.; Lerch, J.P.; Yu, L.X.; Pienkowski, M.; Harrison, R.V.; Henkelman, R.M.; Sled, J.G. Measurement of cerebral blood volume in mouse brain regions using micro-computed tomography. *Neuroimage* **2009**, *47*, 1312–1318. [CrossRef] [PubMed]
26. Anderson, R.; Maga, A.M. A Novel Procedure for Rapid Imaging of Adult Mouse Brains with MicroCT Using Iodine-Based Contrast. *PLoS ONE* **2015**, *10*, e0142974. [CrossRef] [PubMed]
27. Girard, R.; Zeineddine, H.A.; Orsbon, C.; Tan, H.; Moore, T.; Hobson, N.; Shenkar, R.; Lightle, R.; Shi, C.; Fam, M.D.; et al. Micro-computed tomography in murine models of cerebral cavernous malformations as a paradigm for brain disease. *J. Neurosci. Methods* **2016**, *271*, 14–24. [CrossRef] [PubMed]
28. Kirschner, S.; Felix, M.C.; Hartmann, L.; Bierbaum, M.; Maros, M.E.; Kerl, H.U.; Wenz, F.; Glatting, G.; Kramer, M.; Giordano, F.A.; et al. In vivo micro-CT imaging of untreated and irradiated orthotopic glioblastoma xenografts in mice: Capabilities, limitations and a comparison with bioluminescence imaging. *J. Neurooncol.* **2015**, *122*, 245–254. [CrossRef] [PubMed]
29. Wintermark, M.; Sincic, R.; Sridhar, D.; Chien, J.D. Cerebral perfusion CT: Technique and clinical applications. *J. Neuroradiol.* **2008**, *35*, 253–260. [CrossRef] [PubMed]
30. Lin, L.; Bivard, A.; Krishnamurthy, V.; Levi, C.R.; Parsons, M.W. Whole-Brain CT Perfusion to Quantify Acute Ischemic Penumbra and Core. *Radiology* **2016**, *279*, 876–887. [CrossRef] [PubMed]
31. Wintermark, M.; Chioléro, R.; van Melle, G.; Revelly, J.P.; Porchet, F.; Regli, L.; Meuli, R.; Schnyder, P.; Maeder, P. Relationship between brain perfusion computed tomography variables and cerebral perfusion pressure in severe head trauma patients. *Crit. Care Med.* **2004**, *32*, 1579–1587. [CrossRef] [PubMed]
32. Jain, R. Perfusion CT imaging of brain tumors: An overview. *Am. J. Neuroradiol.* **2011**, *32*, 1570–1577. [CrossRef] [PubMed]
33. Wintermark, M.; Reichhart, M.; Cuisenaire, O.; Maeder, P.; Thiran, J.-P.; Schnyder, P.; Bogousslavsky, J.; Meuli, R. Comparison of admission perfusion computed tomography and qualitative diffusion- and perfusion-weighted magnetic resonance imaging in acute stroke patients. *Stroke* **2002**, *33*, 2025–2031. [CrossRef] [PubMed]
34. Wintermark, M.; Meuli, R.; Browaeys, P.; Reichhart, M.; Bogousslavsky, J.; Schnyder, P.; Michel, P. Comparison of CT perfusion and angiography and MRI in selecting stroke patients for acute treatment. *Neurology* **2007**, *68*, 694–697. [CrossRef] [PubMed]
35. Hacke, W.; Furlan, A.J.; Al-Rawi, Y.; Davalos, A.; Fiebach, J.B.; Gruber, F.; Kaste, M.; Lipka, L.J.; Pedraza, S.; Ringleb, P.A.; et al. Intravenous desmoteplase in patients with acute ischaemic stroke selected by MRI perfusion-diffusion weighted imaging or perfusion CT (DIAS-2): A prospective, randomised, double-blind, placebo-controlled study. *Lancet Neurol.* **2009**, *8*, 141–150. [CrossRef]
36. Yeung, T.P.C.; Wang, Y.; He, W.; Urbini, B.; Gafà, R.; Ulazzi, L.; Yartsev, S.; Bauman, G.; Lee, T.Y.; Fainardi, E.; et al. Survival prediction in high-grade gliomas using CT perfusion imaging. *J. Neurooncol.* **2015**, *123*, 93–102. [CrossRef] [PubMed]
37. Phelps, M.E. PET: The merging of biology and imaging into molecular imaging. *J. Nucl. Med.* **2000**, *41*, 661–681. [PubMed]
38. Lameka, K.; Farwell, M.D.; Ichise, M. Positron Emission Tomography. *Handb. Clin. Neurol.* **2016**, *135*, 209–227.
39. Nutt, R. 1999 ICP Distinguished Scientist Award. The history of positron emission tomography. *Mol. Imaging Biol.* **2002**, *4*, 11–26. [PubMed]
40. Otte, A.; Halsband, U. Brain imaging tools in neurosciences. *J. Physiol.* **2006**, *99*, 281–292. [CrossRef] [PubMed]
41. Wagner, H.N., Jr. A brief history of positron emission tomography (PET). *Semin. Nucl. Med.* **1998**, *28*, 213–220. [CrossRef]

42. Ingvar, M.; Eriksson, L.; Rogers, G.A.; Stone-Elander, S.; Widén, L. Rapid feasibility studies of tracers for positron emission tomography: High-resolution PET in small animals with kinetic analysis. *J. Cereb. Blood Flow Metab.* **1991**, *11*, 926–931. [CrossRef]
43. Bloomfield, P.M.; Rajeswaran, S.; Spinks, T.J.; Hume, S.P.; Myers, R.; Ashworth, S.; Clifford, K.M.; Jones, W.F.; Byars, L.G.; Young, J.; et al. The design and physical characteristics of a small animal positron emission tomograph. *Phys. Med. Biol.* **1995**, *40*, 1105–1126. [CrossRef] [PubMed]
44. Yang, Y.; Bec, J.; Zhou, J.; Zhang, M.; Judenhofer, M.S.; Bai, X.; Di, K.; Wu, Y.; Rodriguez, M.; Dokhale, P.; et al. A Prototype High-Resolution Small-Animal PET Scanner Dedicated to Mouse Brain Imaging. *J. Nucl. Med.* **2016**, *57*, 1130–1135. [CrossRef] [PubMed]
45. Herzog, H.; Lerche, C. Advances in Clinical PET/MRI Instrumentation. *PET Clin.* **2016**, *11*, 95–103. [CrossRef] [PubMed]
46. Cabello, J.; Ziegler, S.I. Advances in PET/MR instrumentation and image reconstruction. *Br. J. Radiol.* **2016**, *89*. [CrossRef] [PubMed]
47. Salmon, E.; Ir, C.B.; Hustinx, R. Pitfalls and Limitations of PET/CT in Brain Imaging. *Semin. Nucl. Med.* **2015**, *45*, 541–551. [CrossRef] [PubMed]
48. Townsend, D.W. Positron emission tomography/computed tomography. *Semin. Nucl. Med.* **2008**, *38*, 152–166. [CrossRef] [PubMed]
49. De Galiza Barbosa, F.; Delso, G.; Voert Ter, E.E.G.W.; Huellner, M.W.; Herrmann, K.; Veit-Haibach, P. Multi-technique hybrid imaging in PET/CT and PET/MR: What does the future hold? *Clin. Radiol.* **2016**, *71*, 660–672. [CrossRef] [PubMed]
50. Schöder, H.; Erdi, Y.E.; Larson, S.M.; Yeung, H.W.D. PET/CT: A new imaging technology in nuclear medicine. *Eur. J. Nucl. Med. Mol. Imaging* **2003**, *30*, 1419–1437. [CrossRef] [PubMed]
51. Ell, P.J. The contribution of PET/CT to improved patient management. *Br. J. Radiol.* **2006**, *79*, 32–36. [CrossRef] [PubMed]
52. Alessio, A.M.; Kinahan, P.E.; Cheng, P.M.; Vesselle, H.; Karp, J.S. PET/CT scanner instrumentation, challenges, and solutions. *Radiol. Clin. N. Am.* **2004**, *42*, 1017–1032. [CrossRef] [PubMed]
53. Jadvar, H.; Colletti, P.M. Competitive advantage of PET/MRI. *Eur. J. Radiol.* **2014**, *83*, 84–94. [CrossRef] [PubMed]
54. Gaertner, F.C.; Fürst, S.; Schwaiger, M. PET/MR: A paradigm shift. *Cancer Imaging* **2013**, *13*, 36–52. [CrossRef]
55. Tsoumpas, C.; Visvikis, D.; Loudos, G. Innovations in Small-Animal PET/MR Imaging Instrumentation. *PET Clin.* **2016**, *11*, 105–118. [CrossRef] [PubMed]
56. Garrigue, P.; Giacominio, L.; Bucci, C.; Muzio, V.; Filannino, M.A.; Sabatier, F.; Dignat-George, F.; Pisano, P.; Guillet, B. Single photon emission computed tomography imaging of cerebral blood flow, blood-brain barrier disruption, and apoptosis time course after focal cerebral ischemia in rats. *Int. J. Stroke* **2016**, *11*, 117–126. [CrossRef] [PubMed]
57. Sánchez, F.; Orero, A.; Soriano, A.; Correcher, C.; Conde, P.; González, A.; Hernández, L.; Moliner, L.; Rodríguez-Alvarez, M.J.; Vidal, L.F.; et al. ALBIRA: A small animal PET/SPECT/CT imaging system. *Med. Phys.* **2013**, *40*, 051906. [CrossRef] [PubMed]
58. Balsara, R.D.; Chapman, S.E.; Sander, I.M.; Donahue, D.L.; Liepert, L.; Castellino, F.J.; Leevy, W.M. Non-invasive imaging and analysis of cerebral ischemia in living rats using positron emission tomography with 18F-FDG. *J. Vis. Exp.* **2014**. [CrossRef] [PubMed]
59. Goffin, K.; van Laere, K. Single-photon emission tomography. *Handb. Clin. Neurol.* **2016**, *135*, 241–250. [PubMed]
60. Szigeti, K.; Horváth, I.; Veres, D.S.; Martinecz, B.; Lénárt, N.; Kovács, N.; Bakcsa, E.; Márta, A.; Semjéni, M.; Máthé, D.; et al. A novel SPECT-based approach reveals early mechanisms of central and peripheral inflammation after cerebral ischemia. *J. Cereb. Blood Flow Metab.* **2015**, *35*, 1921–1929. [CrossRef] [PubMed]
61. Lu, F.-M.; Yuan, Z. PET/SPECT molecular imaging in clinical neuroscience: Recent advances in the investigation of CNS diseases. *Quant. Imaging Med. Surg.* **2015**, *5*, 433–447. [PubMed]
62. Baskin, A.; Buchegger, F.; Seimbille, Y.; Ratib, O.; Garibotto, V. PET Molecular Imaging of Hypoxia in Ischemic Stroke: An Update. *Curr. Vasc. Pharmacol.* **2015**, *13*, 209–217. [CrossRef] [PubMed]

63. Kim, S.; Lee, S.; Kim, J.B.; Na, J.O.; Choi, C.U.; Lim, H.-E.; Rha, S.W.; Park, C.G.; Oh, D.J.; Yoo, H.; et al. Concurrent Carotid Inflammation in Acute Coronary Syndrome as Assessed by (18)F-FDG PET/CT: A Possible Mechanistic Link for Ischemic Stroke. *J. Stroke Cerebrovasc. Dis.* **2015**, *24*, 2547–2554. [CrossRef] [PubMed]
64. Heiss, W.-D. PET imaging in ischemic cerebrovascular disease: Current status and future directions. *Neurosci. Bull.* **2014**, *30*, 713–732. [CrossRef] [PubMed]
65. Moraga, A.; Gómez-Vallejo, V.; Cuartero, M.I.; Szczupak, B.; San Sebastián, E.; Markuerkiaga, I.; Pradillo, J.M.; Higuchi, M.; Llop, J.; Moro, M.Á.; et al. Imaging the role of toll-like receptor 4 on cell proliferation and inflammation after cerebral ischemia by positron emission tomography. *J. Cereb. Blood Flow Metab.* **2016**, *36*, 702–708. [CrossRef]
66. Sahathevan, R.; Linden, T.; Villemagne, V.L.; Churilov, L.; Ly, J.V.; Rowe, C.; Donnan, G.; Brodtmann, A. Positron Emission Tomographic Imaging in Stroke: Cross-Sectional and Follow-Up Assessment of Amyloid in Ischemic Stroke. *Stroke* **2016**, *47*, 113–119. [CrossRef] [PubMed]
67. Cai, W.; Guzman, R.; Hsu, A.R.; Wang, H.; Chen, K.; Sun, G.; Gera, A.; Choi, R.; Bliss, T.; He, L.; et al. Positron emission tomography imaging of poststroke angiogenesis. *Stroke* **2009**, *40*, 270–277. [CrossRef] [PubMed]
68. Glaudemans, A.W.; Enting, R.H.; Heesters, M.A.; Dierckx, R.A.; van Rheenen, R.W.; Walenkamp, A.M.; Slart, R.H. Value of ¹¹C-methionine PET in imaging brain tumours and metastases. *Eur. J. Nucl. Med. Mol. Imaging* **2013**, *40*, 615–635. [CrossRef] [PubMed]
69. Singhal, T.; Narayanan, T.K.; Jacobs, M.P.; Bal, C.; Mantil, J.C. ¹¹C-methionine PET for grading and prognostication in gliomas: A comparison study with ¹⁸F-FDG PET and contrast enhancement on MRI. *J. Nucl. Med.* **2012**, *53*, 1709–1715. [CrossRef] [PubMed]
70. Ay, I.; Blasi, F.; Rietz, T.A.; Rotile, N.J.; Kura, S.; Brownell, A.L.; Day, H.; Oliveira, B.L.; Looby, R.J.; Caravan, P. In vivo molecular imaging of thrombosis and thrombolysis using a fibrin-binding positron emission tomographic probe. *Circ. Cardiovasc. Imaging* **2014**, *7*, 697–705. [CrossRef] [PubMed]
71. Montagne, A.; Nation, D.A.; Pa, J.; Sweeney, M.D.; Toga, A.W.; Zlokovic, B.V. Brain imaging of neurovascular dysfunction in Alzheimer's disease. *Acta Neuropathol.* **2016**, *131*, 687–707. [CrossRef] [PubMed]
72. Han, J.-H.; Park, Y.S.; Lee, W.H.; Koong, S.-S.; Min, K.-S.; Lee, M.-S.; Kim, Y.G.; Kim, D.H.; Yi, K.S.; Cha, S.H. Cerebral-perfusion-based single-photon emission computed tomography (SPECT) staging using NeuroGam® in patients with moyamoya disease. *Child's Nerv. Syst.* **2016**, *32*, 1471–1477. [CrossRef] [PubMed]
73. Lauterbur, P.C. Image formation by induced local interactions: Examples employing nuclear magnetic resonance. *Nature* **1973**. [CrossRef]
74. Lauterbur, P.C. Magnetic resonance zeugmatography. *Pure Appl. Chem.* **1974**, *40*, 149–157. [CrossRef]
75. Mansfield, P.; Maudsley, A.A. Medical imaging by NMR. *Br. J. Radiol.* **1977**, *50*, 188–194. [CrossRef] [PubMed]
76. Hollingsworth, K.G. Reducing acquisition time in clinical MRI by data undersampling and compressed sensing reconstruction. *Phys. Med. Biol.* **2015**, *60*, R297–R322. [CrossRef] [PubMed]
77. Feinberg, D.A.; Setsompop, K. Ultra-fast MRI of the human brain with simultaneous multi-slice imaging. *J. Magn. Reson.* **2013**, *229*, 90–100. [CrossRef] [PubMed]
78. Pooley, R.A. AAPM/RSNA physics tutorial for residents: Fundamental physics of MR imaging. *Radiographics* **2005**, *25*, 1087–1099. [CrossRef] [PubMed]
79. Lohrke, J.; Frenzel, T.; Endrikat, J.; Alves, F.C.; Grist, T.M.; Law, M.; Lee, J.M.; Leiner, T.; Li, K.C.; Nikolaou, K.; et al. 25 Years of Contrast-Enhanced MRI: Developments, Current Challenges and Future Perspectives. *Adv. Ther.* **2016**, *33*, 1–28. [CrossRef] [PubMed]
80. MacDonald, M.E.; Frayne, R. Cerebrovascular MRI: A review of state-of-the-art approaches, methods and techniques. *NMR Biomed.* **2015**, *28*, 767–791. [CrossRef] [PubMed]
81. Donahue, M.J.; Strother, M.K.; Hendrikse, J. Novel MRI approaches for assessing cerebral hemodynamics in ischemic cerebrovascular disease. *Stroke* **2012**, *43*, 903–915. [CrossRef] [PubMed]
82. Harteveld, A.A.; van der Kolk, A.G.; Zwanenburg, J.J.M.; Luijten, P.R.; Hendrikse, J. 7-T MRI in Cerebrovascular Diseases: Challenges to Overcome and Initial Results. *Top. Magn. Reson. Imaging* **2016**, *25*, 89–100. [PubMed]
83. Macintosh, B.J.; Graham, S.J. Magnetic resonance imaging to visualize stroke and characterize stroke recovery: A review. *Front. Neurol.* **2013**, *4*. [CrossRef] [PubMed]
84. Biomarkers Definitions Working Group. Biomarkers and surrogate endpoints: Preferred definitions and conceptual framework. *Clin. Pharmacol. Ther.* **2001**, *69*, 89–95.

85. Kidwell, C.S. MRI biomarkers in acute ischemic stroke: A conceptual framework and historical analysis. *Stroke* **2013**, *44*, 570–578. [CrossRef] [PubMed]
86. O’Connor, J.P.B.; Jayson, G.C. Do imaging biomarkers relate to outcome in patients treated with VEGF inhibitors? *Clin. Cancer Res.* **2012**, *18*, 6588–6598. [CrossRef] [PubMed]
87. Emblem, K.E.; Farrar, C.T.; Gerstner, E.R.; Batchelor, T.T.; Borra, R.J.H.; Rosen, B.R.; Sorensen, A.G.; Jain, R.K. Vessel caliber—A potential MRI biomarker of tumour response in clinical trials. *Nat. Rev. Clin. Oncol.* **2014**, *11*, 566–584. [CrossRef] [PubMed]
88. Fantini, S.; Sassaroli, A.; Tgavalekos, K.T.; Kornbluth, J. Cerebral blood flow and autoregulation: Current measurement techniques and prospects for noninvasive optical methods. *Neurophotonics* **2016**, *3*, 031411. [CrossRef] [PubMed]
89. Chang, W.; Huang, M.; Chien, A. Emerging techniques for evaluation of the hemodynamics of intracranial vascular pathology. *Neuroradiol. J.* **2015**, *28*, 19–27. [CrossRef] [PubMed]
90. Markl, M.; Schnell, S.; Wu, C.; Bollache, E.; Jarvis, K.; Barker, A.J.; Robinson, J.D.; Rigsby, C.K. Advanced flow MRI: Emerging techniques and applications. *Clin. Radiol.* **2016**, *71*, 779–795. [CrossRef] [PubMed]
91. Schnell, S.; Wu, C.; Ansari, S.A. Four-dimensional MRI flow examinations in cerebral and extracerebral vessels - ready for clinical routine? *Curr. Opin. Neurol.* **2016**, *29*, 419–428. [CrossRef] [PubMed]
92. Turski, P.; Scarano, A.; Hartman, E.; Clark, Z.; Schubert, T.; Rivera, L.; Wu, Y.; Wieben, O.; Johnson, K. Neurovascular 4DFlow MRI (Phase Contrast MRA): Emerging clinical applications. *Neurovasc. Imaging* **2016**, *2*. [CrossRef]
93. Wählén, A.; Ambarki, K.; Hauksson, J.; Birgander, R.; Malm, J.; Eklund, A. Phase contrast MRI quantification of pulsatile volumes of brain arteries, veins, and cerebrospinal fluids compartments: Repeatability and physiological interactions. *J. Magn. Reson. Imaging* **2012**, *35*, 1055–1062. [CrossRef] [PubMed]
94. Neff, K.W.; Horn, P.; Schmiedek, P.; Düber, C.; Dinter, D.J. 2D Cine Phase-Contrast MRI for Volume Flow Evaluation of the Brain-Supplying Circulation in Moyamoya Disease. *Am. J. Roentgenol.* **2006**, *187*, W107–W115. [CrossRef] [PubMed]
95. Enzmann, D.R.; Ross, M.R.; Marks, M.P.; Pelc, N.J. Blood flow in major cerebral arteries measured by phase-contrast cine MR. *Am. J. Neuroradiol.* **1994**, *15*, 123–129. [PubMed]
96. Yang, Q.; Duan, J.; Fan, Z.; Qu, X.; Xie, Y.; Nguyen, C.; Du, X.; Bi, X.; Li, K.; Ji, X.; et al. Early Detection and Quantification of Cerebral Venous Thrombosis by Magnetic Resonance Black-Blood Thrombus Imaging. *Stroke* **2016**, *47*, 404–409. [CrossRef] [PubMed]
97. Luyopaert, R.; Boujraf, S.; Sourbron, S.; Osteaux, M. Diffusion and perfusion MRI: Basic physics. *Eur. J. Radiol.* **2001**, *38*, 19–27. [CrossRef]
98. Harris, A.D.; Coutts, S.B.; Frayne, R. Diffusion and perfusion MR imaging of acute ischemic stroke. *Magn. Reson. Imaging Clin. N. Am.* **2009**, *17*, 291–313. [CrossRef] [PubMed]
99. Kawada, T. Re: Diagnostic performance of PWI/DWI MRI parameters in discriminating hyper-acute versus acute ischaemic stroke: Finding the best thresholds. *Clin. Radiol.* **2012**, *67*, 1218. [CrossRef] [PubMed]
100. Svolos, P.; Kousi, E.; Kapsalaki, E.; Theodorou, K.; Fezoulidis, I.; Kappas, C.; Tsougos, I. The role of diffusion and perfusion weighted imaging in the differential diagnosis of cerebral tumors: A review and future perspectives. *Cancer Imaging* **2014**, *14*. [CrossRef]
101. Bammer, R. Basic principles of diffusion-weighted imaging. *Eur. J. Radiol.* **2003**, *45*, 169–184. [CrossRef]
102. Hagmann, P.; Jonasson, L.; Maeder, P.; Thiran, J.-P.; Wedeen, V.J.; Meuli, R. Understanding diffusion MR imaging techniques: From scalar diffusion-weighted imaging to diffusion tensor imaging and beyond. *Radiographics* **2006**, *26*, S205–S223. [CrossRef] [PubMed]
103. Van Everdingen, K.J.; van der Grond, J.; Kappelle, L.J.; Ramos, L.M.; Mali, W.P. Diffusion-weighted magnetic resonance imaging in acute stroke. *Stroke* **1998**, *29*, 1783–1790. [CrossRef] [PubMed]
104. Redgrave, J.N.E.; Coutts, S.B.; Schulz, U.G.; Briley, D.; Rothwell, P.M. Systematic review of associations between the presence of acute ischemic lesions on diffusion-weighted imaging and clinical predictors of early stroke risk after transient ischemic attack. *Stroke* **2007**, *38*, 1482–1488. [CrossRef] [PubMed]
105. Mascalchi, M.; Filippi, M.; Floris, R.; Fonda, C.; Gasparotti, R.; Villari, N. Diffusion-weighted MR of the brain: Methodology and clinical application. *Radiol. Med.* **2005**, *109*, 155–197. [PubMed]
106. Copen, W.A.; Schaefer, P.W.; Wu, O. MR perfusion imaging in acute ischemic stroke. *Neuroimaging Clin. N. Am.* **2011**, *21*, 259–283. [CrossRef] [PubMed]

107. Lacerda, S.; Law, M. Magnetic resonance perfusion and permeability imaging in brain tumors. *Neuroimaging Clin. N. Am.* **2009**, *19*, 527–557. [CrossRef] [PubMed]
108. Jackson, A.; O'Connor, J.; Thompson, G.; Mills, S. Magnetic resonance perfusion imaging in neuro-oncology. *Cancer Imaging* **2008**, *8*, 186–199. [CrossRef] [PubMed]
109. Law, M.; Young, R.J.; Babb, J.S.; Peccerelli, N.; Cheang, S.; Gruber, M.L.; Miller, D.C.; Golfinos, J.G.; Zagzag, D.; Johnson, G. Gliomas: Predicting time to progression or survival with cerebral blood volume measurements at dynamic susceptibility-weighted contrast-enhanced perfusion MR imaging. *Radiology* **2008**, *247*, 490–498. [CrossRef] [PubMed]
110. Choi, S.H.; Jung, S.C.; Kim, K.W.; Lee, J.Y.; Choi, Y.; Park, S.H.; Kim, H.S. Perfusion MRI as the predictive/prognostic and pharmacodynamic biomarkers in recurrent malignant glioma treated with bevacizumab: A systematic review and a time-to-event meta-analysis. *J. Neurooncol.* **2016**, *128*, 185–194. [CrossRef] [PubMed]
111. Liu, C.; Li, W.; Tong, K.A.; Yeom, K.W.; Kuzminski, S. Susceptibility-weighted imaging and quantitative susceptibility mapping in the brain. *J. Magn. Reson. Imaging* **2015**, *42*, 23–41. [CrossRef] [PubMed]
112. Liu, S.; Buch, S.; Chen, Y.; Choi, H.-S.; Dai, Y.; Habib, C.; Hu, J.; Jung, J.Y.; Luo, Y.; Utriainen, D.; et al. Susceptibility-weighted imaging: Current status and future directions. *NMR Biomed.* **2016**. [CrossRef] [PubMed]
113. Heyn, C.; Alcaide-Leon, P.; Bharatha, A.; Sussman, M.S.; Kucharczyk, W.; Mandell, D.M. Susceptibility-weighted Imaging in Neurovascular Disease. *Top. Magn. Reson. Imaging* **2016**, *25*, 63–71. [PubMed]
114. Di Ieva, A.; Lam, T.; Alcaide-Leon, P.; Bharatha, A.; Montanera, W.; Cusimano, M.D. Magnetic resonance susceptibility weighted imaging in neurosurgery: Current applications and future perspectives. *J. Neurosurg.* **2015**, *123*, 1463–1475. [CrossRef] [PubMed]
115. Deistung, A.; Schweser, F.; Reichenbach, J.R. Overview of quantitative susceptibility mapping. *NMR Biomed.* **2016**. [CrossRef] [PubMed]
116. Li, W.; Liu, C.; Duong, T.Q.; van Zijl, P.C.M.; Li, X. Susceptibility tensor imaging (STI) of the brain. *NMR Biomed.* **2016**. [CrossRef] [PubMed]
117. Reichenbach, J.R.; Schweser, F.; Serres, B.; Deistung, A. Quantitative Susceptibility Mapping: Concepts and Applications. *Clin. Neuroradiol.* **2015**, *25*, 225–230. [CrossRef] [PubMed]
118. Mikati, A.G.; Tan, H.; Shenkar, R.; Li, L.; Zhang, L.; Guo, X.; Larsson, H.B.; Shi, C.; Liu, T.; Wang, Y.; et al. Dynamic permeability and quantitative susceptibility: Related imaging biomarkers in cerebral cavernous malformations. *Stroke* **2014**, *45*, 598–601. [CrossRef] [PubMed]
119. Tan, H.; Liu, T.; Wu, Y.; Thacker, J.; Shenkar, R.; Mikati, A.G.; Shi, C.; Dykstra, C.; Wang, Y.; Prasad, P.V.; et al. Evaluation of iron content in human cerebral cavernous malformation using quantitative susceptibility mapping. *Investig. Radiol.* **2014**, *49*, 498–504. [CrossRef] [PubMed]
120. Chang, S.; Zhang, J.; Liu, T.; Tsioris, A.J.; Shou, J.; Nguyen, T.; Leifer, D.; Wang, Y.; Kovarlikaya, I. Quantitative Susceptibility Mapping of Intracerebral Hemorrhages at Various Stages. *J. Magn. Reson. Imaging* **2016**, *44*, 420–425. [CrossRef] [PubMed]
121. Wang, S.; Lou, M.; Liu, T.; Cui, D.; Chen, X.; Wang, Y. Hematoma volume measurement in gradient echo MRI using quantitative susceptibility mapping. *Stroke* **2013**, *44*, 2315–2317. [CrossRef] [PubMed]
122. Chen, W.; Zhu, W.; Kovarlikaya, I.; Kovarlikaya, A.; Liu, T.; Wang, S.; Salustri, C.; Wang, Y. Intracranial calcifications and hemorrhages: Characterization with quantitative susceptibility mapping. *Radiology* **2014**, *270*, 496–505. [CrossRef] [PubMed]
123. Wei, H.; Xie, L.; Dibb, R.; Li, W.; Decker, K.; Zhang, Y.; Johnson, G.A.; Liu, C. Imaging whole-brain cytoarchitecture of mouse with MRI-based quantitative susceptibility mapping. *Neuroimage* **2016**, *137*, 107–115. [CrossRef] [PubMed]
124. Dieleman, N.; van der Kolk, A.G.; Zwanenburg, J.J.M.; Harreveld, A.A.; Biessels, G.J.; Luijten, P.R.; Hendrikse, J. Imaging intracranial vessel wall pathology with magnetic resonance imaging: Current prospects and future directions. *Circulation* **2014**, *130*, 192–201. [CrossRef] [PubMed]
125. Alexander, M.D.; Yuan, C.; Rutman, A.; Tirschwell, D.L.; Palagallo, G.; Gandhi, D.; Sekhar, L.N.; Mossa-Basha, M. High-resolution intracranial vessel wall imaging: Imaging beyond the lumen. *J. Neurol. Neurosurg. Psychiatr.* **2016**, *87*, 589–597. [CrossRef] [PubMed]

126. Mossa-Basha, M.; Alexander, M.; Gaddikeri, S.; Yuan, C.; Gandhi, D. Vessel wall imaging for intracranial vascular disease evaluation. *J. Neurointerv. Surg.* **2016**. [CrossRef] [PubMed]
127. De Havenon, A.; Chung, L.; Park, M.; Mossa-Basha, M. Intracranial vessel wall MRI: A review of current indications and future applications. *Neurovasc. Imaging* **2016**, *2*. [CrossRef]
128. Dieleman, N.; Yang, W.; Abrigo, J.M.; Chu, W.C.W.; van der Kolk, A.G.; Siero, J.C.W.; Wong, K.S.; Hendrikse, J.; Chen, X.Y. Magnetic Resonance Imaging of Plaque Morphology, Burden, and Distribution in Patients With Symptomatic Middle Cerebral Artery Stenosis. *Stroke* **2016**, *47*, 1797–1802. [CrossRef] [PubMed]
129. Jiang, Y.; Zhu, C.; Peng, W.; Degnan, A.J.; Chen, L.; Wang, X.; Liu, Q.; Wang, Y.; Xiang, Z.; Teng, Z.; et al. Ex Vivo imaging and plaque type classification of intracranial atherosclerotic plaque using high resolution MRI. *Atherosclerosis* **2016**, *249*, 10–16. [CrossRef] [PubMed]
130. Zhao, D.-L.; Deng, G.; Xie, B.; Ju, S.; Yang, M.; Chen, X.-H.; Teng, G.J. High-resolution MRI of the vessel wall in patients with symptomatic atherosclerotic stenosis of the middle cerebral artery. *J. Clin. Neurosci.* **2015**, *22*, 700–704. [CrossRef] [PubMed]
131. Mossa-Basha, M.; Hwang, W.D.; de Havenon, A.; Hippe, D.; Balu, N.; Becker, K.J.; Tirschwell, D.T.; Hatsukami, T.; Anzai, Y.; Yuan, C. Multicontrast high-resolution vessel wall magnetic resonance imaging and its value in differentiating intracranial vasculopathic processes. *Stroke* **2015**, *46*, 1567–1573. [CrossRef] [PubMed]
132. Zhu, X.-J.; Wang, W.; Liu, Z.-J. High-resolution Magnetic Resonance Vessel Wall Imaging for Intracranial Arterial Stenosis. *Chin. Med. J.* **2016**, *129*, 1363–1370. [PubMed]
133. Gounis, M.J.; van der Marel, K.; Marosfoi, M.; Mazzanti, M.L.; Clarençon, F.; Chueh, J.-Y.; Puri, A.S.; Bogdanov, A.A. Imaging Inflammation in Cerebrovascular Disease. *Stroke* **2015**, *46*, 2991–2997. [CrossRef] [PubMed]
134. Obusez, E.C.; Hui, F.; Hajj-Ali, R.A.; Cerejo, R.; Calabrese, L.H.; Hammad, T.; Jones, S.E. High-resolution MRI vessel wall imaging: Spatial and temporal patterns of reversible cerebral vasoconstriction syndrome and central nervous system vasculitis. *AJR Am. J. Neuroradiol.* **2014**, *35*, 1527–1532. [CrossRef] [PubMed]
135. Matouk, C.C.; Cord, B.J.; Yeung, J.; Malhotra, A.; Johnson, M.H.; Minja, F.J. High-resolution Vessel Wall Magnetic Resonance Imaging in Intracranial Aneurysms and Brain Arteriovenous Malformations. *Top. Magn. Reson. Imaging* **2016**, *25*, 49–55. [PubMed]
136. Yuan, M.; Liu, Z.-Q.; Wang, Z.-Q.; Li, B.; Xu, L.-J.; Xiao, X.-L. High-resolution MR imaging of the arterial wall in moyamoya disease. *Neurosci. Lett.* **2015**, *584*, 77–82. [CrossRef] [PubMed]
137. Ryoo, S.; Cha, J.; Kim, S.J.; Choi, J.W.; Ki, C.-S.; Kim, K.H.; Jeon, P.; Kim, J.S.; Hong, S.C.; Bang, O.Y. High-resolution magnetic resonance wall imaging findings of Moyamoya disease. *Stroke* **2014**, *45*, 2457–2460. [CrossRef] [PubMed]
138. Edjlali, M.; Gentric, J.-C.; Régent-Rodriguez, C.; Trystram, D.; Hassen, W.B.; Lion, S.; Nataf, F.; Raymond, J.; Wieben, O.; Turski, P.; et al. Does aneurysmal wall enhancement on vessel wall MRI help to distinguish stable from unstable intracranial aneurysms? *Stroke* **2014**, *45*, 3704–3706. [CrossRef] [PubMed]
139. Matouk, C.C.; Mandell, D.M.; Gunel, M.; Bulsara, K.R.; Malhotra, A.; Hebert, R.; Johnson, M.H.; Mikulis, D.J.; Minja, F.J. Vessel wall magnetic resonance imaging identifies the site of rupture in patients with multiple intracranial aneurysms: Proof of principle. *Neurosurgery* **2013**, *72*, 492–496. [CrossRef] [PubMed]
140. Nagahata, S.; Nagahata, M.; Obara, M.; Kondo, R.; Minagawa, N.; Sato, S.; Sato, S.; Mouri, W.; Saito, S.; Kayama, T. Wall Enhancement of the Intracranial Aneurysms Revealed by Magnetic Resonance Vessel Wall Imaging Using Three-Dimensional Turbo Spin-Echo Sequence with Motion-Sensitized Driven-Equilibrium: A Sign of Ruptured Aneurysm? *Clin. Neuroradiol.* **2016**, *26*, 277–283. [CrossRef] [PubMed]
141. Obusez, E.C.; Jones, S.E.; Hui, F. Vessel wall MRI for suspected isolated basilar artery dissection. *J. Clin. Neurosci.* **2016**, *27*, 177–179. [CrossRef] [PubMed]
142. Ghoshhajra, B.; Engel, L.-C.; Gregory, T. MR Angiography. In *Magnetic Resonance Angiography Basics to Future*; InTech: Boston, MA, USA, 2012.
143. Ozsarlak, O.; van Goethem, J.W.; Maes, M.; Parizel, P.M. MR angiography of the intracranial vessels: Technical aspects and clinical applications. *Neuroradiology* **2004**, *46*, 955–972. [CrossRef] [PubMed]
144. Prince, M.R. Gadolinium-enhanced MR aortography. *Radiology* **1994**, *191*, 155–164. [CrossRef] [PubMed]
145. Riederer, S.J.; Haider, C.R.; Borisch, E.A.; Weavers, P.T.; Young, P.M. Recent advances in 3D time-resolved contrast-enhanced MR angiography. *J. Magn. Reson. Imaging* **2015**, *42*, 3–22. [CrossRef] [PubMed]

146. Nielsen, Y.W.; Thomsen, H.S. Contrast-enhanced peripheral MRA: Technique and contrast agents. *Acta Radiol.* **2012**, *53*, 769–777. [CrossRef] [PubMed]
147. Marchal, G.; Michiels, J.; Bosmans, H.; van Hecke, P. Contrast-enhanced MRA of the brain. *J. Comput. Assist. Tomogr.* **1992**, *16*, 25–29. [CrossRef] [PubMed]
148. Sohn, C.-H.; Sevick, R.J.; Frayne, R. Contrast-enhanced MR angiography of the intracranial circulation. *Magn. Reson. Imaging Clin. N. Am.* **2003**, *11*, 599–614. [CrossRef]
149. Anzalone, N.; Scotti, R.; Iadanza, A. MR angiography of the carotid arteries and intracranial circulation: Advantage of a high relaxivity contrast agent. *Neuroradiology* **2006**, *48*, 9–17. [CrossRef] [PubMed]
150. Miyazaki, M.; Lee, V.S. Nonenhanced MR angiography. *Radiology* **2008**, *248*, 20–43. [CrossRef] [PubMed]
151. Wheaton, A.J.; Miyazaki, M. Non-contrast enhanced MR angiography: Physical principles. *J. Magn. Reson. Imaging* **2012**, *36*, 286–304. [CrossRef] [PubMed]
152. Neumann, J.-O.; Giese, H.; Nagel, A.M.; Biller, A.; Unterberg, A.; Meinzer, H.-P. MR Angiography at 7T to Visualize Cerebrovascular Territories. *J. Neuroimaging* **2016**. [CrossRef] [PubMed]
153. Anzalone, N.; Tartaro, A. Intracranial MR Angiography. In *Magnetic Resonance Angiography*; Springer: Milan, Italy, 2005; pp. 103–138.
154. Bash, S.; Villablanca, J.P.; Jahan, R.; Duckwiler, G.; Tillis, M.; Kidwell, C.; Saver, J.; Sayre, J. Intracranial vascular stenosis and occlusive disease: Evaluation with CT angiography, MR angiography, and digital subtraction angiography. *Am. J. Neuroradiol.* **2005**, *26*, 1012–1021. [PubMed]
155. Cirillo, M.; Scomazzoni, F.; Cirillo, L.; Cadioli, M.; Simionato, F.; Iadanza, A.; Kirchin, M.; Righi, C.; Anzalone, N. Comparison of 3D TOF-MRA and 3D CE-MRA at 3T for imaging of intracranial aneurysms. *Eur. J. Radiol.* **2013**, *82*, e853–e859. [CrossRef] [PubMed]
156. Hadizadeh, D.R.; Falkenhausen von, M.; Gieseke, J.; Meyer, B.; Urbach, H.; Hoogeveen, R.; Schild, H.H.; Willinek, W.A. Cerebral arteriovenous malformation: Spetzler-Martin classification at subsecond-temporal-resolution four-dimensional MR angiography compared with that at DSA. *Radiology* **2008**, *246*, 205–213. [CrossRef] [PubMed]
157. Campeau, N.G.; Huston, J. Vascular disorders—magnetic resonance angiography: Brain vessels. *Neuroimaging Clin. N. Am.* **2012**, *22*, 207–233. [CrossRef] [PubMed]
158. Frayne, R.; Grist, T.M.; Swan, J.S.; Peters, D.C.; Korosec, F.R.; Mistretta, C.A. 3D MR DSA: Effects of injection protocol and image masking. *J. Magn. Reson. Imaging* **2000**, *12*, 476–487. [CrossRef]
159. Davis, B.; Royalty, K.; Kowarschik, M.; Rohkohl, C.; Oberstar, E.; Aagaard-Kienitz, B.; Niemann, D.; Ozkan, O.; Strother, C.; Mistretta, C. 4D digital subtraction angiography: Implementation and demonstration of feasibility. *AJNR Am. J. Neuroradiol.* **2013**, *34*, 1914–1921. [CrossRef] [PubMed]
160. Grist, T.M.; Mistretta, C.A.; Strother, C.M.; Turski, P.A. Time-resolved angiography: Past, present, and future. *J. Magn. Reson. Imaging* **2012**, *36*, 1273–1286. [CrossRef] [PubMed]
161. Mistretta, C.A.; Grist, T.M. X-ray digital subtraction angiography to magnetic resonance-digital subtraction angiography using three-dimensional TRICKS. Historical perspective and computer simulations: A review. *Investig. Radiol.* **1998**, *33*, 496–505. [CrossRef]
162. Harrington, D.P.; Boxt, L.M.; Murray, P.D. Digital subtraction angiography: Overview of technical principles. *Am. J. Roentgenol.* **1982**, *139*, 781–786. [CrossRef] [PubMed]
163. Stevens, J. Digital subtraction angiography. *Clin. Radiol.* **1989**, *40*, 325–326. [CrossRef]
164. Carmody, R.F.; Seeger, J.F. Intracranial applications of digital subtraction angiography. *Crit. Rev. Diagn. Imaging* **1984**, *23*, 1–40. [CrossRef] [PubMed]
165. Srinivasan, V.M.; Chintalapandi, G.; Duckworth, E.A.M.; Kan, P. Application of 4-Dimensional Digital Subtraction Angiography for Dural Arteriovenous Fistulas. *World Neurosurg.* **2016**, *96*, 24–30. [CrossRef] [PubMed]
166. Wong, S.C.; Nawawi, O.; Ramli, N.; Abd Kadir, K.A. Benefits of 3D rotational DSA compared with 2D DSA in the evaluation of intracranial aneurysm. *Acad. Radiol.* **2012**, *19*, 701–707. [CrossRef] [PubMed]
167. Herzig, R.; Burval, S.; Krupka, B.; Vlachová, I.; Urbánek, K.; Mares, J. Comparison of ultrasonography, CT angiography, and digital subtraction angiography in severe carotid stenoses. *Eur. J. Neurol.* **2004**, *11*, 774–781. [CrossRef] [PubMed]
168. Hung, S.-C.; Liang, M.-L.; Lin, C.-F.; Lin, C.-J.; Guo, W.-Y.; Chang, F.-C.; Wong, T.T.; Chang, C.Y. New grading of moyamoya disease using color-coded parametric quantitative digital subtraction angiography. *J. Chin. Med. Assoc.* **2014**, *77*, 437–442. [CrossRef] [PubMed]

169. Wen, W.-L.; Fang, Y.-B.; Yang, P.-F.; Zhang, Y.-W.; Wu, Y.-N.; Shen, H.; Ge, J.J.; Xu, Y.; Hong, B.; Huang, Q.H.; et al. Parametric Digital Subtraction Angiography Imaging for the Objective Grading of Collateral Flow in Acute Middle Cerebral Artery Occlusion. *World Neurosurg.* **2016**, *88*, 119–125. [CrossRef] [PubMed]
170. Aaslid, R.; Markwalder, T.M.; Nornes, H. Noninvasive transcranial Doppler ultrasound recording of flow velocity in basal cerebral arteries. *J. Neurosurg.* **1982**, *57*, 769–774. [CrossRef] [PubMed]
171. Naqvi, J.; Yap, K.H.; Ahmad, G.; Ghosh, J. Transcranial Doppler ultrasound: A review of the physical principles and major applications in critical care. *Int. J. Vasc. Med.* **2013**, *2013*, 629378. [CrossRef] [PubMed]
172. Topcuoglu, M.A. Transcranial Doppler ultrasound in neurovascular diseases: Diagnostic and therapeutic aspects. *J. Neurochem.* **2012**, *123*, 39–51. [CrossRef] [PubMed]
173. Bathala, L.; Mehndiratta, M.M.; Sharma, V.K. Transcranial doppler: Technique and common findings (Part 1). *Ann. Indian Acad. Neurol.* **2013**, *16*, 174–179. [CrossRef] [PubMed]
174. D’Andrea, A.; Conte, M.; Cavallaro, M.; Scarafili, R.; Riegler, L.; Cocchia, R.; Pezzullo, E.; Carbone, A.; Natale, F.; Santoro, G.; et al. Transcranial Doppler ultrasonography: From methodology to major clinical applications. *World J. Cardiol.* **2016**, *8*, 383–400. [CrossRef] [PubMed]
175. Sharma, A.K.; Bathala, L.; Batra, A.; Mehndiratta, M.M.; Sharma, V.K. Transcranial Doppler: Techniques and advanced applications: Part 2. *Ann. Indian Acad. Neurol.* **2016**, *19*, 102–107. [PubMed]
176. Zhang, Y.; Hong, H.; Cai, W. Photoacoustic imaging. *Cold Spring Harb. Protoc.* **2011**. [CrossRef] [PubMed]
177. Maugh, T.H. Photoacoustic spectroscopy: New uses for an old technique. *Science* **1975**, *188*, 38–39. [CrossRef] [PubMed]
178. Beard, P. Biomedical photoacoustic imaging. *Interface Focus* **2011**, *1*, 602–631. [CrossRef] [PubMed]
179. Li, C.; Wang, L.V. Photoacoustic tomography and sensing in biomedicine. *Phys. Med. Biol.* **2009**, *54*, R59–R97. [CrossRef] [PubMed]
180. Wang, L.V.; Gao, L. Photoacoustic microscopy and computed tomography: From bench to bedside. *Annu. Rev. Biomed. Eng.* **2014**, *16*, 155–185. [CrossRef] [PubMed]
181. Nie, L.; Chen, X. Structural and functional photoacoustic molecular tomography aided by emerging contrast agents. *Chem. Soc. Rev.* **2014**, *43*, 7132–7170. [CrossRef] [PubMed]
182. Wang, X.; Ku, G.; Wegiel, M.A.; Bornhop, D.J.; Stoica, G.; Wang, L.V. Noninvasive photoacoustic angiography of animal brains *in vivo* with near-infrared light and an optical contrast agent. *Opt. Lett.* **2004**, *29*, 730–732. [CrossRef] [PubMed]
183. Xu, H.; Li, Q.; Wang, L.; He, Y.; Shi, J.; Tang, B.; Fan, C. Nanoscale optical probes for cellular imaging. *Chem. Soc. Rev.* **2014**, *43*, 2650–2661. [CrossRef] [PubMed]
184. Wang, D.; Wu, Y.; Xia, J. Review on photoacoustic imaging of the brain using nanoprobes. *Neurophotonics* **2016**, *3*, 010901. [CrossRef] [PubMed]
185. Filonov, G.S.; Krumholz, A.; Xia, J.; Yao, J.; Wang, L.V.; Verkhusha, V.V. Deep-tissue photoacoustic tomography of a genetically encoded near-infrared fluorescent probe. *Angew. Chem. Int. Ed. Engl.* **2012**, *51*, 1448–1451. [CrossRef] [PubMed]
186. Paproski, R.J.; Heinmiller, A.; Wachowicz, K.; Zemp, R.J. Multi-wavelength photoacoustic imaging of inducible tyrosinase reporter gene expression in xenograft tumors. *Sci. Rep.* **2014**, *4*, 5329. [CrossRef] [PubMed]
187. Xia, J.; Yao, J.; Wang, L.V. Photoacoustic tomography: Principles and advances. *Electromagn. Waves* **2014**, *147*, 1–22. [CrossRef]
188. Wang, L.V.; Yao, J. A practical guide to photoacoustic tomography in the life sciences. *Nat. Methods* **2016**, *13*, 627–638. [CrossRef] [PubMed]
189. Zhou, Y.; Yao, J.; Wang, L.V. Tutorial on photoacoustic tomography. *J. Biomed. Opt.* **2016**, *21*. [CrossRef] [PubMed]
190. Wang, L.V.; Hu, S. Photoacoustic tomography: In vivo imaging from organelles to organs. *Science* **2012**, *335*, 1458–1462. [CrossRef] [PubMed]
191. Hu, S.; Maslov, K.; Wang, L.V. Second-generation optical-resolution photoacoustic microscopy with improved sensitivity and speed. *Opt. Lett.* **2011**, *36*, 1134–1136. [CrossRef] [PubMed]
192. Zhang, H.F.; Maslov, K.; Stoica, G.; Wang, L.V. Functional photoacoustic microscopy for high-resolution and noninvasive *in vivo* imaging. *Nat. Biotechnol.* **2006**, *24*, 848–851. [CrossRef] [PubMed]

193. Xia, J.; Chatni, M.R.; Maslov, K.; Guo, Z.; Wang, K.; Anastasio, M.; Wang, L.V. Whole-body ring-shaped confocal photoacoustic computed tomography of small animals in vivo. *J. Biomed. Opt.* **2012**, *17*. [CrossRef] [PubMed]
194. Lin, L.; Xia, J.; Wong, T.T.W.; Li, L.; Wang, L.V. In vivo deep brain imaging of rats using oral-cavity illuminated photoacoustic computed tomography. *J. Biomed. Opt.* **2015**, *20*. [CrossRef] [PubMed]
195. Yoon, T.-J.; Cho, Y.-S. Recent advances in photoacoustic endoscopy. *World. J. Gastrointest. Endosc.* **2013**, *5*, 534–539. [CrossRef] [PubMed]
196. Yao, J.; Wang, L.; Yang, J.-M.; Maslov, K.I.; Wong, T.T.W.; Li, L.; Huang, C.H.; Zou, J.; Wang, L.V. High-speed label-free functional photoacoustic microscopy of mouse brain in action. *Nat. Methods.* **2015**, *12*, 407–410. [CrossRef] [PubMed]
197. Nasirianvanaki, M.; Xia, J.; Wan, H.; Bauer, A.Q.; Culver, J.P.; Wang, L.V. High-resolution photoacoustic tomography of resting-state functional connectivity in the mouse brain. *Proc. Natl. Acad. Sci. USA* **2014**, *111*, 21–26. [PubMed]
198. Ning, B.; Sun, N.; Cao, R.; Chen, R.; Kirk Shung, K.; Hossack, J.A.; Lee, J.M.; Zhou, Q.; Hu, S. Ultrasound-aided Multi-parametric Photoacoustic Microscopy of the Mouse Brain. *Sci. Rep.* **2015**, *5*, 18775. [CrossRef] [PubMed]
199. Tang, J.; Dai, X.; Jiang, H. Wearable scanning photoacoustic brain imaging in behaving rats. *J. Biophoton.* **2016**, *9*, 570–575. [CrossRef] [PubMed]
200. Yao, J.; Wang, L.V. Photoacoustic Brain Imaging: From Microscopic to Macroscopic Scales. *Neurophotonics* **2014**, *1*. [CrossRef] [PubMed]
201. Kneipp, M.; Turner, J.; Hambauer, S.; Krieg, S.M.; Lehmberg, J.; Lindauer, U.; Razansky, D. Functional real-time optoacoustic imaging of middle cerebral artery occlusion in mice. *PLoS ONE* **2014**, *9*, e96118. [CrossRef] [PubMed]
202. Sakadžić, S.; Lee, J.; Boas, D.A.; Ayata, C. High-resolution in vivo optical imaging of stroke injury and repair. *Brain Res.* **2015**, *1623*, 174–192. [CrossRef] [PubMed]
203. Deng, Z.; Wang, Z.; Yang, X.; Luo, Q.; Gong, H. In vivo imaging of hemodynamics and oxygen metabolism in acute focal cerebral ischemic rats with laser speckle imaging and functional photoacoustic microscopy. *J. Biomed. Opt.* **2012**, *17*. [CrossRef] [PubMed]
204. Attia, A.B.E.; Ho, C.J.H.; Chandrasekharan, P.; Balasundaram, G.; Tay, H.C.; Burton, N.C.; Chuang, K.H.; Ntziachristos, V.; Olivo, M. Multispectral optoacoustic and MRI coregistration for molecular imaging of orthotopic model of human glioblastoma. *J. Biophotonics* **2016**, *9*, 701–708. [CrossRef] [PubMed]
205. Ku, G.; Wang, X.; Xie, X.; Stoica, G.; Wang, L.V. Imaging of tumor angiogenesis in rat brains in vivo by photoacoustic tomography. *Appl. Opt.* **2005**, *44*, 770–775. [CrossRef] [PubMed]
206. Fan, Q.; Cheng, K.; Yang, Z.; Zhang, R.; Yang, M.; Hu, X.; Ma, X.; Bu, L.; Lu, X.; Xiong, X.; et al. Perylene-diimide-based nanoparticles as highly efficient photoacoustic agents for deep brain tumor imaging in living mice. *Adv. Mater.* **2015**, *27*, 843–847. [CrossRef] [PubMed]
207. Xu, Z.; Zhu, Q.; Wang, L.V. In vivo photoacoustic tomography of mouse cerebral edema induced by cold injury. *J. Biomed. Opt.* **2011**, *16*. [CrossRef] [PubMed]
208. Tsytarev, V.; Rao, B.; Maslov, K.I.; Li, L.; Wang, L.V. Photoacoustic and optical coherence tomography of epilepsy with high temporal and spatial resolution and dual optical contrasts. *J. Neurosci. Methods.* **2013**, *216*, 142–145. [CrossRef] [PubMed]
209. Yang, S.; Xing, D.; Lao, Y.; Yang, D.; Zeng, L.; Xiang, L.; Chen, W.R. Noninvasive monitoring of traumatic brain injury and post-traumatic rehabilitation with laser-induced photoacoustic imaging. *Appl. Phys. Lett.* **2007**, *90*, 243902. [CrossRef]
210. Guevara, E.; Berti, R.; Londono, I.; Xie, N.; Bellec, P.; Lesage, F.; Lodygensky, G.A. Imaging of an inflammatory injury in the newborn rat brain with photoacoustic tomography. *PLoS ONE* **2013**, *8*, e83045. [CrossRef] [PubMed]
211. Nie, L.; Cai, X.; Maslov, K.; Garcia-Uribe, A.; Anastasio, M.A.; Wang, L.V. Photoacoustic tomography through a whole adult human skull with a photon recycler. *J. Biomed. Opt.* **2012**, *17*. [CrossRef] [PubMed]
212. Nie, L.; Guo, Z.; Wang, L.V. Photoacoustic tomography of monkey brain using virtual point ultrasonic transducers. *J. Biomed. Opt.* **2011**, *16*. [CrossRef] [PubMed]

213. Huang, C.; Nie, L.; Schoonover, R.W.; Guo, Z.; Schirra, C.O.; Anastasio, M.A.; Wang, L.V. Aberration correction for transcranial photoacoustic tomography of primates employing adjunct image data. *J. Biomed. Opt.* **2012**, *17*. [CrossRef] [PubMed]
214. Obermeier, B.; Daneman, R.; Ransohoff, R.M. Development, maintenance and disruption of the blood-brain barrier. *Nat. Med.* **2013**, *19*, 1584–1596. [CrossRef] [PubMed]
215. Daneman, R.; Prat, A. The Blood–Brain Barrier. *Cold Spring Harb. Perspect. Biol.* **2015**, *7*, a020412. [CrossRef] [PubMed]
216. Zhao, Z.; Nelson, A.R.; Betsholtz, C.; Zlokovic, B.V. Establishment and Dysfunction of the Blood-Brain Barrier. *Cell* **2015**, *163*, 1064–1078. [CrossRef] [PubMed]
217. Rosenberg, G.A. Neurological diseases in relation to the blood-brain barrier. *J. Cereb. Blood Flow Metab.* **2012**, *32*, 1139–1151. [CrossRef] [PubMed]
218. Palmer, A.M. The role of the blood-CNS barrier in CNS disorders and their treatment. *Neurobiol. Dis.* **2010**, *37*, 3–12. [CrossRef] [PubMed]
219. Winkler, E.A.; Nishida, Y.; Sagare, A.P.; Rege, S.V.; Bell, R.D.; Perlmutter, D.; Sengillo, J.D.; Hillman, S.; Kong, P.; Nelson, A.R.; et al. GLUT1 reductions exacerbate Alzheimer's disease vasculo-neuronal dysfunction and degeneration. *Nat. Neurosci.* **2015**, *18*, 521–530. [CrossRef] [PubMed]
220. Nguyen, L.N.; Ma, D.; Shui, G.; Wong, P.; Cazenave-Gassiot, A.; Zhang, X.; Wenk, M.R.; Goh, E.L.; Silver, D.L. Mfsd2a is a transporter for the essential omega-3 fatty acid docosahexaenoic acid. *Nature* **2014**, *509*, 503–506. [CrossRef] [PubMed]
221. Ben-Zvi, A.; Lacoste, B.; Kur, E.; Andreone, B.J.; Mayshar, Y.; Yan, H.; Gu, C. Mfsd2a is critical for the formation and function of the blood-brain barrier. *Nature* **2014**, *509*, 507–511. [CrossRef] [PubMed]
222. Luissint, A.-C.; Artus, C.; Glacial, F.; Ganeshamoorthy, K.; Couraud, P.-O. Tight junctions at the blood brain barrier: Physiological architecture and disease-associated dysregulation. *Fluids Barriers CNS* **2012**, *9*. [CrossRef] [PubMed]
223. O'Driscoll, M.C.; Daly, S.B.; Urquhart, J.E.; Black, G.C.M.; Pilz, D.T.; Brockmann, K.; McEntagart, M.; Abdel-Salam, G.; Zaki, M.; Wolf, N.I.; et al. Recessive mutations in the gene encoding the tight junction protein occludin cause band-like calcification with simplified gyration and polymicrogyria. *Am. J. Hum. Genet.* **2010**, *87*, 354–364. [CrossRef] [PubMed]
224. Woodfin, A.; Voisin, M.-B.; Beyrau, M.; Colom, B.; Caille, D.; Diapouli, F.-M.; Nash, G.B.; Chavakis, T.; Albelda, S.M.; Rainger, G.E.; et al. The junctional adhesion molecule JAM-C regulates polarized transendothelial migration of neutrophils in vivo. *Nat. Immunol.* **2011**, *12*, 761–769. [CrossRef] [PubMed]
225. Heye, A.K.; Culling, R.D.; Valdés Hernández, M.D.C.; Thrippleton, M.J.; Wardlaw, J.M. Assessment of blood-brain barrier disruption using dynamic contrast-enhanced MRI. *A systematic review. Neuroimage Clin.* **2014**, *6*, 262–274. [CrossRef] [PubMed]
226. Taheri, S.; Gasparovic, C.; Shah, N.J.; Rosenberg, G.A. Quantitative measurement of blood-brain barrier permeability in human using dynamic contrast-enhanced MRI with fast T1 mapping. *Magn. Reson. Med.* **2011**, *65*, 1036–1042. [CrossRef] [PubMed]
227. Sourbron, S.; Ingrisch, M.; Siebert, A.; Reiser, M.; Herrmann, K. Quantification of cerebral blood flow, cerebral blood volume, and blood-brain-barrier leakage with DCE-MRI. *Magn. Reson. Med.* **2009**, *62*, 205–217. [CrossRef] [PubMed]
228. Veksler, R.; Shelef, I.; Friedman, A. Blood-brain barrier imaging in human neuropathologies. *Arch. Med. Res.* **2014**, *45*, 646–652. [CrossRef] [PubMed]
229. Li, W.; Long, J.A.; Watts, L.T.; Jiang, Z.; Shen, Q.; Li, Y.; Duong, T.Q. A quantitative MRI method for imaging blood-brain barrier leakage in experimental traumatic brain injury. *PLoS ONE* **2014**, *9*, e114173. [CrossRef] [PubMed]
230. Taheri, S.; Gasparovic, C.; Huisa, B.N.; Adair, J.C.; Edmonds, E.; Prestopnik, J.; Grosssetete, M.; Shah, N.J.; Wills, J.; Qualls, C.; et al. Blood-brain barrier permeability abnormalities in vascular cognitive impairment. *Stroke* **2011**, *42*, 2158–2163. [CrossRef] [PubMed]
231. Cramer, S.P.; Larsson, H.B.W. Accurate determination of blood-brain barrier permeability using dynamic contrast-enhanced T1-weighted MRI: A simulation and in vivo study on healthy subjects and multiple sclerosis patients. *J. Cereb. Blood Flow Metab.* **2014**, *34*, 1655–1665. [CrossRef] [PubMed]

232. Van de Haar, H.J.; Jansen, J.F.A.; van Osch, M.J.P.; van Buchem, M.A.; Muller, M.; Wong, S.M.; Hofman, P.A.; Burgmans, S.; Verhey, F.R.; Backes, W.H. Neurovascular unit impairment in early Alzheimer's disease measured with magnetic resonance imaging. *Neurobiol. Aging* **2016**, *45*, 190–196. [CrossRef] [PubMed]
233. Jain, R. Measurements of tumor vascular leakiness using DCE in brain tumors: Clinical applications. *NMR Biomed.* **2013**, *26*, 1042–1049. [CrossRef] [PubMed]
234. Merali, Z.; Wong, T.; Leung, J.; Gao, M.M.; Mikulis, D.; Kassner, A. Dynamic contrast-enhanced MRI and CT provide comparable measurement of blood-brain barrier permeability in a rodent stroke model. *Magn. Reson. Imaging* **2015**, *33*, 1007–1012. [CrossRef] [PubMed]
235. Sorbara, C.; Misgeld, T.; Kerschensteiner, M. In vivo imaging of the diseased nervous system: An update. *Curr. Pharm. Des.* **2012**, *18*, 4465–4470. [CrossRef] [PubMed]
236. Laviña, B.; Gaengel, K. New imaging methods and tools to study vascular biology. *Curr. Opin. Hematol.* **2015**, *22*, 258–266. [CrossRef] [PubMed]
237. Aswendt, M.; Schwarz, M.; Abdelmoula, W.M.; Dijkstra, J.; Dedeurwaerdere, S. Whole-Brain Microscopy Meets in Vivo Neuroimaging: Techniques, Benefits, and Limitations. *Mol. Imaging Biol.* **2016**, *1–9*. [CrossRef] [PubMed]
238. Yang, B.; Treweek, J.B.; Kulkarni, R.P.; Deverman, B.E.; Chen, C.-K.; Lubeck, E.; Shah, S.; Cai, L.; Gradiaru, V. Single-cell phenotyping within transparent intact tissue through whole-body clearing. *Cell* **2014**, *158*, 945–958. [CrossRef] [PubMed]
239. Silvestri, L.; Costantini, I.; Sacconi, L.; Pavone, F.S. Clearing of fixed tissue: A review from a microscopist's perspective. *J. Biomed. Opt.* **2016**, *21*. [CrossRef] [PubMed]
240. Richardson, D.S.; Lichtman, J.W. Clarifying Tissue Clearing. *Cell* **2015**, *162*, 246–257. [CrossRef] [PubMed]
241. Schuermann, A.; Helker, C.S.M.; Herzog, W. Angiogenesis in zebrafish. *Semin. Cell Dev. Biol.* **2014**, *31*, 106–114. [CrossRef] [PubMed]
242. Wilkinson, R.N.; van Eeden, F.J.M. The zebrafish as a model of vascular development and disease. *Prog. Mol. Biol. Transl. Sci.* **2014**, *124*, 93–122. [PubMed]
243. Larina, I.V.; Shen, W.; Kelly, O.G.; Hadjantonakis, A.-K.; Baron, M.H.; Dickinson, M.E. A Membrane Associated mCherry Fluorescent Reporter Line for Studying Vascular Remodeling and Cardiac Function during Murine Embryonic Development. *Anat. Rec.* **2009**, *292*, 333–341. [CrossRef] [PubMed]
244. Fraser, S.T.; Hadjantonakis, A.-K.; Sahr, K.E.; Willey, S.; Kelly, O.G.; Jones, E.A.V.; Dickinson, M.E.; Baron, M.H. Using a histone yellow fluorescent protein fusion for tagging and tracking endothelial cells in ES cells and mice. *Genesis* **2005**, *42*, 162–171. [CrossRef] [PubMed]
245. Ema, M.; Takahashi, S.; Rossant, J. Deletion of the selection cassette, but not cis-acting elements, in targeted Flk1-lacZ allele reveals Flk1 expression in multipotent mesodermal progenitors. *Blood* **2006**, *107*, 111–117. [CrossRef] [PubMed]
246. Ishitobi, H.; Matsumoto, K.; Azami, T.; Itoh, F.; Itoh, S.; Takahashi, S.; Ema, M. Flk1-GFP BAC Tg mice: An animal model for the study of blood vessel development. *Exp. Anim.* **2010**, *59*, 615–622. [CrossRef] [PubMed]
247. Matsumoto, K.; Azami, T.; Otsu, A.; Takase, H.; Ishitobi, H.; Tanaka, J.; Miwa, Y.; Takahashi, S.; Ema, M. Study of normal and pathological blood vessel morphogenesis in Flt1-tdsRed BAC Tg mice. *Genesis* **2012**, *50*, 561–571. [CrossRef] [PubMed]
248. Motoike, T.; Loughna, S.; Perens, E.; Roman, B.L.; Liao, W.; Chau, T.C.; Richardson, C.D.; Kawate, T.; Kuno, J.; Weinstein, B.M.; et al. Universal GFP reporter for the study of vascular development. *Genesis* **2000**, *28*, 75–81. [CrossRef]
249. Davy, A.; Bush, J.O.; Soriano, P. Inhibition of gap junction communication at ectopic Eph/ephrin boundaries underlies craniofrontonasal syndrome. *PLoS Biol.* **2006**, *4*, e315. [CrossRef] [PubMed]
250. Laviña, B.; Gaengel, K.; Castro, M. New transgenic reporter mouse line: New tool to study vascular biology and dynamics. In Presented at the Endothelial Cell Phenotypes in Health & Disease, Gordon Conference, Girona, Spain, 6–11 July 2014.
251. Knowland, D.; Arac, A.; Sekiguchi, K.J.; Hsu, M.; Lutz, S.E.; Perrino, J.; Steinberg, G.K.; Barres, B.A.; Nimmerjahn, A.; Agalliu, D. Stepwise recruitment of transcellular and paracellular pathways underlies blood-brain barrier breakdown in stroke. *Neuron* **2014**, *82*, 603–617. [CrossRef] [PubMed]

252. Winderlich, M.; Keller, L.; Cagna, G.; Broermann, A.; Kamenyeva, O.; Kiefer, F.; Deutsch, U.; Nottebaum, A.F.; Vestweber, D. VE-PTP controls blood vessel development by balancing Tie-2 activity. *J. Cell Biol.* **2009**, *185*, 657–671. [CrossRef] [PubMed]
253. Hägerling, R.; Pollmann, C.; Kremer, L.; Andresen, V.; Kiefer, F. Intravital two-photon microscopy of lymphatic vessel development and function using a transgenic Prox1 promoter-directed mOrange2 reporter mouse. *Biochem. Soc. Trans.* **2011**, *39*, 1674–1681. [CrossRef] [PubMed]
254. Choi, I.; Chung, H.K.; Ramu, S.; Lee, H.N.; Kim, K.E.; Lee, S.; Yoo, J.; Choi, D.; Lee, Y.S.; Aguilar, B.; et al. Visualization of lymphatic vessels by Prox1-promoter directed GFP reporter in a bacterial artificial chromosome-based transgenic mouse. *Blood* **2011**, *117*, 362–365. [CrossRef] [PubMed]
255. Truman, L.A.; Bentley, K.L.; Smith, E.C.; Massaro, S.A. ProxTom lymphatic vessel reporter mice reveal Prox1 expression in the adrenal medulla, megakaryocytes, and platelets. *Am. J. Pathol.* **2012**, *180*, 1715–1725. [CrossRef] [PubMed]
256. Martínez-Corral, I.; Olmeda, D. In vivo imaging of lymphatic vessels in development, wound healing, inflammation, and tumor metastasis. *Proc. Natl. Acad. Sci. USA* **2012**, *109*, 6223–6228. [CrossRef] [PubMed]
257. Calvo, C.-F.; Fontaine, R.H.; Soueid, J.; Tammela, T.; Mäkinen, T.; Alfaro-Cervello, C.; Bonnau, F.; Miguez, A.; Benhaim, L.; Xu, Y.; et al. Vascular endothelial growth factor receptor 3 directly regulates murine neurogenesis. *Genes Dev.* **2011**, *25*, 831–844. [CrossRef] [PubMed]
258. Sevick-Muraca, E.M.; Kwon, S.; Rasmussen, J.C. Emerging lymphatic imaging technologies for mouse and man. *J. Clin. Investig.* **2014**, *124*, 905–914. [CrossRef] [PubMed]
259. Zhu, X.; Bergles, D.E.; Nishiyama, A. NG2 cells generate both oligodendrocytes and gray matter astrocytes. *Development* **2008**, *135*, 145–157. [CrossRef] [PubMed]
260. Gong, S.; Zheng, C.; Doughty, M.L.; Losos, K.; Didkovsky, N.; Schambra, U.B.; Nowak, N.J.; Joyner, A.; Leblanc, G.; Hatten, M.E.; et al. A gene expression atlas of the central nervous system based on bacterial artificial chromosomes. *Nature* **2003**, *425*, 917–925. [CrossRef] [PubMed]
261. Hall, C.N.; Reynell, C.; Gesslein, B.; Hamilton, N.B.; Mishra, A.; Sutherland, B.A.; O'Farrell, F.M.; Buchan, A.M.; Lauritzen, M.; Attwell, D. Capillary pericytes regulate cerebral blood flow in health and disease. *Nature* **2014**, *508*, 55–60. [CrossRef] [PubMed]
262. Riedl, J.; Flynn, K.C.; Raducanu, A.; Gärtner, F.; Beck, G.; Bösl, M.; Bradke, F.; Massberg, S.; Aszodi, A.; Sixt, M.; et al. Lifeact mice for studying F-actin dynamics. *Nat. Methods* **2010**, *7*, 168–169. [CrossRef] [PubMed]
263. Fraccaroli, A.; Franco, C.A.; Rognoni, E.; Neto, F.; Rehberg, M.; Aszodi, A.; Wedlich-Söldner, R.; Pohl, U.; Gerhardt, H.; Montanez, E. Visualization of endothelial actin cytoskeleton in the mouse retina. *PLoS ONE* **2012**, *7*, e47488. [CrossRef] [PubMed]
264. Pickles, S.; Cadieux-Dion, M.; Alvarez, J.I.; Lécuyer, M.-A.; Peyrard, S.L.; Destroismaisons, L.; St-Onge, L.; Terouz, S.; Cossette, P.; Prat, A.; et al. Endo-MitoEGFP mice: A novel transgenic mouse with fluorescently marked mitochondria in microvascular endothelial cells. *PLoS ONE* **2013**, *8*, e74603. [CrossRef] [PubMed]
265. Abe, T.; Fujimori, T. Reporter mouse lines for fluorescence imaging. *Dev. Growth Differ.* **2013**, *55*, 390–405. [CrossRef] [PubMed]
266. Condie, B.G. The untapped potential of the GENSAT mice—A valuable resource for developmental biology. *Genesis* **2016**, *54*, 245–256. [CrossRef] [PubMed]
267. Raichle, M.E. A brief history of human brain mapping. *Trends Neurosci.* **2009**, *32*, 118–126. [CrossRef] [PubMed]
268. Nowinski, W.L. Usefulness of brain atlases in neuroradiology: Current status and future potential. *Neuroradiol. J.* **2016**, *29*, 260–268. [CrossRef] [PubMed]
269. Amunts, K.; Zilles, K. Architectonic Mapping of the Human Brain beyond Brodmann. *Neuron* **2015**, *88*, 1086–1107. [CrossRef] [PubMed]
270. Grillner, S.; Ip, N.; Koch, C.; Koroshetz, W.; Okano, H.; Polachek, M.; Poo, M.M.; Sejnowski, T.J. Worldwide initiatives to advance brain research. *Nat. Neurosci.* **2016**, *19*, 1118–1122. [CrossRef] [PubMed]
271. Lein, E.S.; Hawrylycz, M.J.; Ao, N.; Ayres, M.; Bensinger, A.; Bernard, A.; Boe, A.F.; Boguski, M.S.; Brockway, K.S.; Byrnes, E.J.; et al. Genome-wide atlas of gene expression in the adult mouse brain. *Nature* **2007**, *445*, 168–176. [CrossRef] [PubMed]

272. Hawrylycz, M.J.; Lein, E.S.; Guillozet-Bongaarts, A.L.; Shen, E.H.; Ng, L.; Miller, J.A.; van de Lagemaat, L.N.; Smith, K.A.; Ebbert, A.; Riley, Z.L.; et al. An anatomically comprehensive atlas of the adult human brain transcriptome. *Nature* **2012**, *489*, 391–399. [CrossRef] [PubMed]
273. Miller, J.A.; Ding, S.-L.; Sunkin, S.M.; Smith, K.A.; Ng, L.; Szafer, A.; Ebbert, A.; Riley, Z.L.; Royall, J.J.; Aiona, K.; et al. Transcriptional landscape of the prenatal human brain. *Nature* **2014**, *508*, 199–206. [CrossRef] [PubMed]
274. Bakken, T.E.; Miller, J.A.; Ding, S.-L.; Sunkin, S.M.; Smith, K.A.; Ng, L.; Szafer, A.; Dalley, R.A.; Royall, J.J.; Lemon, T.; et al. A comprehensive transcriptional map of primate brain development. *Nature* **2016**, *535*, 367–375. [CrossRef] [PubMed]
275. Shen, E.H.; Overly, C.C.; Jones, A.R. The Allen Human Brain Atlas: Comprehensive gene expression mapping of the human brain. *Trends Neurosci.* **2012**, *35*, 711–714. [CrossRef] [PubMed]
276. Sunkin, S.M.; Ng, L.; Lau, C.; Dolbeare, T.; Gilbert, T.L.; Thompson, C.L.; Hawrylycz, M.; Dang, C. Allen Brain Atlas: An integrated spatio-temporal portal for exploring the central nervous system. *Nucleic Acids Res.* **2013**, *41*, D996–D1008. [CrossRef] [PubMed]
277. Bakker, R.; Tiesinga, P.; Kötter, R. The Scalable Brain Atlas: Instant Web-Based Access to Public Brain Atlases and Related Content. *Neuroinformatics* **2015**, *13*, 353–366. [CrossRef] [PubMed]
278. Van Essen, D.C.; Ugurbil, K.; Auerbach, E.; Barch, D.; Behrens, T.E.J.; Bucholz, R.; Chang, A.; Chen, L.; Corbetta, M.; Curtiss, S.W.; et al. The Human Connectome Project: A data acquisition perspective. *Neuroimage* **2012**, *62*, 2222–2231. [CrossRef] [PubMed]
279. Glasser, M.F.; Smith, S.M.; Marcus, D.S.; Andersson, J.L.R.; Auerbach, E.J.; Behrens, T.E.J.; Coalson, T.S.; Harms, M.P.; Jenkinson, M.; Moeller, S.; et al. The Human Connectome Project’s neuroimaging approach. *Nat. Neurosci.* **2016**, *19*, 1175–1187. [CrossRef] [PubMed]
280. Ugurbil, K.; Xu, J.; Auerbach, E.J.; Moeller, S.; Vu, A.T.; Duarte-Carvajalino, J.M.; Lenglet, C.; Wu, X.; Schmitter, S.; van de Moorte, P.F.; et al. Pushing spatial and temporal resolution for functional and diffusion MRI in the Human Connectome Project. *Neuroimage* **2013**, *80*, 80–104. [CrossRef] [PubMed]
281. Glasser, M.F.; Coalson, T.S.; Robinson, E.C.; Hacker, C.D.; Harwell, J.; Yacoub, E.; Ugurbil, K.; Andersson, J.; Beckmann, C.F.; Jenkinson, M.; et al. A multi-modal parcellation of human cerebral cortex. *Nature* **2016**, *536*, 171–178. [CrossRef] [PubMed]
282. Amunts, K.; Lepage, C.; Borgeat, L.; Mohlberg, H.; Dickscheid, T.; Rousseau, M.-É.; Bludau, S.; Bazin, P.-L.; Lewis, L.B.; Oros-Peusquens, A.-M.; et al. BigBrain: An Ultra-high-Resolution 3D Human Brain Model. *Science* **2013**, *340*, 1472–1475. [CrossRef] [PubMed]
283. Mohlberg, H.; Eickhoff, S.B.; Schleicher, A.; Zilles, K.; Amunts, K. *A New Processing Pipeline and Release of Cytoarchitectonic Probabilistic Maps—JuBrain*; OHBM: Beijing, China, 2012.
284. Vidoni, E.D. The Whole Brain Atlas. *J. Neurol. Phys. Ther.* **2012**, *36*, 108. [CrossRef]
285. Fan, L.; Li, H.; Zhuo, J.; Zhang, Y.; Wang, J.; Chen, L.; Yang, Z.; Chu, C.; Xie, S.; Laird, A.R.; et al. The Human Brainnetome Atlas: A New Brain Atlas Based on Connectional Architecture. *Cereb. Cortex* **2016**, *26*, 3508–3526. [CrossRef] [PubMed]
286. Gousias, I.S.; Edwards, A.D.; Rutherford, M.A.; Counsell, S.J.; Hajnal, J.V.; Rueckert, D.; Hammers, A. Magnetic resonance imaging of the newborn brain: Manual segmentation of labelled atlases in term-born and preterm infants. *Neuroimage* **2012**, *62*, 1499–1509. [CrossRef] [PubMed]
287. Kuklisova-Murgasova, M.; Aljabar, P.; Srinivasan, L.; Counsell, S.J.; Doria, V.; Serag, A.; Gousias, I.S.; Boardman, J.P.; Rutherford, M.A.; Edwards, A.D.; et al. A dynamic 4D probabilistic atlas of the developing brain. *Neuroimage* **2011**, *54*, 2750–2763. [CrossRef] [PubMed]
288. Hammers, A.; Allom, R.; Koepp, M.J.; Free, S.L.; Myers, R.; Lemieux, L.; Mitchell, T.N.; Brooks, D.J.; Duncan, J.S. Three-dimensional maximum probability atlas of the human brain, with particular reference to the temporal lobe. *Hum. Brain Mapp.* **2003**, *19*, 224–247. [CrossRef] [PubMed]
289. Jenkinson, M.; Beckmann, C.F.; Behrens, T.E.J.; Woolrich, M.W.; Smith, S.M. FSL. *Neuroimage* **2012**, *62*, 782–790. [CrossRef] [PubMed]
290. MacKenzie-Graham, A.; Jones, E.S.; Shattuck, D.W.; Dinov, I.D.; Bota, M.; Toga, A.W. The informatics of a C57BL/6J mouse brain atlas. *Neuroinformatics* **2003**, *1*, 397–410. [CrossRef]
291. Randlett, O.; Wee, C.L.; Naumann, E.A.; Nnaemeka, O.; Schoppik, D.; Fitzgerald, J.E.; Portugues, R.; Lacoste, A.M.; Riegler, C.; Engert, F.; et al. Whole-brain activity mapping onto a zebrafish brain atlas. *Nat. Methods* **2015**, *12*, 1039–1046. [CrossRef] [PubMed]

292. Milyaev, N.; Osumi-Sutherland, D.; Reeve, S.; Burton, N.; Baldock, R.A.; Armstrong, J.D. The Virtual Fly Brain browser and query interface. *Bioinformatics* **2012**, *28*, 411–415. [CrossRef] [PubMed]
293. Mai, J.K.; Majtanik, M.; Paxinos, G. *Atlas of the Human Brain*; Academic Press: Cambridge, MA, USA, 2015.



© 2016 by the author. Licensee MDPI, Basel, Switzerland. This article is an open access article distributed under the terms and conditions of the Creative Commons Attribution (CC BY) license (<http://creativecommons.org/licenses/by/4.0/>).

MDPI AG
St. Alban-Anlage 66
4052 Basel, Switzerland
Tel. +41 61 683 77 34
Fax +41 61 302 89 18
<http://www.mdpi.com>

IJMS Editorial Office
E-mail: ijms@mdpi.com
<http://www.mdpi.com/journal/ijms>



MDPI AG
St. Alban-Anlage 66
4052 Basel
Switzerland

Tel: +41 61 683 77 34
Fax: +41 61 302 89 18
www.mdpi.com



ISBN 978-3-03842-433-8